PhD-FSTM-2022-081
The Faculty of Science, Technology and Medicine

DISSERTATION

Defence held on 15/06/2022 in Esch-sur-Alzette

to obtain the degree of

DOCTEUR DE L'UNIVERSITÉ DU LUXEMBOURG

EN PHYSIQUE

by

Hediyeh MALEKZADSANI NOBAR

Born on 07 July 1986 in Tabriz, (Iran)

FABRICATION AND INVESTIGATION OF PHYSICOCHEMICAL AND STRUCTURAL GRADIENTS FOR BIOSENSING

Dissertation defence committee

Dr. David Duday
Researcher, Luxembourg Institute of Science and Technology

Dr. Sivashankar Krishnamoorthy, Dissertation supervisor
Researcher, Luxembourg Institute of Science and Technology

Dr. Jan Lagerwall**,** Chairman
Professor, Université du Luxembourg

Dr. Imma Ratera
Researcher, Institut de Ciència de Materials de Barcelona

Dr. Miran Mozetič, Vice-Chairman
Professor, Jožef Stefan Institute

Declaration

I hereby declare that the to the best of my knowledge, the research results presented in the current thesis has not been submitted for any other degree or professional qualification, and that the presented material is solely result of my own independent work except where due reference is made in the text of the thesis.

Hediyeh Malekzadsani Nobar

Abstract

Controlling biomolecule-surface interactions with nano- and micro-engineered surfaces is of great interest in biomedical applications such as tissue regeneration and biosensing platforms. Developing high-performance functional bio-interfaces for cell-surface or protein-surface interactions necessitates optimizing the interface by modifying material surface variables. Surface gradients are a category of combinatorial technique that enables monitoring and high-throughput optimization of biomolecule-surface interactions by providing a gradually varying surface parameter(s) on a small scale and across an extended area length. It is elaborated that a surface gradient not only greatly reduces the required time and labour of conducting numerous separate experiments for producing several distinct samples but also minimises the inter-batch errors associated with. In this context, multigradients are particularly promising for advanced bio-interface optimisation since they incorporate two or more separate gradients that evolve independently across different directions. While gradients have been vastly studied in past two decades, reporting different surface gradients of chemistry, topography, or mechanical nature in either nano or larger scales, there have been few studies on multigradients, due to the limited operational flexibility required for generating more than one gradient on the surface.

First, plasma technologies were explored for establishing a suitable fabricating method for generating spatial variation of surface chemistry along a direction. Both the mask-assisted static and maskless dynamic deposition were examined via two different plasma technologies, namely atmospheric pressure plasma and low-pressure plasma. Depending on the electrical conductivity of the chosen substrates and the nature of the coatings, different surface characterisations were performed on the generated samples. Surface chemistry, surface morphology and wettability properties of the treated surfaces were mainly investigated. As a result, two chemistry gradients were reported; first, an oxygen-functional chemistry gradient deposited with a single-step approach via a programmed corona discharge based on the polymerisation of HMDSO with varying flow rates of oxygen. The chemistry gradient consisted of 7 deposition conditions spanning between mostly organic and inorganic coating also exhibiting the surface energy gradient along a polyethylene foil with length of 10 cm. The surface morphology was also altered as oxygen level was increasing, leading to mild gradual surface roughening. Second, a nitrogen-functional chemistry gradient with the specific feature of enhanced water stability was reported via polymerisation of ethylene with gradually varying ammonia flow rates using a mask-assisted static deposition approach with low pressure capacitively coupled radio frequency plasmas. A smooth coating exhibiting a chemistry

gradient consisted of four deposition conditions, and a subsequent surface energy gradient was achieved along 1 cm width of a 2x1cm Si chip.

Following that, a versatile experimental setup was presented for developing the next class of surface gradients, the structural or topography gradients, which benefited from a rational design and soft lithography. As a result, a total of 4 topography gradients were reported, two of which were stochastic density gradients and the other two being periodical nanocluster density and periodical size gradients. The gradient was formed based on time-dependent incubation of the functionalised material surface with the chosen precursor and electrostatic interactions between the two. The main experimental inputs were the precursor flow rate, dimension of the experiment chamber and dimension of the substrate. For material surface functionalisation, various classes of chemistries were employed, including aminosilane monolayers, cross-linked plasma polymer, and copolymer templates for developing either stochastic or periodic arrangements of the surface features. The kinetics of incubation of each functional surface was monitored with real-time QCM before gradient formation allowing a prediction of surface coverage and all the generated gradients were investigated for their surface morphology. The obtained micrographs and the respective experimental plots and theoretical fittings confirmed the successful formation of stochastic and periodical topography gradients. Surface-enhanced Raman spectroscopy (SERS) studies revealed the high potential of gold nanocluster density gradients for SERS-based biosensing applications. However, despite exceptionally strong SERS signals recorded on the nanoparticle density gradient (generated on the plasma polymer template), the SERS response diminished at some spots along the surface, revealing a noncontinuous SERS variation. Meanwhile, gold domes did not demonstrate any enhancement as a function of size variation.

Wettability analyses were performed selectively on the stochastic gold nanoparticle density gradient utilizing both the experimental sessile drop method and theoretical modelling to investigate the probable wetting regime. The theoretical modelling indicated good agreement with the experimental WCAs and indicated Wenzel, full wetting regime.

As the ultimate objective, an orthogonal surface gradient was presented. The approach was based on depositing the previously reported nitrogen-functional chemistry gradient in a perpendicular direction over the unidirectional stochastic gold nanoparticle density gradient. As confirmed by XPS and ToF-SIMS, the surface chemical composition was retained after coating and did not change due to the presence of the underlying conductive gold nanoparticle layer. The surface morphology was significantly altered after being coated with the top plasma

layer, demonstrating an overall decreased roughness variation compared to the unidirectional nanoparticle density gradient. Furthermore, the surface wettability variation was significantly lower when compared to the wettability variation scale of the integrated unidirectional gradients.

Publications associated with this research

Malekzad H, Gallingani T, Barletta F, Gherardi M, Colombo V, Duday D. Single-step deposition of hexamethyldisiloxane surface gradient coatings with a high amplitude of water contact angles over a polyethylene foil. Plasma Processes and Polymers. 2021 Feb;18(2):2000044.

Malekzad H, Beggiato M, Hegemann D, Gaiser S, Duday D, Krishnamoorthy S. Rational route to fabrication of uni-dimensional surface gradients presenting stochastic and periodic arrangement of nanoparticles. Applied Surface Science. 2022 Apr 15;581:151763.

Acknowledgements

I would like to express my gratitude to my supervising team, Dr. David Duday and Dr. Sivashankar Krishnamoorthy, for giving me this chance and providing constant support throughout my four years of PhD studies.

I had the opportunity to receive advice and assistance from several researchers in the NEMC group particularly Dr. Emmanuel Scolan, who contributed with his insightful feedbacks in the last stages of my PhD and all the Biocluster group members, Dr Cesar Pascual Garcia and Dr Jean-Sébastien Thomann from LIST and Prof. Jan Lagerwall from University of Luxembourg, who contributed to my progress with their precious feedbacks.

I also owe to all of the friendly R&D engineers in the Material department, especially Patrick Grysan, Jérôme Bour, and Christèle Vergne, for always being available for help with their analyses and data interpretations.

I would also like to thank all of our external colleagues, especially the plasma group from the University of Bologna, Prof. Vittorio Colombo, Dr Matteo Gherardi, Dr Tommaso Gallingani, and Dr Federica Barletta, as well as the rest of the warm team, for sharing their facilities, knowledge, and support.

In the meanwhile, I'd like to thank the plasma and coating team at EMPA (St. Gallen), Dr. Dirk Hegemann, and Dr. Sandra Gaiser for their extensive collaboration and constant technical and scientific assistance during the second half of my PhD. It was a delight to collaborate and learn from Sandra and Dr. Hegemann.

I would also like to thank all the LIST colleagues who provided me technical assistance or motivations over this long journey, especially my friends from ERIN and MRT departments.

I express my sincere gratitude for the financial assistance provided for this project by FNR PRIDE/15/10935404, which made this research possible.

Finally, a big thank you to my family members for their constant encouragement, endless love, and support during this challenging process.

Table of contents

Declaration **2**

Abstract **3**

Publications associated with this research **6**

Acknowledgements **7**

Table of contents **8**

Acronyms **11**

Major Aims and Scope of the Thesis **15**

Chapter 1: Literature review **18**

1.1 General introduction 18

1.2 Biosensors 18

1.3 Biosensing interface 23

1.3.1 Biosensing application 24

1.3.2 Detection design 26

1.3.3 Surface processing 30

1.3.4 Bio-interface characterisation and iterative design 39

1.4 A combinatorial approach by surface chemistry and surface topography gradients 41

1.4.1 Considerations for the selection of surface gradients 41

1.4.2 One-dimensional chemistry gradient 41

1.4.3 One-dimensional structural gradient 55

1.4.4 Two-dimensional chemistry and structural gradient 63

1.5 Aim of the thesis 67

1.5.1 Fabricating 1-D chemistry gradients 68

1.5.2 Fabricating 1-D topography/structural gradients 68

1.5.3 Fabricating the Orthogonal gradient 69

Chapter 2: Experimental **70**

2.1 Fabrication and synthesis 70

2.1.1 Fabricating the first chemistry gradient: 1-D oxygen-containing chemistry gradient 70

2.1.2 Fabricating the second chemistry gradient: 1-D nitrogen-containing chemistry gradient 75

2.1.3 Fabricating structural gradient 77

2.2 Analysis and surface characterisation 83

2.2.1 FTIR 83

2.2.2 ToF-SIMS 86

2.2.3 Atomic Force Microscopy (AFM) 90

2.2.4 Water contact angle (WCA) 93

2.2.5 X-ray Photoelectron Spectroscopy (XPS) 101

2.2.6 Scanning Electron Microscopy (SEM) 106

2.2.7 Surface-Enhanced Raman Spectroscopy (SERS) 108

2.2.8 Nanoparticle analysis 110

2.2.9 Monitoring surface-particle interactions via QCM 115

Chapter 3: Unidirectional chemistry gradients 117

3.1 Introduction 117

3.2 1-D Oxygen Functional Chemistry Gradient 119

3.2.1 Summary of the fabrication 121

3.3 1-D nitrogen-functional chemistry gradients 123

3.3.1 Summary of the fabrication 128

3.4 Results and discussions 129

3.4.1 1-D oxygen-functional chemistry gradient 129

3.4.2 1-D nitrogen-functional chemistry gradient 141

3.4.3 Properties of chemistry gradients 154

3.5 Conclusion....162
3.6 Perspectives and potential applications of the chemistry gradients....164
Chapter 4: Unidirectional stochastic and periodical topography gradients 166
4.1 Introduction....166
4.2 Fabrication of Nanostructure Gradients....167
4.2.1 Setup....167
4.2.2 Fabrication of nanoparticle gradients with a stochastic arrangement of nanoparticles....169
4.3 Fabrication of nanoparticle gradients with a periodic arrangement of nanoparticles 174
4.4 Properties of nanoparticle gradients....183
4.4.1 Surface-Enhanced Raman spectroscopic response on nanoparticle gradients.183
4.4.2 Wettability characteristics of nanoparticle gradients....189
4.5 Conclusion and Perspectives....192
Chapter 5: Fabrication of orthogonal surface gradient..... 194
5.1 Introduction....194
5.2 Fabrication of orthogonal gradient....195
5.2.1 Elemental composition of the top layer (the chemistry gradient)....198
5.2.2 Molecular composition of the top layer....206
5.2.3 Morphology of the surface before applying the top coating....212
5.2.4 Morphology of the 2D gradient surface (after applying the top coating)....215
5.3 Properties of the 2D gradient: Wettability of the surface....219
5.4 Conclusion and perspectives....225
Chapter 6: Conclusion and Future Outlook..... 227
References 230

Acronyms

Abbreviation	Definition
AA	Acrylic acid
APTES	(3-aminopropyl)-trimethoxysilane
Ar	Argon
AFM	Atomic Force Microscopy
ALD	Atomic layer deposition
ATR-FTIR	Attenuated total reflection Infrared Fourier transform spectroscopy
APD	Avalanche photodiode detector
AuNP	Gold nanoparticle
BSA	Bovine serum albumin
CAGR	Compound annual growth rate
CVD	Chemical vapour deposition
CNC	Computer numerical control
CPS	Counts per second
c(RGDfK)	Cyclic arginine-glycine-aspartic acid-D-phenylalaninelysine
DLS	Dynamic light scattering
DOE	Design of experiment
EM	Electromagnetic

e-μCP	Electrical microcontact printing
EPO	European Patent Office
FIB	Focused ion beam
FWHM	Full width at half maximum
GAS	Gas-aggregated nanoparticle source
HIM	Helium Ion Microscopy
HMDSO	Hexamethyldisiloxane
HFW	Horizontal field width
LDV	Laser Doppler Velocimetry
LCST	Lower critical solution temperature
MSC	Mesenchymal stem cell
MLD	Molecular-layer deposition
MW	Molecular weight
nTP	Nanotransfer printing
NND	Nearest neighbouring distance
1-NT	1-naphthalenethiol
OD	Octadiene
OTS	Octyltrichlorosilane
PVD	Physical vapour deposition
ppHex	Plasma polymerised hexane
PB	Poisson–Boltzmann
PAAm	Polyacrylamide
PE	Polyethylene

PEG	Polyethlene glycol
PEI	Poly (ethylene imine)
PS-b-PVP	Polystyrene-block-polyvinyl pyridine
pSi	Porous silicon
QCM	Quartz crystal microbalance
RF	Radio frequency
RSA	Random sequential adsorption theory
RCO	Rat calvarial osteoblasts
RIE	Reactive ion etching
RI	Refractive index
ROS	Reactive oxygen species
REC	Relative elemental concentration
R&D	Research and development
RMS	Root mean square roughness
r	Roughness factor
SEM	Scanning Electron Microscopy
STM	Scanning tunnelling microscopy
SAMs	Self-assembled monolayers
SERS	Surface-enhanced Raman spectroscopy
SCCM	Standard cubic centimetre per minute
SLPM	Standard litre per minute
SL	Soft lithography
SPR	Surface plasmon resonance
T-NIL	Thermal nanoimprint lithography

3D	Three-dimensional
TLD	Through lens detector
ToF-SIMS	Time-of-Flight Secondary Ion Mass Spectrometry
TO	Transversal optical mode
TFBA	4-trifluoromethylbenzaldehyde
UV-NIL	Ultraviolet nanoimprint lithography
WCA	Water contact angle
WIPO	World Intellectual Property Organisation
XPS	X-ray Photoelectron Spectroscopy

Major Aims and Scope of the Thesis

The project is aimed at demonstrating the significance of using surface gradients as a new type of optimization tool for developing a functional bio-interface. The research effort initially focuses on identifying appropriate surface processing methods, generating chemical and topography gradients, and evaluating the surface properties of each created unidirectional gradient. Later, the possibility of combining a chemistry variable and a topography variable in a single surface is investigated, to retain (or possibly improve) the gradient properties of each individual gradient.

The entire procedure is summarized below:

- Identify the critical plasma parameters that allow fast deposition of a continuous gradient coating which display wide range of water contact angles reflecting large but gradual surface chemistry shift from fully inorganic to fully organic surface (oxygen content variation).
- Utilise the optimised process parameters of previously investigated nitrogen-functional plasma-polymerised coatings with high water resistance features to form a chemistry gradient coating with varying nitrogen content.
- Exploit adsorption isotherms obtained from real-time QCM to design an experimental scheme that allows using time as a controlling factor in order to tune surface density of the adsorbate and develop a density gradient.
- Demonstrate the applicability of the design (time as the controlling factor) to form stochastic and periodical topography gradients e.g., nanoparticle density and size gradients on various functional homogenous and patterned coatings.
- Investigate potential applications of the developed topography gradients for SER-based biosensing platforms.
- Develop multigradient by combing two gradient of different classes and investigate the conditions required for maintaining high amplitude in water contact angle variations along the direction of both gradients.

Chapter 1 of the thesis is a comprehensive introduction and literature review including description of the investigated topics with discussions on the aim and applications of each. The topics are covered in descending trend starting from a more general look and wider perspective

to more focused one. Therefore, initially biosensors as analysis tools are introduced then, the biosensing interface and the involved dynamics. Finally, combinatorial approaches for bio-interface modification applications are described with a specific focus on surface gradients with examples starting from Uni-directional gradients leading to orthogonal gradients.

Chapter 2 provides all the implemented procedures for preparing functional layers, synthesis of nanoparticles, and gradient fabrications, as well as theoretical background and instrumental specifications of all the tools utilised for analysis and characterisation of the samples.
Starting from chapter 3, each chapter is dedicated to one specific category of surface gradients, with a special introduction to the topic, results and discussion section and conclusion and future perspectives. Chapter 3 and chapter 4 represent two already published papers and chapter 5 will be the subject of a future publication.

Chapter 3 discusses the fabrication and surface properties of two Uni-directional chemistry gradients i.e.,1) oxygen-functional and 2) nitrogen-functional chemistry gradients generated using maskless approach via atmospheric pressure plasma jet and mask-assisted approach via low pressure glow discharge respectively. Surface chemistry characterisation results both elemental and molecular were reported after analysing the samples aiming to investigate the evolution of surface chemistry along with the deposited coatings as a result of variation in density and type of surface functional groups. The resulting surface wettability was also investigated as one of the key gradient characteristics due to a wide range of applications in material and biomedical fields.
The results of the first chemistry gradient are published at:
https://doi.org/10.1002/ppap.202000044

Chapter 4 reports on the fabrication procedure and results of two set of Uni-directional topography/structural gradients. After the introduction, first, the preliminary considerations and rational design are explained. Then the first set of topography gradients is presented as nanoparticle density gradients in two separate subcategories of stochastic and periodical gradients.
The first section includes the results for stochastic gradients using two homogenous amine-functional functional coatings based on i) self-assembled monolayers and ii) plasma

polymerised bilayer thin film on one hand, and results of periodic gradient, using the block copolymer templates on the other hand.

Then, the second section was presented as nanoparticle size/dimension gradient fabricated based on time-dependent in situ growth of inorganic nanoparticles using the previous copolymer template.

In this chapter, gradient properties are provided after evaluating the gradients with surface-enhanced Raman spectroscopy and wettability analysis. The theoretical wettability equations are demonstrated after modelling the surface topography of the stochastic density gradient on plasma polymerised bilayer aiming to investigate the relation between the observed wettability values along the gradient with other surface variables i.e., chemistry and roughness.

The results of the first set of topography gradient, the Unidirectional nanoparticle density gradients, are published at: https://doi.org/10.1016/j.apsusc.2021.151763

Chapter 5 reports a gradient developed by combining two independent variables of a different kind (i.e., chemistry gradient and topography gradient) in one sample to form 2D or orthogonal gradient. The aim was to demonstrate that, while the new gradient is formed with the same approaches as those used to form the individual representative unidirectional gradients and despite surface displaying very similar chemical properties, the wettability characteristic of the new gradient is fully altered due to change in surface topography (morphology, roughness). Therefore, it was suggested that the thickness of the top coating (chemistry gradient) could be optimised to maintain similar wettability variation trend as the underlying unidirectional gradients while the durability of the coating in aqueous media is largely preserved. The optimised coating would also maintain the SERS activity of the underlying gold nanoparticle gradient to some extent. This would be the subject of further future investigations.

Chapter 1: Literature review

1.1 General introduction

The main objective of this chapter is to provide a brief introduction to biosensors as a tool, before focusing on bio-interfaces, which are the key and most complex components of a biosensing device, with a specific emphasis on the necessity of optimising them. The last part will deal with surface graded bio-interfaces, the main topic of the subsequent chapters. Chapter 2 will present the processes and characterisation tools used for surface-graded bio-interfaces; chapter 3 will discuss the surface chemical gradients specifically developed in this work; chapter 4 will present the surface nanotopographical gradients obtained in this work and finally, chapter 5 will show some examples of 2D orthogonal gradients combining surface chemical gradients with nanotopographical gradients.

1.2 Biosensors

In recent decades, biosensors have emerged as the new generation of bioanalytical devices and have rapidly garnered significant attention due to their compact design, versatility and ease of application where accuracy and speed in detection are essential. The existence of several commercialised biosensors and the increasing interest in them prove their success over well-established classic analytical devices, which require centralised laboratory settings, considerably high instrumentation costs, a complicated interface, and well-trained operators. Portable biosensors can play a vital role, especially where rapid screening tests are required in remote areas with poor accessibility to clinical facilities.

A typical biosensing device consists of the following components (Figure 1):

I) A receptor, which selectively binds and recognises the targeted analyte/pathogen. A typical biosensor utilises one or a combination of several bioreceptors which are classified as antibodies, enzymes, whole-cell, nucleic acids, aptamers, etc. The name of a biosensor will also reflect the choice of bioreceptor, for instance, immunosensors are biosensors in which antibodies are the main sensing agents.

II) An interfacing surface (bio-interface), which provides a platform for sensing and where the receptor is immobilised and brought into contact with the analyte and its environment. The biosensing interface is a surface which is tailored for its surface chemistry and topography.

III) A transduction system to transform a sensing event into an output signal. Based on the information to be transduced, there are numerous types of transducers available, however, the most widely reported for biosensor fabrication are electrochemical, optical, piezoelectric, pH electrode, etc. For instance, if the mass variation is the information investigated, based on the binding of the analyte to its receptor, then a piezoelectric resonator, e.g. Quartz crystal microbalance (QCM) sensor might be the transducer of choice.

IV) Series of electrical devices to process the electrical signal, amplify and visualise the results, and a software, display and control interface.

The following scheme presents different components of a typical biosensor:

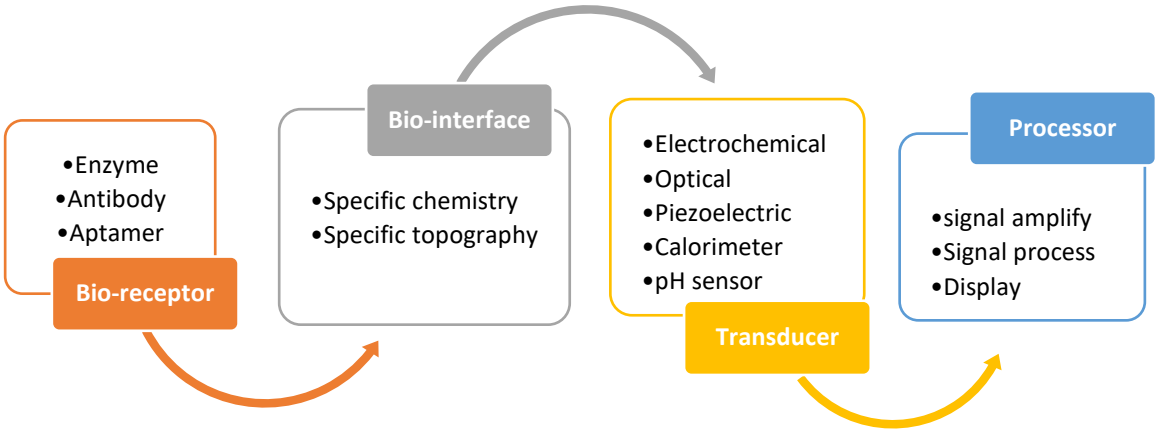

Figure 1. Different components of a typical biosensing device are presented with some examples for each component.

Biosensing is a huge market with an expected compound annual growth rate (CAGR) of around 8% from 2016 to 2026. In 2020, the total volume was USD 22.4 billion globally and USD 6-7 billion in the USA (Figure 3 & Figure 4). The most widely used biosensors are by far electrochemical ones followed by optical ones, with both growing fast (Figure 3). The main market is by far the medical one[1], which is expected to grow in parallel to the global population growth. It is accompanied by healthcare demands, i.e. diagnostics and treatment for chronic diseases (e.g. diabetes) as well as emerging infectious pandemic diseases (e.g. COVID-19). Then, agriculture and the environment are the next biggest markets and have also seen a large increase in volume. Considering one key player in the biosensing market, Abbott, its annual

[1] https://www.printedelectronicsnow.com/contents/view_breaking-news/2019-07-09/global-biosensors-market-to-register-81-cagr-through-2026-grand-view-research/

sales report shows a total of $10.7 billion, with $2.4 billion dedicated to COVID-19 diagnostic testing-related sales in 2020[2]. Next, population growth has implications for the environment, in particular, pollution caused by industrial wastewater and the need for the detection of those pollutants. The other market requiring attention to prevent food-borne diseases and food frauds, as concerns growing populations, is food contaminants. Some of the main key players in Europe for molecular biosensors are Abbott, Siemens, Nova biomedical, Sysmex, and Dynamic Biosensors. Several graphs are presented in Figure 2 indicating the volume and growth trend of the commercialised biosensors in the US market, based on i) type of biosensor and ii) field of application. The statistics and graphs are provided by www.grandviewrearch.com.

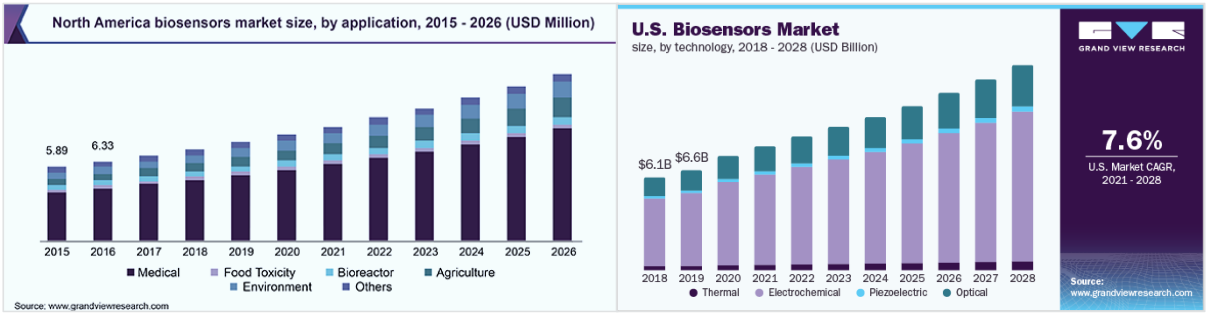

Figure 2. The US biosensor market size and predicted growth trend as a function of A) application and B) biosensor type, are presented for the years 2015-2026 and 2018-2028 respectively. Both graphs are accessible via free content published at: www.grandviewresearch.com.

The number of commercialised biosensors is still not equivalent to the tremendous output of publications in this field, especially considering that the larger share of the biosensing market is focused on very few types of biomarkers/analytes. However, the growing number of published patents in the field, as the initial output of the R&D activities and motivators of commercialised future biosensors is highly promising. The graphs in Figure 3 present the number of grants published between 2017 and 2020 based on research published by Sévérine Perbal from the Luxembourg Institute of Science and Technology:

[2] https://abbott.mediaroom.com

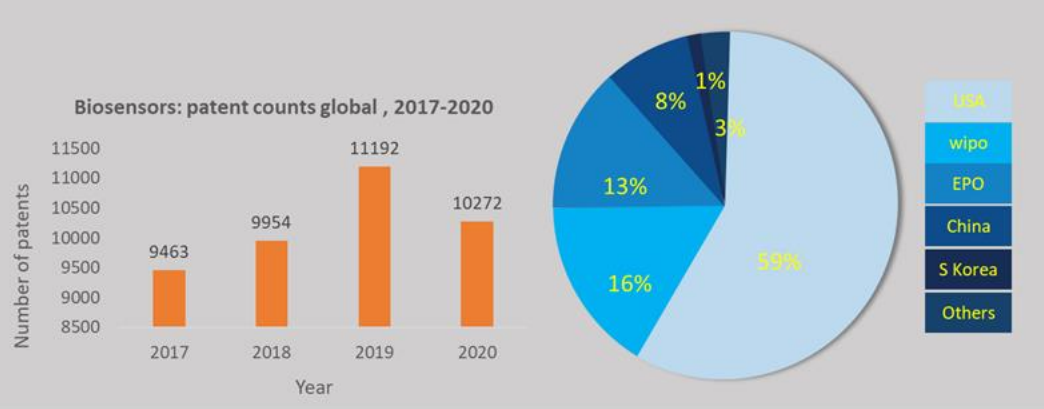

Figure 3. The number of globally published patents in biosensor field for 2017-2020 are demonstrated in the bar graph. The pie chart presents the share of patent holders by country/organisation.

Based on this market study, the highest patents were registered in 2020, showing an increasing trend from 2017. It should be noted that the lower graph corresponding to 2020 (compared to 2019), is due to the ongoing publication process of the registered patents. The key patent holders were identified as Samsung Electronics, Genentech, and the University of California and the countries/organisations with the highest contributions were found to be the USA, followed by the World Intellectual Property Organisation (WIPO) and the European Patent Office (EPO).

The increasing application demands from the health and food sectors, and the interest and authorisation from governments, as well as the ever-increasing demand for unique features such as miniaturisation, portability and reliability across various industries, are factors which could explain this increasing trend. In fact, the commercially available sensors, with applications in the health sector, and lab applications all share the features of reliability, user-friendliness and miniaturised design, as well as a reasonable price (see Figure 4)

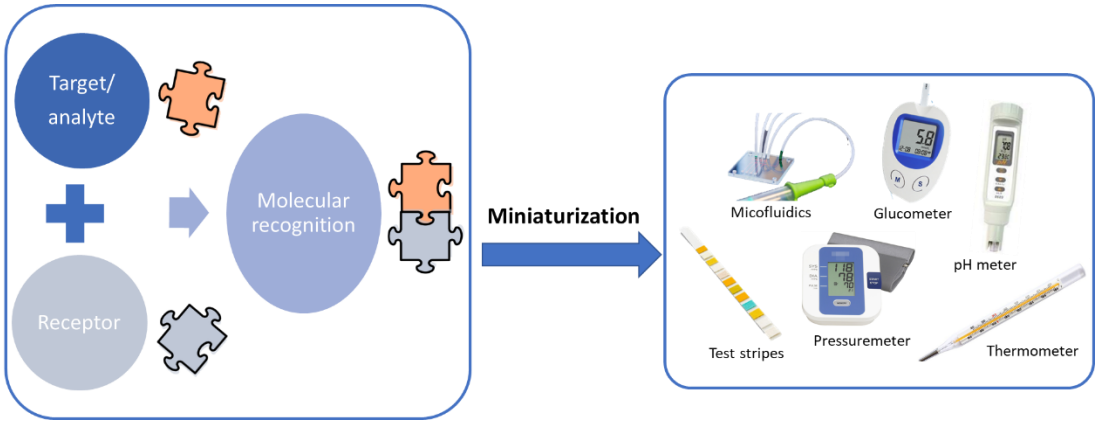

Figure 4. Molecular recognition event sensors are integrated into miniaturized devices to provide reliable and easily accessible household and laboratory sensors.

The commercialisation of biosensors, like any other business, depends on research and development (R&D) on one hand and the market demand for the product on the other hand. Innovative R&D strategies are empowered with technological advancements, creating competitiveness with the existing old strategies (1). While utilising nanomaterials has largely improved biosensing performance e.g., faster signal transduction, higher sensitivity, lower detection limit, etc., extensive multidisciplinary R&D processes, which can last for several years and incur high expenses, are a major drawback. For instance, a nanobiosensor in the medical field is estimated to take approximately 5 years and cost US$40 million to enter the market (2). Therefore, smart R&D strategies that establish a counterbalance between technology, cost and time could motivate investments and enable the commercialisation of nanobiosensors.

A broad range of factors determines the overall performance of a biosensor, each needing to be considered separately in R&D activities. Some performance-defining criteria are the right selection of the receptor (e.g. the high affinity and selectivity to the targeted analyte, availability, ease of production, durability, reproducibility, etc.) (3) along with the technological advancements in the fabrication of transduction systems which impart improved sensitivity in detection. However, as will be discussed in detail in the following sections, a bio-interface, being probably the most sensitive and challenging segment, plays a considerable defining role in the performance of a biosensor. Optimising the interface is a multidisciplinary challenge due to the complex nature of the interface, which requires expertise from different fields of chemistry, material science, engineering, etc. This platform must be optimised for its various surface properties, which are mainly surface chemistry (e.g. functional groups and thin film properties), as well as surface physical features (e.g. surface topography, mechanical

properties, etc.). The bio-interface needs to be optimised both for general properties, regardless of the bioreceptor and the transduction pathway (e.g., stability in air and a model physiological medium), and the very specific aspects required for a unique type of biosensor (e.g., high electron-transfer rate for electrochemical biosensors). With that being said, it is necessary to look at the bio-interface design and the potential challenges in developing and optimising a bio-interface in more detail.

1.3 Biosensing interface

A biosensing interface is an essential part of a biosensing device, which strongly determines the ultimate detection performance. Since the biointerface is integrated into the signal transduction section and is in direct contact with the bioreceptor/analyte pair, its development requires skills in the interplay between chemistry, material science, physics, and biology.

Figure 5 is intended to illustrate the complex environment in which a bio-interface is positioned. As can be seen in the scheme, there are numerous important aspects/properties to be optimised for each component that makes up a bio-interface. The complexity is due to the numerous variables involved, which might potentially impact the detection output. Taking material surface as an example, there are numerous characteristics which are tailored according to the choice of bio-receptor, analyte, and the transduction system. For instance, if a pathogen should be able to be detected using an electrochemical immunosensor, the choice of substrate, i.e., the electrode surface as well as the surface chemistry, is dictated by using electrically conductive materials that accelerate electron transfer. Biocompatibility is also clearly an essential requirement for the bio-interface material regardless of all the biosensor types and application. Also, the selected surface chemistry and topography should ensure the optimal density of the immobilised receptor (antibody in this case) which retains the function of the probe and allows the binding of more analytes. On the other hand, based on the transduction pathway, the bioreceptor must be labelled with an electro-active signal-transducing tag or an equivalent.

In the following sections, the general steps involved to achieve a fully functional bio-interface are introduced in chronological order.

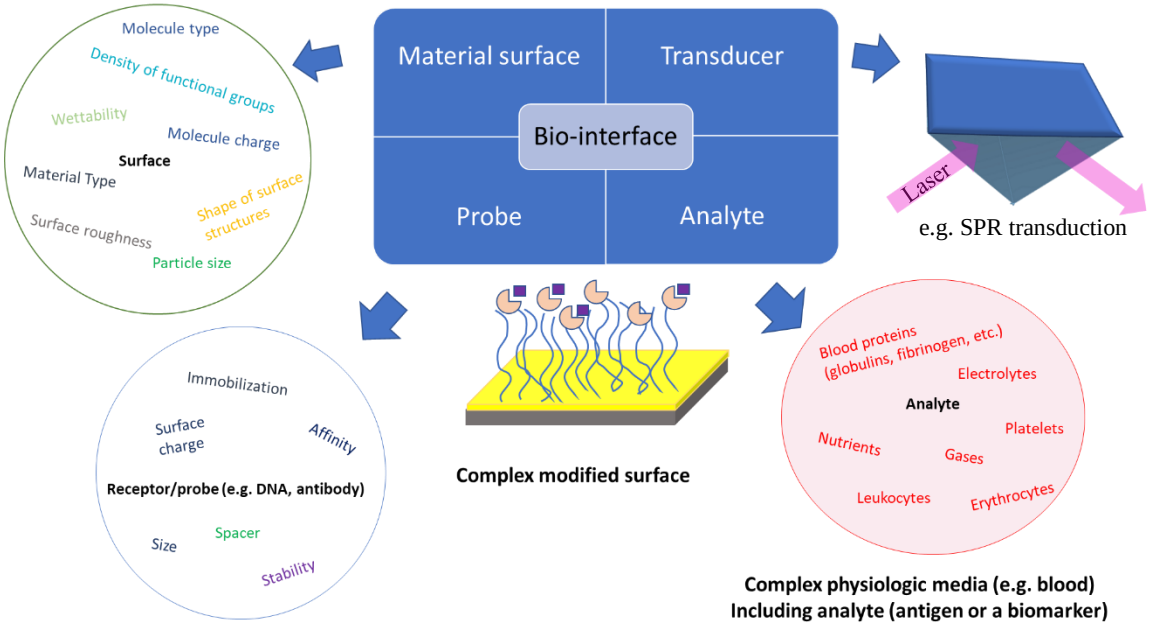

Figure 5. The bio-interface is a surface located at the intersection of four elements: material surface, transducer, analyte and probe. As can be seen, each element includes many features and parameters that play either an independent or concurrent role. Every single parameter is a factor that defines the output of the bioassay or generally a biomolecule-surface interaction. This illustrates how unrealistic it is to precisely foresee the behaviour of such a complex system, underlining the need for the optimisation of the interface considering as many parameters as possible.

1.3.1 Biosensing application

As illustrated in Figure 6, the detection strategy is designed depending on the targeted end application, and the biointerface is processed and optimised in order to develop a functional bio-interface.

When defining the end application, the following main questions are addressed:

- -What is the analyte (e.g., chemical, disease biomarker, bacteria, etc.) and the sample size to be detected?
- Where will the device be used? e.g., industry, clinical lab, home, remote rural locations, etc. This would define the degree of robustness, complexity, durability, compactness, portability, etc.
- What is the area of the bio-interface considering the analyte size and the transduction system? Bacteria and cells require a bigger surface area (up to several microns) while small chemical toxicants occupy a much smaller area (sub nanometres). For example,

a nanosized field-effect transistor surface requires only nm^2 coverage with the bio-receptor while conventional electrode surfaces for electrochemical detections require mm^2 surface coverage.

- What should the characteristics of the surface be in terms of chemistry and topography? This question is accompanied by many relevant sub-questions e.g. what surface chemistry and chemical interaction is preferred to immobilise the bio-receptor on the surface?

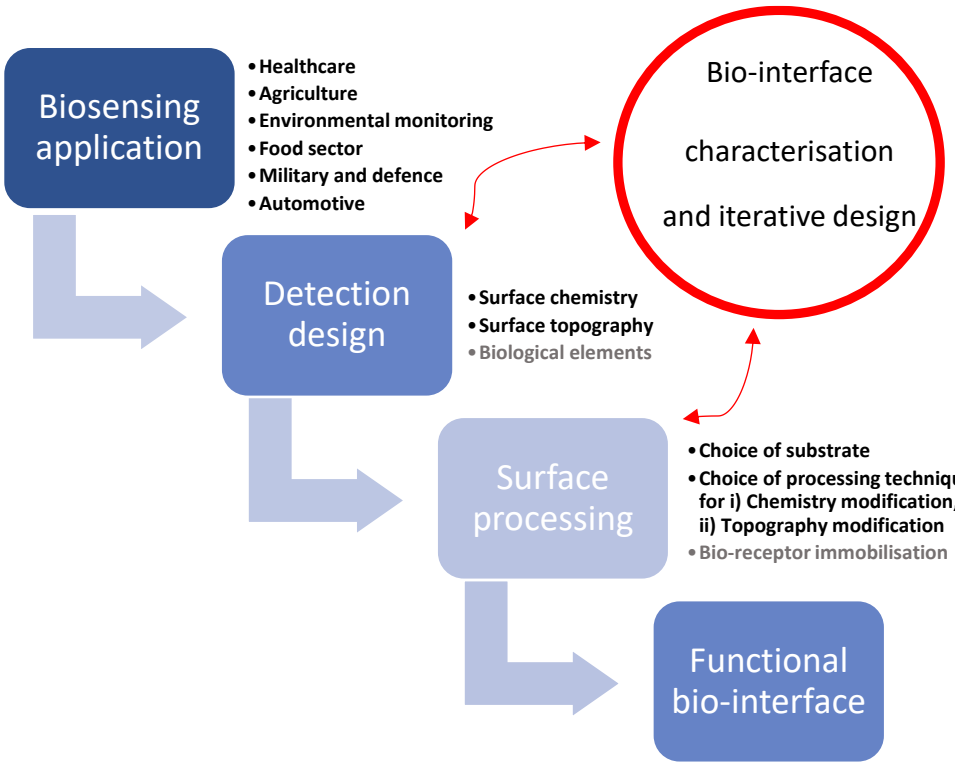

Figure 6. The pathway toward fabricating a highly performing functional bio-interface is illustrated. The process starts from the i) end application and then moves on to ii) designing the sensing interface followed by iii) selecting the right material and processing approaches to implement the design and finally, iv) analysing the bio-interface and taking iterative approaches (going back and forth between the second and third stages) until the desired optimisation is achieved.

Also, besides biocompatibility and bio-receptor immobilisation, a bio-interface should be tailored based on the transduction approach, e.g. if it is employed for optical transduction, a bio-interface surface material must be optically responsive. Meanwhile, for bio-interfaces developed for cell studies, surface topography and surface mechanical properties (stiffness, etc.) are usually switched to promote specific cell behaviours. The topography variation

combined with chemistry variation are combined to tune the surface wettability characteristic which is a key surface property for many biomedical investigations.

1.3.2 Detection design

After defining the end application and before starting to process the bio-interface, the detection scheme needs to be designed in terms of the required surface chemistry, surface topography and biological elements, as the three key players of a functional bio-interface. The properties and impact of each three items are briefly described in the sections below.

1.3.2.1 Surface chemistry

The surface is chemically modified by coating, activating or introducing specific functional groups/substances to the substrate surface, which can be organic, inorganic or hybrid organic-inorganic. The surface chemistry is modified to impart specific characteristics or functions to the bio-interface. Surface chemistry is usually tuned to:

- ***Immobilise the bio-receptor:***

One challenge of developing a bio-interface is immobilising the bioreceptor, which can be of a different nature. Immobilising the protein-based bioreceptors, such as enzymes and antibodies, requires either covalent bonding or strong electrostatic interactions with the functional groups on the surface. Meanwhile, the protein-surface interaction has an indirect implication for cell studies. For instance, for over two decades, the interaction of adhesion-promoting proteins such as fibronectin and vitronectin with various surfaces of gradually varying chemistry (hence wettability) has been ongoing to unravel cell-surface interactions (4). Taking antibodies as an example, while increasing the number of antibody receptors on the surface is desirable, the necessity of improving the orientation of the antibody cannot be overlooked. It is possible to guide and control the orientation of antibodies by tailoring surface chemistry. This is carried out either through surface functionalisation with chemical groups to modify hydrophobicity and surface charge and/or the pre-treatment of the surface with specific proteins (i.e. proteins A and G), which favour immobilisation of the antibody through the Fc-fragment (5).

- ***Integrate the surface with the transduction section***

Since the modified surface interfaces the substrate and the transduction system, the surface coating should be adopted based on the chosen transduction pathway. For instance, for electrochemical biosensors, electrochemically active coatings are essential and for optical transduction, optically active coatings.

- ***Impart biocompatible properties***

Every bio-interface requires some general and some specific mechanical properties depending on the application. One general requirement for every material that will be in contact with biological elements is its bio-compatibility, meaning that it should not alter the function of biological elements. Meanwhile, biomaterials which are employed for medical applications and intended to be directly in contact with the body for regenerative or restorative approaches may also be required to be non-toxic, biologically active or biologically inert, etc.

- ***Stability of the biosensing interface***

As biosensing is usually conducted in an aqueous medium, maximising the stability in water and the specific pH of the sensing environment is essential for the top-coating, especially for water-soluble polar chemical functional groups. Also, the top coating should be durable while being stored in the air and ambient temperature conditions.

- ***Mechanical properties of biomaterials for medical applications***

Depending on the targeted application, specific mechanical properties are critical for the proper functioning of biomaterials. For instance, when developing biomimetic tissues, such as scaffolds for bone tissue engineering, some mechanical properties such as elasticity, stress resistance, fracture resistance, fatigue, etc., are tailored to match the organ site that they will be implanted in (6).

- ***Modulating surface wettability***

Surface wettability is a function of two surface characteristics, surface chemistry and surface topography, which can be either modified individually or together to impart the desired wettability. Treating a surface with strongly polar groups (carbonyl, carboxylic, etc.) with high density increases surface energy and consequently, a water droplet interacts strongly with a surface leading to the partial or full spreading of the droplet after contact with the surface. Reversely, apolar groups (e.g., fluorinated functional groups) decrease in surface energy causing water molecules in droplets to condense and strongly bind to each other. As a consequence, the water droplet is partially or fully repelled from the surface. Surface molecules with moderate polarity or moderate apolarity, are positioned between these two extreme cases which induce moderate hydrophilicity or hydrophobicity respectively. Many processes in the biomedical field that rely on surface adsorption (physisorption, chemisorption, etc.) are influenced by surface wettability. For instance, it has been observed that surface chemistry, combined with surface nanotexturing, affects bioreceptor immobilisation by altering the wettability of the surface (7).

1.3.2.2 Surface Topography

Surface topography is the next defining property in developing bio-interfaces and has several implications for biomedical applications. Surface topography is often switched to:

- ***Allow the investigation of cell behaviours***

It is demonstrated that the engineering nanoscale surface feature (protuberance), which has a similar size to the cell adhesion receptors, triggers signalling pathways mediated by integrins (the adhesion receptors on tip of filopodia) (8). For instance, in several cell studies using a surface nanopillar with different height values generated with lithography techniques, it was shown that the focal adhesions of density, maturation, cytoskeletal organisation, cell morphology and cell spreading are influenced by the height of the pillars (9, 10). The spacing between surface structures can also affect cells and trigger specific behaviours in different types of cells. This can be attributed to the size of microvilli or pseudopodia and can be tuned for optimum cell spreading and orientation (11). Other studies on the impact of interpillar properties on the differentiation of various stem cells proved the impact of the nanopillar spacing on the polarisation of the cell body, the extension of cellular projection and the alignment of these projections (12).

The other important feature of the surface protuberances is the aspect ratio, which defines the stiffness/rigidity of structures and may provoke a different response manifesting in the morphology of stem cells such as stretching and elongation (13). There is a recent report on fabricating pillar arrays with a gradient of pillar properties (size, height, density), which vary independently (14). This and similar studies are particularly promising for cell studies and the development of biomaterials for tissue regeneration, as well as implant applications.

- ***Improve the density of bioreceptors***

The 3D structure of surface topographies offers more binding sites for bio-receptors compared to the plane surface, especially nanostructures owing to their higher surface-to-volume ratio which enhances the surface area for anchoring a higher number of bio-receptors, which in turn enhances the sensitivity of detection. Besides the density of bioreceptors, for successful biorecognition, immobilisation (whether implemented through physical adsorption or covalent binding) should ensure bioactivity (especially in the case of protein bioreceptors), which requires the retention of their native conformation and the right orientation on the surface (15).

- ***Enhance transduction sensitivity***

Besides the implication of surface protuberance for cell studies, surfaces modified with controlled nanoscale surface features are employed for biosensing applications. For instance, the spacing between plasmonic noble nanoparticles is tailored to transduce the sensing output through a plasmon coupling effect. Hotspots generated by closely packed nanostructures benefit by achieving such a low sensitivity that a single molecule can be detected (16) and can be also adapted for biosensing applications (17). Besides the interparticle/inter-structure gap, the size (18) and morphology (e.g. the shape of nanoparticles) (19) of the features affect the magnitude of field enhancement, and hence, can influence detection sensitivity. For instance, in a systematic study of the effect of surface topography on the biosensing output, the correlation between the size of the gold nanoparticles, on a surface with closely-packed particles, and the sensitivity of the biosensing output was studied using nanoparticles with varying dimensions. The highest optical response to refractive index variations of the surrounding medium upon introducing Streptavidin was observed for a nanoparticle of around 40 nm in size (20).

- ***Controlling wettability***

One other way to control the surface-biomolecule interaction is to tune surface roughness properties (e.g., roughening the surface) either on their own or in combination with varying surface chemistries to impart the desired wetting characteristic, which either enhances or inhibits the interaction of specific biomolecules with the surface.

1.3.2.3 Biological elements

Biological elements intended to selectively bind and recognise specific analytes can be divided into two categories of natural and synthetic receptors. While enzymes, antibodies, nucleic acids and cells are natural receptors, aptamers are regarded as synthetic or biomimetic receptors.

The choice of receptors for specific detection applications depends on several aspects e.g., selectivity, availability, cost considerations, stability in specific temperature and pH conditions, etc. For instance, in a study focused on developing nanophotonic Label-Free Biosensors for detecting Covid-19, in order to select the right detection strategy between the potential candidates i.e. genomic detection (based on using e.g. DNA), intact virus detection (e.g. antibodies, aptamers, etc.) and serological assays (e.g. using viral lysates), and accordingly, the right bio-receptor type, several comparisons were carried out with some of them summarised below (21):

- ***Specificity or selectivity***

Antibodies have proven to have high selectivity and high binding affinity to the target.

- ***Costs of production***

The antibodies are proven to be more costly than Recombinant antibody fragments, glycans and aptamers.

- ***Lower detection limits (sensitivity)***

The Tagged stem-loop probes, amplification plus DNA probes have been highlighted as those with the lowest sensitivity.

- ***Stability***

DNA probes have been highlighted as being more stable than protein probes.

- ***Ethical aspects***

Antibodies require the use of animals while recombinant antibody fragments and aptamer receptors do not require the use of animals for production.

The abovementioned aspects, along with the optimal quantity of probe to be immobilised, surface immobilisation strategy and the required reagents, balance between high surface coverage and steric hindrance, etc., must be investigated when designing a detection strategy.

1.3.3 Surface processing

1.3.3.1 Choice of substrate

The choice of the substrate is usually defined by:

i) the transduction technique (type of biosensor), which will be utilised for detection:

While Si wafers are usually adaptable substrates of choice for developing the biosensing interface, some techniques require the use of specifically designed substrates. For instance, for developing optical plasmonic substrates, the Si substrate must be developed with a plasmon-active material i.e. either a thin noble metal e.g. gold for fabricating a typical surface plasmon resonance (SPR) biosensing bio-interface or noble metal nanomaterials for biosensing based on surface-enhanced Raman scattering and surface-enhanced Fluorescence spectroscopy techniques.

Chips for some transduction techniques are also commercially available. For instance, for the QCM transduction technique, a specific round chip including the quartz resonator is available. Also, electrochemical transducers are usually conductive metallic electrodes with a surface modified with electro-active materials such as metallic nanoparticles, quantum dots, graphene, etc.

ii) the characterisation techniques, which foresee the use of:

Optical surface characterisation and imaging techniques e.g. optical microscopes, usually require the use of an optically transparent substrate e.g. glass. Therefore, even if the Si is the material of choice, the same modifications can be applied separately on a glass substrate and used for optical characterisations. Unlike optical imaging and characterisations, for several surface chemistry characterisation techniques such as XPS, TOF-SIMS, as well as electron beam microscopy, electrically conductive materials such as intrinsic Si are required. On the other hand, techniques such as ATR-FTIR and Helium Ion Microscopy (HIM) can be implemented on both conductive and non-conductive materials.

1.3.3.2 Surface chemistry modification

Numerous techniques have been developed for tuning the chemistry of the surface without affecting the bulk material properties. This is accomplished by introducing organic or inorganic molecules/substances in the form of a monolayer, polymeric thin films, nanoparticles, etc. (see Figure 7).

- ***Thin film coatings:***

Thin films are thin layers of coatings, which are deposited on a substrate with a thickness usually varying from the nanoscale up to a few micrometres. These coatings are developed with the desired surface properties e.g. surface functional groups for immobilising molecules/biomolecules and/or are utilised as a platform to initiate reactions. As illustrated, the thin layer can be a metal, composite, compound (e.g. oxides) or polymer (e.g. plasma-polymerised) nature. Thin films are extensively investigated as a layer to protect the bulk material or impart the desired chemical or topographical properties without affecting the bulk material. The main advantage of these techniques is the flexibility in the choice of the substrate to deposit. Thin film deposition techniques can be implemented via i) physical (PVD) vapour deposition, ii) chemical vapour deposition (CVD) and iii) solution-based techniques (electrochemical, dip-coating, spin-coating, sol-gel, chemical bath deposition, etc.) (22).

i) PVD is usually used to deposit metallic layers on the surface by depositing atoms after evaporation or sputtering. In the evaporation method, after vaporising the bulk material, the vapour of atoms is transferred to the vacuum chamber and condensed on a substrate generating a thin film layer, which is adhered to the substrate (23). PVD techniques include ion plating, ion implantation, sputtering and laser-surface alloying (23). PVD is well-suited to the deposition of inorganic, and especially metal, layers on conductive substrates.

ii) Gas or vapour-phase surface functionalisation with mainly organic coatings, and chemical vapour deposition (CVD), encompasses a vast variety of techniques each adapted for a specific

application. Some of the CVD techniques that are exploited to deposit conformal, substrate-independent polymeric coatings with modifiable fouling behaviours are plasma-enhanced CVD (PECVD) and initiated CVD (iCVD)/photoinitiated CVD (piCVD). (24). Atomic layer deposition (ALD) is the other innovative gas-phase technique used to apply inorganic surface functionalities (metallic compounds, nanostructures, oxides, etc.) with atomic-level control via vapour-phase and successive surface reactions (25). While it is possible to fabricate more advanced coatings via CVD with high flexibility of the surface functional groups, the disadvantage of this is the need for rather complex and costly instrumentation especially compared to conventional solution-based techniques.

iii) Classic solution-based techniques (e.g., spin coating and dip-coating) use a setup mainly based on casting the solution, including the deposition material, on a substrate followed by solvent evaporation or curing step. These techniques can be carried out with simple automation, without using costly instrumentation (e.g., vacuum systems) and can be implemented on a variety of substrates. The other popular solution-based surface functionalisation technique is the electro-deposition of functional organic and inorganic materials, e.g. deposition of carbon Reduced Graphene Oxide thin films on sensor surfaces (26).

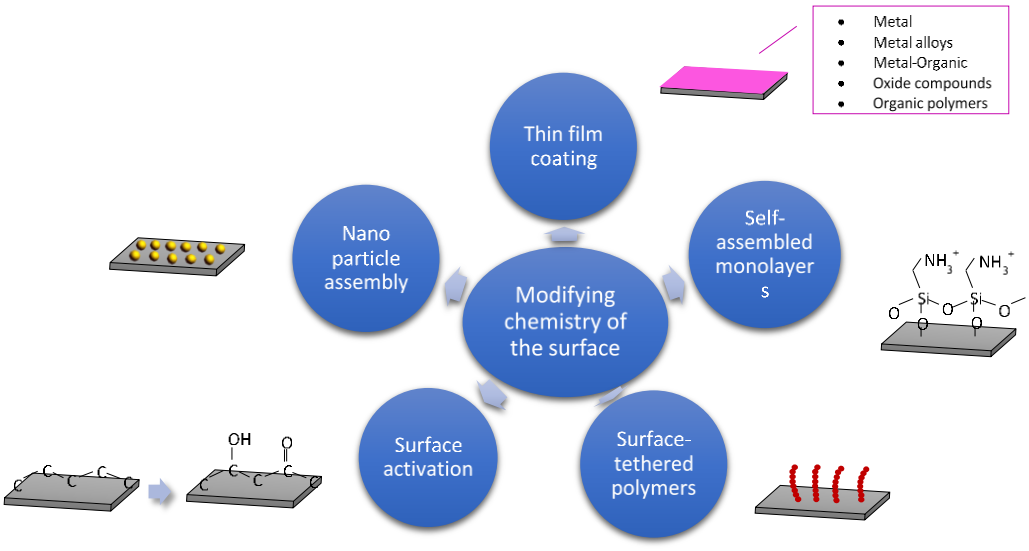

Figure 7. Several popular pathways to impart chemical functionality to a surface.

- ***Self-assembled monolayers (SAMs)***

These coatings are monolayers of molecules that spontaneously assemble on the surface through either electrostatic bonding or other chemical interactions (e.g., chemisorption). These monolayers are advantageous due to them offering ordered and well-defined surface chemistry yet is limited to the choice of substrate (e.g. thiolated alkanes are applied to metallic surfaces like gold and silver and, silanes are applied to oxide surface such as silica) and the need for employing organic solvents.

SAMs are tailored according to the substrate type in the tail of the molecule where it is anchored to the surface and a vast selection of functional groups may be added to the other end (head) of the molecule, where biomolecules are immobilised. SAMs are very important for controlling the orientation of the binding biomolecules, protecting them against denaturation by shielding them from the substrate surface and preventing the non-selective adsorption of proteins on the substrate surfaces (27). Frequently, SAMs are deposited via solution-phase techniques, vapour-phase techniques or the molecular-layer deposition (MLD) method as an alternative to conventional vapour-phase deposition (28).

- ***Surface-tethered polymers (polymer brushes)***

Polymer brushes are a popular class of surface-tethered materials that have been extensively investigated to switch solid surface properties. The polymeric changes are grafted onto a solid surface through different pathways. For instance, end-modified chains can bind to the functional groups present on the modified surface (the graft to approach) or polymerisation can be directly synthesised from the surface (the graft from approach) via anionic, cationic and free radical polymerisations, etc. after applying initiator groups on the substrate (29).

Despite similarities with SAMs, polymer brushes offer higher design flexibility (e.g. possibility to tailor their molecular weight, graft density, etc.) and a higher density of functional groups owing to their three-dimensional (3D) structure and accordingly, the possibility of binding with more numbers of biomolecules per unit area than the 2D SAMs with confined reactivity (30).

- ***Surface activation***

Activation is usually regarded as a surface pre-treatment process which is carried out before the surface is coated or an experiment being conducted on the surface. It is intended to make the surface ready for a reaction either by cleaning or improving some surface properties (oxidising the surface). Classic techniques include the immersion of the substrate inside piranha solution (1:4/H_2O_2:H_2SO_4), UV ozone treatment or plasma activation (i.e., reactive ion etching).

These techniques modify the surface temporarily, meaning that the original surface is readily recovered after some time. Furthermore, the selection of chemical groups that can be imparted to the surface using these techniques is limited.

- ***Nanoparticle assembly***

Metallic nanoparticles and especially noble metal nanoparticles are utilised in biosensor design for multiple applications, owing to their excellent features. Electrodeposition is one of the most popular approaches to generating metal nanoparticles on an electrode surface either alone (31) or in the form of a nanocomposite (32). Alternatively, surface-modified metallic nanoparticles are synthesised separately via one of the classic well-established methods (e.g. Turkevic method) and then stabilised on the surface based on electrostatic interactions with the substrate simply by incubation of the substrate with colloidal suspension. Metallic nanoparticles might take on several roles in bio-interface design due to the high surface-to-volume ratio and excellent optical and electrical properties. For instance, NPs can be employed as a platform to immobilise bioreceptors (in any type of biosensors), as an electron wire (in electrochemical biosensors), as a catalyser (to facilitate a reaction e.g. between a chemiluminescent and its substrates), a mass sensitivity amplifier (in piezoelectric biosensors) and also in order to amplify refractive index (RI) variations in plasmonic biosensors (33).

1.3.3.3 Surface topography modification

Tailoring the surface topography of the bio-interface to enhance biomolecule-surface interactions is accomplished through two main approaches:

a) Indirectly through chemistry, i.e., the deposition of particles/polymers or thin film, which can also be combined with lithography to generate the desired surface structures. It should be noted that the roughness of the surface is often unintentionally varied during plasma deposition, especially when employing oxygen during polymerisation which must be controlled when modifying the chemistry of the surface.

b) Directly by manipulation of the surface texture of the bulk material e.g. changing the microstructure of the polymer surface by heating, partial melting and eliminating porosity (which switches a porous hydrophobic surface to a smooth hydrophilic surface) (34) or particle erosion followed by time-controlled chemical polishing (35).

Controlling events in a nano-bio interface, where biophysiochemical interactions between nanomaterials and biological elements occur, is essential for vast varieties of biomedical applications e.g. nanodiagnostics, nanotherapeutics, nanotheranostics, regenerative

nanomedicine, etc. (36). This implies the need for tuning various nanomaterial properties including topographic cues through the right fabrication techniques.

Nanofabrication encompasses numerous techniques that have been widely reported for surface modification and offers the advantages of reproducible and high-resolution nanoscale patterns and structures. Figure 8 is intended to classify several classes of nanofabrication which are summarised in (37).

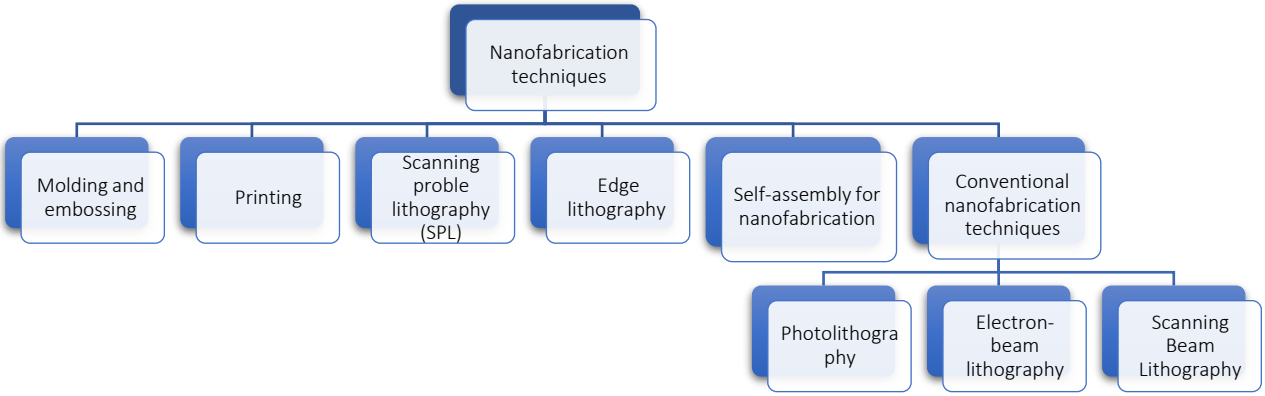

Figure 8. A classification of nanofabrication techniques.

- ***Moulding and embossing***

Nano hot-embossing and injection moulding are two typical techniques based on employing replicas for the mass production of nanoscale features on a large surface area.

Hot embossing is operated based on a simple principle of heating the mould and material to a certain temperature higher than the glass transition temperature of the material for a while, as mould is gradually pressed into the workpiece up to a certain degree. After a hold time, the pressure is decreased, and the mould is detached.

On the other hand, the injection moulding process involves the injection of the molten material into the cavity of the replica, allowing it to cool down and then detaching the replica.

While the main advantage of these processes is the simplicity of the fabrication strategy and high throughput, the fabrication often suffers from frequently occurring defected features due to the small size of the features being impacted by the high thermal stress, adhesion and friction in the interface between the replica and the material (38).

- ***Printing***

With printing techniques, structures are transferred to the desired surface using a patterned stamp. Nanotransfer printing (nTP) and Electrical microcontact printing (e-μCP) are two extensions of the micro contact printing technique which are utilised to transfer the patterns to the surface. In the first approach, after coating the stamp with the desired material (e.g. thiolated SAMs), the stamp is pressed into the surface of the substrate and then released to allow pattern transfer based on a selected strategy e.g. covalent binding between thiolated alkanes to a gold surface. In the second approach, however, after contact between the coated stamp (e.g. gold coated stamp and n-dopped silicon surface) and the surface is established, a voltage is applied in the interface between the surface and stamp to allow electrostatic charge patterning over the surface, which is responsive to electrostatic potential (39).

- ***SPL***

In SPL techniques, a sharp-tipped probe is used to directly transfer patterns onto a surface with high resolution and precision either via the deposition of materials to the surface or the abrasion of the existing surface coating. The major techniques of SPL used for nanofabrication are (40):

- Scanning tunnelling microscopy (STM) which patterns the surface via positioning atoms of the surface material via a specific ST tip.
- Dip-pen nanolithography pattern surface via the depositing of materials (SAMs, nanoparticles, etc.) using an inked tip (atomic force microscopy (AFM) tip) and bringing it into contact with surface.
- Nanoshaving, which operates based on removing the surface coating locally (e.g. SAMs) with AFM tip.
- Scanning electrochemical oxidation, which patterns the surface with selective and local oxidation of the surface.

The disadvantage of these techniques is their slow writing time, which limits their application to patterning small areas.

- ***Edge lithography***

The edge lithography technique is based on employing the micrometric edges of a stamp to transfer patterns to the surface on the nano or microscale (41). Edge lithography includes various techniques, with one of the most popular of them being phase-shifting edge lithography, which is similar in process to the photolithography approach due to the feature that induces a phase shift on the UV beam via the edges of an elastomeric stamp to generate the desired nanoscale features. The patterned photoresist can be further utilised for a variety of

applications e.g. to deposit nanoparticles on the confined areas (39). Edge lithography offers the advantages of high throughput and cost-effectiveness, however, it is limited in generating complex surface patterns.

- ***Self-assembly for nanofabrication***

Nanofabrication with self-assembled colloidal particles, colloidal lithography, is a class of nanofabrication that allows surface decoration with colloids of different natures e.g. polymeric particles, metals, magnetic and semi-conductor particles and with controlled size and shape. After coating the surface with colloidal particles, they may be directly employed either without a top coating or after further coating with, for example, an organic top layer to form a homogenous patterned surface which can be used for biomedical applications. Alternatively, they may be utilised as an etch mask to develop secondary surface topographies such as nanopillars. Several methods have been practised for surface immobilisation with colloidal particles such as electrostatic interaction between functionalised colloidal particles and activated surfaces, drop-casting, spin-casting, biotin-avidin, electrophoretic deposition of colloids, etc. (42).

These techniques offer high throughput, cost-effective and simple approaches to pattern surfaces with nanoscaled features. However, reproducibility of the surface topography is limited, due to degrees of heterogeneity in the size and shape of the synthesised particles and repulsion between adjacent particles. Hence, if well-ordered arrays with high precision are required, these techniques need to be combined with other multistep lithography techniques.

- ***Conventional nanofabrication techniques***

Conventional nanofabrication techniques involve writing techniques such as UV lithography, x-ray lithography, ion-beam lithography, e-beam lithography, etc. where radiation of different sources is used to interact with a substrate coated with a radiation-sensitive resist to transfer patterns with high resolution and high precision either directly or using a mask. In typical lithography approaches such as UV and x-ray lithography, UV and X-ray beams are passed through a mask with defined shapes to interact with desired regions on the resist surface and depending on the solubility of the selected photoresist type, either the exposed regions or non-exposed regions are developed (removed). The exposure process is followed by a developing step, where the resist is allowed to incubate in a developing solvent and finally, the pattern transfer step is carried out with different possible pathways depending on the targeted application i.e. lift-off, etching, doping, re-growth (43). Developing nanoscaled patterns with

photolithography and x-ray lithography techniques over an extended area requires the use of masters, which are developed with e-beam lithography or scanning probe microscopy techniques. For biomedical applications, the patterns need to be transferred to the biocompatible polymers using masters, however, these masters are expensive and not easily accessible for biologists. Figure 9 illustrates the general steps and some common pathways involved in nanofabrication using conventional lithography.

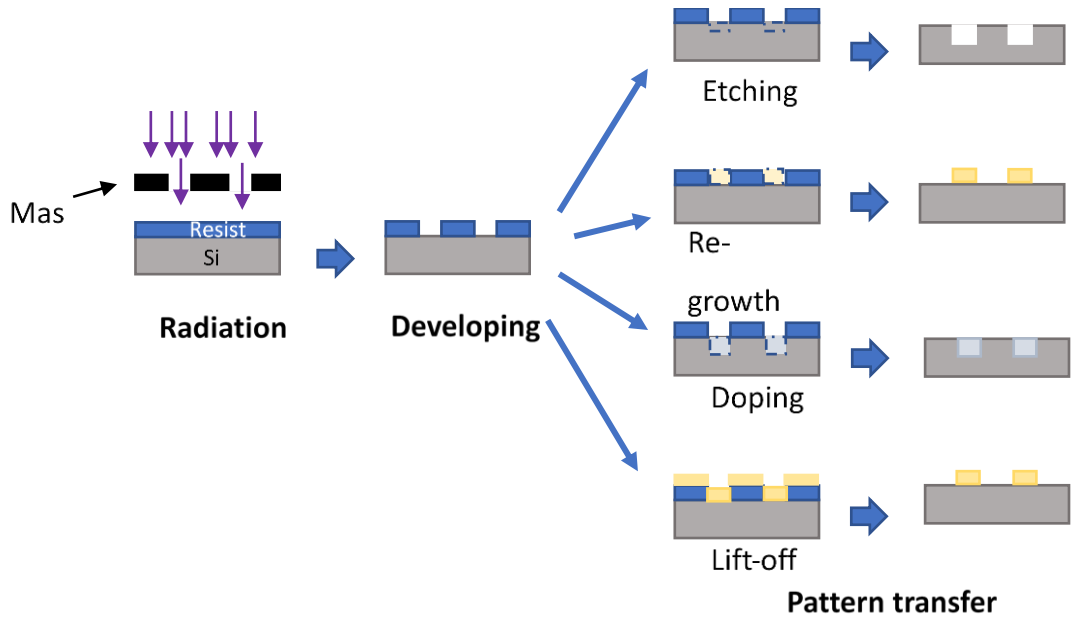

Figure 9. Various stages are involved in a typical lithography process starting from the mask-assisted exposure of the resist-coated substrate to radiation, developing and pattern transfer.

In the following sections, more details on the commonly reported techniques for processing the surface and fabricating topography gradients along with advantages/disadvantages will be introduced.

1.3.3.4 Biomolecule immobilisation

Before utilising bioreceptors for biorecognition assays, they should be stabilised on the surface in a way that allows easier exposure to the analyte and recognition. Biomolecule

immobilisation is a broad field which is out of the scope of the current thesis however, the routes can be generally classified into crosslinking, covalent, adsorption, entrapment, affinity, etc. More detailed information about the immobilisation strategies can be found in the literature (44-47).

1.3.4 Bio-interface characterisation and iterative design

- **Classic iterative approach**

As illustrated in Figure 5, there are many complexities surrounding an interface and each impacts the sensing assay to some degree. The ideal situation is to be able to monitor and tune out as many parameters as possible. Several iterations need to be carried out to optimise the output signal by repeating the design and process steps. Considering this loop, feasibility in terms of time on one hand and the costs required for resources and personnel on the other are remarkably limiting factors. For this reason, although ideally, numerous experiments need to be performed to approach a high degree of optimisation, using predictive approaches i.e., design of experiment (DOE), only a narrow range of interface parameters are considered, and the rest are eliminated. Hence, only a partial optimisation is achieved. Considering the literature, most studies have focused on DOE rather than investigating inclusive optimisation tools, which motivates the search for solutions to overcome the disadvantages of classic optimisation.

- **Surface gradient – a combinatorial approach**

Combinatorial approaches not only enable a single bio-interface variable to be studied on a larger scale but also can be switched to study multiple variables concurrently. This would avoid the need for numerous iterations, which is time-intensive, labour and resource-intensive and intrinsically susceptible to variations of experimental results between batches.

One attractive class of combinatorial approaches for screening the optimum variable is surface gradients, in which, rather than producing a library of random values, the spatial and gradually varying values are generated over a solid surface.

A bio-interface with gradually varied property correlates that surface property with an observed bioassay outcome. Meaning that a proper screening method can be employed to map the bioassay and spot the optimal surface conditions for certain targeted behaviour. In this sense, surface gradients offer a position-dependent combinatorial approach through the gradual

distribution of a single property/multiple properties over the surface and enable a reliable, economic, fast and high throughput screening method.

Figure 10 illustrates a simplistic view to answer why a sample with a gradually varying surface property is needed to find optimum conditions for a specific application. As we know, surface chemistry can be tuned to alter surface wettability, one of the effective parameters which define the attachment of the proteins to the surface. Here a specific protein with a hydrophobic outer domain is assumed as a model to predict surface adherence. As can be seen, the surface interaction of different proteins can be easily probed by preparing a gradient of hydrophobicity in a single experiment. Otherwise, studying the impact of a wide range of conditions requires the preparation of several individual samples, which is both time-consuming and resource-intensive. Meanwhile, because of the variation in experimental conditions, especially if several samples are prepared over a long period, the experimental outcome might be not reliable (48).

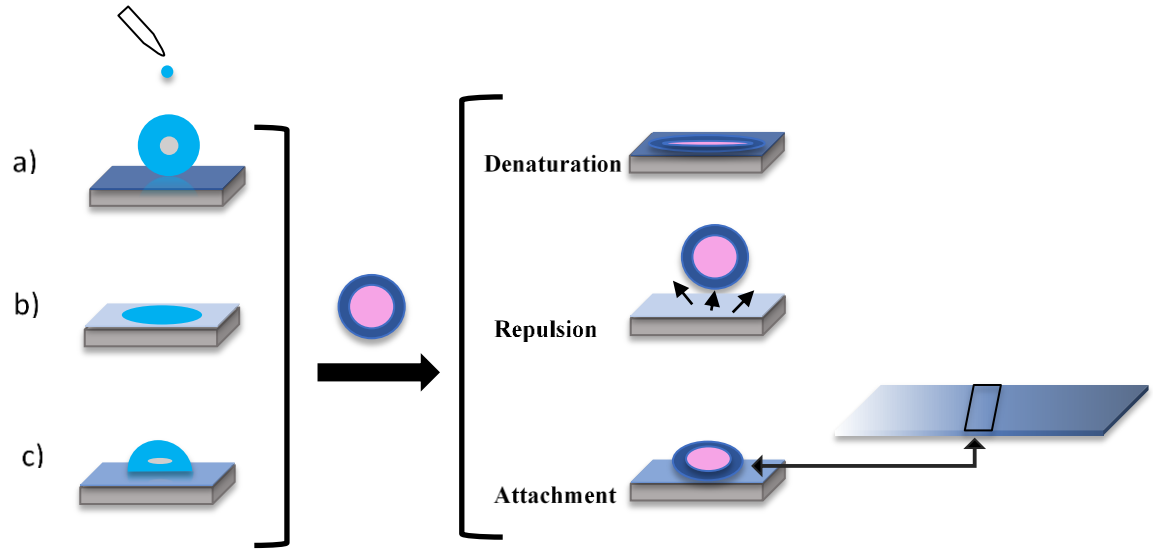

Figure 10. Protein with a hydrophobic shell is applied on surfaces with a) extreme hydrophobicity, b) extreme hydrophilicity and c) moderate hydrophilicity. The first interaction leads to irreversible strong hydrophobic-hydrophobic interaction causing protein denaturation due to the deformation of the structure. The second interaction with the surface causes repulsion of the protein from the superhydrophilic surface and the third surface allows optimal interaction due to protein attachment and the retainment of protein activity. This moderate hydrophilicity can be spotted by developing a wettability gradient and applying protein to several points followed by characterisation through imaging techniques.

1.4 A combinatorial approach by surface chemistry and surface topography gradients

1.4.1 Considerations for the selection of surface gradients

While perfectly developed surface chemistry gradients or precisely confined reproducible surface topography gradients are desirable for optimising the bio-interface, transferring the methodology from the lab to real-life applications is decided after a counterbalance between the high performance (low limit of detection, selectivity, etc.), high throughput, and costs of R&D and fabrication process. As an example of developing gradually varying surface topography, although several advanced nanofabrication techniques are possible candidates to generate highly reproducible features with high precision and control, a simple, cost-effective and versatile experimental design that allows sufficient control for developing specific surface topography in a faster experimental time without using time-consuming and expensive instrumentation is highly desirable. The requirements for chemistry gradient fabrication, on the other hand, are generally fast and automatable deposition techniques which allows the easy tuning of surface chemistry, high stability of the coating and avoiding toxic or environmentally hazardous solvents.

1.4.2 One-dimensional chemistry gradient

One of the attributes of the spatial gradient is the dimension of the variation. Controlling the chemistry variation of the surface in one direction without altering the other independent variables is desirable for many biomedical applications as already described. This control, at the molecular level and over a wide range and extended gradient length are however also considerably challenging.

Controlling the chemistry of surfaces with high resolution at the molecular level has been extensively studied using Self-Assembled Monolayers (SAMs) or graft polymers fabricated with various polymerisation techniques (49) as well as plasma-generated polymers.

Here, the commonly employed techniques are classified based on the control factor employed for gradient fabrication:

1.4.2.1 Time as the control factor

- ***Diffusion***

Diffusion is a popular technique for developing a continuous chemistry gradient. The diffusion gradient is implemented by placing a barrier, such as a parallel or tilted mask, in front of the source of volatile molecules to limit and direct the molecules in a particular direction (50). In

the solution phase, two solvents of different densities are prepared with one of the solvents containing the desired compound, which has a lower density. The experimental vessel contains a sample with a functionalised surface placed in a vertical position to the sidewall of the vessel. Upon injecting the low-density solution from an inlet close to the lower part of the vessel, the gradual vertical diffusion of the low-density solvent containing the desired compound allows the gradual interaction of the compound with the pre-functionalised surface forming density gradient (51).

- ***Dip-coating***

Dip coating is a technique, which is based on the insertion/withdrawal of a sample inside the coating solution. The control factor is the time of surface incubation with the coating material, which is tuned to define the interaction time of the particles/molecules with the surface and as a result, a spatial density gradient in the direction of the movement is generated. As the time of the surface incubation with the coating solution is controlled precisely with commercially available dip-coaters, this technique offers a higher degree of control over the chemistry gradient than the diffusion technique.

1.4.2.2 pH as the control factor

pH can be used as a modulator to selectively alter the surface-stabilised functional groups. For instance, pH variation was used to generate a composition gradient with a reversible covalent bonding feature. The gradient was developed based on gradual pH variation when a substrate pre-treated with aldehyde groups was gradually withdrawn from a vessel containing varieties of amino-functional SAMs with different pKa values (52). This, and the similarly developed unique pH-triggered gradients, is a solution-based technique and is dependent on substrate chemistry (e.g. SAMs or functional polymers).

1.4.2.3 Temperature as the control factor

In some gradient studies, temperature variation was used as a control to generate a polymer gradient by tuning the grafting density of the tethered polymer on a surface by placing a platform connected to cooling and heating sources from two sides, under the sample. The fabricated gradient manifested a wettability gradient due to variation in the number of anchoring carboxylic acid groups along the surface generated by a gradient of polymer chain grafting density (53). This technique is not applicable for heat-sensitive substrates and materials but is suitable for thermoresponsive materials with tuneable lower critical solution

temperature (LCST) behaviour. However, the chemistry gradients developed via temperature as control are material-dependent as the employed precursors need to be responsive to these stimuli and also the substrate should not be prone to degradations under heat variations.

1.4.2.4 Light (or electron-radiation) as the control factor

Polymer-based chemistry gradients are also fabricated using light to initiate polymerisation and to control the thickness (density) of polymer brushes (54). This methodology is based on light-mediated polymerisation and is suitable for generating a gradient from photo-responsive materials. Other creative ways have been investigated to generate gradient chemistry (and consequently a wettability gradient) based on gradual desorption via electron irradiation and the exchange of non-polar chemical groups (i.e. methyl containing groups) to highly polar groups, such as carboxylic acid terminated or vice versa (55, 56). Similar to temperature-enabled gradients, the chemistry gradients developed using light stimuli are usually material-dependent as the precursors need to be light-responsive.

1.4.2.5 Most common techniques for generating chemical gradients

To date, several techniques have been reported for generating chemical gradients with some of the most popular illustrated in

Figure 11. Below, the commonly employed techniques for fabricating a 1-D chemistry gradient with an emphasis on the main advantage and limiting features are listed following the classification in Table 1.

- ***Dip-coating or infusion withdrawal (Figure 11b)***

This technique generates a thickness (or density) gradient of a specific functional group in the direction of variation in time of the surface incubation with the coating material. Varieties of commercially available dip coating devices with a rather simple setup and easy usage enable the possibility of covering samples of different sizes (large and small areas) with a precisely adjustable linear speed. However, there are speed limits to motorised (for fast) and piezo (for low rates) dip coaters and the quantity of the adsorbed material on the surface will be limited by the evaporation speed of the liquid front, unlike the equilibrium adsorption modes.

- ***Diffusion techniques (Figure 11d, 11h, 11f)***

Diffusion-enabled gradients offer technical simplicity and extendibility of the length of the intended gradient however, for solution-based diffusion experiments, at least two organic

solvents (with potential hazards) must be used, which implies the need for extensive organic waste treatment.

- ***Printing techniques (Figure 11c)***

Printing techniques generally work based on employing a stamp which applies the coating to the surface with a concentration gradient, due to the specific design of the stamp (e.g. thickness). Printing allows minimal consumption of precursors (and solvents) and hence avoids the need for the organic waste treatment issue of the former technique. It also offers an enhanced resolution of the applied chemistry and the possibility of surface patterning. However, the size and area of the contact are dictated by the stamp, meaning that it is not tuneable during the experiment.

- ***Electrochemical techniques (Figure 11e)***

The electrochemical fabrication of a chemistry gradient is a solution-based technique that offers dynamic spatial control of the deposited coating. The methods reported for electrochemistry-enabled chemistry gradients are as follows (57): i) **Mass Transfer**: a diffusion and concentration gradient of the electrochemically produced species with respect to the distance from the electrode can be translated into a chemistry gradient by different pathways; ii) **In-plane potential gradient:** An in-plane potential gradient applied along the electrode forms a gradient in reactivity and can be employed to generate a chemistry gradient; iii) **Electrochemical reactions combined with other techniques** (e.g. dip-coating): For instance, an electrochemical reaction of the surface with the incubation solution (electrolyte) during a time-controlled dip-coating process has been reported for generating a chemistry gradient. The selected material can be organic and inorganic, however, the choice is still limited to electrochemically active materials.

- ***Polymer grafting with temperature control (Figure 11g)***

Controlling the grafting density via a temperature gradient is a simple and high-throughput technique, however, the technique is limited by the material chosen (mainly suited for organic polymers) and is not applicable for heat-sensitive substrates. The roughness of the surface coating needs to be monitored as this is likely to be impacted depending on the material of choice.

- ***pH-enabled gradient***

Manipulating the pH of the solution enables selective surface functionalisation and forming a concentration gradient of the desired chemical groups along the modified surface. Using this

technique, the possibility of reversible covalent functionalisation is also explored. The disadvantage of the technique was time-intensiveness due to preparation requirements and the strict requirement of using deionised water.

- ***Polymerisation with light control***

Gradient polymerisation with light control is usually implemented based on either variation in irradiation time (or irradiation intensity) or the concentration gradient of the monomer along the surface. In the literature, for chemistry gradients fabricated by light control, lower lateral resolutions with nanometre length modifications were reported. However, this technique is intrinsically limited to organic light-responsive materials.

- ***Plasma polymerisation***

In plasma-enabled gradients, the chemical composition and film thickness (deposition rate) is controlled by both plasma electrical inputs and kinetic inputs i.e., flow rates and type/concentration of the employed precursors, to affect the degree and mechanism of precursor fragmentation leading to the gradual variation of chemical composition. Plasma techniques for generating surface chemistry gradients can be used on large surface areas with extended lengths (several cm) or on small surface areas with the assistance of a mask.

Some plasma methods are limited to gradually altering the surface of an already existing coating to develop a wettability gradient (58, 59), which can have the drawbacks of roughening the surface and incorporating an uncontrolled chemical group, other techniques, on the other hand, are based on the spatially controlled deposition of the intended chemical functional groups. (60, 61). One major drawback of the plasma-enabled gradient is the less-defined surface chemistry due to the 3D structure of the coating with the larger diversity of the existing functional groups.

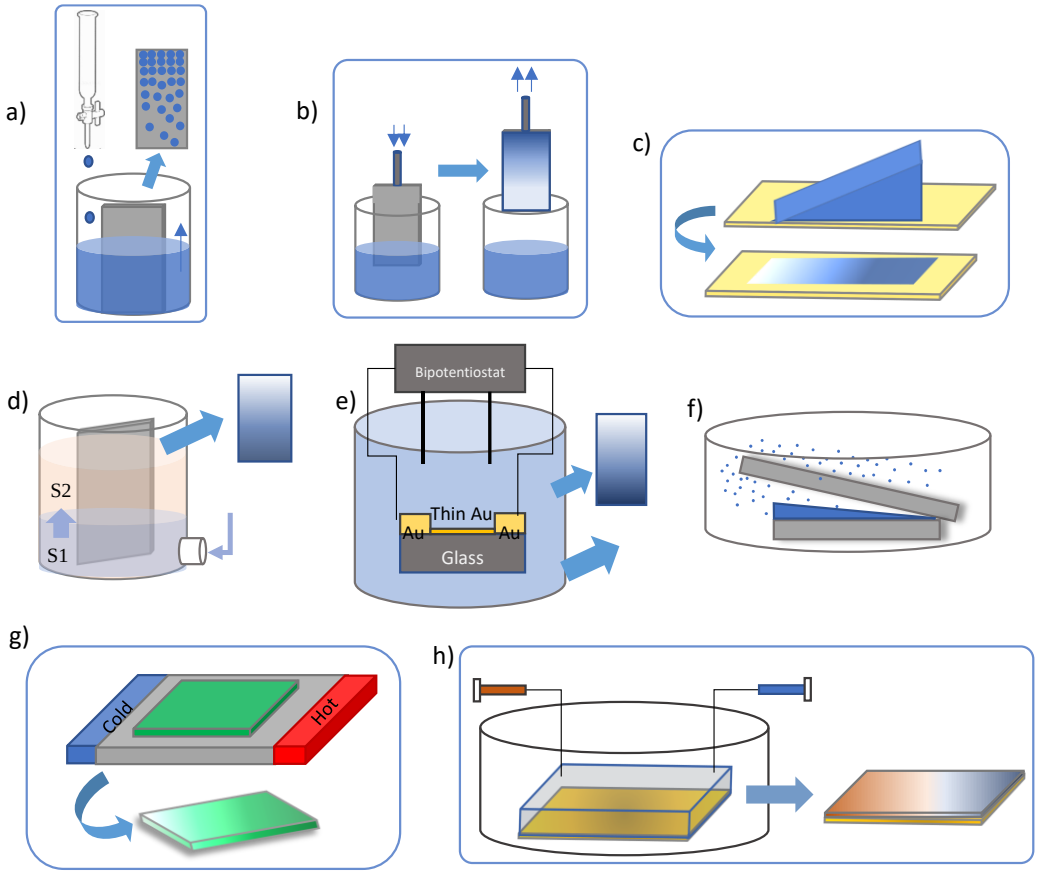

Figure 11. Some examples of the 1-D chemistry gradients reported so far. The details of most of the illustrated techniques are summarised in Table 1. The techniques are: a) Drop-wise introduction of negatively charged particles to interact with an aminosilane-coated substrate (ref.118), b) The gradual Infusion-withdrawal of substrate within a solution of alkanesilanes (ref.69), c) A stamp with variable thickness immersed in alkanethiol was used to print a concentration gradient on a gold substrate used to generate a chemistry gradient (ref.1), d) A functionalised substrate was immersed in a first solution and upon gradual diffusion of the second solution, a gradient was formed in a vertical direction, e) polymerisation of methylacrylate was performed by gradually varying the electrical potential of gold electrodes in the presence of a catalyst (ref.80) , f) A plasma polymer gradient formed using an inclined mask as a barrier to control the diffusion of deposited species (ref.114), g) Temperature variation was used to change the grafting density of the tethered polymer and form a carboxylic acid group gradient (ref.59), and, h) Cross-diffusion technique for generating the gradient of two alkanethiols on gold and through a gel matrix (ref.51).

Table 1. Detailed information for some of the techniques developed for fabricating a unidirectional surface chemistry gradient with the main advantages/disadvantages and potential or investigated applications. The rating is intended to show the author's preferred technique based on the criteria described in the text.

Technique	Gradient precursor	Gradient length scale	Surface variables (besides surface chemistry)	Developed or potential application	Ref.	Rating
Dip coating or infusion-withdrawal	SAMs (e.g., organosilane), polymer brushes, inorganic	mm-cm	Polarity, wettability, coating thickness, surface charge	Stationary-phase gradient chromatography, liquid droplet motion, protein adsorption, cell studies, etc.	(62-67)	****
Diffusion phenomena (vapour phase, liquid phase diffusion)	SAMs (organosilanes, alkanethiols), polydopamine	mm-cm	Wettability, thickness	Protein adhesion, cell adhesion, detergent adsorption, cell motility	(51, 68-72)	***
Printing (µcontact printing, inkjet printing)	Alkanethiol, organosilane	µm-mm	Oleophobicity, wettability, surface topography	protein adsorption and cellular attachment	(73, 74)	***
Electrochemical techniques	Inorganic (e.g. metals), organic polymers	mm-cm	Thickness, surface plasmon resonance shift, wettability	cell studies, fabricating conducting and electrochromic polymers	(75-79)	****
Polymer grafting with temperature control	Organic polymer	mm-cm	Wettability, roughness, thickness, crystallinity of Bridgman, polymer grafting variation	Heat-resistant materials, heat and optical conversion materials, optoelectronics, biomaterials	(80)	***
pH-enabled gradient	SAMs, polymers	µm, mm	Wettability, topography variation, thickness, adhesion forces	Printing and erasing SAMs, protein adsorption	(52, 81-83)	****

Polymerisation with light control (photopolymerisation, UV-induced gradual ozone oxidation, etc.)	Polymer brushes, SAMs	nm	Thickness, graft density	Protein adsorption, cell attachment	(84-89)	***
Plasma polymerisation	Organic monomers, gases	mm	Explained in the next table	Explained in the next table	Explained in the next table	*****

1.4.2.6 The preferred method as indicated by ranking

Based on the discussions on the advantages and drawbacks of each technique, the method of choice for fabricating a chemistry gradient in the framework of the current thesis is plasma polymerisation. Further reasons for using plasma as the preferred method for tuning surface chemistry to develop the bio-interface are discussed in a review published in 1982 by Yasuda et al. (90), one of the pioneers in the plasma field, regarding the advantages of plasma polymerised thin films for biomedical applications. The overall advantages are summarised as suitable coating properties, such as conformity, good adhesion to the deposited substrate and physical/chemical durability, and specific advantages for bio-interface applications are attributed to the biocompatibility of these coatings, in terms of blood and tissue compatibility for cell and biomolecule adhesion, being non-toxic and chemically inert, the possibility of controlling transport of substances in or outside the biomaterial, etc. Since then, tremendous interest and efforts have developed in the application of plasma for developing a bio-interface or modifying a biomaterial surface.

As shown in Figure 12, several strategies have been developed to generate a film thickness gradient (or polymer concentration gradient) such as using a fixed mask, which allows a slope of diffusion or moving the sample with increasing speed under the slit of the fixed mask allowing for variation in the time of exposure of the sample to the polymer. On the other hand, a plasma gradient is also generated by varying the polymer functional groups through copolymerisation and introducing two precursors with a varying flow rate ratio based on moving the substrate at a constant speed under the slit of a mask (91).

The properties and pros/cons of each plasma-enabled gradient technique (as illustrated in Figure 12) are listed below:

- ***Time of exposure (Figure 12a)***

This approach is based on gradually moving the sample position under the mask slit (or vice versa) and offers a continuous gradient. The fabrication of the chemistry gradient is fast, and the only requirement is an easy mask set-up, however, gradient formation using this technique can be adversely impacted by diffusion under the mask while displacing the sample or mask.

- ***The flow rate ratio of precursors (Figure 12b)***

Similar to the previous technique, the sample or mask is gradually displaced to form a gradient, however, in this technique, more than one precursor is employed and the flow rate of one precursor is varied with respect to the other precursor to form a composition gradient. A continuous gradient is formed using an easy mask set-up but, due to using the mask, diffusion during displacement is inevitable if it is not well controlled.

- ***Diffusion (Figure 12c)***

This technique offers the possibility of forming a continuous gradient using a static mask. Although this simplified the technique, less spatial control is achieved due to the diffusion of the material under the mask.

- ***Precursor flow rate ratio and frequency/voltage variation (Figure 12d)***

An automated moving jet allows the direct deposition of the precursor(s) from the nozzle on the surface. Based on the targeted composition gradient, one or multiple precursors can be used and where multiple precursors are required, variations in the precursor flow rate ratio can be combined by variations in plasma electrical parameters (frequency/voltage). The technique is advantageous due to the fast forming of a continuous gradient without the need for a mask.

- ***The precursor flow rate ratio and power input (Figure 12e)***

This technique may be preferred if it is necessary to coat a small surface area with high precision (suitable for surface patterning) with minimal diffusion under the mask. However, unlike the previous techniques, a distinct gradient is formed with an increased risk of oxygen exposure during the dismantling/mantling of the mask after each deposition.

Some reported examples for each of the plasma techniques with the precursors, plasma specifications, generated gradient attributes and potential/developed applications utilised are summarised in Table 2.

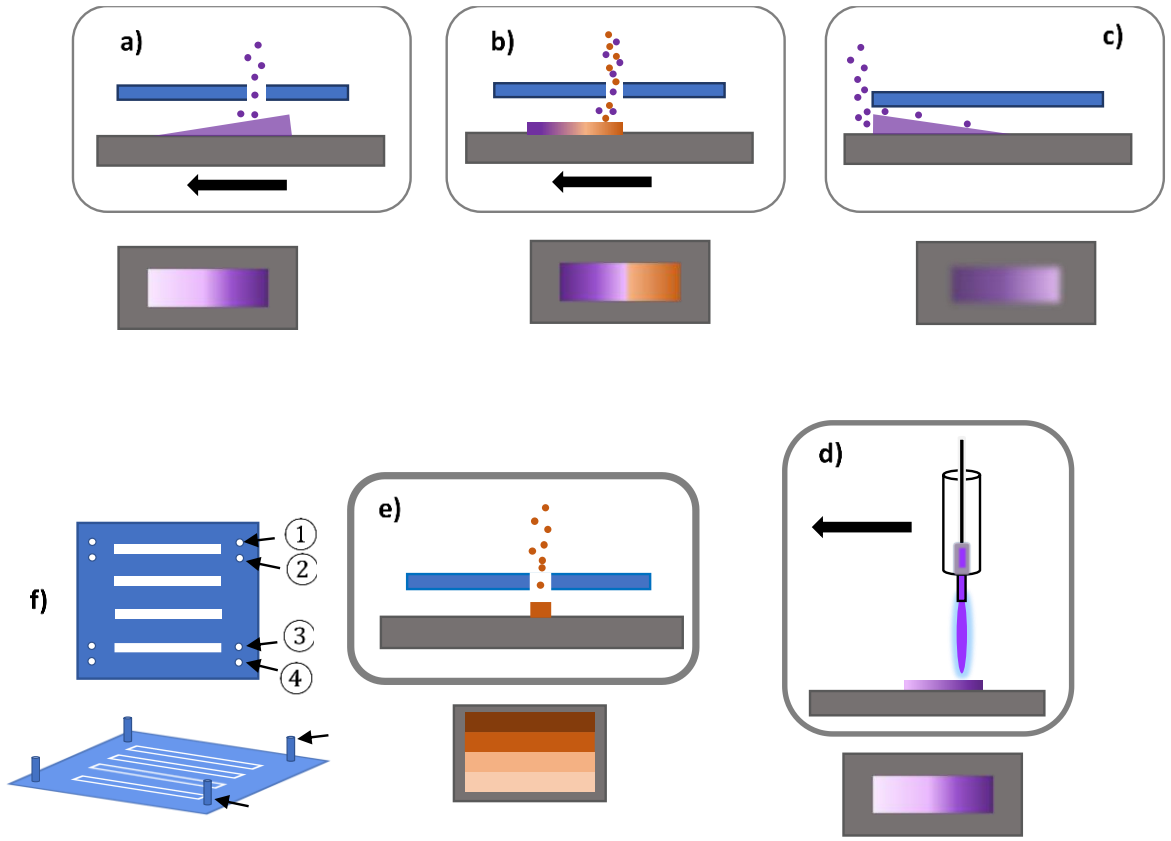

Figure 12. Representation of plasma polymer gradients obtained by a) polymerising one monomer by displacing the sample holder at an increasing rate under the mask slit (time of exposure is changed), b) Copolymerisation of two polymers by displacing the sample holder at a fixed rate under the mask (flow-rate ratio of the precursors is changed), c) Polymerisation of a monomer and diffusion under the mask from the open-end, under fixed conditions (diffusion length is the variable), d) direct writing with an automated plasma jet, moving at a fixed speed along the substrate and gradually applying the varying parameters such as precursor flow ratio, power, etc. e) Polymerisation under the mask in fixed conditions and repetition of the steps using several different precursors/deposition conditions (here 4 plasma conditions with the same precursors, but a varying power and precursor ratio are intended) and, e) a possible mask configuration for obtaining the previous gradient (d). For each distinct coating, prior to deposition, the screws on the sample holder are placed in the corresponding hole in the cover. More explanations on deposition with masking device are provided in Chapter 2 (2.1.2.1).

Table 2. Plasma polymerisation techniques for generating surface chemistry gradients.

Technical detail	Precursor (s)	Plasma properties	Gradient length	Resulting surface variables	Developed/ potential application	Ref.
Tilted mask	CO_2/C_2H_4	Capacitively-coupled RF plasma	15mm	Thickness, wettability, crosslinking, roughness	Release coating in a pressure-sensitive adhesive (PSA) tapes	(92)
	Octadiene/ acrylic acid /diethylene glycol dimethyl ether	Capacitively-coupled RF plasma	30mm	Thickness, wettability (20° variation, average WCA is 35°)	Stem cell behaviour	(93)
	Octadiene/ acrylic acid	Capacitively-coupled RF plasma	30mm	Wettability, topography	Stem cell differentiation	(50)
Diffusion through a mask fixed on the sample	Hexane	RF plasma	10mm	Thickness variation	Cell attachment and morphology	(94)
	Allylamine	RF plasma	10mm	Wettability variation (15° to 90°)	Cell behaviour on a nitrogen gradient	(107)
	Allylamine/hexane	ICP, RF plasma	8mm	Wettability (60°–93°), thickness, topography	Cell surface interaction	(108)
	Hexane	RF plasma	4 and 6mm (radial and linear respectively)	Thickness, wettability (93.4° ± 0.3 to 35.2°± 0.5 for linear and 92.3° ± 0.8 to 54° ± 3 for the radial gradient)	Cell surface interaction	(113)
Moving sample under plasma/mask	N_2/O_2/ tetraethylorthosilicate	Dielectric Barrier Discharge (DBD)	20mm	Thickness, topography	Optimising film properties such as film density	(95)
	1,7-octadiene/ allylamine	RF plasma	13mm	-	Stem cell differentiation	(104)
Maskless deposition	Diethylene glycol	RF plasma/ knife edge top electrode and the sample placed perpendicularly to this electrode	30mm	Wettability, thickness variation	Protein adsorption	(96)
	Dimethyl ether		10mm	Wettability, thickness variation	Protein adsorption and cell attachment	(97)
	Octadiene/ acrylic acid	Inductively coupled RF plasma chamber	12mm; 13mm. 13mm	Thickness (OD-end 6.3nnm, AA-end 5nm); wettability (88-47°); Halogen concentration variation	IgG adsorption. Embryonic stem cell behaviours. Chemisorption of halogenated epoxides to surface carboxylic acids.	(97), (98), (99)

Shielding/deshielding of the sample by moving the coverslip	Ethanol/ propionaldehyde	RF plasma	10mm; 13mm	Not defined	Streptavidin binding to aldehyde gradient.	(101), (102)
	1,7-octadiene/ allylamine	RF plasma	15mm	Thickness variation	Stem cell neural differentiation Plasma-assisted fabrication of a polymer brush gradient.	(98)
	1,7-octadiene/ allylamine	Inductively coupled RF plasma chamber	12mm	Wettability (80°-68°), topography	Protein adsorption	(105)
	Ethyl 2-bromoisobutyrate/ ethanol	RF plasma	10mm	Thickness variation	Plasma-assisted fabrication of a polymer brush gradient	(106)

Gradient formation through plasma polymerisation is usually conducted in order to introduce polar functional groups, especially amino-functional and oxygen functional groups, using carboxylic acids (e.g. acrylic acid), polyethers (e.g. PEG) and amines (e.g. allylamine). This is due to their implication for bioassays (probe binding, cell attachment, etc.), apolar hydrocarbons using hexane, octadiene, etc. or the combination of polar and apolar groups to form gradients which are widely reported and aim to study cell behaviours (99).

Using multiple precursors enhances the chance of generating chemistry variations with a larger diversity of functional groups compared to single precursor consumption, as well as better control of the resulting wettability gradient. Some of the frequently reported chemistry variations using plasma technologies are summarised below based on the surface functional groups:

- ***Nitrogen-functional surface gradients***

Nitrogen-functional groups can be inserted into plasma polymers either by employing a) polymerisable monomers (i.e., allylamine) or b) non-polymerisable precursors (N_2, NH_3). The choice of precursor for generating nitrogen-functional plasma gradients has been dominated by the polymerisable nitrogen-functional precursors/monomers. The reason for this may be the already existing C-N bonding in these monomers which carries the expectation of achieving more predictable chemistry of the resulting polymer to get closer to a mono-functional surface coating (primary amine ≫ other nitrogen groups).

Vandenabeele et al. (100) conducted a comparative study of ammonia/ethylene and cyclopropylamine and pointed out that while high deposition rates and higher incorporation

of N to C have been proven for the polymerisable precursor (i.e. cyclopropylamine), higher selectivity of the NH_2 content was not found for any precursor at high plasma powers (60 and 100 W). However, a higher selectivity of amine at mild powers (30 W) was observed for the ethylene/ammonia pair and the overall high nitrile for cyclopropylamine plasma polymer functional groups.

Due to the importance of amine groups for either the covalent immobilisation of proteins or the electrostatic interaction of negatively charged biomolecules with positively charged amine groups in physiological pH, mono-functional primary amine-containing surfaces are ideal for better investigating biomolecule surface interactions (101).

As mentioned previously, most of the compositional gradients formed by polymerisable nitrogen-containing monomers are based on forming a gradient of nonpolar hydrocarbon groups in one direction using a hydrocarbon monomer (e.g. OD) and negatively-charged nitrogen-functional species in the opposite direction using nitrogen-functional monomer (e.g. allylamine)(102, 103).

For instance, in a relevant study, a plasma-deposited bilayer of glycol dimethyl ether (DG) thickness gradient was formed on top of the acrylic acid layer with the help of an inclined mask. The uppermost layer was known as a low-fouling material, and the sub-layer was known as a high-fouling material. The study investigated the dependence of the plasma deposition time and accordingly, the depth of the DG layer at the thickest part, on the number of adsorbed cell-adhesion promoting proteins and finally, cell behaviour. When DG was deposited in 5 minutes, there were more proteins adsorbed on the surface, increasing the cell adhesion compared to a DG gradient deposited in10 minutes. The position of the functional group and its density as a function of depth may have contributed to this effect (93).

Owing to the flexibility of the surface chemistry (104), the possibility of achieving high nitrogen concentration (40%) (105) and improved aqueous stability (106), plasma polymerisation with reactive non-polymerisable nitrogen-containing gases and hydrocarbon pairs are good alternatives for developing nitrogen-functional chemistry gradients.

Although there have been reports on developing coatings with non-polymerisable nitrogen-containing gases and hydrocarbon pairs, to the best of our knowledge, the current thesis reports on a nitrogen-functional chemistry gradient developed with NH_3/C_2H_4 with unique stable properties for the first time. The coatings were deposited on a single chip in static form using a masking device via the gradual variation of NH_3 with respect to ethylene. Furthermore, the tuning power input and the device also allowed the coating of 20 chips of 20x10 mm size concurrently, in each deposition. When ammonia was supposed to be

extended above a certain level, to prevent film loss in aqueous media, which is normally inevitable due to a higher presence of unstable ammonia functional groups, bilayer coatings were deposited rather than a monolayer. The bilayer consisted of a crosslinked supporting bottom coating and a highly functional (and less crosslinked) top thin layer based on the methodology investigated by Vandenbossche et al. (107).

- ***Oxygen-functional surface gradients***

Besides nitrogen-functional gradients, the plasma-enabled oxygen functional gradients are widely used in several fields of material science, especially the microfluidics field, to enhance droplet motion, and the biomedical field (cell adherence etc.). It should be noted that when the wettability gradient is the ultimate goal of the study, especially if it aims to approach higher values of hydrophilicity within a gradient range, oxygen-functional precursors are the better choice compared to the nitrogen-functional groups, as the latter is generally less hydrophilic. Some of the 1-D oxygen-functional gradients reported are based on strategies such as gradually increasing the concentration (flow rate) of an oxygen-functional monomer (i.e. acrylic acid) while simultaneously decreasing the concentration of a second monomer (i.e. allylamine) in discharge (108) or the fixed concentration of monomers (i.e. CO_2/C_2H_4) and the thickness gradient of oxygen-functional film formed by a static inclined mask that inhibits the diffusion of the plasma-deposited species (92).

An alternative strategy exploited in the framework of the present thesis is the gradual introduction of oxygen (gradually increasing flow rate) during the polymerisation of a monomer that usually yields a hydrophobic (hydrocarbon-rich) coating. For this purpose, the popular plasma polymer precursor, HMDSO, was selected, with its advantages of volatility in atmospheric pressure, and of being a commercially available, cheap, non-flammable and almost non-toxic chemical (109).

HMDSO has been intensively utilised as precursor for plasma polymerisation with applications in developing anti-scratch, anti-corrosion coatings, in food packaging as a barrier layer, and in pharmaceutical packaging, among others (110).

Based on this selection, using a programmable corona discharge, a gradient coating was obtained with surface chemistry and wettability extending from hydrophobic organic to hydrophilic and inorganic. Distinct coatings deposited with a combination of HMDSO and O_2 have already been widely investigated using different, and mostly low-pressure, plasma techniques (111-118). However, to the best of our knowledge, this is the first report of a programmed atmospheric pressure corona jet being utilised for the dynamic deposition of a

gradient coating mainly by varying oxygen to the HMDSO flow rate. The advantage of this technique is that it is more suitable for industrial applications with the possibility of upscaling owing to atmospheric-pressure deposition and the avoidance of vacuum systems. Further experimental and characterisation results will be fully discussed in the following chapters.

1.4.3 One-dimensional structural gradient

As explained, the surface morphology, apart from its impact on material studies, especially for adhesion and tribology, is also highly important for biology since the morphology can initiate a biologic response (protein adsorption, cell adhesion, stem cell differentiation, etc.) when the biomolecules are applied to the surface. Therefore, for developing the interface, the systematic study of the biology response as a function of morphology variation enables a deep understanding of the impact of the factors involved (35, 119).

As previously mentioned, direct and indirect approaches could be employed to alter the topography of the surface or top coating. In a study based on a direct approach, the optimal surface standard roughness values (e.g., R_q, R_a, etc.) required for an osteoblast response were investigated by generating surface roughness gradients of a total 10-20 mm length generated via a two-step method of i) sandblasting the surface, followed by ii) time-controlled chemical polishing for gradual surface curvature removal (35, 120-122). The other reported roughness gradient fabrication method for studying cell behaviour was based on generating surface wrinkles in a multi-step procedure of polymer stretching and applying strain via one-directional gradual oxidisation by reactive ion etching and release (123, 124).

Where porous materials and the correlation of pore size as a function of distance is required, e.g. for the development of biomimicking materials, an electrochemical approach and mainly, anodization is proposed for generating a surface nanopore diameter gradient (125, 126).

The indirect approaches for developing varying surface structures can be classified as conventional and unconventional lithography techniques:

1.4.3.1 Conventional lithography techniques

It is possible to generate well-controlled and reproducible patterns with nanoscale structures using lithography techniques. Some of the reported surface gradient patterns developed to date using lithography techniques are stripes, dots and squares with variable width, size and spacing (127), grooves with varying spacing or size (128), pillars with grading height, spacing and diameter (10, 13), and nano-needles with varying spacing (129).

The steps in fabricating patterns with lithography are generally based on coating the surface with a suitable resist, irradiation then transferring the pattern onto the surface with or without a mask, developing patterns by removing the unwanted resist, and the final reactive ion etching step. The generation of the gradient pattern in the maskless techniques of electron beam lithography and maskless photolithography is implemented by initially designing the gradient pattern by generating command codes and manual design, respectively. Due to the long writing time and consequently the low throughput, electron beam lithography techniques are used only complementary to other techniques and mainly to develop masters to define gradient patterns. The other advanced direct-writing maskless technique that has been utilised for generating grading surface patterns on a wide surface area is the dip-pen lithography technique (127, 130). The main disadvantages of using the conventional lithography techniques for fabricating a structure gradient are the multi-step processes and the complex and expensive instrumentation which require a good level of training to handle the experiment.

1.4.3.2 Unconventional lithography techniques

The two main classes of unconventional lithography techniques that have been frequently utilised for developing topography gradients are imprinting and colloidal lithography, with a few reports on other techniques, for example, contact printing techniques. Some unconventional lithography approaches which have been reported for fabricating surface topography gradients are illustrated in Figure13 . It should be noted that in most of these approaches, there is a template/master which was previously developed using one of the conventional lithography approaches.

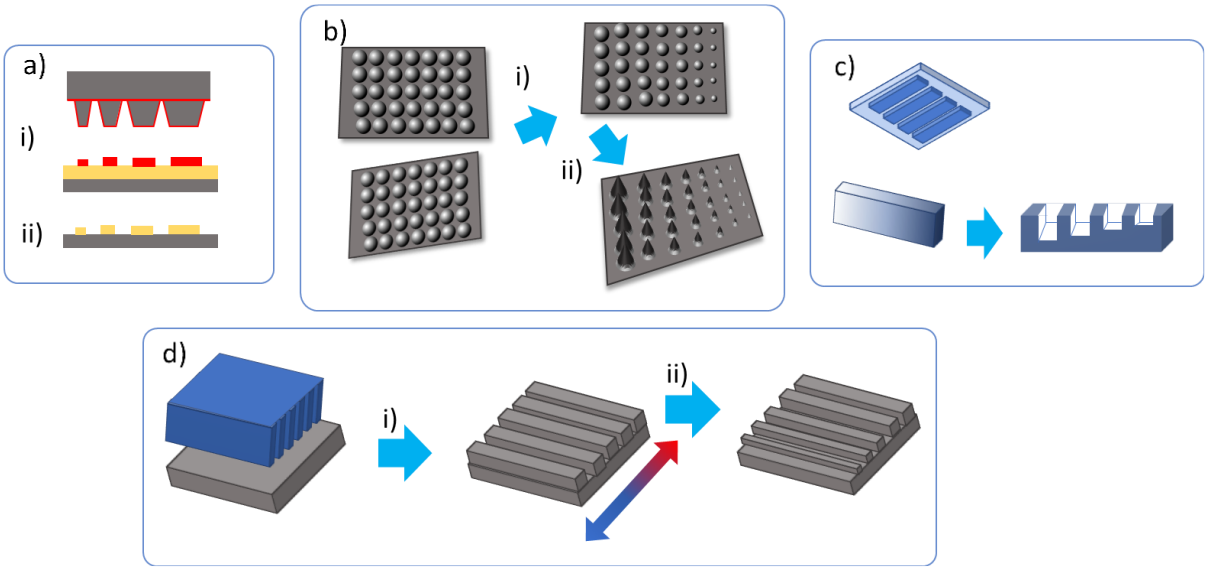

Figure 13. Selected topography gradients produced by lithography approaches a) Contact printing is used to form nano- to micro-metre arrays in two steps: i) contact printing using PDMS array tips with varying tip width followed by ii) etching the gold to transfer the gradient array on the metal layer (ref. (131)). b) A graded silicone cone array is developed with colloidal lithography and inclined reactive ion etching via the following steps: i) a substrate decorated with microsphere array and oxygen PLASMA etching on the tilted substrate (inclined etching) followed by ii) vertical etching with CHF3/sf6 plasma (ref. (132)). c) The height gradient is fabricated via the imprinting technique: i) initially, a film with a viscosity gradient was developed by applying a gradient temperature to a thermo-curable elastomer; i) imprinting was applied with a stamp with the desired features under uniform pressure followed by final stress relaxation (ref. (133)). And d) the height gradient was formed by nanoimprinting by i) a nanoimprinting approach on polystyrene film, as a substrate, followed by ii) annealing under a temperature gradient ref. (134).

- ***Nanoimprint lithography***

Nanoimprinting techniques are high throughput and cost-effective techniques which have frequently been used for generating topography gradients. The main approaches implemented based on nanoimprinting are soft lithography (SL), thermal nanoimprint lithography (T-NIL), and UV-NIL which are based on transferring patterns onto a surface using a template, which is in turn fabricated by one of the conventional lithography techniques. In the SL technique, self-assembly is used to transfer colloidal spheres onto the surface followed by subsequent etching to form ordered patterns. While T-NIL, is implemented to develop patterns by thermal curing when the template is pressed to the thermoplastic surface material, the UV-NIL technique is implemented by UV curing of the resist after bringing it into contact with the patterned template on the surface (135). Some of the imprinting techniques which have been utilised for fabricating topography gradients are presented in Figure13 (c, d).

- ***Colloidal lithography***

Despite its similarities with soft lithography, colloidal lithography can be utilised to form 3-D geometrical structures (136). The colloidal lithography technique has been used for surface engineering in the conventional form of self-assembled closely packed arrays of nanoparticles or by using template spheres such as polystyrene to define the shape of the metallic nanoparticle arrays (e.g. hexagonal, square arrays) and control the spacing. However, by using angled-resolved colloidal lithography, which is based on metal vapour deposition after templating/masking, it is possible to obtain control over the size and shape of the metallic nanoparticles formed (137). Gradients of gold nanostructures in different shapes (bars, dot pairs and rings) were fabricated by angular deposition of gold vapour (137).

Interface modification with noble metal colloids is especially interesting for developing biosensing interfaces with surface-enhanced Raman scattering or nanoparticle surface plasmon resonance spectroscopy transduction techniques. The properties of nanoparticle structures as an individual and periodic array must be controlled as they alter the optical response. For instance, interparticle distance alters the wavelength of the plasmon resonance wavelength as well as its damping properties (138).

One simple method used for modifying the surface topography with colloidal lithography is based on using the infusion-withdrawal technique to form gradually varying densities/sizes of surface structures using colloidal dispersions. For instance, Kunzler et al. grafted the substrate with poly(ethylene imine) (PEI) and gradually immersed the substrate with an adjusted speed inside the beaker containing silica nanoparticles. The time-controlled incubation of the sample surface with the solution resulted in the formation of a spatial silica nanoparticle density gradient, which was later used for cell adhesion studies (139).

The other method similar to infusion-withdrawal is the dropwise introduction of the particles, allowing the gradual increase of the liquid along the substrate using a microfluidic pump to precisely control the flow rate of the particle solution (as studied in the framework of the present thesis). More studies of nanoparticle gradients based on colloidal lithography are listed in Table 3. Figure 14 is intended to illustrate the process of fabricating each of the colloidal lithography techniques

Table 3. Nano- and micro-roughness gradients are fabricated by utilising colloidal particles via different methods. The rating presented (stars) is intended to show the author's choice based on different criteria as described in the text.

Technique	Material/substrate	Surface variables	Gradient length	Developed or potential application	Ref.	Rating
Using a chemistry gradient template	Au NPs (16.9 ± 1.8 nm) deposited on APTES and surface-tethered polyacrylamide (PAAm)	The spacing of NPs, plasmon resonance variation	45 mm x 12 mm (sample size)	NA	(140)	***
	15 or 40 nm AuNPs modified with 2-mercaptosuccinic Acid	Spacing of NPs	12 mm		(141)	
	100 nm polystyrene NPs modified with carboxylic acid	Spacing of NPs	3mm		(142)	
Dropwise introduction of the colloid solution and time-dependent exposure of the surface to the particles	8 nm silver and 12 or 20 nm gold particles modified with proteins (BSA, etc.) deposited on poly L-lysine coated glass	Spacing of NPs	22 mm x30 mm	The protein-cell interaction studies	(143)	*****
Gradual immersion/dip coating	16 nm AuNPs on plasma polymerised allylamine film/glass	The spacing of NPs, height analysis with AFM	13 mm	Applicable for improving the efficiency and reliability of AFM nanoparticle metrology	(144)	****
	Si NPs (73 nm) deposited on Si substrate coated with poly(ethylene imine) (PEI)	Spacing of NPs	10nm	Studying the proliferation and morphology of rat calvarial osteoblasts (RCO)	(139)	
	6 nm AuNPs functionalised with c(-RGDfK-)	Spacing of NPs	10 mm	Cell adhesion and morphology study on the RGDfk gradient	(145)	
	38nm AuNPs modified with 2-mercaprosuccinic acid	Spacing of NPs, wettability	12 mm	Cell-surface interactions	(146)	
	73 nm Si NPs on PEI coated Si	Spacing of NPs, wettability	10 mm	Applications in microelectromechanical, nanoelectromechanical devices and micro/nanorobotics	(147)	

	12.1 nm Si NPs on PEI-coated Si	Spacing of NPs, wettability, and adhesion force studies	10 mm	Cell-surface interaction studies	(148)	
	AuNPs of 16, 38 and 68 nm modified with 2-mercaprosuccinic acid on allylamine and acrylamide	Spacing of NPs	13 mm	Studying the impact of gradient on material adhesion and related theoretical modelling	(149)	
Ion diffusion by controlling the ionic strength of particle solution	AuNPs of 10 nm modified with PEG deposited on octanedithiol or mercaptoethylamine modified gold substrate	Spacing of NPs, wettability, surface plasmon resonance	10 × 11 mm surface	Studying microbial adhesion through SPR-based imaging	(150)	***
Temperature gradient applied on the substrate after dip-coating it with colloids	PS microspheres (with a diameter of 240 nm) on Si	Morphology of particles, wettability (88.7°-148.1°), roughness (RMS)	Few mm scale	NA	(151)	***

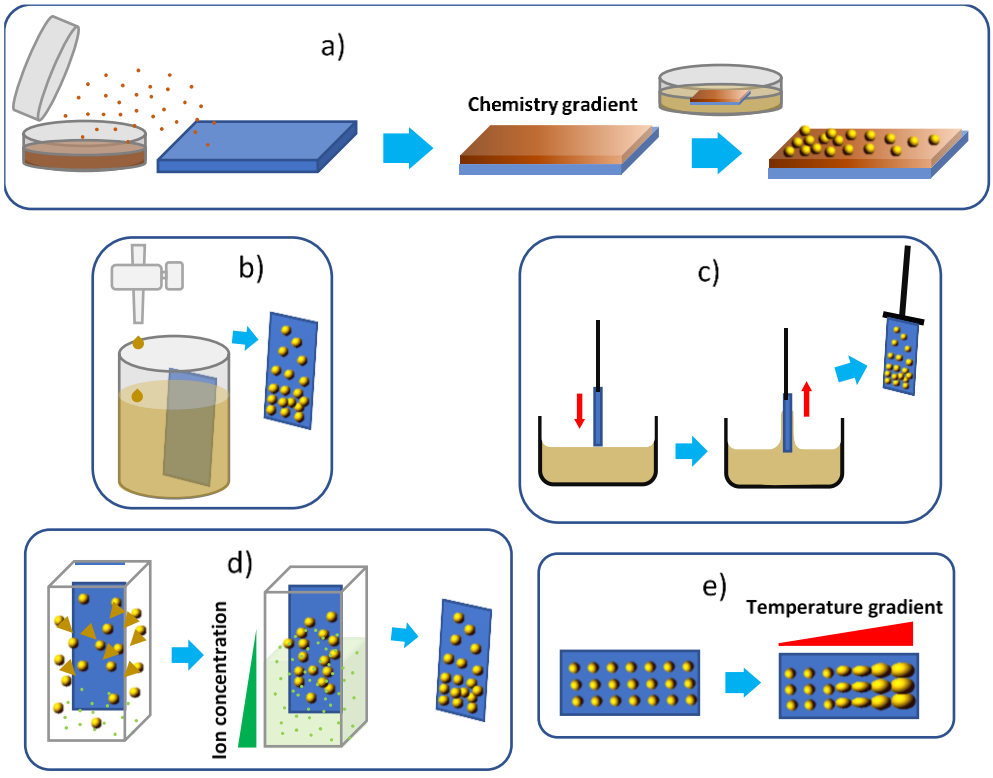

Figure 14. Some of the pathways for fabricating a particle density (or spacing) gradient-based on colloidal lithography are presented: a) A chemistry gradient generated by diffusion control is used

to develop the particle density gradient. Particles interact with the functionalised surface through electrostatic interactions and as a result, the region with the highest concentration of functional groups immobilises a larger number of oppositely charged particles. b) Stop-wide introduction of colloids (e.g. gold colloids) to the pre-treated surface (sulphur-terminated SAMs), c) Infusion-withdrawal of the pre-treated surface inside the colloidal suspension, d) a buffer with high ionic strength is introduced from the bottom into a vessel in which a thiol-modified chip is placed vertically inside a gold nanoparticle suspension with low ionic strength solvent. As a result, colloids gradually diffuse in the direction with a high concentration of ions, finally immobilising on the surface with a spacing gradient, e) a temperature gradient is applied to a surface which is covered homogenously with colloidal particles. As a result, the morphology of the heated particles will change gradually, forming a topography gradient along the chip.

The approaches presented in Table 3 can be categorised into the following sections based on the control factor:

- ***Chemistry gradient to direct assemblies of colloidal nanoparticles (Figure 14a)***

As the name suggests, this approach is based on an initial step of fabricating a chemistry gradient as the more intensive experimental stage and then the second simple stage of incubating the template with colloidal dispersions.

Bhat et al. fabricated the gold nanoparticle density gradient by initially templating a substrate with an aminosilane polymer gradient with varying molecular weight or polymer grafting density before dipping it inside a nanoparticle solution to establish electrostatic interaction between negatively-charged particles and a positively-charged amino surface (152). In another report, an aminosilane gradient was generated on a substrate by diffusion control of the aminosilane vapour. Then, the amino-coated surface was immersed in the citrate-capped gold nanaoparticles to form a gradient of nanoparticles (153).

While the maximum achievable surface coverage with colloids is mainly a function of time in dip-coating and drop-wise methods, the maximum coverage in this method is a function of the density of interacting surface polar functional groups.

- ***Incubation time is the main factor (Figure 14 b,c)***

Similar to the chemistry gradient, it is possible to form structural gradients with dip-coating or a drop-wise introduction of the colloidal particles.

Here, either chip insertion/withdrawal with a controlled linear rate (in dip coating) or liquid raise with a controlled volumetric rate (drop-wise method) would allow spatial control over the interaction of the colloids/precursor with the pre-treated chip, which is placed vertically inside

a container. As a result, a particle density/size gradient could be established as a function of the time of incubation.

The approach is inexpensive and implementable with a simple set-up which also allows good control of the generated gradient slope. The other important advantage of these methods is the possibility of implementing a rational design prior to gradient fabrication in order to estimate the approximate time needed for maximum surface coverage (on the extreme edge of the gradient). This can be accomplished with techniques such as real-time QCM-D monitoring of the surface during interaction with the colloids/precursor.

- ***Ionic strength is the control factor to direct the diffusing colloids (Figure 14d)***

In an innovative approach, the ion concentration along the vessel was used as a control to guide gradient formation (ref (106)). In the relevant study, the experimental container included vertically placed pre-treated chip and colloidal particles dispersed in a low ionic strength solvent. Immediately after the gradual injection of the second solvent with high ionic strength from the bottom, an ionic concentration gradient was formed by the gradual downwards diffusion of the charged particles. The diffusing particles gradually interacted with the chip surface to form a nanoparticle density gradient along the surface.

- ***Temperature control (Figure 14e)***

Temperature has been used as a factor to form a structural gradient by physically changing the morphology of the surface-decorated structures. This is because the temperature gradient has been proven to affect the morphology of the colloids deposited on the surface. Simplicity and reproducibility have been highlighted as the main advantages of this technique.

1.4.3.2.1 Method of choice as indicated by ranking

The method of choice in the framework of the current thesis was based on avoiding the techniques based on using organic solvents which require waste treatment as well as the approaches which were material or substrate-dependent. Based on the latter criteria, the temperature-responsive gradient was one of the last methods of choice to fabricate the topography gradient. As stated before, diffusion techniques, although predictable through theoretical estimations, allow less control in the selection of the increment between variables compared to dip-coating and dropwise methods. While the speed of the injection of the second solvent can be controlled, the diffusion of the particles will follow its own pathway. Finally, to avoid drawbacks, and benefit from the simple design and possibility of high throughput and

good control degree on the gradient attributes, the drop-wise introduction of colloidal dispersion/ions with time-control was selected as the method of choice.

In the current thesis, as one alternative to a homogenously-modified surface which was gradually brought in contact with the colloidal dispersion/precursor by time-control (Figure 13 b), a chemically patterned surface was used to translate chemistry patterns into topographical structures to form two new gradients of nanocluster density gradient and nanodom-size gradient, which have not been previously reported. For this purpose, ordered arrays of reverse micellar templates were formed based on the microphase separation of block copolymers. Microphase-separated block copolymers spontaneously form periodic arrays of domains with defined size and separation, which can attract nanoparticles based on electrostatic interactions, transferring the patterns to nanoparticle assemblies. Usually, nanoparticles are attracted to one phase or block of the copolymer while being repelled from the other phase based on electrostatic charge (154). Bhat et al. have extensively studied the correlation between polymer properties i.e., the polymer molecular weight and polymer grafting density (MW/σ) and the size and distribution of nanoparticles in a polymer brush gradient (155-157). This could allow a chemistry gradient to be formed via the gradual tuning of grafting variables as a template to generate a nanoparticle density gradient.

1.4.4 Two-dimensional chemistry and structural gradient

A two-dimensional gradient is referred to as the perpendicular variation of two independent surface parameters. This class of surface gradients allows monitoring the biologic response as a function of two variables concurrently. It is highly desirable to investigate the biomolecule response to multivariate gradients as this offers more information than a single gradient in less time. As discussed in previous sections, the biomolecule-surface interactions are highly affected by both surface chemistry and surface morphology hence, the dual optimisation offers more advantages compared to individually fabricated morphology and chemistry gradients.

Some of the reported orthogonal gradients are illustrated in Figure 15.

1.4.4.1 The orthogonal gradient of two surface properties from the same category (chemistry or topography)

There have been reports of an orthogonal surface gradient generated from two surface variables of the same category (e.g., both chemical or both topographical). Some of the examples are summarised below:

- ***Vapour diffusion technique/polymerisation via "grafting from" technique (Figure 15 a)***

  One of the early studies of an orthogonal gradient with both chemistry gradients was conducted by Bhat et al. to investigate the impact of the thickness and density of the surface grafted polymer brush on nanoparticle assemblies (157). The study was carried out using two ~~different precursors and~~ two different approaches, first using a vapour diffusion technique to form a molecular weight gradient and then, via radical polymerisation based on grafting from approach to fabricate a grafting density gradient. The study allowed the impact of two chemical aspects of the polymeric surfaces on nanoparticle assembly to be investigated concurrently.

- ***Photolithography for the generation of a master and injection moulding to transfer patterns (Figure 15 b)***

  In another instance, the orthogonal variation of two surface topography parameters, the groove depth and groove spacing, was fabricated by a multi-step procedure including photolithography and dry etching to generate masters followed by an injection moulding technique to transfer patterns to the desired material surface. The orthogonal gradient fabricated offered the possibility of upscaling the process and allowed the systematic and simultaneous investigation of the response of different cells to two topography clues (94).

1.4.4.2 The orthogonal gradient of two different surface properties

- ***Electrochemistry approach (Figure 15c)***

  In an orthogonal gradient of a topography and chemistry study, the electrochemistry approach was utilised to generate a Si pore size gradient in one direction by anodisation in an etching solution and varying current density followed by the electrografting of the ethyl-6-bromohexanoate polymer brushes in the perpendicular direction by gradual variation of current density during reaction time. The orthogonal gradient prepared was used to study mesenchymal stem cell (MSC) behaviour after functionalising the chemical gradient with amino-terminated cyclic arginine-glycine-aspartic acid-D-phenylalaninelysine (c(RGDfK)) (158). The approach was advantageous due to the use of one technique (i.e. electrochemistry) to fabricate two gradients of different types, which avoided the need for a second instrument and shortens the process preparation time. Furthermore, an electrochemical approach intrinsically offers the possibility of scaling up the gradient fabrication.

- ***Photolithography for master fabrication followed by hot embossing/static mask-assisted plasma polymerisation (Figure 15d)***

The other orthogonal chemistry and topography gradient combination was reported by Yang et al. The group fabricated grooves with varying widths (5μm-95μm) by mask-enabled photolithography to fabricate the master and then patterns were transferred to the surface using a hot embossing technique. In the next stage, a plasma gradient coating with two precursors of allylamine and hexane was deposited with diffusion control (using a coverslip placed on the sample) in a perpendicular direction to the first gradient aiming to generate amine concentration gradient. The orthogonal gradient was used to study cell proliferation and morphology in response to surface chemistry and surface topography variations (159). While the hot embossing technique offers an inexpensive approach with the possibility of upscaling the process of gradient formation, a chemistry gradient with plasma polymerisation offers the advantages of fast, substrate-independent, environmentally friendly vapour phase deposition, which is implantable with a simple and affordable mask design.

Table 4 summarises the abovementioned case studies in order to give further details about the materials, gradient attributes, possible or investigated applications and the ranking based on the author's choice.

1.4.4.3 The methods of choice

In the current thesis, it was decided to investigate a 2D gradient consisting of two variables of different categories. The ranking in the table is based on the author's preference of fabricating the chemistry gradient with plasma polymerisation, and the preferred method for developing a topography gradient is a technique that allows a simpler, inexpensive setup and avoids complex instrumentation with fewer processing steps. Therefore, we have chosen to develop an orthogonal gradient consisting of a structural gradient of a nanoparticle density gradient developed by a time-controlled colloidal lithography approach based on optimising the time required for maximum surface coverage. Then, a static mask-assisted plasma-enabled nitrogen-functional chemistry gradient was fabricated in a perpendicular direction to the topography variations.

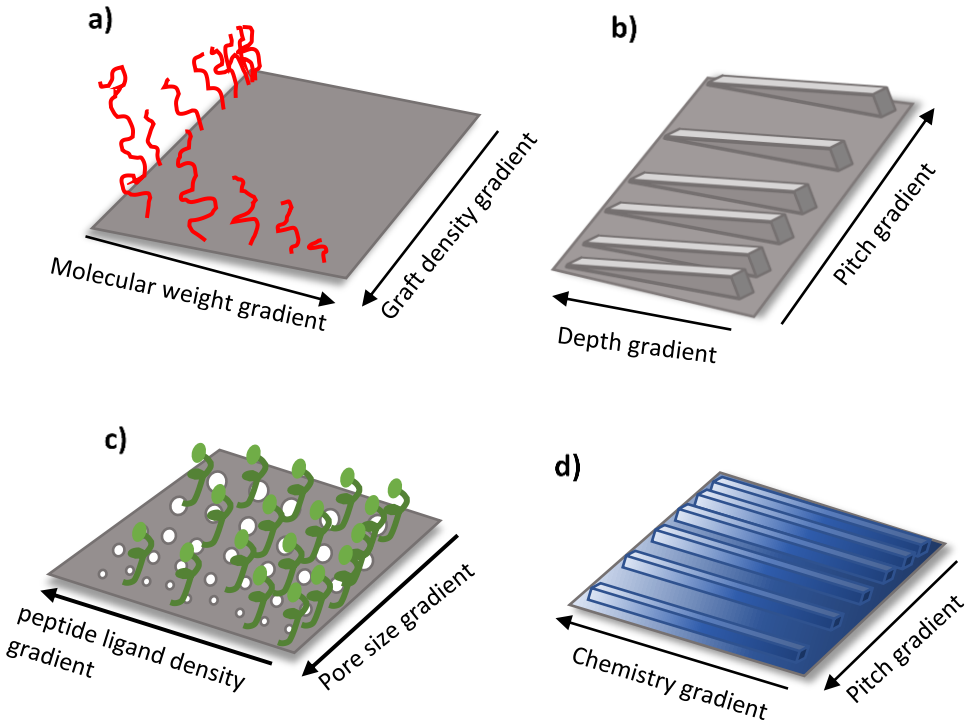

Figure 15. Several examples of the reported orthogonal gradients are presented: a) The two perpendicular chemistry gradients of molecular weight and graft density; b) The two perpendicular topography gradients of pitch and depth of the grooves; c) the topography gradient of pore size perpendicular to the chemistry gradient of peptide ligand density and, d) the topography gradient of groove pitch perpendicular to the chemical group density gradient.

Table 4. Some orthogonal gradients reported in the literature, with corresponding gradient attributes and applications are presented. The ratings are intended to show the author's preference.

Technique (gradient 1/gradient 2)	Precursors/substrate	Surface variables	Gradient length	Developed or potential application	Ref.	Rating
Chemistry gradient template to control the structural gradient: organosilane vapour diffusion technique / "grafting from" technique using atom transfer radical polymerisation	Octyltrichlorosilane (OTS) for gradient 1 and Poly(2-(dimethylamino) ethyl methacrylate) for gradient 2, silica substrate	Molecular weight (MW) and grafting density (σ) variation leading to gold nanoparticle density gradient	Total dimension: 60 mm × 5 mm	To study the assembly of nanoparticles on grafted polymer surfaces	(157)	***
Lithography methods: Photolithography and reactive etching to form masters, then an injection moulding step transferred patterns.	Hexane (ppHex) film was deposited via plasma polymerisation in the master.	Pitch and depth of grooves	Total dimension: 10 mm x 10 mm	Investigation of the response of several types of cells to the topographical clues	(94)	***
Electrochemistry approach: Anodisation /electrografting	The topography gradient and the chemistry gradient of ethyl-6-bromohexanoate was functionalised with arginine-glycine-aspartic acid was generated on a porous Si substrate	Pore size gradient and ethyl-6-bromohexanoate group density variation	Chemistry gradient: 14 mm, topography gradient: 12 mm	To investigate stem cell behaviour	(158)	***
Lithography methods: Photolithography for master fabrication followed by hot embossing/plasma polymerisation	The groove width and allylamine (ppAAm) plasma gradient were implemented on a Si substrate	Groove width gradient and amine-group concentration gradient	Total dimension: 10 mm x 10 mm	To study cell proliferation and morphology	(159)	****

1.5 Aim of the thesis

In the present thesis, rather than developing a full biosensor, we concentrated solely on the material surface, with a special focus on developing a versatile bio-interface optimisation tool which can be utilised to improve surface physicochemical properties. The proposed platform has potential applications for developing both plasmonic substrates for biosensing i.e. surface-

enhanced Raman scattering as well as a platform for conducting tissue-engineering studies or many other studies needing complex combinatorial tools.

We believe that surface gradients are the best tool for optimising the physiochemical biointerface properties from many aspects, as discussed before. In this thesis, we aimed to prepare functional molecular and structural gradients for biosensing applications by controlling interactions between surface and molecular-level species as a function of distance across the surface. For this purpose, initially, several 1-D chemistry and 1-D topography (structural) gradients were developed and investigated for surface characteristics and gradient attributes. Then, as the ultimate objective, we explored the possibility of developing orthogonal gradients by varying two different categories of surface properties, i.e., i) a gold nanoparticle density gradient generated on the surface of a plasma-enabled nitrogen-functional homogenous bilayer coating, which was later coated with ii) a %N gradient of 4 distinct coatings deposited with a masking device and with a gradual increase of the NH_3 flow rate with respect to ethylene (NH_3/C_2H_4).

1.5.1 Fabricating 1-D chemistry gradients

We employed two separate plasma techniques, each with a different method for preparing 1-D surface chemistry gradients. With the first technique, the objective was to generate a density gradient of the oxygen-containing functional group along the surface using a hexamethyldisiloxane precursor and gradually increasing the oxygen flow rate. For a continuous surface gradient, the atmospheric pressure corona jet was programmed to move along the fixed polypropylene sample at certain intervals and deposit the coating according to the pre-adjusted electrical plasma and spatial displacement conditions. By developing the surface chemistry gradient, the ideal was to achieve a wide range of wettability from highly hydrophobic to a completely wettable surface.

The second approach for fabricating a chemistry gradient was attempted in static mode using low-pressure capacitively-coupled RF plasma and using a mask to generate a density gradient of groups containing nitrogen. The mask design was adapted to implement the deposition precisely onto the defined areas for each amino-functional coating. The deposition parameters were selected accordingly to ensure the highest chemical stability in aqueous media for those coatings with a higher nitrogen content (N%).

1.5.2 Fabricating 1-D topography/structural gradients

The second objective was to introduce a simple fabrication method for generating 1-D structural gradients on templated surfaces, using a colloidal lithography technique. The idea

was to obtain the maximum surface coverage possible with structures, relying on a rational design which was made by considering the kinetics of adsorption using QCM mass-time curves obtained in real-time after a colloidal suspension/salt solution was incubated with each template. Based on this, the optimum flow rate required for the controlled introduction of the colloidal suspension/salt solution was calculated. Upon the dropwise introduction of the fluid with the determined rate, the gradually rising fluid generated a gradient in the time of incubation on the surface, which manifested itself as the density/size gradient of surface nanostrucutres. More details on the up will be provided in chapter 2 (2.1.3).

1.5.3 Fabricating the Orthogonal gradient

Increasing the number of independent variables (or increasing the dimension of a gradient) increases the degree of freedom, giving higher selectivity and control over the surface characteristics. Therefore, after evaluation of the results for 1-D gradients, the goal was to demonstrate the possibility of combining the two independent variables in one single sample, or other words, the double optimisation of surface properties. Since both the topography and chemistry clues impact biomolecule-surface interactions, the simultaneous variation of both types of variables and assessment of the biological response is more advantageous than studying only one type of variable. As will be shown, depositing the top coating (1-D chemistry gradient) on the topography gradient requires careful optimisation of the coating thickness, as a thicker coating affects the roughness and morphology of the surface. This optimisation of the thickness to retain the roughness factor needs to be done without sacrificing the stability of amino-functional coating in aqueous media since a thinner coating is more susceptible to dissolution in water. It was observed that a thick coating (similar to or bigger than the diameter of the nanoparticles) would decrease the overall roughness factor parameter and diminish wettability variation for the hydrophilic and slightly hydrophilic coatings. On the other hand, apart from the topography and chemistry variation, due to the plasmonic feature of the underlying gold nanoparticles, the thinnest possible coating that allows benefits from this feature for developing plasmonic bio-interfaces could be a subject for future studies.

Chapter 2: Experimental

This chapter lays out all the fabrication steps of the coatings and synthesis of materials developed in the framework of the current thesis, along with theories of the characterisation methods employed with the relevant instrumentational specifications.

Beginning with the coatings, first, preparation steps for the two different plasma-enabled chemistry gradient coatings are introduced and next, the two different stochastic and two different periodical and time-controlled unidirectional topography gradients are presented (in total, four coatings).

Finally, the selected method for fabricating orthogonal (2D) gradients by combining one of the selected unidirectional chemistry gradients with one of the selected topography gradients are introduced.

The next section is dedicated to surface characterisation and particle analysis methods. The specifications of the characterisation instruments and the user-adjusted parameters are briefly presented followed by the underlying theory and principles of each characterisation method.

2.1 Fabrication and synthesis

2.1.1 Fabricating the first chemistry gradient: 1-D oxygen-containing chemistry gradient

2.1.1.1 -plasma phenomenon

Plasma, whether as a naturally occurring phenomenon (solar corona, lightning strikes, etc.) or industrial plasma, is characterised based on two parameters: electron temperature and electron density. For instance, solar core, stars and fusion reactors tend to have a high temperature and electron density while the industrial plasmas used for routine material surface treatment (whether thermal or non-thermal) are identified with relatively lower temperatures and electron density. For instance, capacitively coupled plasma and corona discharge, which are used for material treatment and film deposition, have electron densities and electron temperatures of 10^{16} e/m^3 , 10^{14}-10^{17} e/m^3 and 4x 10^4 K , T<500 K, respectively (160, 161), compared to 10^{32} e/m^3 and 2x 10^7 K in stars (162).

Figure 16 shows how various plasmas are positioned based on electron density and electron temperature.

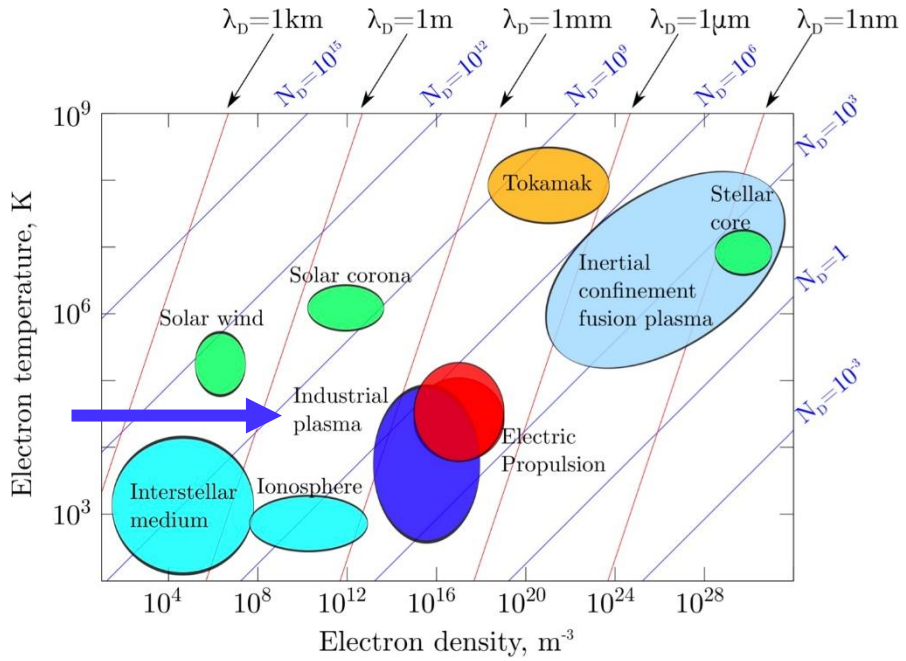

Figure 16. Various types of natural and artificial plasma are positioned based on electron temperature and electron density. Obtained from: https://pdml.engr.tamu.edu

Plasma offers a media that can be utilised to initiate reactions through fragmentation, ionisation, the recombination of molecules and the formation/deposition of polymers. For instance, some of the mechanisms investigated for plasma-assisted polymerisation in low-pressure glow discharge plasma are i) classical chain-growth polymerisation based on the formation of either radicals or ions that are produced inside the plasma, ii) ion-molecule reactions where ions produced by fragmentation play the main role, iii) monomer fragmentation-poly-recombination, which yields irregular and randomly shaped structures, etc. (163). Atmospheric pressure plasma, such as corona jets are widely applied for the treatment of heat and vacuum-sensitive material surfaces, ranging from synthetic polymers to body tissues and food, without damaging/altering the material. Corona operates under an open atmosphere and demonstrates a filamentary discharge which is capable of coating smaller areas and can be automated for batch processing.

Several types of plasma technologies are adapted for film coating and surface modification approaches, which are chosen depending on several considerations e.g. the sensitivity of the material to be treated, required homogeneity, and the dimension of the treated area. Film deposition with nonthermal atmospheric-pressure plasma jets including corona jets has been

studied extensively as they offer the advantages of affordability, (due to avoiding expensive vacuum systems) and the possibility of treating thermo-sensitive substrates.

The corona discharge is a filamentary discharge usually formed on a sharp tip, or the edge of an electrode as a result of strong electric fields and relatively low applied voltages in atmospheric pressure (164). The corona is also known as one-electrode plasma since discharge is formed between an electrode and an insulating platform, rather than between two electrodes (165). Corona discharge has been widely employed in the coating industry for the modification of polymer surfaces, especially polyolefins, namely polyethylene and polypropylene, which aim to increase surface adhesion, and printability with inks, imparting of laminability and modification of the surface energy of polymers (166, 167). Corona-enhanced chemical vapour deposition techniques have been adapted for the deposition of organosilane coatings, which have well-recognised chemistry with a wide range of applications (168-170). Herein, the fabrication of the density gradient of the oxygen-functional group is presented with a one-step process using a corona jet. The advantages of plasma polymerisation, including the tunability of surface chemistry, substrate-independent polymerisation, gas-phase deposition and the possibility of deposition on heat-sensitive substrates, are combined with the design of the corona jet, which enables maskless and up-scalable surface deposition.

Hexamethyldisiloxane, a well-known organosilicon molecule, was selected as the polymerisation precursor since it has been extensively investigated, and the mechanism of film growth and polymerisation is broadly discussed. Incorporating an oxidant such as oxygen increases the diversity attainable in the chemical composition and wettability characteristics of the thin film. The gradient formation was based on the gradual incorporation of oxygen into the plasma system, which eliminates methyl groups from the initial organic precursor and is substituted in the polymer chain during polymerisation up to the point where ideally all the methyl moieties are finally eliminated and a silicate polymer network (silicon atom linked to four oxygen ones), a purely inorganic coating, is formed. Some part of the polymerisation process is demonstrated in Figure 17.

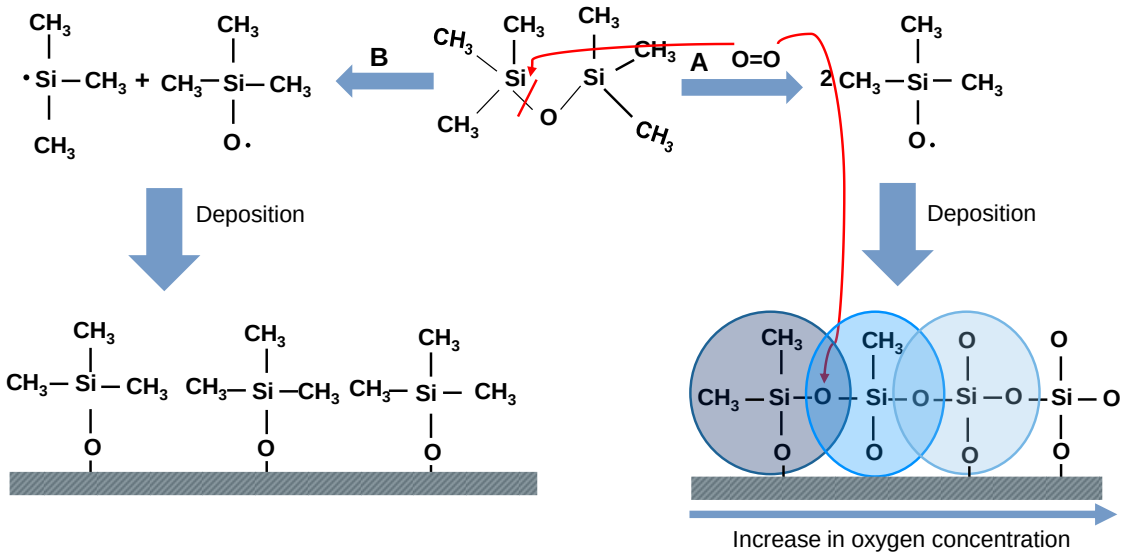

Figure 17. The steps involved in the plasma-assisted polymerisation of siloxane obtained from (171).

A fully automated corona jet system from AlmaPlasma srl connected to a computer numerical control (CNC) pantograph and remotely controlled high-voltage pulse generator (AlmaPULSE, AlmaPlasma Srl) was used to deposit the coatings. A remotely controlled liquid and gas console with four mass flow controllers (EL-FLOW, Bronkhorst), a liquid flow meter (miniCORI flow, Bronkhorst), and a controlled evaporation mixer comprised the flow system (CEM, Bronkhorst). A single high-voltage electrode was the plasma source, of AlmaJET, fixed on the head of the CNC system as previously described in (172), suited for localized plasma depositions. The three gas streams were introduced during the operation through separate inlets, as follows: i) The primary gas was injected into the plasma discharge zone via channel I at the top section of the source. It included 2.0 slpm of argon (Ar) as a carrier, 0.2 g/h (0.0043 ml/min) of hexamethyldisiloxane (HMDSO, Sigma Aldrich), and progressively changing oxygen levels ranging from 0 to 400 ml/min (0 to 0.4 slpm). These are also reported as percentages (0–7.4%), for the ratio of oxygen to the whole argon supply in the discharge or, molar ratios of oxygen to the monomer flow rate (O_2/HMDSO): 0, 17, 35, 70, 175, 262, 350, were introduced to deposit the chemistry gradient; ii) The secondary gas of 3 slpm Ar, was introduced through a channel below the downstream of the high-voltage electrode tip; iii) A shield gas with 3 slpm of nitrogen (N_2), was also introduced at the exit of the plasma source through a separate channel in order to contain the plasma from the surrounding atmosphere. After preliminary trials, 15 mm distance between the exit of the plasma jet and the surface of

the substrate was defined as the optimal distance. Two types of coatings were deposited on polyethylene foil with approximately 500 µm thickness: a) individually or statistically deposited coatings and b) the continuously deposited gradient coating or dynamic deposition. The statically deposited coatings were approximately 2 cm in size deposited for 60 seconds, and the dynamic deposition (the gradient) was carried out at a rate of 15 mm/min.

Figure 18. depicts the AlmaJET configuration, including gas supply inlets and the filamentary corona discharge.

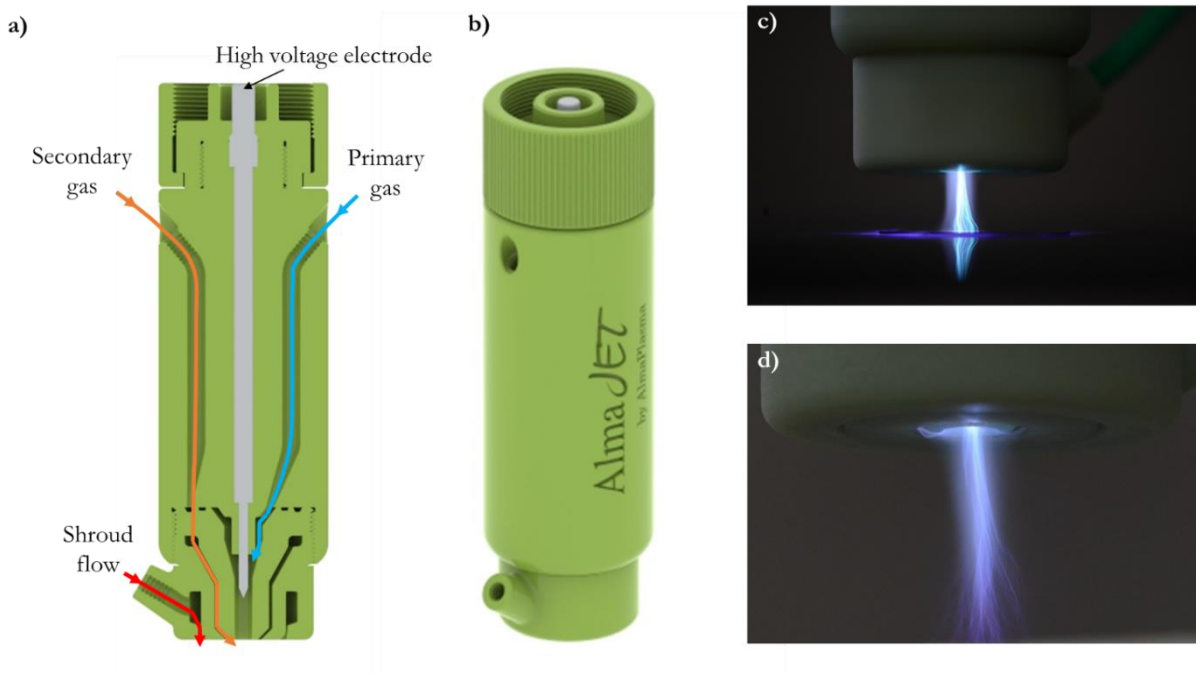

Figure 18. The corona jet source setup. a) The three channels for gas supply and the high voltage electrode; b) 3D view of the jet; c) Plasma treatment of a substrate; d) The closer view of the free-flow discharge.

2.1.1.2 Deposition of spots

The static mode deposition of HMDSO polymers was implemented on polyethylene transparent films for a 60-second time duration. Seven coatings were deposited using the static mode, starting from the first sample which was deposited in the absence of oxygen, gradually increasing the O_2 admixture up to 400 ml/min i.e., 7.4% O_2 content.

2.1.1.3 Dynamic deposition

After the optimisation of the plasma parameters for static deposition, similar settings were applied for dynamic deposition with a process rate of 15 mm/min. (i.e., the speed at which the

plasma jet was displaced along the surface). The oxygen flow rate started from 0 to 80 ml/min O_2 (0-5.7%) and electrical parameters were maintained consistent at 12 kV-12 kHz; however, when the flow rate exceeded 80 ml/min (5.7%), to provide more energy for efficient gas dissociation and to prevent jet quenching due to the higher suppliance of O_2 molecules, the electrical parameters were switched to 15 kV-15 kHz.

2.1.2 Fabricating the second chemistry gradient: 1-D nitrogen-containing chemistry gradient

2.1.2.1 Deposition conditions and mask design

Plasma-polymerised amino-functional coatings have been investigated for a variety of applications, in areas ranging from the medical field (173) to material science e.g. to increase interfacial adhesion in fibre-based composites by establishing amine bonds between the fibre surface with epoxy groups of the resins (174), through the dying and coloration of textile surfaces by binding dye molecules with a NH_3/C_2H_4 polymerised coating (175), and the selectivity improvement of the proton over co-ions after coating ion-exchange membranes (i.e. Nafion®) with an NH_3/C_2H_4 coating for ion-selective electrode fabrication (176).

The amino-functional density gradient was fabricated based on the set-up described in (107). Briefly, a capacitively-coupled plasma with a 13.56 MHz radiofrequency (RF) source was used to deposit the coatings (See Figure 19). The chemistry gradient was generated by employing a static masking device and by adjusting the precursor ratio (NH_3/C_2H_4) and power input. As shown in Figure 20, a total of four distinct areas, each corresponding to a deposition condition were formed by using the mask and tuning plasma parameters.

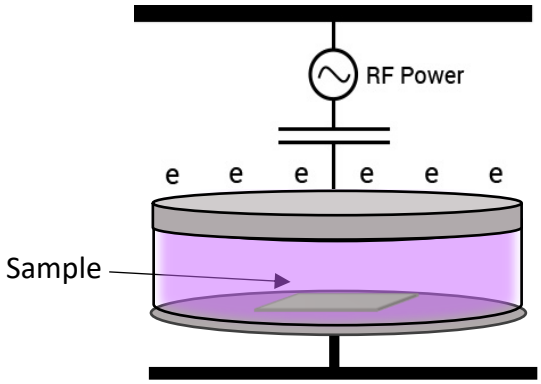

Figure 19. A cylindrical plasma chamber in the symmetrical setup involves two plane parallel electrodes, one connected to the RF source and the other grounded.

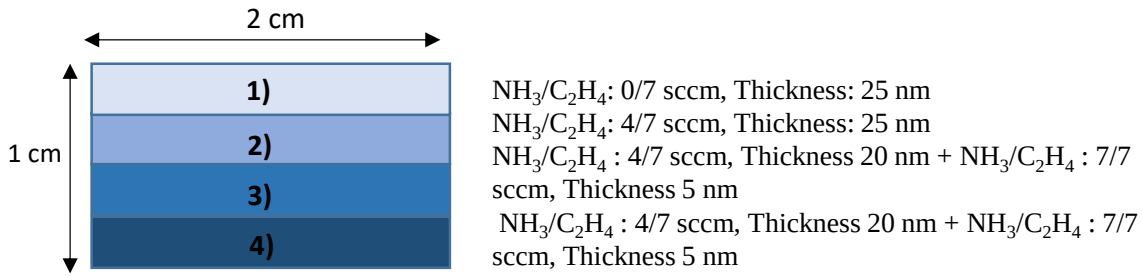

Figure 20. Mask-enabled chemistry gradient along the width of the chip.

The mask allowed the deposition of four distinct areas along the width of the sample and perpendicular to the nanoparticle density gradient. For this, a polymeric (PEEK polymer) masking device was fabricated, consisting of two parts, a plate including grooves to place chips and a cover with narrow slits, to partially cover the sample. Each slit was 2.5 mm wide and 10 cm long. The samples were fixed inside the grooves of the plate, then the cover was fixed on the plate using one of the two pins. After assembling the two parts, the whole mask was placed inside the capacitively coupled plasma chamber for the first deposition. After the deposition of the first coating, the cap of the mask was removed and fixed on the second pin. After completion of the second coating, the cover was inverted by 180° and the third and last coating was deposited by displacing the cover slits on top of the plate using the two pins. The vertical distance between the plate and cover was adjusted to minimise the diffusion of plasma under the plate. 20 numbers of 2x1 cm chips were able to be coated simultaneously by the fabricated mask. An overview of the device is shown in Figure 21. The double pressure in the last coating was generated manually by adjusting the plate valve leading to the vacuum pump, because when the valve is partly closed, the pressure increases, as new gas is introduced into the reactor continuously during deposition.

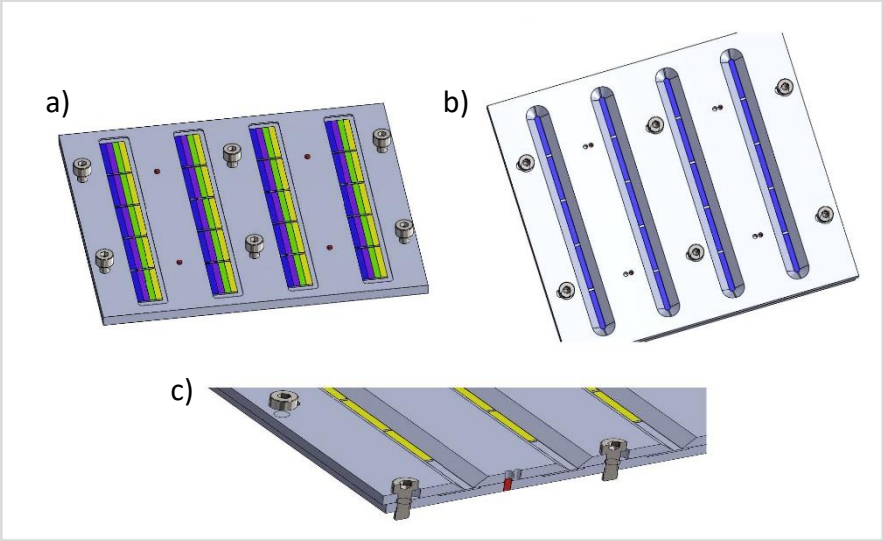

Figure 21. The mask design: a) plate with grooves containing samples, b) cover containing slits, c) side view of the two parts fixed with screws

2.1.3 Fabricating structural gradient

All the structural gradients in this section are generated based on electrostatic interactions between the solid substrate, which is functionalised with positively charged domains, and negatively charged particles/molecules in the liquid phase. The time factor allows the number of particles/molecules interacting with the surface to be controlled, hence providing a tool for gradually generating a varying size or density of the surface nanostructures along the substrate. The experimental setup that we have proposed uses spatial control to enable different times of exposure of the surface to the particles/molecules which are introduced to the experimental vessel (see Figure 22).

The experimental setup is designed to set the maximum surface coverage time and correlate the number of adsorbed particles on the surface, with the time of incubation at each point along the length. The gradient was prepared on a chip, which was placed vertically inside a vial containing an aqueous suspension of nanoparticles or a precursor solution that rose gradually. The increase in volume expands the exposed length of the chip to the solution linearly and indirectly controls the duration of exposure of the different points of the chip. The time of exposure, in turn, controls the adsorbate's surface density and, as a result, the nanoparticle densities or size of the generated nanoparticles. Prior knowledge of the surface density of the adsorbate versus the duration of exposure from the adsorption isotherm, measured using a quartz crystal microbalance (QCM), allows the process parameters to be determined rationally.

The rate of volume increase determines the rate of the exposure length, which may be accurately controlled using a microfluidic pump with a given flow rate (f) and the selection of a vessel with an appropriate cross-section (which in our case was cylindrical, with radius r). The following are the design criteria that allow us to convert the time dependency of the processes, as acquired from QCM, into the spatial relation of the ultimate gradient: (a) QCM provides the time (t) necessary to reach the maximum surface coverage or density (N) with the adsorbate; (b) the defined length of the gradient (L), and the time (t) to achieve the surface density N, were placed in equation 1 to determine the rate of increase in the height of the solution (the same as the distance of the chip exposed to the solution). A microfluidic pressure pump dedicated to droplet formation with µl/min flow rates with minimal pulses (ideally pulseless) was used to set a flow rate, f, considering the cross-section of the experiment vial (which, in this case, is a cylindrical vial with a radius r), to measure the equivalent volume increase required for the desired height increase (Eq (2.1)). Based on the equation, t_l gives the length of exposure of any place at a distance l from the start of the gradient. where t_l is determined by the distance of the point from the start, and the speed of increase of height of the solution front (Eq (2.2)).

$$f = \pi r^2 L t \qquad (2.1)$$

$$t_l = \frac{t\ (L-l)}{L} \qquad (2.2)$$

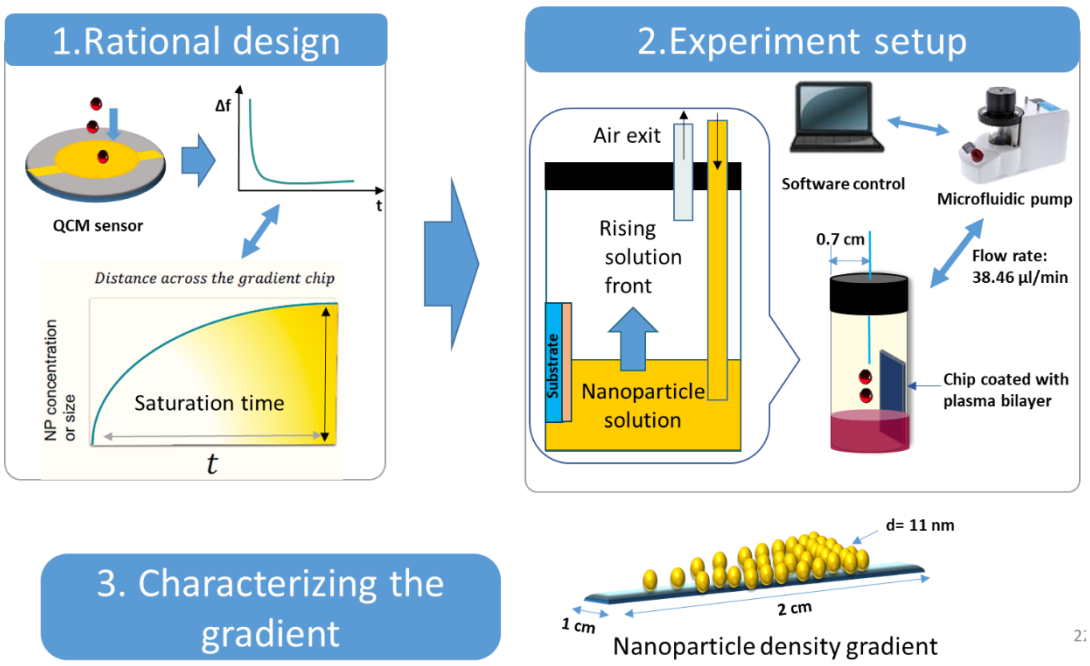

Figure 22. ***Fabrication process starting from QCM measurements by monitoring nanoparticle interaction with each functionalised surface, converting the recorded kinetic curves to mass variation vs time to allow the estimation of the incubation time required for surface saturation, followed by a gradient experiment based on the dropwise introduction of nanoparticle dispersion inside a vessel using flow rate obtained from saturation time. When fluid travels upwards and covers the sample surface, time-dependent surface coverage based on the electrostatic adsorption of the particles with surface functional groups/domains leads to the distribution of particles along the vertical direction and the formation of density gradient.***

2.1.3.1 Synthesis of citrate-capped gold nanoparticles

Citrate-capped gold nanoparticles were synthesised based on the Turkevich method under the reflux system (177). Citrate is used both as stabilising and reducing agent and upon reaction with a hydrogen tetrachloroaurate ($HAuCl_4$) solution, reduces the ionic Au^{3+} to colloidal gold particles. In summary, 30 mL of a gold chloride solution (1.02 mM) was heated to boiling point while the solvent was being refluxed. After boiling, a 6 mL of 38.80 mM sodium citrate solution was transferred to the flask via its side inlet and was allowed to react for 10 minutes until a wine-red colour appeared.

2.1.3.2 Fabrication of templates

- ***Self-Assembled Monolayers***

The vapour phase deposition approach was used to create a monolayer of (3-aminopropyl)-trimethoxysilane (APTES) on silicon and glass substrates. First, the substrates were cleaned

with reactive ion etching (Oxford Plasmalab 80, UK), by O_2 plasma (15 mtorr, 100 mW) for 3 minutes.

The substrates with the activated surfaces were placed inside a vacuum desiccator and incubated with APTES vapours under the pressure of approximately $5x10^{-3}$ mTorr for 2h. Finally, samples were rinsed with isopropyl alcohol and dried.

- ***CHN plasma bilayer***

Using a previously developed approach (107), smooth amino-containing CHN plasma polymer layers were generated using RF-driven capacitively coupled discharge in a vacuum reactor. A bilayer coating was designed to enhance the chemical stability of the upper amine functional layer in aqueous media, as polar amine groups have a natural tendency to dissolve inside protic solvents which leads to the decomposition of the deposited thin layer. As a result, a vertical gradient of plasma polymers was deposited, consisting of a strongly crosslinked platform layer and a less crosslinked amino-functional upper thin layer with a total thickness of 20 nm by tuning the power input and plasma precursor (NH_3/C_2H_4) flow ratio. The high input power resulted in intensive fragmentation and a more crosslinked and less functional layer, while a decrease in power and increase in ammonia ratio led to the generation of a maximum 1 nm upper functional layer with higher nitrogen content. The deposition conditions are summarised in Table 5. Summary of plasma deposition conditions for the thin films employed in different steps. for all the plasma-deposited coatings using capacitively coupled plasma which are discussed in this manuscript.

- ***Fabrication of micellar templates***

The micellar templates were developed using a previously published method (178). Briefly, thin-film templates of PS-b-P2VP were spin-coated on Si and glass substrates followed by subsequent heating and solvent evaporation steps. Micellar substrates were further etched by reactive ion etching to better define patterns and remove any leftover polymers between micelles for developing gold nanoclusters. As each reverse micelle was utilised as a template for fabricating a nanoparticle cluster, the desired template size and cluster spacing were tailored using an oxygen reactive plasma etching process.

Table 5. Summary of plasma deposition conditions for the thin films employed in different steps.

Properties	**Thickness (nm)**		**NH_3/C_2H_4 ratio (sccm/sccm)**	**Power (W)**	**Pressure (mbar)**	**Deposition time (s)**	
CHN platform							
Top layer	1		7/7	50	0.1	10	
Base layer	19		4/7	70	0.1	60	
Chemistry gradient							
Coating 1	25	10	0/7	70	0.1	150	60
Coating 2	25	10	4/7	70	0.1	166	66
Coating 3	5 (tl) + 20 (bl)	1 (tl) + 10 (bl)	7/7 (tl) + 4/7(bl)	50 (tl)/70(bl)	0.1/0.1	63/133	13/66
Coating 4	5 (tl) + 20 (bl)	1 (tl) + 10 (bl)	7/7 (tl) + 4/7(bl)	50 (tl)/70(bl)	0.2 (tl)/0.1 (bl)	52/133	10/66
Properties	**Thickness (nm)**		**NH_3/C_2H_4 ratio (sccm)**	**Power (W)**	**Pressure (mbar)**	**Deposition time (s)**	

tl: top layer, bl: bottom layer

2.1.3.3 Fabricating gold nanoparticle and gold nanocluster/nanodom gradients

Systematic studies to define a robust protocol that correlates the process and surface structure require numerous experiments to be conducted. As a result, a simplistic method for fabricating 1-D spatial gradients using metal nanoparticles/nanostructures of varying density and/or size is very desirable. We present a simple protocol based on the time-dependent physisorption or chemisorption of colloidal particles from aqueous media on a solid surface. The gradient set-up was based on certain rational design criteria as shown in Figure 22. It was assumed that the strong electrostatic irreversible interaction between particles and substrate follows the random sequential adsorption theory (RSA) model in which the maximum surface coverage predicted

for an infinite time of incubation t_∞ is 54.7% for high ionic strengths. The following equation provides the surface coverage fraction θ as a function of time:

$$\frac{d\theta}{dt} = k_a \ n.B(\theta) - k_d \tag{2.3}$$

where n is the bulk concentration of particles, k_a and k_d, are rates of adsorption and desorption respectively, and B(θ) is the blocking function with the maximum value of 1, corresponding to the free surface at the beginning of adsorption. More in-depth analysis has been attempted to define the blocking function and the saturation coverage considering the geometry of the substrate.

The Langmuir adsorption model assumes that $B(\theta) = \theta_\infty - \theta$ and that the adsorption is reversible. The θ_∞ is called the jamming limit or saturation coverage. Rearranging the previous equation by replacing B(θ), we obtain the Langmuir adsorption equation:

$$\theta = \frac{k_{eq}{}^{n}}{1+ k_{eq}{}^{n}} \ \theta_\infty \tag{2.4}$$

Where, $K_{eq}=k_a/k_d$.

Via Monte Carlo calculations, it is possible to obtain theoretical values of B(θ) and θ_∞ for different surface geometries (179). Figure 23 depicts two surfaces with different surface geometries and the same length/diameter to demonstrate the influence of surface topography variation on surface coverage. Curved geometries obviously adopt a greater number of particles as compared to a flat surface of the same length.

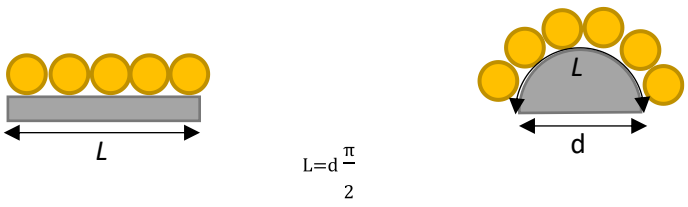

Figure 23. The occupancies of the one-dimensional flat surface and the hemisphere surface are compared. Particles of the same size occupy the hemisphere with a perimeter of L more than the flat substrate with the length of L.

However, as mentioned, Langmuir describes reversible adsorption in an equilibrium system. For non-ideal systems, the empirical Freundlich isotherm can be employed:

$$q_e = k_f C_e^n \quad (2.5)$$

The logarithmic form of the equation can be written as:

$$\log q_e = \log k_f + n \log C_e \quad (2.6)$$

where q_e is the equilibrium quantity of solute adsorbed per unit weight of the solid, k_f denotes the Freundlich constant, n denotes the Freundlich exponent, and C_e represents the equilibrium concentration of solute in the solution (180). From an energy aspect, according to Langmuir, all the adsorption sites for the adsorbate have identical energy and according to Freundlich, there is heterogeneity which causes a logarithmic decrease of adsorption energy when the surface coverage increases (181). To satisfy the conditions of both isotherms, attempts have been made to merge both equations.

The Sip's equation known as Langmuir-Freundlich is a versatile combination of both isotherms (182):

$$q = \frac{Q_m \ (K_a C_{eq})^n}{(K_a C_{eq})^n + 1} \quad (2.7)$$

where q is the amount of adsorbate (mg/g), Q_m indicates the system's absorption capability (mg of sorbate/ g sorbent), K_a is the adsorption affinity constant (L/mg), C_e is the equilibrium concentration of solute and n is the index of heterogeneity.

2.2 Analysis and surface characterisation

The evaluation step is crucial after fabrication and we have used classic and modern characterisation tools for all coatings and gradients (chemical and topography). Here, the theoretical description and the instrumental specifications are provided for each type.

2.2.1 FTIR

2.2.1.1 Method

Chemical characterisation was performed on samples using ATR mode of Agilent Cary 660 FTIR spectrometer, equipped with monolithic diamond crystal with the beam set at 45°, performing 32 scans with a scan resolution of 4 cm^{-1}. Following data acquisition, each spectrum was subjected to a baseline correction. The spectra were normalised to a prominent characteristic peak of the substrate, the CH_2 stretching band at ~ 2913 cm^{-1}, since it was constant and was not involved in the polymerisation reaction. The deconvolution was performed (by Origin lab software) on the Si-O-Si wide peak at 1000-1250 cm^{-1} in all spectra

for the static deposition mode as well as linear gradients based on Gaussian curve fitting. The peak was deconvoluted to the corresponding different vibrational modes all assigned to Si-O-Si.

2.2.1.2 Theory of FTIR

The molecular level characterisation of organic materials, e.g., polymers is possible through vibrational spectroscopy and by studying the vibrational modes of groups of bounded atoms, as a result of excitation with incident light. The energy gap between the excited vibration state and the initial state is shown in the following formula:

$$E_{vib} = E_{n+1} - E_n = hc\tilde{\nu} \quad (2.9)$$

Different vibrational modes are possible, with stretching, bending, and torsion being the main modes, and each mode appears at different frequencies. The total theoretical normal modes for a molecule with N atoms are calculated by 3N - 6. Two dominant vibrational spectroscopy techniques for chemical composition characterisation are Infrared (IR) spectroscopy and Raman Spectroscopy, which are selected based on the responsiveness of the molecule or group of bonded atoms to either dipole moment changes (IR) or polarizability (Raman) (183).

As mentioned, the applicability of IR spectroscopy relies on the nature of the chemical bonds of interest. The basic intention of using IR is to record the changes in the intensity of IR electromagnetic radiation at each frequency, after interaction with a material, which is obtained in a form of the spectrum showing the ratio of the intensity before and after the light Interaction plotted versus frequency. Since the first commercialisation of IR spectrometers in 1940, the technique has witnessed numerous advancements. The biggest progress was the integration of the Michelson interferometer as the dispersing element, and the Fourier transform (FT) to convert the signal to the conventional intensity-frequency output, which led to considerable enhancement in the sensitivity of the IR. There are three defining parameters in each FT-IR spectrum; i) peak position, which is used for qualitative analysis and the identification of the bonds, ii) the peak width, which gives information about the homogeneity of the chemical bonding or any bond defects and iii) the area under the peak (integration of the peak intensity), which is utilised for acquiring quantitative information (184).

FTIR emerged as a routine surface analysis tool after the technical improvements, due to some advantages over other surface analysis techniques i.e., no need for operation under high vacuum and non-destructive to the samples. The most widely employed FTIR spectroscopy techniques for surface analysis are transmission and techniques based on reflection (185).

In this work, we selected ATR mode for both the identification and quantification of the deposited polymer films.

Attenuated total reflectance (ATR) is a technique based on internal reflection phenomena and consists of a crystal with a high refractive index, which is brought into contact with the sample with a lower refractive index. When the IR beam reaches the interface between the crystal and sample, part of it will be refracted into the sample. However, according to the law of refraction, when the angle of the incident light increases to a critical point, the beam will not be refracted into the sample but will undergo several refractions inside the crystal, which is attributed to the internal refraction (see Figure 24). The critical angle is obtained by the equation below, known as Snell's law:

$$\theta_c = \sin^{-1} {}^{n_s}/_{n_c} \qquad (2.10)$$

While θ_c is the critical angle, and n_s and n_c are the refractive index for the sample and the crystal, respectively.

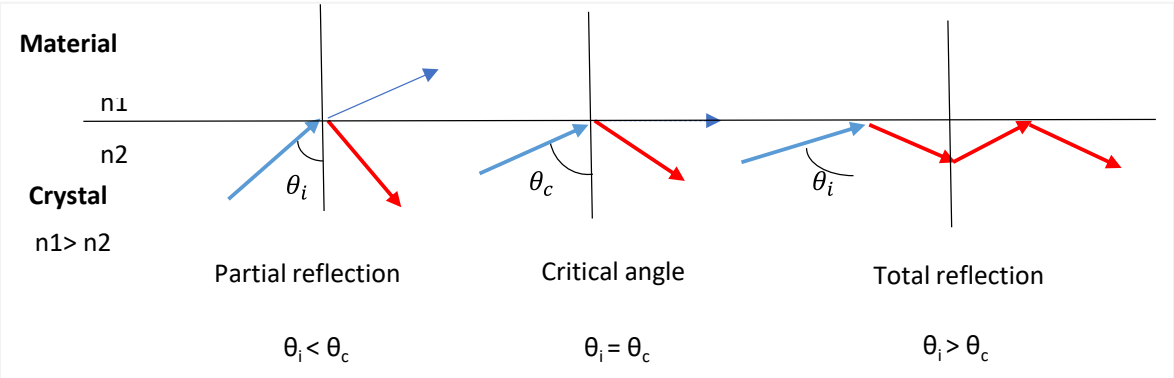

Figure 24. The reflection and refraction of the light beam travelling between two materials with different refractive indexes.

When the angle of incident is higher than the critical value, the two beams, incident and refractive, might interfere, leading to the increased amplitude of IR at the point of internal refraction. These points are placed a few microns above the crystal surface, called evanescent waves or hot spots. The beam in these particular points is partially absorbed by the sample and attenuated, and then it will be transmitted to the detector. The penetration depth of the beam inside the sample can be obtained by the following equation:

$$DP = {}^{1}/_{[2\pi W n_c\,(sin^2\,\theta - n_{sc}^2)^{0.5}]} \qquad (2.11)$$

where DP is Depth of penetration, W is Wavenumber, n_c equals the refractive index of crystal, n_s is the refractive index of the sample, θ is the incident angle and $n_{sc} = {}^{n_s}/_{n_c}$

As is evident from the formula, the penetration depth is reversely proportionate to the wavelength; therefore, for higher wavelengths, the DP will be lower, leading to low intensity or peak height. The other parameter, reversely proportionate to the DP, is the incident angle which can be adjusted through plugins to obtain the desired intensity by optimising the DP (186). The basic schematic of the ATR-FTIR instrument is represented in Figure 25:

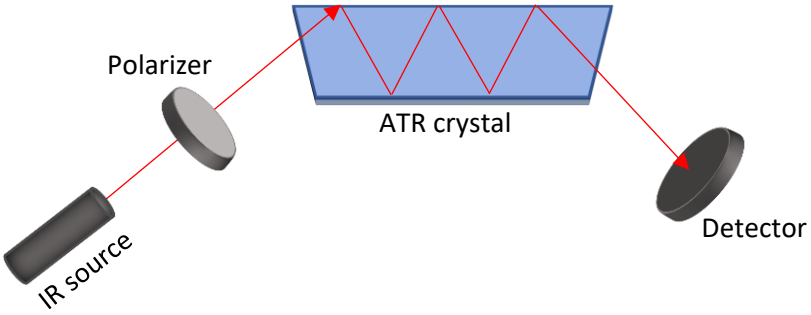

Figure 25. Basic schematic representing ATR-FTIR instrument components.

2.2.2 ToF-SIMS

2.2.2.1 Method

The ToF-SIMS characterisation was performed on the chemistry gradients developed by plasma polymerisation aiming to understand the local chemistry of the surface based on the detected molecular fragments, which give clues about the polymerisation mechanism. The analyses were performed using an IonToF ToFSIMS.V (Münster, Germany) equipped with a 25 keV pulsed Bi^{3+} cluster ion source delivering 0.48 pA target current for surface spectra and imaging experiments. Since the primary ion beam is rastered all over the sample (usually over 500 x 500 μm^2), the single spectra obtained on this surface may be utilised for retroactive image extraction of any secondary ion's lateral diswastribution. In this study, stage scan mode was

performed, allowing ion images from both the positively and negatively-charged secondary ions, with large size.

2.2.2.2 Theory of the technique

Time-of-Flight Secondary Ion Mass Spectrometry (TOF-SIMS) is a potent surface-sensitive chemical analysis tool capable of analysing almost any type of material with precise information on chemical composition and molecular structure in a local monolayer level with high sensitivity and high mass and lateral resolution.

As depicted in Figure 26, the static SIMS is based on sputtering a solid material surface with low numbers of the primary ion beam ($\leqq 10^{11}$ ions per cm^2), which causes successive collisions of atoms and as a result of receiving the kinetic energy of the primary beam, some atoms may return to the surface and finally be ejected as neutral particles, positive or negative secondary ions (187).

A time of flight (TOF) mass analyser coupled with static SIMS has resulted in several advantages over previously adapted quadrupole analysers for the acquisition of mass spectra owing to its high transmission, inherent panoramic registration as well as the possibility of providing an unlimited mass (m/z) range, which enables the detection of high molecular weight polymers (188).

After sputtering, the ejected ions from the surface are directed to the mass analyser, however, they need to enter the flight path of the mass analyser simultaneously or with minimal pauses, therefore, pulses are applied during the sputtering or surface bombardment. Accordingly, all those ions enter the flight path under an accelerating fixed voltage with almost the same kinetic energy. Considering the abovementioned assumptions, the mass of the entering ions is calculated by the following equation:

$$\frac{m}{z} = \frac{2\,U_{ac}\,T^2}{L^2} \qquad (2.12)$$

Where T is the time of flight, L is the flight path and U_{ac} is the accelerating fixed voltage (187).

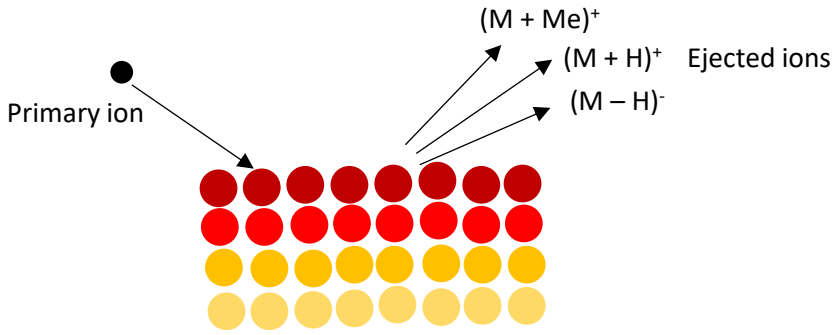

Figure 26. Static SIMS process of sputtering metal surface with primary ion and the emitted secondary ions as a result of collisions.

In addition to spectroscopy, the TOF-SIMS imaging mode is established to provide information on the lateral distribution of the material. Imaging is obtained by focused pulsed ion irradiation of the surface using an ion microscope followed by the position-sensitive detection of the secondary ions from every pixel.

In imaging systems with a TOF analyser, there is a compromise between lateral resolution, which requires long pulses, and mass resolution, which in contrast, requires short pulses. Therefore, while for spectroscopy the spatial resolution limits can go beyond 50 nm, for pulsed imaging, the limits at best are in the range of 50-80 nm, which can worsen by increasing the mass resolution. Images provide both the topography and material contrast and may also be used to reconstruct the spectra for the given region of the image (189). Since every image carries a tremendous amount of data and every pixel of the image carries the information of a full spectrum, sometimes it is desirable to select a small portion of every image and extract the corresponding spectrum. This is especially useful when there is a chemical inhomogeneity (e.g. two interfacing materials (190)) or a distinct surface structure that needs to be focused on and studied separately.

A basic schema showing the instrumentation of TOF-SIMS and the output corresponding to dynamic (depth profiling), static SIMS and imaging modes are provided in Figure 27.

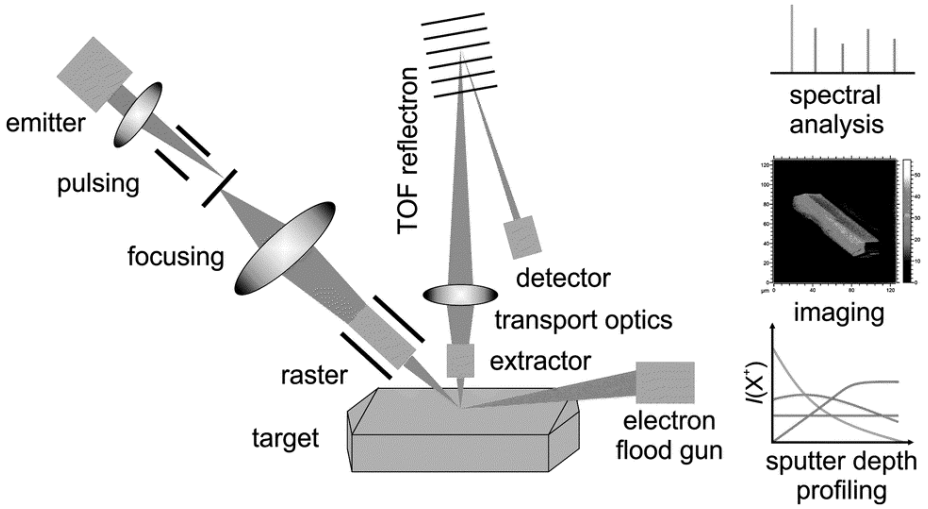

Figure 27. TOF-SIMS instrumentation and components (17).

2.2.2.2.1 Analysis

The molecular surface analysis with TOF-SIMS is usually achieved based on three forms of information: i) Total area mass spectrum, ii) Chemical mapping and iii) imaging. Additionally, depth profiling is preferred if the sub-layers of the material surface need to be investigated and 3D imaging can also be obtained to study the distribution of materials.

The collected fragments are analysed, and all the corresponding m/z values are plotted versus the intensity/frequency of each detected fragment in the form of the mass spectrum. The peak assignments allow the identification of the corresponding fragments and can provide evidence about the fragment or molecule of origin. Then, the spatial distribution of a fragment corresponding to any peak of desire in the spectrum can be mapped by producing its corresponding image in the scanned region; this is called chemical mapping. In other words, once a total ion image is obtained, the chemical mapping is used to locate the corresponding fragment (molecule, element, etc) in the big picture. Alternatively, a selected small region of interest on the total ion image is selected to depict its corresponding mass spectrum.

The abovementioned information acquisition pathways are explained with examples in Figure 28 related to the amine density gradient, which is developed by plasma polymerisation in the framework of the current thesis.

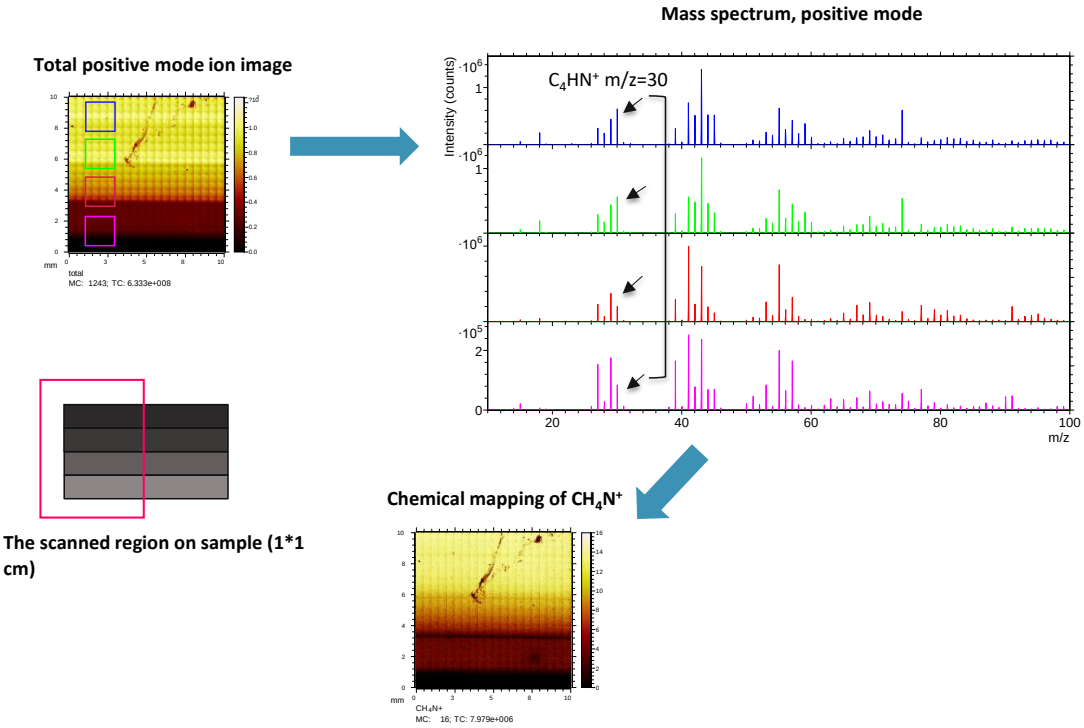

Figure 28. Molecular analysis steps of an amino-functional gradient with TOF-SIMS on a 1x1 cm region on the sample surface. 4 selected regions of interest over the total ion image were selected for positive scan mode. After investigating the total ion spectrum, the chemical mapping of the primary amino peaks was conducted and converted to the corresponding micrograph.

2.2.3 Atomic Force Microscopy (AFM)

2.2.3.1 Method

AFM analysis was implemented via an Innova microscope (Bruker, Santa Barbara) using tapping mode and image acquisition in the air in AC mode at scan rates ranging between 0.5-1 Hz. A semi-contact silicon cantilever (RTESP; Bruker) with a spring constant of 40 Nm^{-1} was used. The topography mapping of the surface coatings was carried out by fixing the initial resonance amplitude of the tip. The SPIP image processing software (ImageMet) was used, and the manual tilt correction was applied to the images. In addition to SPIP, Nanoscope analysis (provided by Bruker) and Gwyddion open-source software were used where necessary for image visualisation and further topography analysis (particle analysis, drawing surface profiles, etc).

2.2.3.2 Theory of AFM

Atomic force microscopy is used for surface profiling with a resolution down to the atomic level. Surface profiling by AFM works based on scanning the sample surface with a tip

connected to a cantilever spring and a deflection sensor. The basic illustration showing the AFM setup and working principle is presented in Figure 29.

The 3D surface topography image is obtained by measuring the force between the tip and the surface, which is a function of tip-surface proximity and cantilever deflection. Below, there is a basic schema of an AFM instrument (191).

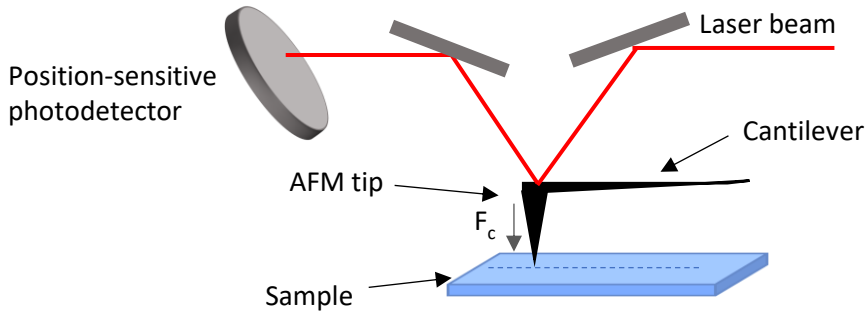

Figure 29. A basic representation of an AFM instrument.

The operation principle of static AFM can be summarised as the translation of force to deflection as observed in the following equation (192):

$$q = \frac{F_c}{k} \tag{2.13}$$

Where q is deflection, F_c is the force between tip and sample and k is the cantilever constant.

Dynamic AFM is developed to avoid the possibility of damaging soft sample surfaces such as polymers and biomolecules by employing high force values in contact mode. In dynamic mode, besides cantilever deflection, and oscillation amplitude, the frequency and phase shift are also recorded. Tapping mode is a dynamic mode in which the oscillation of tip-cantilever occurs at the resonance frequency of the cantilever spring. Upon these oscillations, while scanning the sample, the proximity between the tip and surface is adjusted by a modulator in such a way as to keep the amplitude at a constant value (193).

- ***Roughness parameters***

Surface topography is a critical physical property of a material surface, which can directly or indirectly affect other physical and biologic phenomena. The impact of surface roughness on the material surface wettability is a well-known effect, which has motivated researchers to

incorporate suitable topography into the material surface, aiming to impart new characteristics such as developing superhydrophobic self-cleaning surfaces (194) or anti-fouling surfaces for the marine industry (195).

There are several roughness parameters that can be obtained by various AFM software, each useful for characterising specific surface textures. The two popular roughness parameters that are reported most frequently are Ra, the arithmetic roughness average of the surface, and Rq, the root mean square of the surface roughness. These parameters are suitable for describing gaussian asperity heights but not asperities with complex sub-asperities. Ra and Rq values should be considered with caution since two very different surface structures can show the same Ra and Rq values, which can be misleading. Therefore, this parameter should be used to compare similar surface structures.

In this work, we have used R_q to compare the surface roughness of the coatings deposited with plasma polymers and nanoparticle-coated surfaces.

R_a and R_q are calculated by the following equations:

$$R_a = \frac{1}{L}\int_0^L |z - m|\ dx \tag{2.14}$$

$$R_q{}^2 = \frac{1}{L}\int_0^L (z^2)\, dx \tag{2.15}$$

Z is the height measured from the reference line and L is the profile length (196).

M is the mean line, which is defined as the line dividing the whole profile into two identical sections, meaning that the area above the line is equal to the area below the line, as shown in Figure 30.

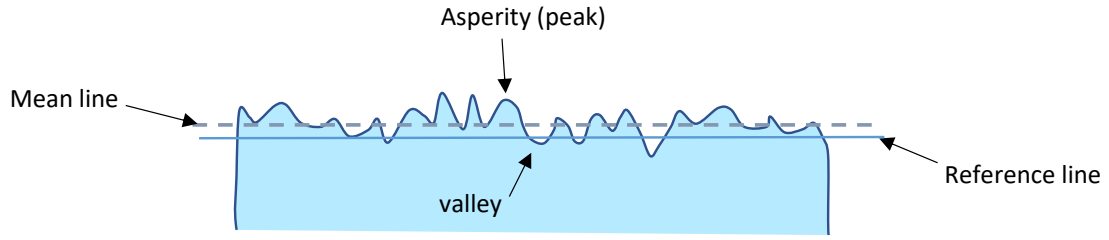

Figure 30. Height profile z(x) of an imaginary surface and relevant components are illustrated.

Using the instrumentation described in the method section, four images were selected to be obtained from the AFM tapping mode scans: the forward and back height profiles, phase and amplitude images. The forward height profiles were used to obtain the desired roughness parameters (R_q and roughness factor) using the aforementioned image processors.

2.2.4 Water contact angle (WCA)

2.2.4.1 Method

For surface wettability studies, the drop shape analyser (DSA30, KRUSS) was used to measure the static water contact angles. A small volume of a distilled water droplet (e.g., 2 µl) was dispensed on the sample surface and the Young-Laplace technique was used to determine the contact angle.

2.2.4.2 Theory of WCA

Wettability measurement is a well-established surface analysis tool, which is generally based on determining the contact angle that a liquid droplet makes with the horizontal axis of the surface. Mapping the surface water contact angle (WCA) can provide useful clues about both the chemistry and roughness of the material surface. The first mention of measuring the static WCA was reported by Young in 1805. The equation is based on the assumption that upon placing a droplet on a material surface, the equilibrium contact angle is calculated by considering that the horizontal component of the surface tension of three interfacing materials (liquid/gas, gas/solid, solid/liquid) is sum to zero at the contact line (197) (see Figure 31).

$$\Upsilon_{LG}\cos\theta = (\Upsilon_{GS} - \Upsilon_{LS}) \qquad (2.16)$$

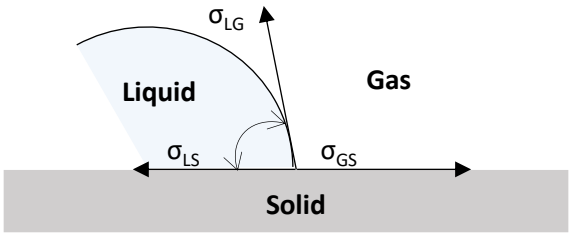

Figure 31. The three interfacial forces, when a water droplet is placed on a solid surface.

The static CA or sessile drop method can be conducted by employing varieties of liquids (mainly water) with known surface tensions, depending on the information they are intending

to obtain. Regarding the WCA studies, a contact angle below 90° is an indicator of a hydrophilic surface probably bearing ionic functional groups, with the most extreme case being when full droplet spreading is observed (superhydrophilic surface < 10°). And contact angles of more than 90° indicate hydrophobic or water repellent surfaces including methyl functional groups or fluorinated hydrocarbons with the extreme theoretical case > 150° known as superhydrophobicity.

Besides surface chemistry, the surface texture is the other factor that determines the surface wetting characteristics. The classic surface wetting regimes influenced by the surface texture are presented in Figure 32. According to Wenzel, the surface roughness factor r, which is defined by the measured actual surface area divided by the projected area should be included in Young's equation to modify the CA equation for roughened material surfaces (198):

$$\Upsilon_{LG}\cos\theta = r(\Upsilon_{GS} - \Upsilon_{LS}) \quad (2.17)$$

In Wenzel's regime, it is considered that the droplet penetrates into the material surface and follows the surface texture. Cassie-Baxter extended the CA equation for roughened surfaces to the porous or chemically heterogeneous surfaces:

$$\cos\theta' = \sigma_1\cos\theta_1 + \sigma_2\cos\theta_2 \quad (2.18)$$

where θ_1, θ_2 are WCAs of each surface region, and σ_1 and σ_2 are the corresponding surfaces. In the case of a porous material, σ_1 is the surface for the solid material and σ_2 is the air space or open areas. Where the droplet resides on a porous material with air-filled cavities, the surface energy of solid/gas will be zero and $\cos\theta$ equal to one (199):

$$\cos\theta' = \sigma_1\cos\theta_1 + \sigma_2 \quad (2.19)$$

By replacing surface areas with a surface fraction of the solid material, *f*, in equation (2.18), the wettability equations for heterogeneous surfaces are (200):

$\cos\theta' = 1 - f + f\cos\theta_1$, for a hydrophilic material with θ_2= 0° (2.20)

$\cos\theta' = -1 + f(\cos\theta_1 + 1)$, for a hydrophobic material with θ_2= 180° (2.21)

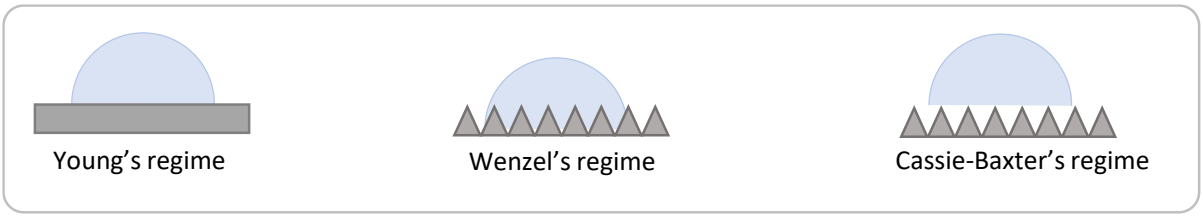

Figure 32. Different wetting regimes for unroughened and roughened surfaces: a) Young's regime, b) Wenzel's regime and c) Cassie-Baxter's regime.

2.2.4.2.1 Measuring dynamic contact angle

Regardless of the approach, a dynamic contact angle is utilised to measure the dynamic response of the surface features as a result of interacting with the water droplet. In this mode, the droplet is stimulated to slide over an unwetted surface and then it is retracted from the wetted surface, recording the angles (201). The common techniques used to measure the dynamic water contact angles are mainly based on tilting plate, changing droplet volume, and immersion/emersion of the sample inside liquid as illustrated in Figure 33.

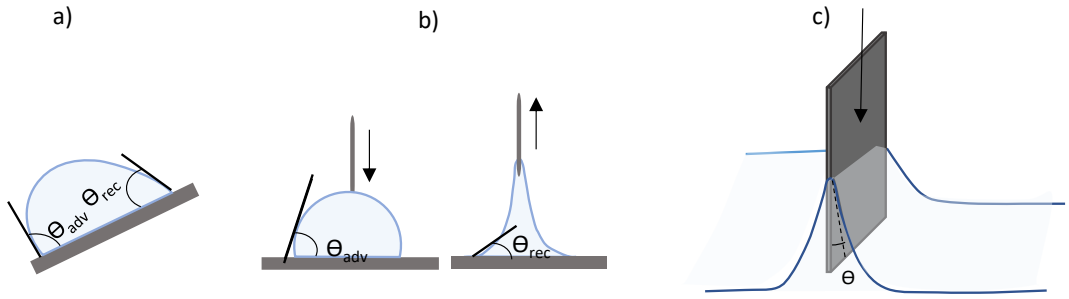

Figure 33. The dynamic water contact angle techniques with a) tilting-plate goniometry b) captive-drop goniometry and c) Wilhelmy-balance tensiometry.

Measuring the dynamic angle allows defining the hysteresis of a treated surface, which is described as the deviation between the advancing and receding angle. An ideal smooth and homogenous surface is expected to show identical advancing and receding angles and therefore present zero hystereses. However, real surfaces are not smooth (especially patterned surfaces) and show hysteresis, which can be considerable depending on the magnitude of the surface roughness. The hysteresis analysis is usually advised for hydrophobic, superhydrophobic and aged material surfaces however, static contact angle measurements on 3D hydrophilic surfaces with polar groups may also not be adequate or accurate due to the strong adsorption of water droplets on the surface (202).

Since plasma-deposited polymers exhibit a complex 3D structure, we decided to report the dynamic angles on both the samples prepared by plasma deposition and the patterned surfaces with particles. To this end, goniometry techniques were preferred.

The tilting plate goniometry technique was performed in manual mode after initially levelling the tilting stage and calibrating the light intensity and resolution of the camera by placing a droplet on a sample surface and slowly rotating the stage that held the sample. It was concluded that, in order to initiate the rolling of a water droplet on hydrophilic amino-functional surfaces by tilting, larger droplet volumes (>16 μl) should be selected. Even then, the droplets were frequently stuck and did not roll off due to the nature of the material (plasma coating) and the water affinity with the surface. Meanwhile, since one single volume is selected per experiment, the effect of the volume variation is not considered in this method. This led us to look for an alternative method for measuring dynamic angles.

The dynamic angle measurements with volume variation are based on measuring advancing and receding contact angles as a function of change in the baseline length imposed by volume variation. Initially, a droplet of a selected volume is dispensed and brought into contact with the surface. Then, a low dispensing rate is adjusted to increase the volume of the droplet for a few minutes while the advancing angles were recorded. Finally, the dispensing process was stopped, and the droplet was removed gradually at the same rate while receding contact angles were recorded. Figure 34 illustrates the process of obtaining advancing and receding angles based on a gradual variation of the droplet volume. The droplet shape analysis is done by applying a proper image fitting approach, based on the fit that best follows the shape of the droplet and the baseline, and later, contact angles are plotted versus the baseline.

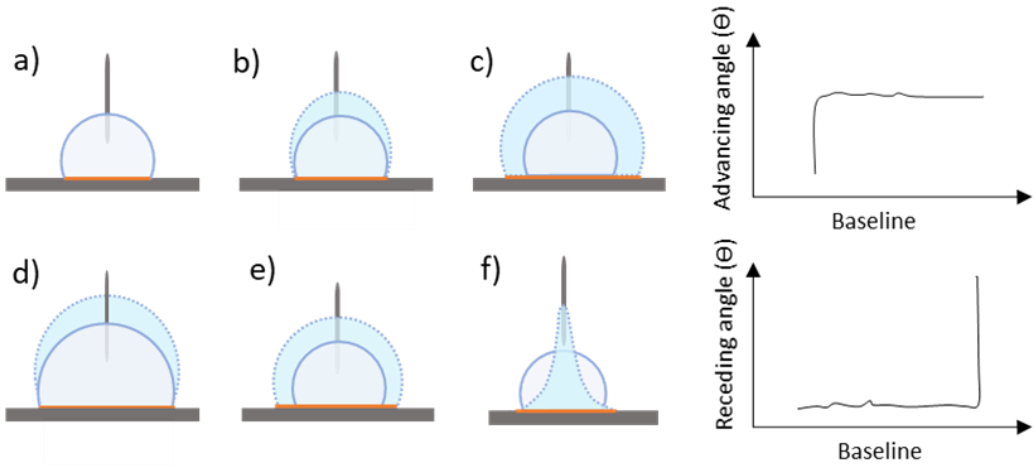

Figure 34. The steps involved in measuring dynamic angles by gradually increasing the droplet volume by dispensing the drop at a slow fixed-rate (a-c) and gradually decreasing the water droplet volume by removing the droplet (d-f).

The advancing and receding angles were selected and averaged on the flattest region of the obtained curve. The advancing angles were obtained after reaching a plateau where contact angles remained the same by increasing the baseline and receding angles were averaged for the region before a point at which contact angles were continuously increased while the baseline remained constant. Since dynamic water contact angle measurements require a larger surface region (due to the increase in droplet volume) to implement, we used representative homogenous coatings in a larger sample size rather than narrow gradient coatings. Gradient coatings were investigated for wettability features by static measurement only and by using small water droplets (0.3-1 µl).

2.2.4.2.2 Relation between the surface roughness factor and surface wettability

Besides these roughness parameters, there is another parameter, the roughness factor (r), with its main application in surface wettability studies. The roughness factor is dimensionless and is described as the real surface of the topography divided by the projected surface (203). This parameter can be obtained from any AFM interface for random topographies or can be calculated for well-defined surface structures with a known number of features, dimensions and the projected area. The goal was to develop a model to predict the wettability behaviour of the fabricated gradients. Depending on the estimated wettability regime (Cassie-Baxter, Wenzel), the total surface roughness factor or the roughness factor of the wetted structures was considered.

To describe the procedure that we used to calculate the roughness factor, each type of gradient should be considered separately. Figure 35 Illustrates a two-particle system with defined particle diameter and the interparticle distance, residing on a homogenously modified surface which is fully covered with a water droplet.

- ***The full wetting regime***

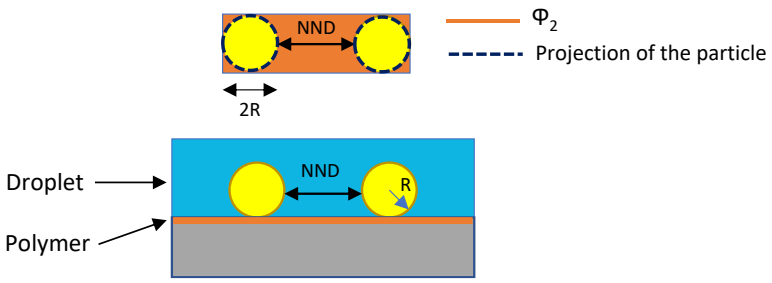

Figure 35. The top and side views of a two-particle system with a certain interparticle system are presented. The particles are assumed to be fully wetted by the water droplet.

In this situation, if a hydrophilic surface is totally covered by a water droplet, and the surface is heterogeneous and rough, the following equation derived by Cassie et al. might be used to explain the wetting regime:

$$\cos\theta^* = f_1 \cos\theta_1 + f_2 \cos\theta_2 = r\varphi_1 \cos\theta_1 + \varphi_2 \cos\theta_2 \qquad 2.22$$

where θ*= Apparent contact angle, r= roughness of the wetted area, θ_1 = WCA of intrinsic citrate-capped gold nanoparticle, θ_2 = WCA of CHN plasma polymer, and Φ_1, Φ_2 surface fractions of gold nanoparticle and plasma polymer, respectively.

As described in the equation, we need to consider the surface fraction for two materials, citrate-capped gold nanoparticles and the coating on the substrate, as well as considering the roughness factor of the surface. For ease of calculation, we can consider a two-particle system confined in an area as shown in Figure (20). In the image, the top and side views of the particles are provided, immobilised on plasma polymer with a certain interparticle gap.

Based on this model, the roughness factor of the wetted particles can be written as:

$$\boldsymbol{r\varphi_1} = \frac{2Area\ of\ the\ sphere}{2Projected\ area\ of\ the\ sphere\ (circle)} = 4 \qquad 2.23$$

$$\boldsymbol{\varphi_1} = {}^{2\pi R^2}/_{2R(4R+NND)} = \frac{\pi R}{4R+NND} \qquad 2.24$$

Here, NND is the distance between the nearest neighbouring particles measured from the exterior border of one particle to the border of the next particle.

By replacing the 2.23 and 2.24 equations in the equation 2.22 and (1-Φ_1) for Φ_2, we obtain the following equation for the full wetting regime, which we will call Wenzel here:

$$\boldsymbol{\cos\theta^*} = 4\cos\theta_1 + \left(1 - \left(\frac{\pi R}{4R+NND}\right)\right)\cos\theta_2 \qquad 2.25$$

$$\boldsymbol{\theta^* = \cos^{-1}}(4\cos\theta_1 + \left(1 - \left(\frac{\pi R}{4R+NND}\right)\right)\cos\theta_2) \qquad 2.26$$

- ***The partial wetting regime***

The second possibility is that the air is trapped under the water droplet as a barrier limiting the contact of the droplet to some fraction of the gold nanoparticle surface as shown in Figure 36. Therefore, considering equation 2.1, the θ_2 is WCA of air (not polymer) and will be 180°. We can thus rearrange the equation as follows:

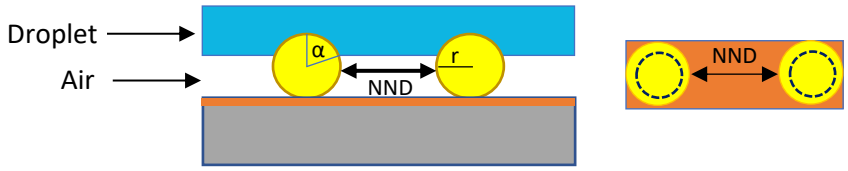

Figure 36. The top and side views of a two-particle system in partial wetting mode.

$$\cos\theta^* = f_1\cos\theta_1 + f_2\cos\theta_2 = r\varphi_1\cos\theta_1 + \varphi_1 - 1 \qquad 2.27$$

where f_1 is the fraction of wetted solid, f_2 is the fraction of air in contact with the droplet.

$$f_1 = \frac{2A_{spherical\ cap}}{2Projected\ area\ of\ the\ sphere\ (circle)} = \frac{2\pi R^2\ (1-\cos\alpha)}{\pi R^2(\sin\alpha)^2} = \frac{2(1-\cos\alpha)}{(\sin\alpha)^2} \quad 2.28$$

$$\varphi_1 = \frac{2\pi R^2(\sin\alpha)^2}{(4R+NND)2R} \quad 2.29$$

$$\theta^* = \cos^{-1}\left(\left(\frac{2\pi R^2\,(1-\cos\alpha)}{\pi R^2(\sin\alpha)^2}\right)\cos\theta_1 - 1 + \frac{2\pi R^2(\sin\alpha)^2}{(4R+NND)2R}\right) \quad 2.30$$

- ***The full wetting of the coated particles***

If the particles are covered with a top layer, depending on the conformality of the coating, the thickness of the coating and the separation between particles, different scenarios can be expected. As an example, for particles covered with a conformal coating as thick as the diameter of the particle, depending on the separation, the following topographies shown in Figure 37 are expected.

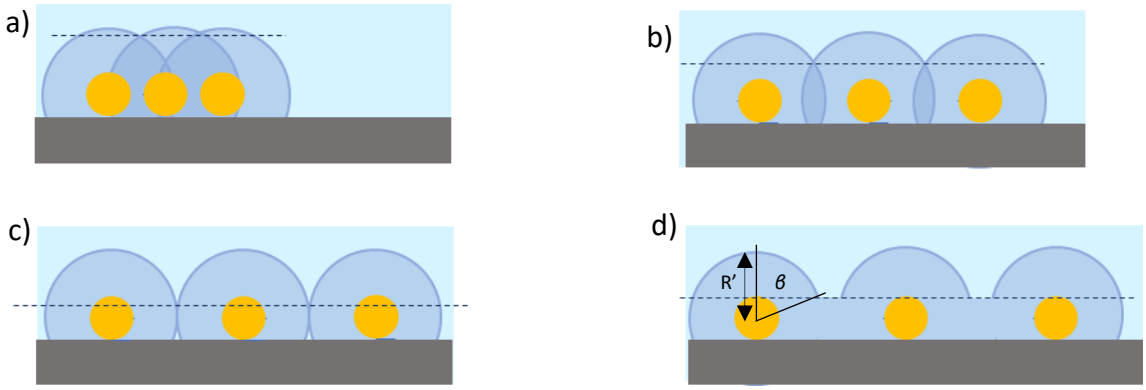

Figure 37. Surface topography of a three-particle system symbolising 11 nm size particles coated with a 10 nm top conformal coating with a) 3 nm, b) 15 nm, c) 20 nm and d) 24 nm separation between particles. The blue dashed line shows the cavity, hence, the level at which the water droplet might penetrate.

It is expected from the images that a water droplet would come into contact with an initially smooth topography considering the slight curvatures formed above the dashed lines (a). However, with a gradual increase in the separation, an evolution in asperities and an increase

in the roughness is expected (b), reaching a maximum value in 20 nm, where tangent hemisphere structures are observed (c). After this point, the spherical cap structures indicate a declined curvature and decrease in surface roughness (d). The real surface after a 20 nm interparticle separation is calculated by multiplying the fixed surface area (spherical cap) by N (number of particles). The wettability model considered for this type of coating follows the classic Wenzel regime (see equation 2.16). The experimental and calculated theoretical WCA curves measured for 2D gradients are presented and discussed in Chapter 5 (5.3).

To develop the model, as with uncoated particles, we can assume a two-particle system confined in an area fully wetted with the droplet. Based on this assumption, the roughness factor can be expressed as:

$$r = \frac{[2(curved\ area\ of\ spherical\ cap)+(whole\ area-2\ (projected\ area\ of\ spherical\ cap))]}{Whole\ area} \quad 2.31$$

$$r = \left(\frac{2\pi R'(1-\cos\beta)+4R'+s-\pi R'\,(\sin^2\beta)}{4R'+s}\right) \quad 2.32$$

While β is the angle between a vertical line from the centre of the sphere and a line which can be drawn from the centre to the lowest contact region with the droplet, R' is the radius of the polymeric sphere coated around the particles and s is the border-to-border distance between two polymeric spheres.

$$If\ s \geq 0,\ \mathcal{P} = 73.12° = 1.28\ radian \rightarrow NND \geq 20\ nm \quad 2.33$$

$$If\ s < 0, \qquad r = 1 \rightarrow 10\ nm < NND < 20\ nm \quad 2.34$$

By replacing equation 2.32 in equation (2.17) for the homogenous rough surface, the wetting angle can be obtained from the following equation for $NND \geq 20\ nm$:

$$\theta^* = \cos^{-1}\left(\left(\frac{2\pi R'(1-\cos\beta)+4R'+s-\pi R'\,(\sin^2\beta)}{4R'+s}\right)\cos\theta\right) \quad 2.35$$

2.2.5 X-ray Photoelectron Spectroscopy (XPS)

2.2.5.1 Method

Elemental characterisation and quantification were implemented by X-ray photoelectron spectroscopy (XPS) using a Kratos Axis-Ultra DLD instrument consisting of an Al Kα source (1486.6 eV), pass energy of 20 eV and an energy resolution of 0.5 eV. A flooding gun accelerated low energy electrons were utilised to correct the charging effect on the sample

surface. CasaXPS-2315 software was used for processing XPS spectra and data treatment. The C1s main component at 285.0 eV was used as the internal standard for calibration of the spectrum. The analysis area was 700 µm x 300 µm and the interval between each scanned area was 500 µm.

2.2.5.2 Theory

2.2.5.2.1 Instrumentation

X-ray photoelectron spectroscopy (XPS) is a chemical analysis tool that has found widespread use in elemental studies of a wide range of materials. The technology has primarily used an X-Ray beam source and an electron energy analyzer or detector in a high vacuum. The output of the analysing technique can be used to interpret the elemental information, the chemical state of each element, the three-dimensional distribution of the material, the thickness, and uniformity of the deposited films (204).

The technique works based on a physical phenomenon, the photoelectric effect, which is defined as a dipole interaction in which the energy of the incident photon is completely transferred to the bound electron and expended to its ejection. The kinetic energy of the ejecting electron is equivalent to the energy difference between the energy of the colliding photon and the binding energy of the electron:

$$E_b = h\nu - E_k \tag{2.36}$$

In this equation, E_b represents the binding energy of the electron, E_k denotes the kinetic energy of the electron and hv is the energy of photon (with h and *v* being Planck's constant and the X-ray frequency respectively).

The basic schema of the X-Ray analysis process from the incident photon to the recorded elemental spectrum is illustrated in Figure 38.

The electrons removed from the very depth of the sample are not detected due to the overall low kinetic energies of the XPS electrophotons (0-1500 eV), therefore, the XPS is mainly a surface-sensitive technique. After ejection, the electrons arriving at the detector are simultaneously counted and the number is converted to the intensity and binding energy of the electrons, are calculated from kinetic energies, resulting in a spectrum which is used to identify the nature of corresponding atoms (205, 206). Besides identification, XPS spectra provide an excellent means for quantifying each element after applying the necessary corrections to the position and shape of the peaks.

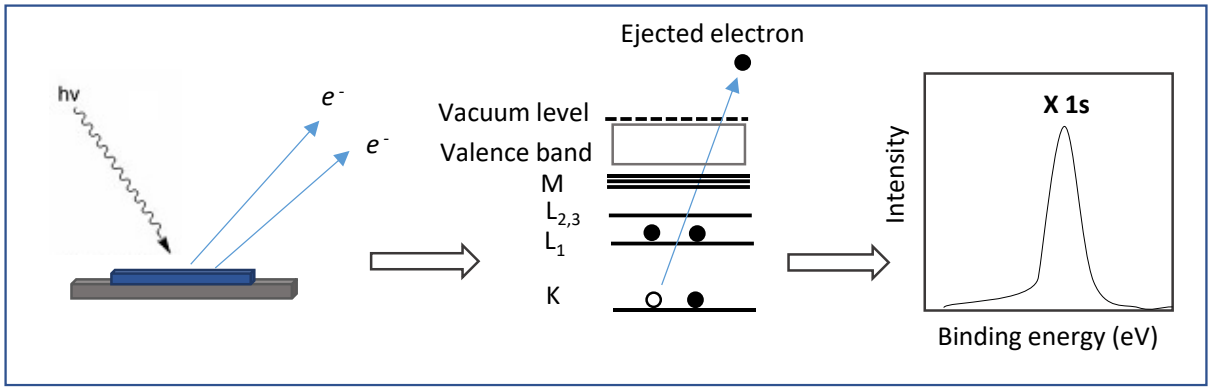

Figure 38. Basic schematic description of XPS and the resulting spectrum

Despite XPS being a routine surface chemistry analysis tool, when characterising plasma polymers, there are many uncertainties in interpretations due to the random, highly crosslinked and complex structure of the plasma polymers. This implies that the curve shape and binding energy of the peak components of the plasma polymers (e.g., C1s components) may not follow the classic polymers of similar structures causing challenges in the surface chemistry analyses.

These different behaviours of the plasma polymers compared to the similar conventional polymers with well-defined chemistry mostly stem from the fragmentation of the initial monomers followed by recombination and hence deviation from the initial precursor chemistry. These in turn depend on many factors, mainly power input but also other factors such as deposition time and monomer feed rate. Some typical difficulties which are underlined regarding the identification of the carbon components are as follows: i) Peak fitting of C1s may need to be explained with more than one approach as, peak components with similar binding energies are not clearly separated, usually due to the increased half bandwidth of the curve (FWHM) possibly arising from exotic radical fragments which are not encountered in classic polymers; ii) The overlapping of the peak components due to the broadening of the FWHM as a result of variable chain length and the crosslinking degree in plasma polymers; iii) Chemical damages which stem from the plasma-UV exposure of the molecules forming unexpected fragments; iv) Radical-induced post-oxidation, which is frequently encountered by plasma polymers due to active surface radicals which can react readily with air/moisture during storage (207). Similar difficulties due to the band broadening of C1s and overlapping of C-O and C-N are faced in the current thesis during the interpretation of the amino-functional plasma polymers which are discussed in detail in Chapter 3 (3.4.2.1) and Chapter 5 (5.2.1).

2.2.5.2.2 Analysis procedure

Data treatment with XPS involves visualising data via a spectrum which is initially useful for the identification of key surface elements as the energy is characteristic of a specific element and can later be used for extracting quantitative data by obtaining high-resolution peaks for each element and integrating the area under peaks.

After collecting and analysing electrons by the detector, the spectrum is plotted based on counts per second (cps) versus either the kinetic energy or binding energy of electrons. The binding elements (via ionic or covalent bonds) can represent a shift in binding energy when compared to free elements, called a chemical shift. When the elemental charge state moves from negative charge values to a neutral (zero state) to a positive state, the binding energy increases. For instance, if we consider sulphur in its different oxidation states (-2, 0, +4, +6), the binding energy varies gradually from -1.4 to 5.5 eV.

There is a form of shifting which occurs due to non-conducting materials (such as organic coatings) and can vary by the thickness of the material. This charge effect needs to be corrected during data processing so that all the peaks appearing in a spectrum are manually shifted to a fixed value. This value is the binding energy of the adventitious C1s spectral component (C-C, C-H), which is 284.8 eV. Some peaks, especially C1s, are not single peaks as can be understood from the asymmetrical peak hiding information about the binding environment. Hence, they must be deconvoluted to access the information about the neighbouring functional groups. The high-resolution curve fitting is done by the experts usually using the popular XPS analysis software, CasaXPS. The peak fitting allows the separation of all the peak components corresponding to e.g., aliphatic C-H, aromatic, ketones, acids, esters, alcohols and the area under the peak and peak height defines the quantity and contribution of each functional group.

The procedure is explained using the examples from the current thesis demonstrating the survey scan and high-resolution peaks acquisition (see Figure 39).

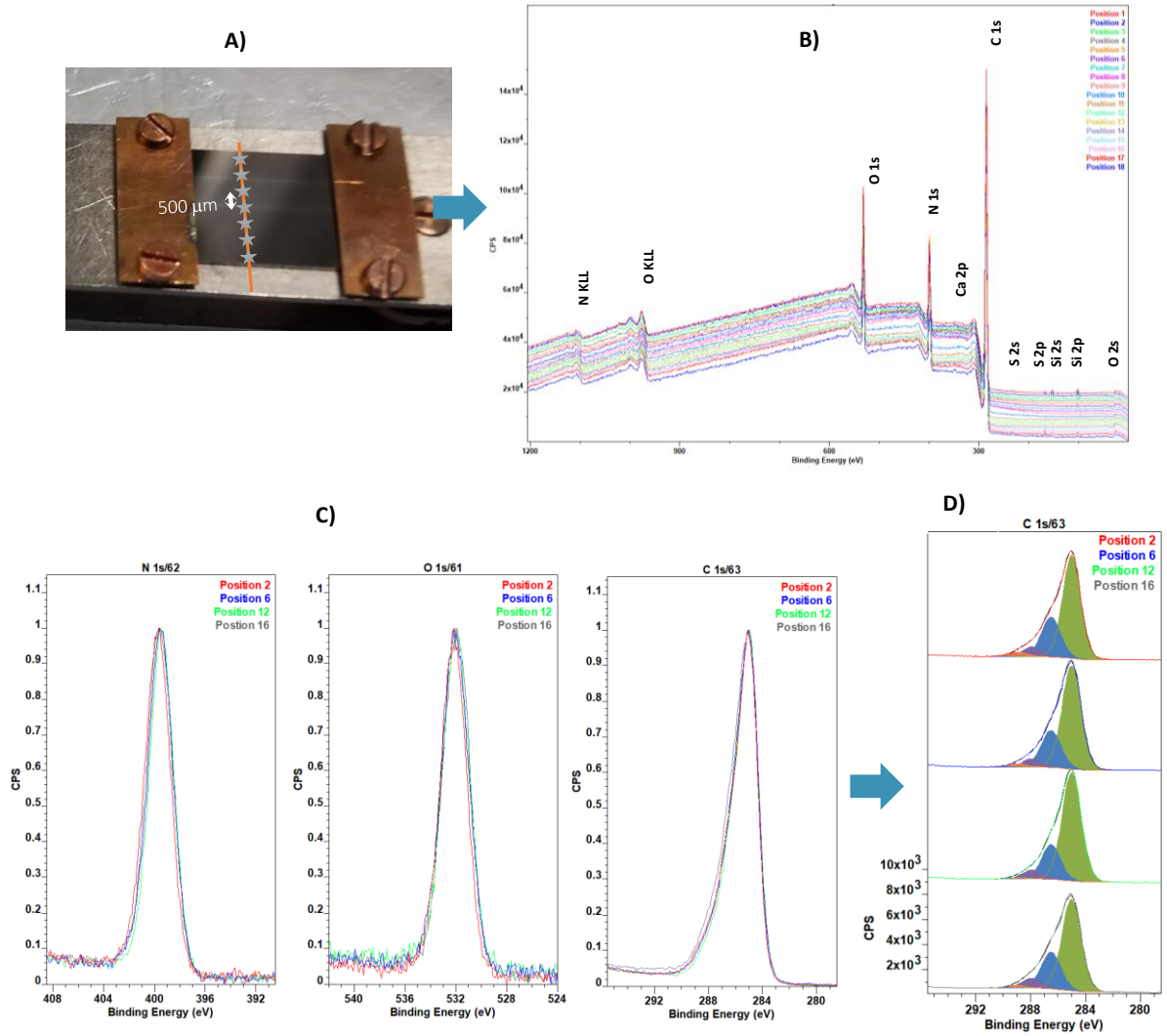

Sample Identifier	C-(C,H) %	C-(O,N) %	O-C-O/(N)-C=O %	O-C=O %
Position 2	65	27	6	3
Position 6	67	25	5	2
Position 12	71	22	6	1
Position 16	64	27	7	2

Figure 39. XPS elemental analysis of the amine functional group gradient surface coating deposited by plasma polymerisation: A) The original sample was placed in a sample holder prior to analysis. The 18 positions were scanned at 500 µm intervals along the chemistry gradient direction. B) The whole XPS spectrum, along with the attributed elemental peaks obtained on each of the 18 positions. C) The three high-resolution peaks corresponding to the key investigated elements, nitrogen 1s, oxygen 1s and carbon 1s, are defined in positions 2, 6, 12 and 16, each representing a specific plasma deposition condition and D) curve fitting of C1s on the 4 positions (2, 6, 12 and 16) and the resulted contributing functional group peaks. The table shows corresponding functional groups defined by colours.

2.2.6 Scanning Electron Microscopy (SEM)

2.2.6.1 Method

The surface of the gold nanoparticle-coated sample was imaged using a Helios NanoLab™ 650 (FEI, Eindhoven. Netherland) scanning electron microscope equipped with a dual-beam focused ion beam (FIB) and scanning electron microscopy. The electrical parameters were adjusted to an acceleration voltage of 2 kV and a current of 25 pA, and the working distance was adjusted to 4 mm. Due to the metallic and conductive nature of the top coating, images were obtained without considerable charging. However, the polymer-coated sample surfaces demonstrated considerable charging despite lowering the voltage and hence were analysed using an ORION NanoFab - Helium Ion Microscope (Zeiss Microscopy). The image processing was accomplished using several plugins provided by the ImageJ processing program. The particle distribution analysis was accomplished by setting the scale of the processed image to the original scale indicated on the image and then after converting the image to binary mode, the threshold was set to define the particles from the background, and the particle size range and circularity was adjusted manually, then the information regarding the particle number, size, area, and perimeter was obtained by automatic analysis.

2.2.6.2 *Theory of SEM*

Directing the electron beam to the material surface may lead to different processes such as the reflection of electrons or transference of the kinetic energy to the atomic electrons of the material surface, leading to the ejection of secondary electrons from the surface. Depending on the nature of the interaction i.e., elastic or inelastic, the signal received from the surface may differ. The possible signals generated upon the interaction of an electron beam with the material are illustrated in Figure 40.

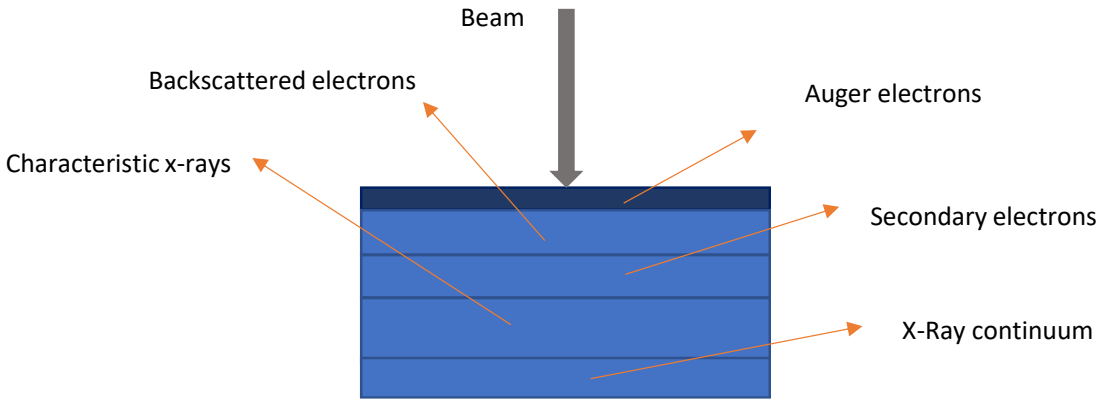

Figure 40. Several reactions that may occur as a result of electron beam contact with various layers of a solid material

Imaging by scanning electron microscopy (SEM) functions based on utilising an electron probe by which the primary electron beam generated usually from a heated source is transmitted to the material surface in a focused manner. As usual ion source such as tungsten produces a big spot with lower resolution, and lenses and apertures are used to improve the focus. When the probe moves along the surface, it scans two perpendicular axes simultaneously and the ejected secondary electrons from the scanned rectangular area are collected and subsequently converted to the corresponding image (208, 209).

2.2.6.2.1 Analysis procedure

The scanning was accomplished by initially placing the sample on the dedicated sample holder inside the instrument and taking a photo of the sample surface and its position, closing the chamber door and vacuuming the chamber. For metallic nanoparticle-coated samples, the adjusted parameter combination to accelerate electrons was set at 2 kV and 25 pA. Using the interface, the stage was moved manually to adjust the sample under the beam by clicking on the desired edge on the photo; after seeing the image of the edge, the magnification was increased gradually while attempting to focus on the image. Besides focusing, other adjustments such as astigmatism were checked to improve the image resolution while continuously increasing the magnification. The electron beam was also centred using the controls and image contrast was improved. When the resolution seemed to be acceptable, the vertical distance between the tip and the sample surface was decreased gradually to the structured standard distance (4mm) while attempting to improve the focus and astigmatism each time.

Since the particles to be scanned were as small as 10-20 nm in diameter, in order to visualise the particles, it was necessary to further increase the resolution. Therefore, the immersion mode was switched (with the through lens detector (TLD)). The focus and astigmatism were adjusted after increasing the magnification ratio, typically to 200,000 for monodispersed nanoparticle samples corresponding to a 1.04 μm horizontal field width (HFW) until particles with a maximum possible resolution were observed. This process (improving the focus and astigmatism) was repeated each time while moving along the gradient direction on the sample with 0.5 mm intervals and saving the images. The magnification adjusted for larger surface structures (nanoclusters and nanodoms) was 100,000 corresponding to a field of 2.07 μm.

2.2.7 Surface-Enhanced Raman Spectroscopy (SERS)

2.2.7.1 Method

SERS measurements were performed with a microscope-attached micro-Raman system (Renishaw InVia, UK), a Peltier cooled CCD, and a 633 nm excitation LASER. The system was pre-attached to a Leica microscope, and the Laser was connected through a 50 X, 0.5 NA objective lens. Internal Silicon calibration was conducted prior to each experiment, with a peak centred at 520 cm^{-1}. WIRE 5.0 software, provided by the manufacturer, was used for data processing. To remove unwanted/fluorescence background from the signals, the default values were used for baseline subtraction. The measurements were conducted in focusing mode at 10 separate sites on the same sample in order to obtain standard deviations. All of the spectral signals were normalized with regard to exposure time and incident powers using OriginPro software, in order to track the signal intensity dependence on the analyte concentration. The spectral ranges were selected based on the most significant peak, which indicated the presence of analyte molecules.

To measure SERS signal, the aim was to coat the substrates with a SERS-responsive chemical, 1-naphthalenethiol (1-NT). For the surface 1-NT functionalisation, the substrates were incubated overnight in an ethanolic solution of systematically increasing concentrations (μM to pM range) of 1-NT, then rinsed with ethanol and dried prior to SERS measurements.

2.2.7.2 Theory of SERs

Surface-enhanced Raman spectroscopy (SERS) has served as a powerful tool for molecular diagnostics and sensor integration. Although the spectra obtained by Raman spectroscopy provide a fingerprint for the identification of a wide range of materials, the Raman signal is intrinsically weak.

When a material is irradiated by photons, its interaction with the material leads to either elastic or inelastic scattering. Although the elastic scattering leads to scattered photons with the same energy as the incident ones (i.e., Rayleigh), the scattered photons from inelastic interaction have lower energy than the incident ones (Raman Stokes and anti-Stokes). The scattered beam contains useful information about vibrational modes of materials. Figure 41 presents different possible scattering modes and the vibrational energy states involved. The Raman output can be expressed in the form of Raman power shown in the following equation:

$$P = KN\,I\,\sigma_K \tag{2.36}$$

In this equation, where P is the detected power, K is a proportionality constant, N is the number of molecules irradiated by the photon, I describe the intensity of the laser beam, and σ_k denotes the differential cross-section of the k-th normal mode of the molecule. Considering the lower cross-sections of the various types of scattering, only Stokes Raman bands are considered and shown in spectra. See the following figure for various types of scattering.

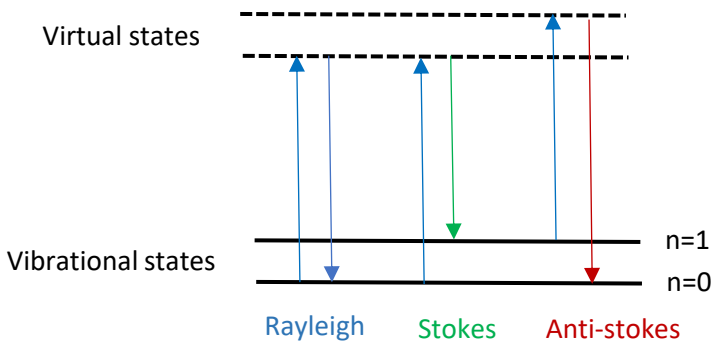

Figure 41. In Rayleigh scattering, the vibrational transition happens to the same vibrational energy level as the excitation level while in Stokes, the vibrational transition is to a higher level and in anti-stokes the transition occurs to the lower energy level.

Enhancement of the Raman scattering of a molecule stabilised on a plasmonic surface made a great revolution in the optical characterisation of materials. This enhancement can be obtained either by chemical or electromagnetic pathways. The chemical effect is usually due to the charge-transfer complex formation between the molecule and the metal surface causing optical absorption, which falls in a similar spectral region to the laser spectra, enhancing the Raman

scattering of some bonds. The electromagnetic enhancement is done i) as a result of plasmon excitation of the metallic substrate, which provides a stronger field than the laser beam field for the excitation and scattering of the molecule (known as a local effect); ii) due to the surrounding of the molecule e.g. whether the molecule is in vacuum or placed between a metal-liquid interface (210).

2.2.8 Nanoparticle analysis

After the synthesis of nanoparticles based on the selected protocol, it is crucial to assess the quality of the particles i.e., monodispersity and charge distribution, as well as the concentration and size. The common nanoparticle analysis tools for routine laboratory studies are absorbance spectroscopy, dynamic light scattering (DLS) and Zeta potential sizer.

2.2.8.1 Method

The particle analyses were performed using a Malvern Zetasizer Nano ZS device equipped with a 4 mW, 633 nm laser and an avalanche photodiode detector (APD). A special precaution was taken when transferring the liquid to the dedicated cuvette/cell since any remaining air bubbles inside the vessel proved to contribute to considerable errors in size and zeta values. For particle size analysis with DLS, a small volume of the colloidal dispersion was transferred inside a disposable microcuvette (40 µl) and placed inside the Malvern. The cuvette shape was selected using the interface, temperature, material type and properties of the dispersant liquid (e.g., viscosity, refractive index). For the zeta potential measurement, after introducing the sample by syringe inside the dedicated cell and placing the cell inside the device, the measurement mode was set to zeta in the interface and the corresponding settings, including the dispersant properties and the type of the zeta cell, were adjusted in the interface. Then after several runs, the required statistics related to zeta potential were obtained in the form of curves and tables.

2.2.8.2 Theory

DLS measures the size distribution of colloidal particles and operates based on laser irradiation on particles, recording the variation in the intensity of the scattered laser beam and correlating the scattered light fluctuations to the particle size. A simple schema for the DLS instrument is presented in Figure 42.

When a photon interacts with a particle, if the particle size is $1/10^{th}$ of the wavelength of the incident light, the scattering of the light follows Rayleigh scattering in which the energy of the excitation and scattering are the same. However, beyond this threshold value, the scattering is

inelastic and is called anisotropic Mie scattering, in which the scattering occurs more intensely in the direction of the incident photon (211). The dispersed colloidal particles move randomly as a result of the Brownian effect of solvent molecules and as they move, the scattered light changes. The diffusion of Brownian particles can be formulated using the single-particle diffusion coefficient described by the Stokes-Einstein equation for a single particle:

$$D_o = \frac{KT}{6\pi qr} \tag{2.37}$$

Here, where the k is the Boltzmann's constant, T describes the temperature, q denotes the viscosity of the Newtonian solvent and r is the radius of the particle. This applies to single particles and infinitely diluted solutions. For collectively diffusing Brownian particles, the gradient in concentration decreases over time:

$$\frac{\partial p}{\partial t} = D_c \nabla^2 P \tag{2.38}$$

Where Dc is the collective diffusion and P is the density of particles.

And the relaxation time for spherical Brownian particles is expressed as (212):

$$\tau = \frac{m}{6\pi qr} \tag{2.39}$$

Here, m is the mass of the particles.

The time-dependent correlation function is used to express the correlation between two dynamic properties that are changing as a function of time. This concept has been applied successfully to many physical phenomena. The noise signal for an independent fluctuating property over an average time is described as:

$$\langle A \rangle = \lim_{T\to\infty} \frac{1}{T} \int_0^T dt\, A(t) \tag{2.40}$$

In the case of two times of t and t+τ, and for a very small value of τ, the A(t+τ) and A(t) are similar, however, when τ increases, we will have the increase in deviation from similarity as in the case of fluctuations. We then have this autocorrection equation (213):

$$\langle A(0)A(\tau) \rangle = \lim_{T\to\infty} \frac{1}{T} \int_0^T dt\, A(t)\, A(t+\tau) \tag{2.41}$$

The autocorrelation function for a monodispersed particle for a short decay τ is:

$$G(t) = 1 + b.e^{-2\tau.D_t\, q^2} \tag{2.42}$$

Here, b is a constant specific to the optics, D_t is the translational diffusion coefficient and q is the scattering vector, which can be obtained from:

$$|q| = \frac{4\pi n_0}{\lambda_0 \ \sin\theta/_2} \tag{2.43}$$

where n_o denotes the refractive index (RI) of the solvent, λ_o describes wavelength in a vacuum and θ shows scattering angle.

By plotting the G(t) versus q, D_t can be obtained, and the radius of the particle can be extracted from the single-particle diffusion coefficient D equation (2.37) (21).

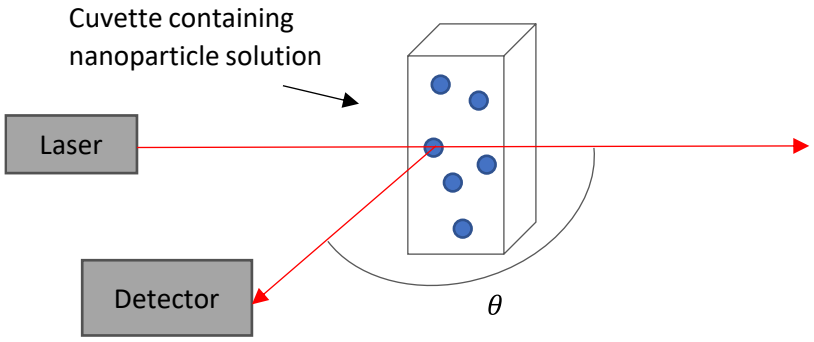

Figure 42. Basic set-up representing the DLS instrument.

-Zeta Potential

The other parameter, which is of high importance for dispersed colloids is surface zeta potential which is an expression of the particle surface charge. When a charged colloidal particle is dispersed in a solvent, the oppositely charged ions are attracted toward these particles forming a Stern layer. The other oppositely charged ions continuously diffuse toward this layer. However, because of repulsion forces from this layer and also between each other, an equilibrium of attraction and repulsion is established. Farther from the Stern layer, a diffuse layer of counter-ions is formed to neutralise the charge. These two layers together constitute an electrical double layer, with a thickness defined by the type and concentration of ions involved (see Figure 43). This thickness value is described by the Debye- Hückel equation:

$$\kappa = \left(\frac{e^2 \ \sum n_i z_i^2}{\varepsilon k_B T}\right)^{\frac{1}{2}} \tag{2.44}$$

where κ is the Debye-Hückel parameter and 1/κ the thickness of the double layer, n_i, k_B, T, z_i, ε are, the charge, the number of ions of type i per unit volume in bulk, the Boltzmann constant, the temperate, the elementary charge of ion i, and the permittivity, respectively.

Due to charge separation, there is a potential between the colloidal particles and any point in the bulk of the suspension. In the Stern layer, this potential declines linearly and in the diffuse layer, this decline follows an exponential trend until it reaches zero in the boundary of the electrical double layer (214).

Using the Poisson–Boltzmann (PB) expression of potential, we have:

$$\nabla^2\psi = \frac{-e\sum_i {n_i}^b z_i\, e^{-\frac{z_i e\psi}{KT}}}{\varepsilon} \tag{2.45}$$

where ψ demonstrates the electrical potential. The one-dimensional form of the PB expression, assuming that the surface charge is distributed uniformly within a planar sheet with negligible dimensions, is (215):

$$\frac{d^2\psi}{dx^2} = \frac{-e\sum_i {n_i}^b z_i\, e^{-\frac{z_i e\psi}{KT}}}{\varepsilon} \tag{2.46}$$

By relating the electromobility of the particles in suspension and their surface potential, estimations of zeta potential can be obtained. For example, for a small particle with a radius r, if **κ**r < 0.1 when **κ**r is the ratio of radius to electric double layer thickness, we have this expression:

$$\psi = \frac{3\mu\eta}{2\varepsilon\ D} = \zeta \tag{2.47}$$

where ζ is zeta potential, μ is the electromobility of the colloidal particle as its velocity divided by electric field, ε the permittivity of vacuum and η is the viscosity of the surrounding liquid (216). In the commercial zeta sizer, the electromobility of colloids is measured by Laser Doppler Velocimetry (LDV), which is based on illuminating colloids with a laser beam and translating the fluctuations in the scattered beam to electromobility. Then, this value is converted to measure the zeta potential following Henry's equation:

$$\mu = \frac{2z\varepsilon}{3\eta}\, f(\kappa r) \tag{2.48}$$

The f(**κ**r) refers to Henry's function and usually, the values of 3/2 or 1 are attributed to this function in the expression (217).

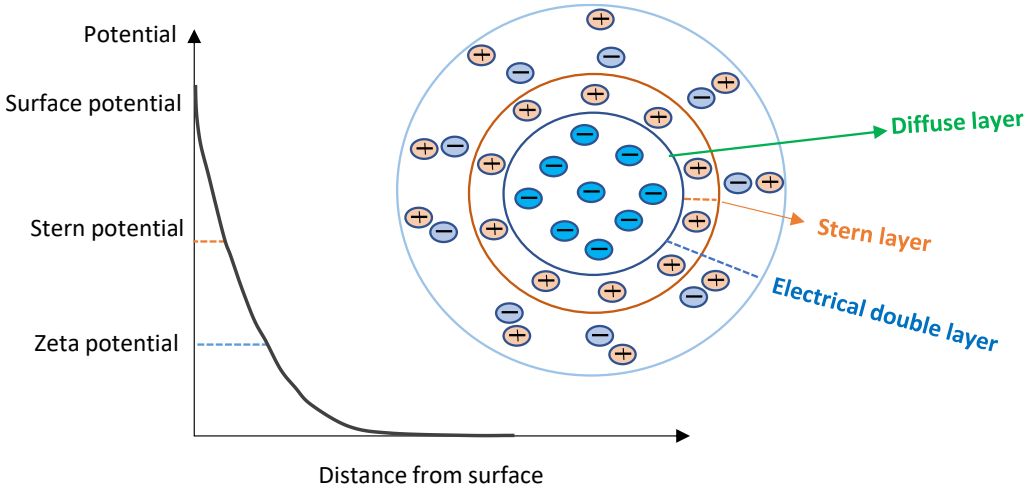

Figure 43. Double electrical layer generated around a negatively-charged colloidal particles

-Absorbance

Metallic nanoparticles show characteristic absorption peaks in the UV-Vis region due to plasma resonances or interband transitions. Copper, silver and gold particles, which have colourful suspension, show intense peaks in the visible region. For most metallic particles within the range of 3-20 nm, the dependence of the absorbance spectra on the particle size is negligible and is only related to the volume of particles in the solution. The absorbance intensity for spherical and hollow spherical shells is calculated from the following equation provided that the solution is sufficiently dilute:

$$A = \frac{CNl}{2.303} \tag{2.49}$$

Here C is the absorbance cross-section, N describes the number per unit volume of particles and *l* describes the length of the optical pathway.

The cross-section in water medium for the mentioned size range can be obtained from:

$$C = {}^{18\pi\upsilon\varepsilon_2}\Big/_{l\,((\varepsilon_1+2)^2+\varepsilon_2^2)} \tag{2.50}$$

where υ is the wavelength in the surrounding medium, V is the volume of the particles and $\varepsilon_1 + i\varepsilon_2 = \varepsilon$ is the complex relative permittivity of the metal relative to that of the solvent. For colloidal particles, the broadening in spectra can be observed because of polydispersity, aggregation, or shape deviation (218).

Since both the concentration and the size of colloidal nanoparticles can be measured using the optical absorbance spectroscopy and the resulted UV-Vis spectrum (219), we assessed the synthesised gold nanoparticles with UV-Vis spectroscopy. The resulted peak shape and absorbance wavelength as well as the intensity were compared to the optimised reference nanoparticle sample to ensure the quality of the synthesis. A sharp symmetric peak (the surface plasmon peak) located at 520 nm with the intensity of 2.5-3 was considered as the primary indicator of a properly synthesised 11 nm spherical citrate-capped gold nanoparticle dispersion. After this initial qualitative assessment, further investigations were conducted using DLS and zeta sizer to confirm the size, monodispersity and zeta potential of the synthesised colloidal nanoparticles.

2.2.9 Monitoring surface-particle interactions via QCM

2.2.9.1 Method

The QCM-D measurements were conducted with Q-Sense E1 system to interpret the kinetic behaviour of nanoparticle adsorption. The measurement started by first obtaining a stable baseline for the pure electrolyte (NaCl) of known ionic strength and pH value. After obtaining the baseline, the colloidal gold solution was flushed through the surface functionalised SiO_2 QCM chip which was previously functionalised with each template coating (e.g., micelles, CHN bilayer, APES) at a constant flow rate, and the subsequent frequency variation versus time upon mass uptake over substrate was plotted simultaneously. The frequency variation versus time was then converted to mass variation versus time as will be explained in the following section.

2.2.9.2 Theory

The piezoelectric quartz crystal microbalance (QCM) is a mass-sensitive transducer which is used to characterise adsorbate by monitoring the adsorption process. The system consists of a single quartz crystal squeezed between two electrodes. The crystal resonates at its resonance frequency upon connection to an external driving oscillator circuit. The mechanism is based on translating mass uptake or mass removal to the frequency change. Sauerbrey's equation (Eq. 2.51) is used to measure the frequency variation and accordingly, surface coverage variation versus time of incubation (220).

$$\Delta m = -\Delta f . \frac{C}{n} \tag{2.51}$$

While Δf is the recorded frequency difference before and after mass loading, C describes the mass sensitivity constant (C = 17.7 ng cm^{-2} Hz^{-1} for a 5 MHz crystal) and n demonstrates overtone numbers (odd numbers).

This equation is valid only if the mass is distributed homogenously over the electrode since it is much smaller than the weight of the quartz crystal. Meanwhile, the particle should be rigidly attached to the material surface (221). The viscoelastic or softly deposited films cause the oscillation to lose energy and show deviation from Sauerbrey's equation.

The QCM-D allows real-time monitoring of the adsorption process and provides detailed information about the mechanism of a binding reaction. In this mode, besides the frequency change, the energy loss (dissipation change, ΔD) is also recorded to obtain the mass variation of a viscoelastic film. This allows additional information about the deposited film to be investigated, e.g. conformational changes, crosslinking, and swelling (222).

Chapter 3: Unidirectional chemistry gradients

3.1 Introduction

The chemistry of the bio-interface is tailored to initiate specific biological reactions. This is typically done by either modifying the original surface or by imparting a new chemical character to the surface through the application of thin-film coatings, monolayers, etc. For instance, some surface-bound functional groups, e.g., NH_2, COOH, CH_x and CF_x groups, are already known to promote protein adsorption and generally biofouling applications. As a result, surfaces with these functionalities are generated and used, for example, in the biomedical field, in tissue regeneration studies, and for developing biosensors, drug release systems, etc. In contrast, hydroxyl, ether and thiol groups reduce biofouling processes and can be used in maritime sector (ship building) or developing antimicrobial surfaces (223, 224). The systematic study of the impact of chemistry variables, such as the quantity or density of specific chemical elements/chemical groups on the bioreaction outcome, requires creative optimisation approaches, which not only minimise the number of required experiments, cost of resources, and time but also avoid inter-batch errors by keeping experimental conditions identical. The ideal solution is to optimise the biointerface by processing a single sample surface running a single experiment that offers the gradual distribution of a chemistry variable in one direction. In this regard, unidirectional surface chemistry gradients allow the systematic monitoring of the impact of a surface chemistry condition on an experimental outcome by drawing a spatial relation between them. For instance, cell adhesion along the gradient surface can be followed by correlating it to the chemistry (e.g. oxygen-to-carbon content ratio) of each investigated point on the gradient and finally spotting the surface condition that allows optimum cell adhesion maximising a targeted biological function, e.g. proliferation, differentiation, etc. The application of surface chemistry gradients is not limited to optimisation but is also applicable in medicine to drive a biological phenomenon, such as cell motility, which is a consequence of the cell response to the gradient of a specific material and is generally known as chemoattractant (225).

The gradient approach has been explored as a new class of combinatorial approaches, which has the potential for full interface optimisation compared to the partial optimisation attained by the classic DOE approach. There have been numerous studies in material and biomedical fields, investigating various surface clues, such as surface chemistry, topography, and the mechanical properties benefitting surface gradients. However, the aim is to get as close as possible to the ideal of exploring gradient fabrication approaches with less sophisticated operating conditions,

which enables an upscale in production and ensures reproducibility, achieving a wide range of variation over a large distance to map the impact of a greater number of surface interactions and attaining a linear correlation between the surface variable and reaction output.

There are several classes of materials and approaches reported so far for developing chemistry gradients, as discussed in detail in chapter 1 (1.4.2). Not all those introduced approaches provide the simultaneous control over surface properties at different scales (from nano to macro), nor do they all provide upscaling and flexibility in design. Plasma polymerisation techniques tackle most of these disadvantages, as well as offering the additional advantages of being eco-friendly (due to solvent-free reactions), ensuring a dense presence of the intended functional groups (226), adaptable to every substrate type, and having readily switchable chemistry. Therefore, plasma has been selected as the material of choice for developing chemistry gradients in the current work. A specific plasma technology may be preferred over another technology based on specific coating requirements in terms of homogeneity, stability, and the choice of substrate (e.g., dimension, thermosensitivity, etc.).

Contrary to conventional polymers, plasma polymers allow the independent tailoring of the mechanical and chemical stability of polymer coatings, without the need for structural changes during their synthesis (227, 228). Surface gradients based on plasma approaches can be categorised as i) introducing a reactive gas (e.g., oxygen) over a material surface to activate surface functional groups or ii) polymerisation of a monomer/precursor and deposition on a surface. Although the first approach was initially investigated in recent decades for generating chemistry (and wettability) gradients, it has now been fully replaced with the deposition approach due to a lack of required stability and minimal flexibility in achievable surface chemistry.

The coating properties can be altered during deposition by changing the plasma electrical parameters or precursor concentration (flow rate). The commonly practised approaches for generating a gradient in chemical composition are to tune plasma power input directly or tune the voltage and frequency of discharge, vary the precursor content (i.e., flow rate) or the ratio of precursors flow rates (when multiple precursors are employed), etc. These approaches allow the precursor fragmentation level and polymerisation to be controlled, however, in order to obtain a spatial distribution in the composition along a certain direction on the surface, these approaches should be accompanied by either the moving the sample with respect to the plasma source or the use of a mask.

Due to the implication of oxygen and nitrogen functional groups in bio-interface platforms, and based on the plasma technology merits, we aimed to introduce two different experimental gradient approaches i) maskless and dynamic deposition with atmospheric pressure corona discharge for developing a unidirectional gradient of oxygen content and ii) mask-enabled static deposition with a low-pressure glow discharge for generating a unidirectional gradient of nitrogen content.

The first approach that will be introduced here is the first report of a programmed moving jet capable of depositing an oxygen-functional gradient in a single run, offering the advantages of high throughput and a wide scale of variation in surface chemistry. The oxygen content gradient was formed by benefitting from an HMDSO precursor, which allows the switch from a fully organic to an almost fully inorganic coating and satisfactory wettability variation (110°-40°)(229).

The second approach that will be discussed offers a highly homogenous and reproducible nitrogen-functional plasma-polymerised thin bilayer, deposited statically using capacitively coupled low-pressure plasma and a masking agent. As the focus of the experimental design was to preserve the functionality of the coating for a high-performing biointerface, the nitrogen content variation scale was designed (0-11.45%) to ensure the highest stability under physiological aqueous conditions.

3.2 1-D Oxygen Functional Chemistry Gradient

Plasma provides enough energy for the monomer dissociation required for polymerisation and film formation. The compositional properties of the deposited coating are determined by both the gas phase and surface phase processes. Since plasma polymerisation is not as straightforward as traditional polymer synthesis techniques, it necessitates a thorough analysis of the underlying film growth mechanisms.

HMDSO is a popular siloxane frequently used as a precursor/monomer for plasma polymerisation with a wide range of applications in the coating industry, e.g. for corrosion protection (230), anti-scratch protection coatings for plastic substrates (231), food packaging (232), etc. There have been several investigations into the HMDSO plasma polymerisation pathways and main film-forming species under different plasma technologies (233-236). This monomer has been used to develop coatings with diverse chemical properties from purely organic, with low surface energy to purely inorganic, with high surface energy. It has been

reported that the addition of oxygen as a reacting gas, during HMDSO polymerisation with fixed monomer concentration and power input conditions, not only allows the incorporation of oxygen inside the polymer structure but also increases the deposition rate, and decreases organic features (carbon content) of the coating (237). It has been suggested that under atmospheric pressure plasma conditions in the presence of pure HMDSO plasma, decomposition and polymerisation occur mainly on the substrate, yielding a polymer similar to the initial monomer while after oxygen introduction, the reaction mechanism changes so that decomposition is increased, mainly occurring in the gas phase due to reactive oxygen radicals followed by the adsorption of active intermediate products on the surface, forming silica-like polymers (238).

The chemical film growth pathway for both HMDSO and HMDSO+O_2 was investigated experimentally (defining stoichiometry from XPS measurements) and theoretically with simulation studies, which suggested different film growth pathways for both, the high probability of Si—O bond breakage of the monomer rather than Si—C in the presence of O_2 under cold and atmospheric pressure plasma conditions, and $(CH_3)_3$—Si—O and Si—$(CH_3)_3$ as the main two dissociation products with $(CH_3)_3$—Si—O being the main film-forming radical, as shown in the following polymerisation mechanism (see Figure 44) (239).

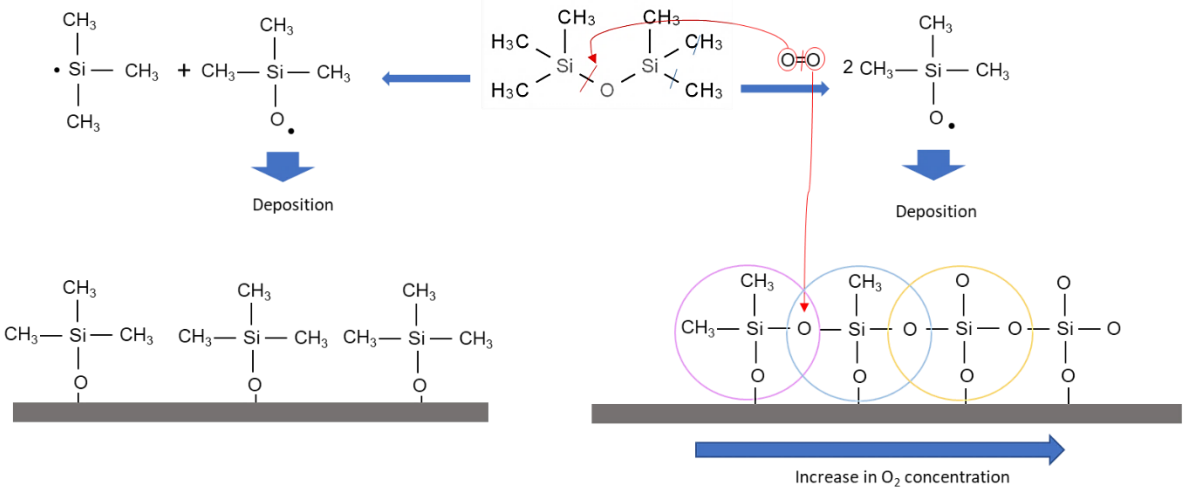

Figure 44. Plasma-polymerised HMDSO deposition and possible growth mechanism in the presence and absence of oxygen. The schema is inspired by the study published in (239).

As can be seen in Figure 44, there are three main sites for monomer dissociation: Si-O, Si-C and C-H. The initial dissociation under atmospheric pressure plasma is attributed to Si-O bond breakage, which is expected to occur in the gas phase. This allows the production of the main

film-forming fragment and its deposition on the surface. The oxygen radical then follows the polymerisation in the surface phase, by continuously eliminating CH_3 groups by breaking Si-C bonds and replacing carbon groups. A higher concentration of oxygen obviously enables higher carbon elimination and increases oxygen incorporation in the polymer structure. The C-H bond dissociation may also occur under certain conditions, leading to polymer crosslinking and a more complex polymer structure, which is avoided here for the simplicity of the discussion.

Another similar study confirms the above mechanism by evaluating three dominant fragments of $(CH_3)_2SiO_2$, CH_3SiO_3 and SiO_4 based on XPS analysis and the curve fitting of Si 2p core-level peaks for several HMDSO polymerised films deposited with varying oxygen admixture (m 0 to 80%.). Based on the study, the highest oxygen admixture yielded a larger amount of SiO_4 followed by CH_3SiO_3 and $(CH_3)_2SiO_2$, respectively. On the other hand, when the deposition was carried out in the absence of oxygen, the trend was the opposite with $(CH_3)_2SiO_2$ the most abundant fragment followed by CH_3SiO_3 and then SiO_4 (240). This demonstrates that in the absence of oxygen, HMDSO follows a mechanism where the main film-forming species is $(CH_3)_2SiO_2$ with two methyl functional groups. However, by increasing the oxygen concentration, carbons are eliminated and at the same time, the contribution of oxygen in the coating increases to the level at which a carbon-free coating, similar to glass (silica) is achieved.

The abovementioned considerations allowed an experimental scheme to be designed to deposit a continuous gradient of the oxygen functional gradient coating, starting with a pure HMDSO monomer followed by the gradual introduction of oxygen with an increasing flow rate while the plasma jet moved at a constant speed along the surface. The goal was to achieve a gradient with two extremes in composition, that is, organic HMDSO-like and inorganic silica-like coatings on two opposing sides of the gradient, in order to achieve a maximum possible chemistry and wettability variation for the monomer of choice.

3.2.1 Summary of the fabrication

The fabrication of the continuous gradient coating containing oxygen was based on the plasma polymerisation of HMDSO in the presence of oxygen gas. Before depositing the gradient coating, the initial discharge stability and film characteristics were assessed following a series of static depositions using various voltage and frequency combinations. After achieving the appropriate deposition conditions, 7 representative static coatings (See Table 6) were defined

as the reference samples and were then programmed into the jet to deposit the continuous gradient coating on polyethylene foil (PE) as a substrate.

Table 6. 7 deposition conditions applied for the deposition of both the statically deposited reference samples and gradient coatings.

Deposition conditions	**1**	**2**	**3**	**4**	**5**	**6**	**7**
Electrical parameters	12kV-12kHz	12kV-12kHz	12kV-12kHz	12kV-12kHz	15kV-15kHz	15kV-15kHz	15kV-15kHz
O_2 flow rate (slpm)	0	0.02	0.04	0.08	0.2	0.3	0.4

The carrier gas (Argon), shielding gas (N_2) and monomer (HMDSO) were introduced with constant concentrations from the corresponding channels as follows: channel I: 2 slpm Ar + 0.2 g/h HMDSO + xO_2; channel II :3 slpm Ar; shield channel: 3 slpm N_2. During dynamic deposition, the jet was set to move at the constant rate of 15 mm/min. along the PE depositing each condition. For the schema of the plasma jet and more details on the experimental setup please refer to Chapter 2 (2.1.1.1) and Figure 18.

These deposition conditions were chosen after the evaluation of the coating features with FTIR and static water contact angle results, and the examination of the physical properties of the discharge and the coatings. The width of the coating was limited by the size of the discharge and the length was set to approx. 10 cm. Based on this, two conditions out of total seven conditions were considered for the extreme deposition conditions (a coating with high highest hydrocarbon content and the fully inorganic coating) and the remaining 5 conditions were selected in a way that the magnitude of the chemistry and wettability variation of each was meaningful from the previous condition but not large enough to miss a coating, which could otherwise offer interesting surface properties. For the first four deposition conditions, moderate electrical parameters were adjusted however, at a higher concentration of oxygen (0.2 slpm and higher) electrical parameters had to be increased in order to supply enough energy for the dissociation of all the oxygen molecules and efficient polymerisation. On the other hand, during initial tests, a further increase in oxygen (beyond 0.4 slpm), and electrical parameters was shown to drastically increase the wettability of the deposited coating up to full droplet spreading, however, this resulted in unstable and unreliable discharge, as well as defects on the polymeric substrate (PE). Therefore, the oxygen concentration of 0-0.4 slpm and two sets of voltage and frequency combinations of 12kV-12kHz and 15kV-15kHz were selected as the optimum experimental parameters.

3.3 1-D nitrogen-functional chemistry gradients

The significance of amine and oxygen functional coatings in providing bioactive surfaces has been well-documented in the biomedical field. This might be accomplished by tuning surface chemistry and surface charge to impart the intended selectivity necessary for attracting a target biomolecule (e.g. a certain cell line) to the surface (241). Meanwhile, the application of nitrogen-functional plasma polymers in the textile industry has been demonstrated (242).

Plasma-polymerised nitrogen functional coatings can be created by i) combining a non-polymerisable reactive nitrogen-containing gas (e.g., ammonia, N_2) with a hydrocarbon gas or ii) employing a monomer (e.g. allylamine) that already includes nitrogen functional groups. It has been established that the first strategy allows greater flexibility in creating the desired chemical groups when the proper deposition parameters (gas flow rate ratio, power input, pressure, etc) are applied (104). The organic polymer network, which binds to heteroatoms to form functional groups, is provided by using a hydrocarbon molecule (CH_4, C_2H_4, C_2H_2, etc). When searching within hydrocarbon gases for polymerisation, numerous criteria such as deposition rate, chemical flexibility, and proportion of integrated heteroatoms (N, O, etc.), are taken into account (104, 241, 243). For instance, for nitrogen-containing non-polymerisable gases, more $–NH_x$ groups were expected to be generated using ammonia (NH_3) than with N_2 (244). For the purpose of this study, ethylene and ammonia precursors were selected with varying reactive gas to hydrocarbon ratios, power input and pressure, in order to develop coatings with gradually varying nitrogen (and primary amine) content. The optimistic polymerisation pathway for the copolymerisation of ethylene and ammonia is radical chain growth copolymerisation, which, in an ideal scenario, could lead to the following polymerisation pathway:

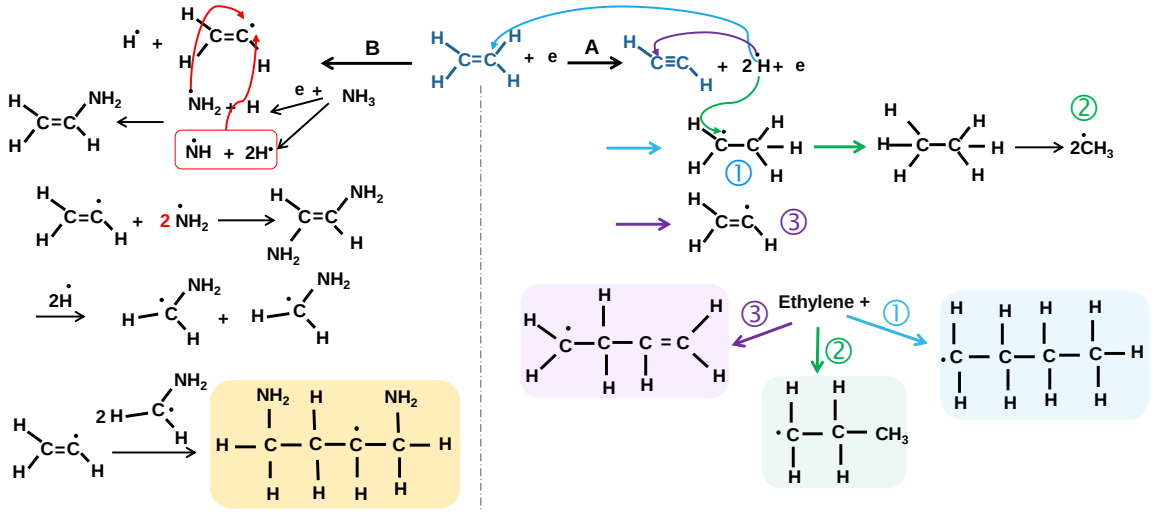

However, the fragmentation, followed by the poly-recombination mechanism (atomic polymerisation), competes with the main radical-induced pathway (163) leading to several irregular structures. Therefore, while it is ideal for obtaining a well-defined polymer structure, the plasma polymer coating obtained is rather far from this expectation as will be discussed based on XPS analysis in 4.2.1. However, it has been attempted to enhance the primary amine selectivity based on the deposition conditions (precursor ratio, pressure, power input, etc.) and preferred plasma technique. In this regard, based on a previous study (245, 246), it has been demonstrated that the low-pressure plasma used for NH_3/ethylene polymerisation offers higher amino selectivity ([NH_2]/N: 32% vs 17%) than atmospheric pressure plasma under similar conditions, therefore, capacitively coupled plasma with an RF source has been selected in the framework of this study.

The main focus of the current study is to utilise the optimum deposition conditions explored in the series of previous studies (106, 247, 248) to produce highly stable amino-functional coatings in aqueous media, which ensures the durable function of the developed gradient for real-world applications. Therefore, it was decided to benefit from the bilayer design proposed in these studies, which is based on a vertical chemistry gradient with a thicker base layer with a highly crosslinked and less functional coating that supports the upper thin layer with a high functionality group containing primary amino functional groups that prevent it from leaching into the aqueous medium.

-Theoretical considerations of the process

The correlation between the polymer deposition rate and the energy input is described using the following equations (244).

$$\frac{R_m}{F} = G\exp(-\frac{E_a}{W/_F}) \qquad 3.1$$

This equation, namely the Yasuda equation, describes the correlation between the W/F, or power input, F the monomer gas flow rate, G a reactor-dependent geometrical factor and E_a, which is the minimum activation energy required to promote polymerisation. Empirical calculations are expected to demonstrate a linear relationship between mass deposition rate (Rm) and power input at low energy input (energy-deficient zone) and dependence of Rm on the monomer flow rate (F) at higher energy input (monomer-deficient zone).

On the other hand, based on the adsorption model, the deposition rate is directly proportional to particle flux densities at the substrate, which implies that the concentration of all the different molecules contributing to plasma polymerisation should also be considered:

$$R_{pol} = \sum_\mu \sigma_\mu n_\mu j_x \qquad 3.2$$

σ_μ is the reaction cross-section for the integration of monomer molecules into the thin film due to collisions with energetic particles of the flow j_x, and n_μ is the surface concentration of monomer molecules. Therefore, it is suggested that the flow rates of all contributing gases included in polymerisation should be combined as follows:

$$F = F_m + aF_c \qquad 3.3$$

Here, F_m is the monomer flow rate, while F_c is the non-polymerisable reactive gas flow rate, and a is a weighting constant which is specific for each combination of precursors.

To define the polymerisation region where the polymerisation process is controlled by radicals (and not by ion-induced polymerisation), it is logical to initially visualise experimental deposition rates of each deposited coating (determined from ellipsometry measurements) as a function of the energy input and as a function of the reactive gas flow rate for each deposition condition. Later, having theoretical activation energy for a specific precursor set, and using equation 3.1, the theoretical linear plots (the Arrhenius-like) are drawn, showing deposition rate variation as a function of energy inputs. Comparing the experimental and theoretical plot, one can observe the region in which the experimental values fit well with the theory, as well as regions where there is a deviation. Generally, equation 3.1 can be utilised to study the

polymerisation process based on deposition rate as a function of i) monomer flow rate; ii) reactive gas flow rate; and iii) power input. For example, the study below demonstrates how the reactive gas-ratio variation affects the deposition mechanism under different energy inputs.

A study (237) conducted aiming to compare the deposition mechanism of 5 different reactive gas/monomer combinations, each with different flow factors (a), confirmed the application of the abovementioned equations for tuning film properties through suitable deposition conditions (See Figure 45).

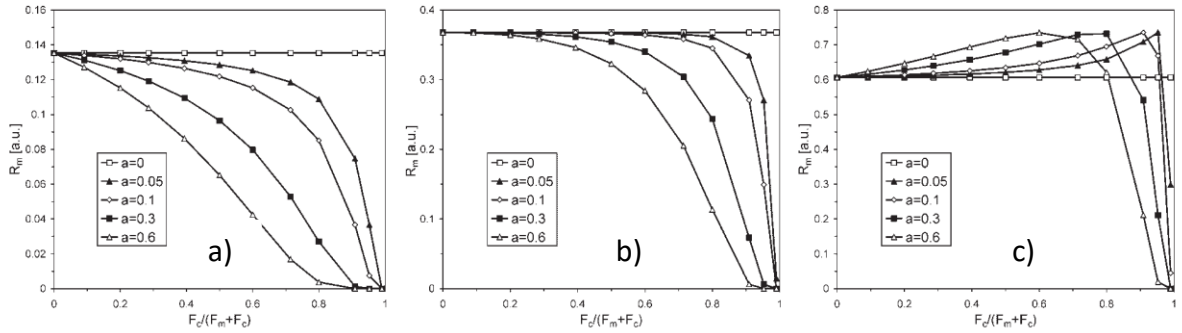

Figure 45. Deposition rates obtained from Equation (1) for several precursor combinations with different a factors presented as a function of the reactive gas/total gas ratio for constant monomer flow (Fm). The energy inputs were 0.5 Ea (left), Ea (middle), and 2 Ea (right). From left for A) 0.5Ea: the region is an energy-deficient region with E <Ea. Therefore, by increasing the reactive gas, the deposition rates decrease due to less available energy per reactive gas to dissociate and undergo polymerisation. This effect is more pronounced for higher (a) values. B) Ea=E, meaning that above a certain increase in the reactive gas ratio, the deposition rates drop sharply, as we are still in the energy-limiting regime. C) Ea<E : the region become a monomer-deficient region, therefore, at higher energies, where sufficient energy is provided per reactive gas, a gradual increase in deposition rates is observed for a wide range of reactive gas/monomer ratios. An abrupt and sharp decrease occurs when the reactive gas content starts getting larger than the monomer flow rate. Adapted with permission from (237).

As depicted, there are three different energy input values, which define the deposition rate variation trend with respect to the reactive gas ratio. For an energy input lower than or equal to E_a (Figure 45a and Figure 45b), a decreasing trend in deposition rates is observed upon increase in reactive gas content since the energy input is low and not sufficient to cause the fragmentation and polymerisation of the added precursor (energy-deficient region). This trend is more significant for higher flow-rate factors. On the other hand, for energy inputs higher than E_a (monomer deficient region) (as shown in Figure 45c), there is an abundance of energy for the fragmentation and polymerisation of the added gas, hence, the linear increase in deposition rate values is observed (polymerisation region). However, this increase faces an

abrupt and sharp decrease by a further increase in the reactive gas ratio, possibly due to the etching effect competing with the deposition. This suggests that it is possible to obtain a thicker coating with a higher contribution of reactive gas in the polymerisation process (higher content of heteroatoms, e.g., O and N) on selecting the raical-induced polymerisation region where $E_a<E$ and the deposition rate increases linearly with the increase in the reactive gas ratio (considering the constant total gas content).

-Design strategy

In total, four deposition conditions were selected for the nitrogen-functional chemistry gradient based on the design strategy inspired by the work published at (107), which is depicted in Figure 46 as an example coating. The two out of four coatings were deposited based on a similar strategy. Figure 46 depicts an Arrhenius-like plot for NH_3/C_2H_4 with two different constant flow-rate ratios against a variable energy input. The strategy involved depositing the first thicker layer (about 19 nm) with a lower ammonia ratio (4/7) and a higher power input to supply enough energy for rapid monomer fragmentation, increased crosslinking, high deposition rates (higher thickness), and higher hydrocarbon content. The power was then reduced slightly to generate an intermediate coating with a lower deposition rate. In the current work, this step was eliminated for the creation of gradient coatings. Next, the ammonia ratio was increased (from 4/7 to 1/1) and the power input was decreased to lower fragmentation and form a thinner layer with a higher incorporation of nitrogen functionality inside the polymer.
Additionally, attempting to further increase the nitrogen incorporation, the effect of pressure was assessed by increasing the chamber pressure (double-folded) while the other deposition parameters remained constant, as preliminary research had shown that further increasing the ammonia ratio beyond 7/7 only resulted in etching rather than film growth and increase in the percentage of N. The following section describes the deposition settings, power input, deposition time, and precursor ratio.

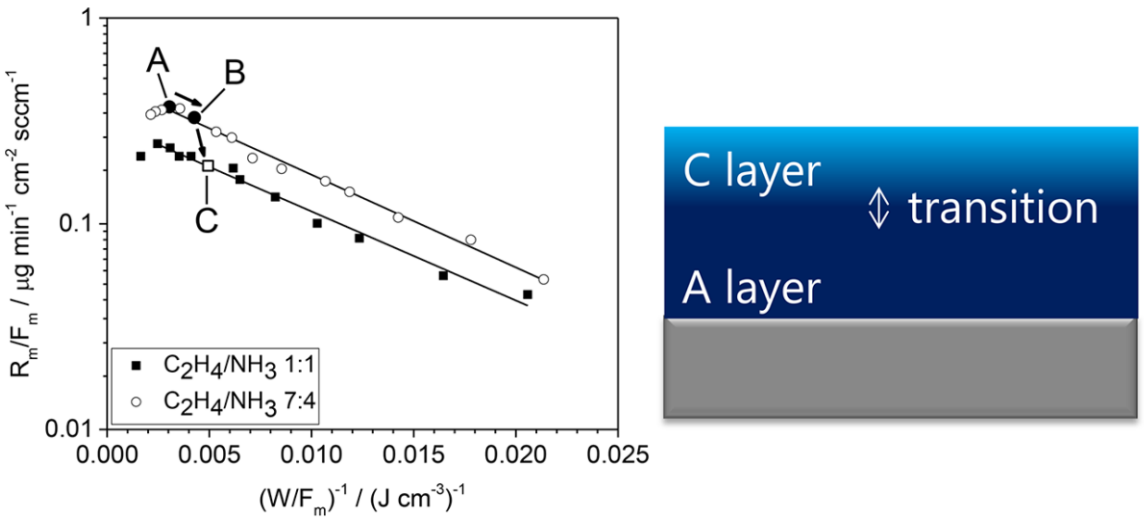

Figure 46. The mass deposition rate per monomer gas flow (Rm/Fm) is plotted versus the inverse energy input per monomer gas flow [(W/Fm)$^{-1}$ for ethylene and ammonia precursor combination, based on equation 1. F_m is the gas flow rate of ethylene as the polymerisable precursor. The linear line indicates the Arrhenius regimes, in which deposition is governed by radicals. The base layer A is deposited as shown in the figure by applying high energy input, then slightly reducing the power to achieve intermediate B conditions, and lastly increasing the gas flow ratio to deposit the top layer C. The schema of the expected vertical chemistry gradient coating is displayed on the right. Adapted with permission from (107).

3.3.1 Summary of the fabrication

The fabrication of the nitrogen- containing chemistry gradient was implemented using NH_3/ethylene as polymerisation precursors and a masking device for the static deposition of each of the four conditions consecutively. The masking device consisted of two compartments, the plate on which to place samples and the cover with the slits. The creative design enabled all four conditions to be deposited by simply displacing the cover of the mask, as described in chapter 2. (2.1.2.1) and Figure 21. The gradient was formed by depositing the first coating without nitrogen introduction and depositing the other three distinct coatings with a gradual increase in the nitrogen content by adjusting power input and deposition rates to obtain the intended thickness and nitrogen content. Due to the considerable increase in the nitrogen groups in the third and fourth regions, and the instability of the nitrogen groups in the aqueous media, the supporting platform layer with its high hydrocarbon content and high crosslinking degree was deposited first before the top thin functional nitrogen coating. Details of all experimental parameters for depositing the four distinct coatings are listed in Table 7. Plasma parameters including power input, precursor ratio, pressure and deposition time for the 4 distinct coatings.

Table 7. Plasma parameters including power input, precursor ratio, pressure and deposition time for the 4 distinct coatings.

Properties	Thickness (nm)		NH_3/C_2H_4 ratio	Power (W)	Pressure (mbar)	Deposition time (s)	
Coating 1	25	10	0/7	70	0.1	150	60
Coating 2	25	10	4/7	70	0.1	166	66
Coating 3	5 (tl) + 20 (bl)	1 (tl) + 10 (bl)	7/7 (tl) + 4/7(bl)	50 (tl)/70(bl)	0.1/0.1	63/133	13/66
Coating 4	5 (tl) + 20 (bl)	1 (tl) + 10 (bl)	7/7 (tl) + 4/7(bl)	50 (tl)/70(bl)	0.2 (tl)/0.1 (bl)	52/133	10/66

Tl: top layer, bl: bottom layer

To avoid minor cross-contamination, first those coatings with higher nitrogen content were deposited and lastly the coating with the absence of ammonia. The chamber was cleaned between each deposition and was also purged with argon to provide clean deposition conditions.

3.4 Results and discussions

3.4.1 1-D oxygen-functional chemistry gradient

3.4.1.1 Chemical Identification with ATR-FTIR

ATR-FTIR was performed for the molecular-level analysis of the organic thin film properties, for both static and dynamic deposition modes immediately after the deposition process. ATR-FTIR is a non-destructive analysis approach and provides a rapid identification of the surface functional groups, which can also be adopted for quantitative analysis.

- ***Statically deposited sample analysis***

The statically deposited samples were characterised with ATR-FTIR in the middle of the coating. The background was corrected, and the peaks were normalised to one of the two sharp peaks at ~2,913 cm^{-1} related to the PE substrate, which is attributed to the stretching vibration of CH_2. The FTIR spectra for all the 7 distinct coatings are presented in Figure 47.

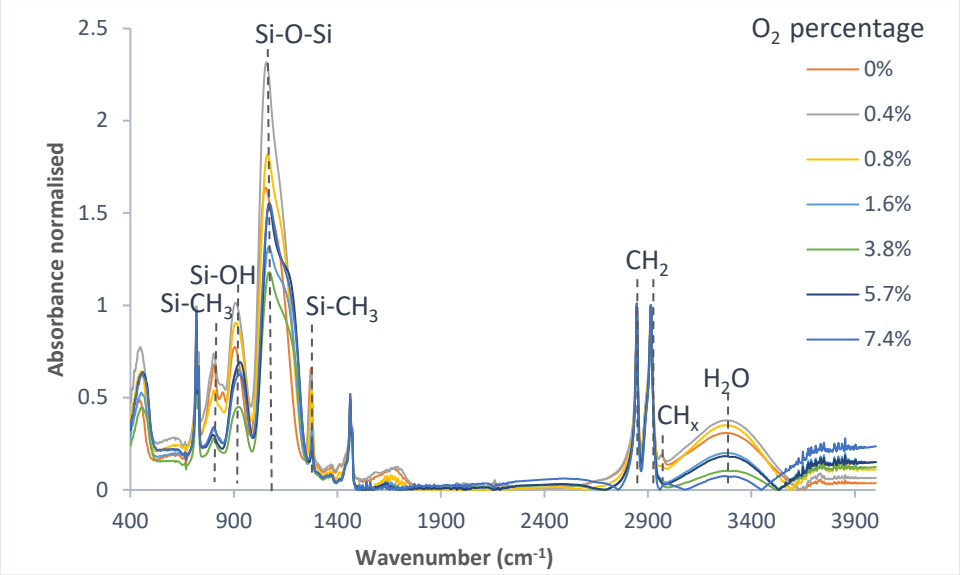

Figure 47. Normalised FTIR spectra for the statically deposited HMDSO polymer coatings with increasing O_2 admixture.

The prominent peaks representing the plasma-polymerised HMDSO include two typical characteristic peaks of organosilicons: i) Si-O-Si asymmetric stretching vibration, which includes the following the transversal optical vibration modes, TO3 occurring between 1000 and 1150 cm-1, representing the in-phase (back-and-forth) stretching vibration of oxygen atoms along the Si-O bond axis, and TO4 appearing between 1150 and 1200 cm-1, corresponding to the out-of-phase stretching of Si-O as a result of glass-like coating formation and possible defects (e.g. porosity, contamination, non-stoichiometry); and ii) Si-CH_3 symmetric deformation vibration mode (1260 cm^{-1}). The remaining peaks are attributed to the O-H vibration (at 3000-3600 cm^{-1}), the rocking vibration of CH_3 in Si–$(CH_3)_3$ or/and TO of Si-O-Si (at 800 cm^{-1}), the Si–OH band located at 925 cm^{-1} and the C–H_3 at 2965 cm^{-1}. The rest of the recognised peaks were originated from the substrate at 720 cm^{-1}, 1470 cm^{-1} and two sharp peaks at 2850 and 2915 cm^{-1} representing CH_2 group.

After the introduction of oxygen and further fragmentation of the precursor, as expected, oxygen containing moieties progressively replaced methyl groups inside the polymer, until all six methyl groups of HMDSO were replaced, shifting the coating character from its initial hybrid organic-inorganic nature to an almost purely inorganic, silica-like coating. This can best be observed with the decreasing trend of the Si-CH_3 peak at 1260 cm^{-1}. See Figure 48 for the magnified view of the decreasing Si-CH_3 peaks as a function of oxygen concentration.

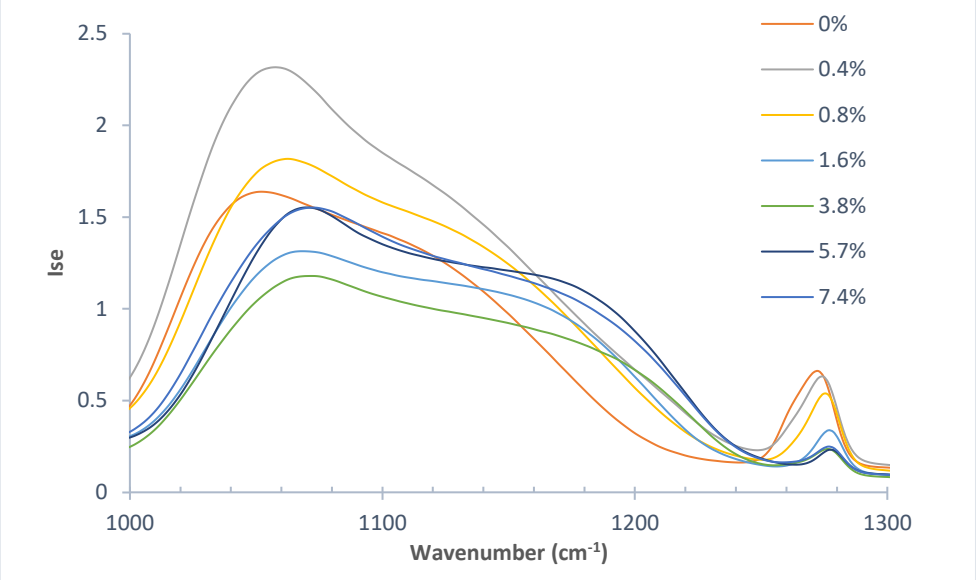

Figure 48. Magnified FTIR spectra of the coatings deposited in static mode for the wavenumbers 1000-1300 cm^{-1}.

Unlike the clear decreasing trend of Si-CH_3, which was due to change in the nature of the coating caused by a gradually increasing oxygen content, interpreting, and comparing Si-O-Si peaks in different coatings was more difficult, implying that quantifying and plotting a trend would not be informative. The position and the intensity attributed to different vibration modes may be impacted by the chemical and conformational environment induced by the coating deposition and the inorganic silicate polymerisation, leading to constraints in the vibrations of the moieties. As a result, it was not expected that the peak intensity would be proportional to the coating thickness. Furthermore, except for the first deposition condition, which was performed without oxygen introduction, the thickness of the other coatings was expected to remain constant because, in all six deposition conditions, excess of oxygen was always present, even at the lowest introduced percentage compared to the fixed flow rate of HMDSO. This is evident in the similar intensities of the peaks in the original FTIR spectra of the static coatings before normalising them to the substrate peak. The primary variable would be the size of the clusters, which will be discussed further in the surface topography study.

The area corresponding to the CH_3 peaks is expected to decrease by increasing the oxygen content and the reticulation ratio. Figure 49 represents the integration of the (Si-)CH_3 peak versus the oxygen flow rate for the seven coatings. As expected, the area of the CH_3 peak decreased as the oxygen flow rate in the plasma discharge increased, suggesting that the oxygen

was replaced by carbon in the coating. The very similar carbon content variation results were reported (239) for coatings deposited with HMDSO/xO_2 using an atmospheric plasma jet (with helium as the carrier). In the study, the area of the Si-CH_3 peak (spotted at 1260 cm^{-1}) was plotted against oxygen flow rates varying between (0.02–0.4%). The carbon content variation was displayed as a function of the oxygen admixture, which showed an almost parabolic increase versus the oxygen flow rate (249). There have been a small number other studies on plasma polymerisation via the administration of varying degrees of O_2/HMDSO using a different plasma setup (in terms of pressure, reactor, etc.) all proving a decrease in carbon content when oxygen was increased in O_2/HMDSO admixture (237, 250).

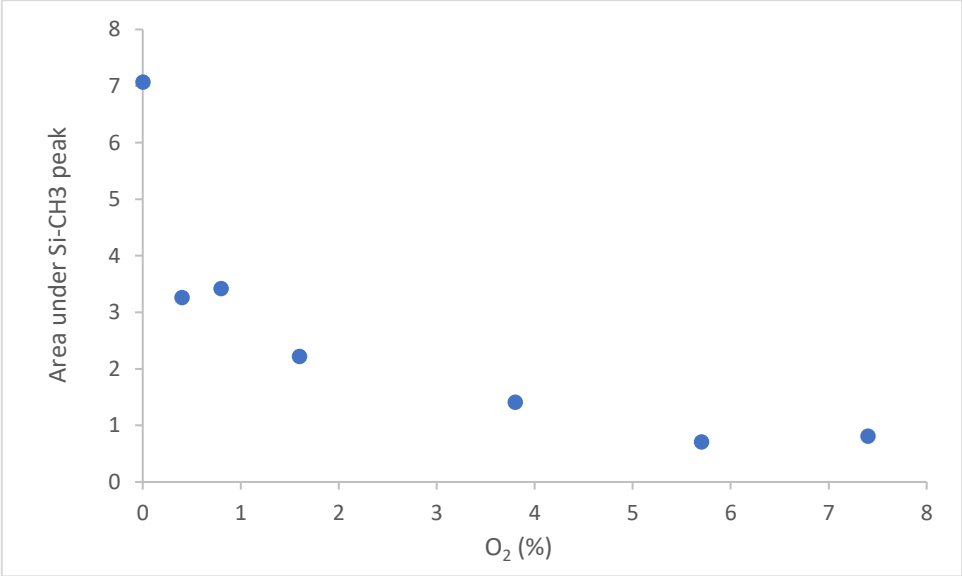

Figure 49. The presentation of surface carbon content variation as a function of increase in oxygen content on each individual coating (static depositions) after integration of the area under peaks corresponding to the Si-CH_3 band, recognised at around 1270 cm^{-1}.

However, there is no considerable decrease of the following transversal optical vibrations of rocking mode (TO1), bending mode (TO2) and stretching mode (TO3) at a constant amount of matter, which is due to it being constrained in the "glassy-like coating" rather than the "polymer-like coating". While not significant, there is a decrease of Si-OH and H_2O bond intensities, which can be correlated to full conversion of silanol groups to silica network when the oxygen flow rate increased, similar to the results obtained after the silica coatings were moderately heat treated in the presence of moisture levels. Comparing the Si-O-Si peaks in seven spectra, there was a considerable increase in the evolution of the right shoulder of the

peak at 1150-1200 cm^{-1} (See Figure 48), corresponding to transversal optical mode 4, TO4, along with the widening of the Si-O-Si peak and a shift to higher wavenumbers. This phenomenon is especially observable after the introduction of 3.8% oxygen, which is a clear indication of the evolution of a silica-like coating with an increased number of defects (pores, non-stoichiometry, or impurities such as C or N) (31). The ATR-FTIR results are in accordance with the literature for the plasma deposition of the HMDSO precursor via atmospheric plasma glow discharge, under a varying oxygen flow rate (0-20%). It is reported that when the oxygen percentage increased, the Si-O-Si peak developed a shoulder spanning from 1100-1200 cm^{-1}, while the $Si(CH_3)_n$ peak at 1260-1280 cm^{-1} and $Si-CH_3$ at 800 cm^{-1} declined concurrently (251).

- ***Dynamically deposited sample analysis***

FTIR analysis was performed on the dynamically deposited sample, in the centre of the gradient coating on the area representing each of the seven deposition conditions (see Figure 50 and Figure 51).

The peaks identified in the spectra at positions along the dynamically deposited coating were identical to those found in the statically deposited coatings. The spectra were interpreted as indicated in the preceding section, and the results on peak behaviour, including differences in peak intensity, location, and area, are comparable to the statically deposited samples. As shown in Figure 52, the variation in the peak area of the $(Si-)CH_3$ bond (at 1270 cm^{-1}) versus the spatial position along the gradient followed a similar declining trend, indicating a decrease in the organic nature of the coating due to the gradual admission of oxygen. Furthermore, based on the evolution of the TO4 bond, as the gradient coating progressed and the glass-like structure evolved, the structural defects increased, and the organic properties of the gradient was decreased.

Despite exhibiting a similar tendency, gradient coating peaks were likely to have slower variations than static deposition. This might have originated from a non-instantaneous variation (a few milli second) caused by the mass flow controller in the programmed plasma jet, resulting in a more gradual transition from one O_2 flow set in one condition to the other condition, which in turn resulted in a more gradual change in the characteristics of the coating. In contrast, because the statically deposited samples were treated individually and after a stable O_2 gas flow, they demonstrated sharp transitions between each condition. Also, when compared to the static condition, the structural defects increased at the gradient coating as the oxygen content increased, although with a slower variation. This can be explained by the decreased concentration of oxygen near the substrate caused by the jet displacement, which also added

nitrogen from the air. As a result, the saturation point was not clearly apparent, as opposed to the considerable saturation state reported for the static condition.

To summarise, Si-CH_3 was chosen as the most relevant peak to study coating behaviours under a slow oxygen intake. This peak showed a gradual variation upon an increase in the oxygen admixture, hence, the variation of this peak represented C/O variation and was used for quantification purposes. A cursory examination of the Si-O-Si peak revealed no continuous variation pattern, making interpretation rather difficult. However, a general comparison indicated two separate surface chemistries for the depositions carried out before and after the introduction of 0.8 percent O_2. Since it reflects the occurrence of fundamental change in the polymer nature, the Si-O-Si peak intensity changes and position shifts were not employed as a direct reference for quantification. The underlying vibrational modes of Si-O-Si obtained after peak deconvolution, TO1, TO2, and TO3, remained stable when oxygen was increased. Nevertheless, fluctuation in the peak shape and intensity of TO4, particularly after the addition of 3.8% oxygen, clearly proved the formation of a silica-like polymer. On the other hand, the decrease in the strength of the Si-OH and H_2O bonds suggested the domination of the Si-O-Si network at a higher oxygen admixture. While both sets of coatings, statically and dynamically formed, showed fairly comparable chemistry variations, the reduction in the Si-CH_3 peak intensity for the statically deposited coatings was sharper compared to the gradient coating. As previously stated, the moving jet and the flow meter's response time during deposition, combination with air during movement, and other factors may have resulted in coatings that were likely a blend of the two deposition conditions. The static depositions, on the other hand, were treated with a stable oxygen flow, thereby representing all characteristics of the applied settings.

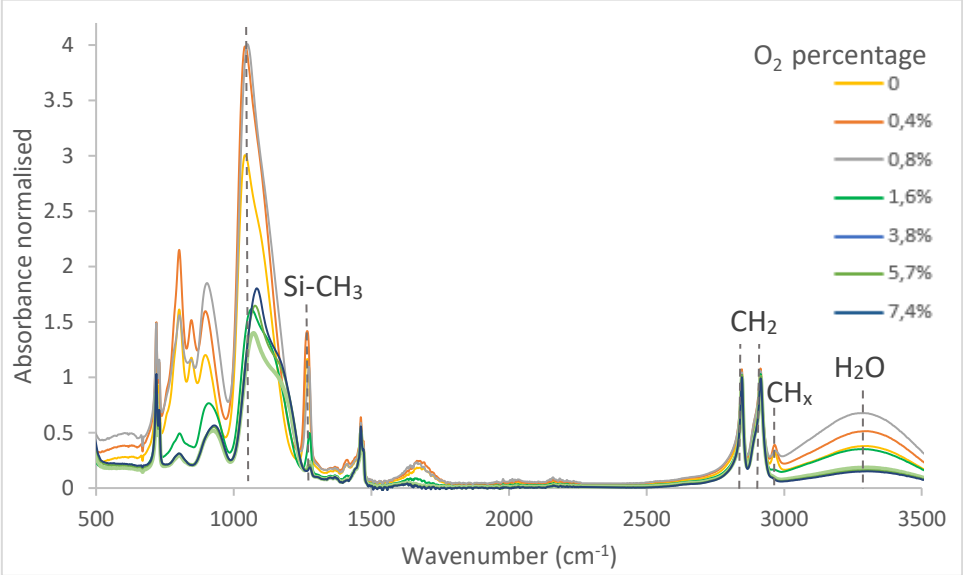

Figure 50. Normalised FTIR spectra for the dynamically deposited HMDSO polymer coating as a function of increase in the O_2 content (0-7.4% O_2) after baseline correction. The scan was performed at the centre of the gradient coating.

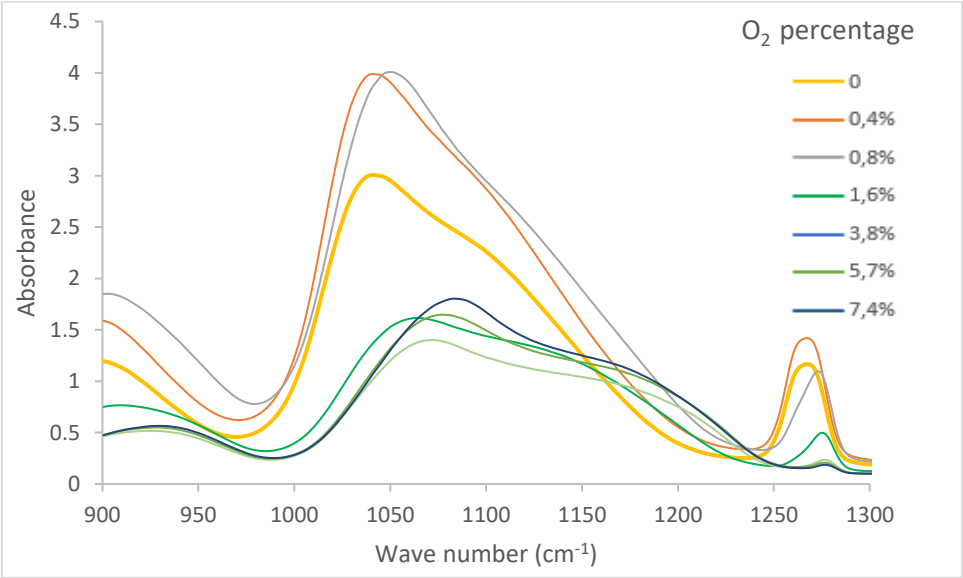

Figure 51. Magnified FTIR spectra of the gradient coating 950-1300 cm^{-1}.

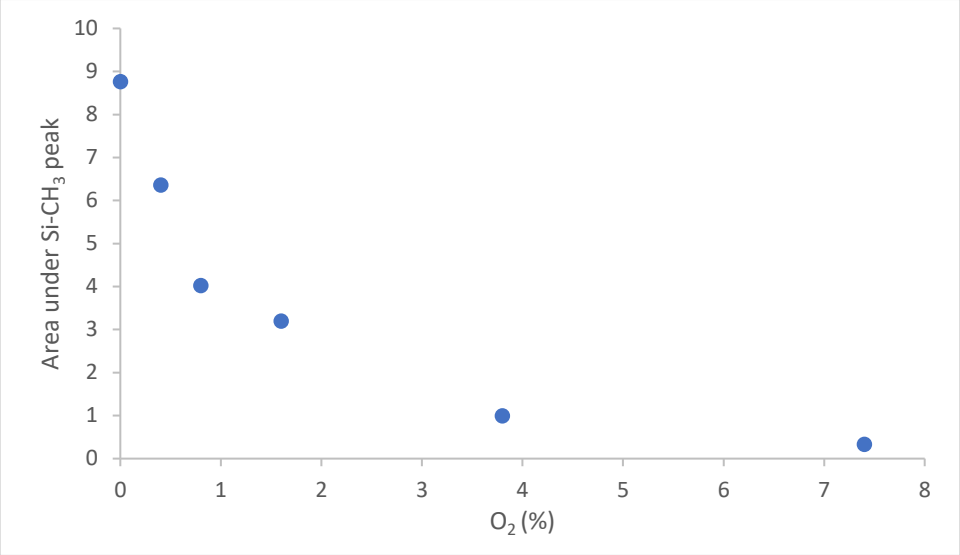

Figure 52. The presentation of surface carbon content variation as a function of increase in oxygen admixture along the gradient coating after integration of the area under peaks corresponding to the Si-CH_3 band, recognised at 1270 cm^{-1}.

3.4.1.2 AFM analysis

- ***Statically deposited samples***

The statically deposited samples were evaluated for surface topography using the AFM tapping mode. We expected to see a trend in the roughness of the surface and the grain size of the surface features upon gradual increase in oxygen content of the plasma. As shown in Figure 53, starting from the coating deposited in the absence of oxygen flow, the surface topography evolved from a smooth surface with slight protuberances to a rough surface with well-defined clusters in the last sample, which was deposited with the maximum oxygen flow rate. This pattern is also obvious in Figure 54, which displays the variation plots of the two surface roughness indicators, the root mean square roughness (R_q) versus oxygen flow rate and roughness factor (r), as a function of oxygen flow rate. Even though the maximum variation was approximately 30 nm in total for R_q with r always remaining below 1.30, the variation trend reflects how the introduction of oxygen affected the coating surface properties. According to the R_q plot, there was an initial quick increase in roughness when oxygen was introduced (phase 1), but once the critical oxygen rate was reached, additional increases in the oxygen rate had no effect on the roughness. This semi-constant situation, shown by a plateau on the curve (phase 2), indicated that fragmentation and film growth had reached a maximum, presumably due to an equilibrium state between polymer cluster development/agglomeration and the etching process. It can be hypothesised that the roughening of the surface and increase in the

grain size were a result of rapid fragmentation of the monomer by increase in reactive oxygen species (ROS) content, followed by the gas-phase formation of polymer cluster aggregates (252). The subsequent deposition of these aggregates on the surface may have led to the formation of larger particles and finally roughening of the surface.

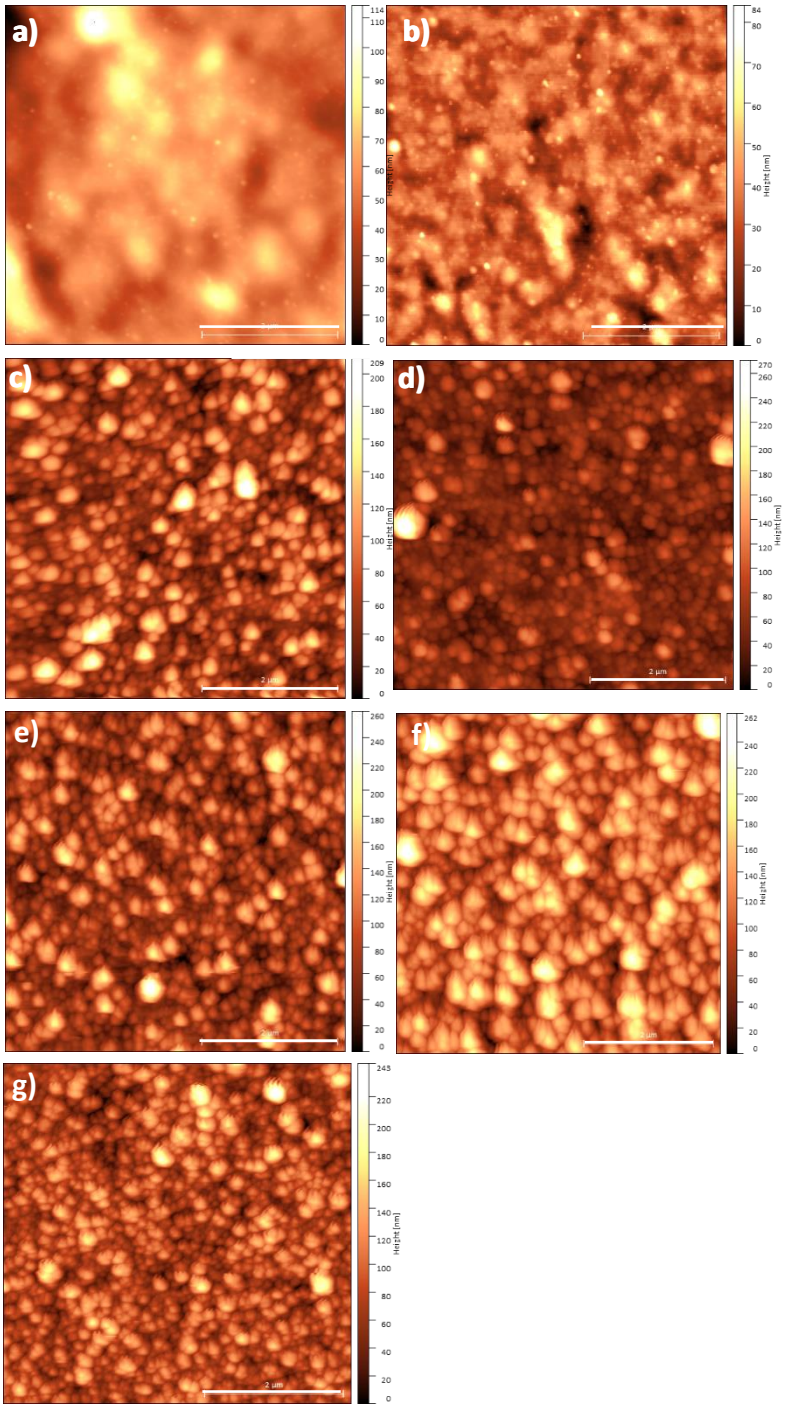

Figure 53. AFM tapping mode micrographs of the HMDSO coatings deposited in static mode as a function of increase in O_2 content. The measurements were taken in the centre of each coating. a) 0% O_2, b) 0.4% O_2, c) 0.8% O_2, d) 1.6% O_2, e) 3.8% O_2, f) 5.7% O_2, g) 7.4% O_2. The micrographs

were obtained after scanning a 5 µm x 5 µm area on each depositions with a 0.7 Hz scan rate. Scale bars correspond to 2µm length along the surface.

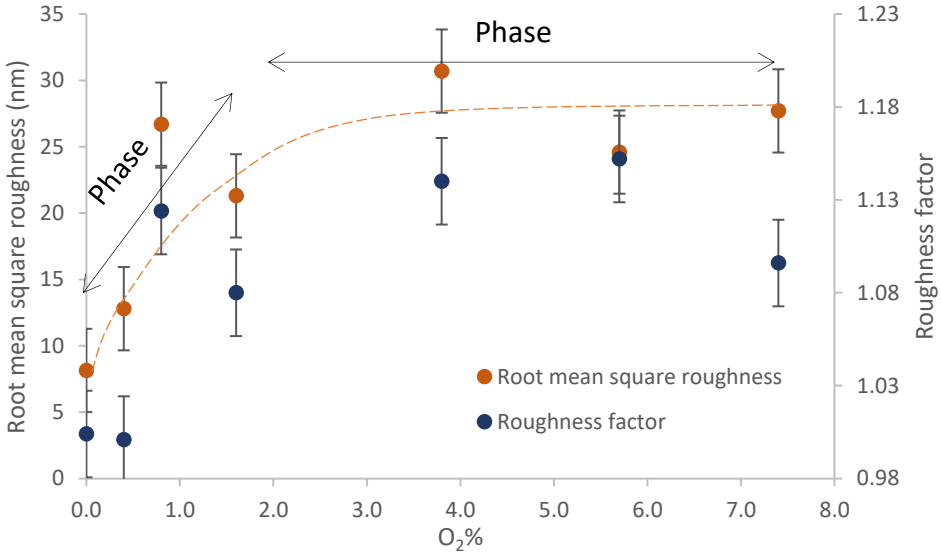

Figure 54. The surface roughness variation for statically deposited HMDSO coatings as a function of increase in oxygen admixture in the plasma gas. The values were obtained from processing AFM micrographs after two scans on each selected region.

- ***Dynamically deposited samples***

AFM was used to characterise the gradient coating deposited with a moving jet at numerous points along the surface coating. By increasing the oxygen flow rate, a tendency comparable to static depositions was seen for gradient coating. Moving from the area where the sample was deposited in the absence of oxygen to the region where it was deposited with 7.4% oxygen, the small perturbations on the surface gradually grew, coalesced, and evolved into well-defined particles during the gradual introduction of oxygen, eventually leading to the rough surface with larger particle grains (see Figure 55).

The roughness variation and the mechanisms involved in the evolution of the coating are presented as separate phases in Figure 56. The evolution trend is similar to the evolution of static depositions, with the exception that, in the gradient coating, three distinct phases can be identified in the plot, representing roughness versus gradient length. Phase 1 was related to the first step of O_2 introduction, when the precursor was only partially decomposed, and grains had just begun to form gradually. When the oxygen flow rate was increased further and the precursor was fully decomposed, larger, well-defined grains were deposited on the surface, leading to the maximum surface roughness value (Phase 2). This rise was visible in the height profiles shown in the Figure 55 at the right panel of each AFM micrograph. The roughness

peak was followed by a decreasing trend, which could be classified as the third phase, observed at higher oxygen rates due to a possible etching effect caused by the over-production of oxygen radicals when the precursor was completely fragmented, and the polymer growth phase was already completed. The roughness variation attained for the gradient coating was 10-70 nm based on the resulting R_q values.

In contrast to the statically deposited coatings, the variation trend found for phase 1, where the precursor started decomposing, was slower for dynamically deposited coatings, with the peak value reaching 70 nm vs 30 nm. In other words, the equilibrium condition (between growth and etching) was reached earlier in static depositions. However, there was a substantial declining trend following the peak value, which was labelled as phase 3 for the gradient coating, indicating that the etching rate surpassed the gas phase growth rate, resulting in a decrease in particle size and R_q values. Aside from gas-phase etching, the grains deposited on the surface could also undergo etching at the highest O_2 flow rate, however, it is expected to be significantly lower than the gas-phase etching, where conditions are severe, and clusters are easily etched. Because the gas phase etching step for static depositions following the peak value was substantially slower, there was no evident descending value of roughness and grain size (semi-constant state).

Based on AFM analyses, the differences observed for the two deposition conditions (static and dynamic) can be attributed to the movement of the plasma jet during deposition, resulting in a different combination of the ROS and the air exposure of the discharge, which explain appearance of larger polymer clusters on the surface and the significant etching rate at a critical oxygen levels for dynamically deposited coating compared to statically deposited coatings. Furthermore, the more gradual variation in phase 1 can be explained by the previously noted delays in response time caused by the flow meter during dynamic deposition, resulting in a slower change of the coating from its organic-inorganic character with a smoother surface topography to an inorganic coating with roughened surface.

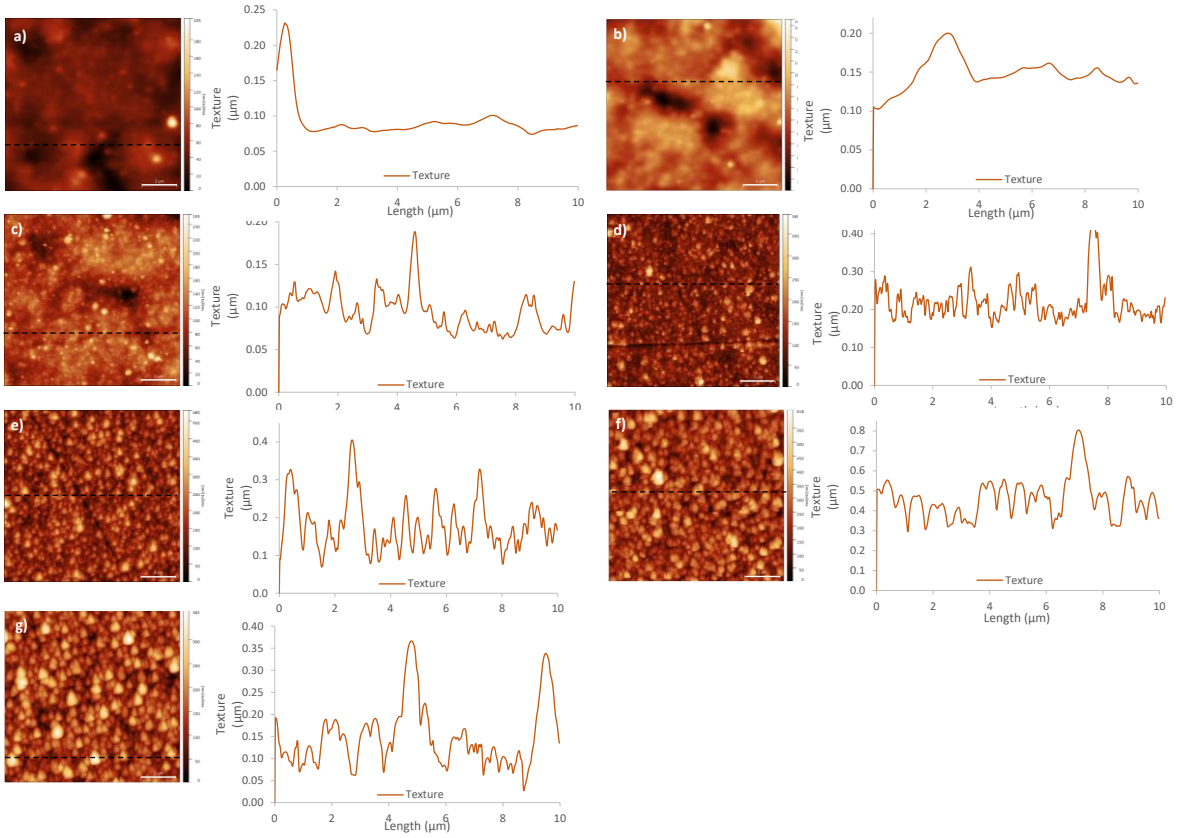

Figure 55. AFM tapping mode micrographs of the dynamically deosited HMDSO plasma polymer coating upon gradual increase in O_2 values (on the left) and the corresponding height profile of each scanned area displayed for a random line drawn over the surface (on the right). a) starting position at 0 mm, deposited without O_2, b) 10 mm distance from the start point deposited with 0.4 % O_2, c) 20 mm distance from the start deposited with 0.8% O_2, d) 52 mm from the start deposited with 1.6% O_2, e) 67 mm distance from the start and deposited 3.8% O_2, f) 97 mm distance from the start deposited with 5.7% O_2 and, g) 125mm away from the start deposited with 7.4% O_2. Scale bars correspond to 2µm length along the surface.

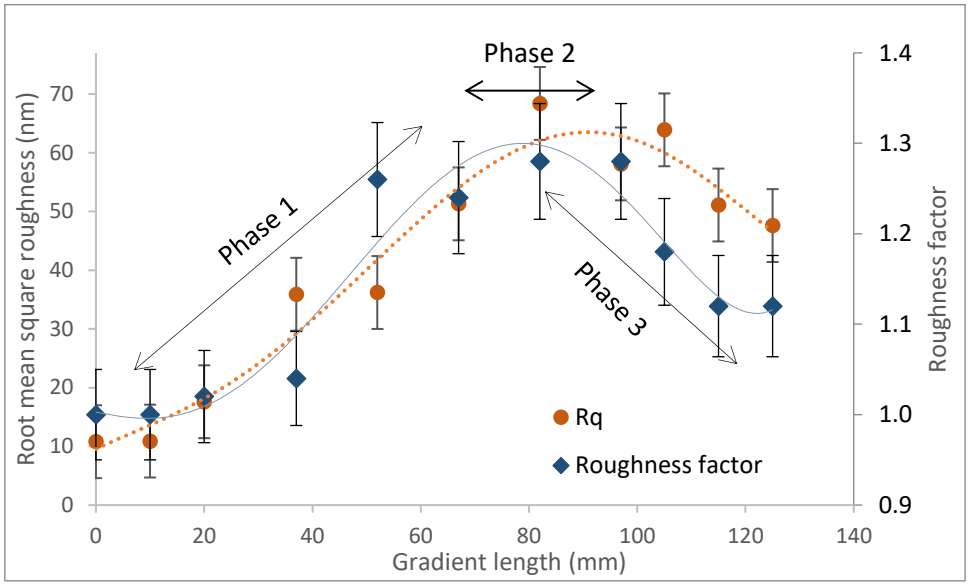

Figure 56. The surface roughness variation along the gradient coating upon gradual introduction of oxygen admixture (0%-7.4%) displayed versus distance on the gradient from the starting point. The values were obtained from processing AFM micrographs after two scans on each selected region.

3.4.2 1-D nitrogen-functional chemistry gradient

3.4.2.1 Elemental analysis with XPS

The elemental analysis of the surface coating was performed using XPS at 18 positions separated by 500 µm along the chemistry gradient containing nitrogen. The scanning was started from the first region, deposited in the absence of ammonia, which was 500 µm away from the edge of the sample. The last scanning point was in region 4, with the maximum ammonia input, located about 900 mm far from the edge.

Figure 57 shows the compilation of the XPS spectra obtained for all the positions, which are expressed as counts per second (cps) versus binding energy (eV). The main identified peaks in the spectra are attributed to C 1s, N1s, O1s, O2s, O KLL, NKLL, of which the three elemental peaks, C 1s, N1s, O1s, were selected for high-resolution scanning to quantify the coating and investigate the surface chemistry. To present the quantification results, the relative elemental concentration (REC) for each investigated element was calculated based on the following equation:

$$REC = \frac{x}{N+C+O} \times 100\%$$

In order to present the variation of the three elemental peaks, four random points, each representative of the corresponding regions, were selected (see Figure 58). The nitrogen and oxygen peak intensities increased in parallel, demonstrated by scanning from the first region with minimum nitrogen to the last region with the highest nitrogen functional groups. However, the carbon peak intensity followed a slightly decreasing trend. This is because carbon content is always abundant in the organic polymer (71.3-92.4%) even for the maximum values of the precursor ratio (NH_3/C_2H_4) that was introduced into the plasma (7/7), as a hydrocarbon backbone is inevitable for the existence of nitrogen functionalities in the polymer coating.

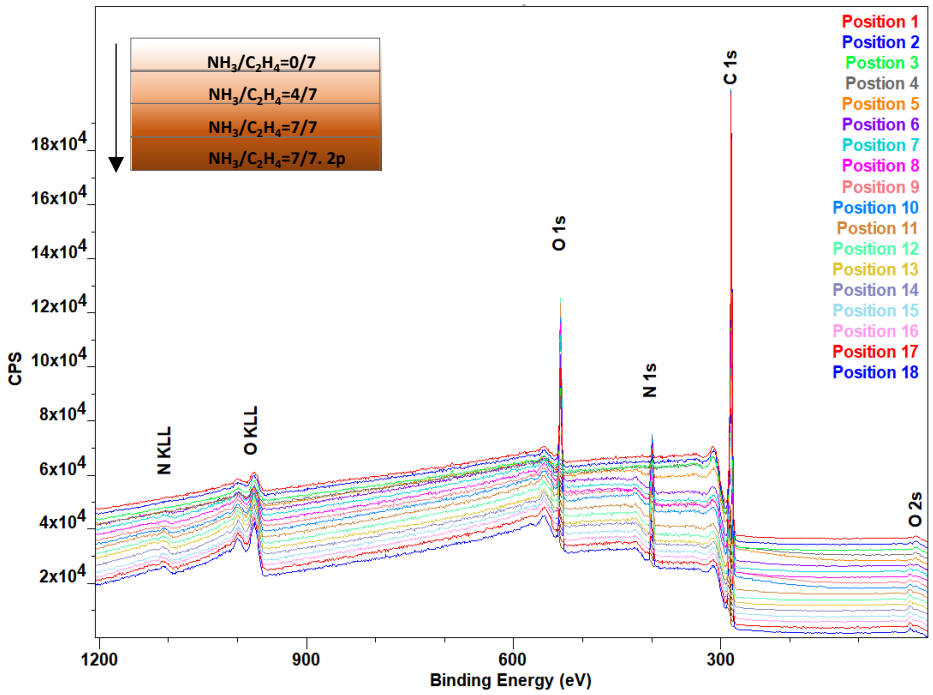

Figure 57. The cumulative XPS spectra of all 18 points scanned along the plasma polymer chemistry gradient. Position 1 corresponds to the point with the lowest nitrogen content (absence of ammonia in the plasma) and position 18 corresponds to the region with maximum ammonia introduction.

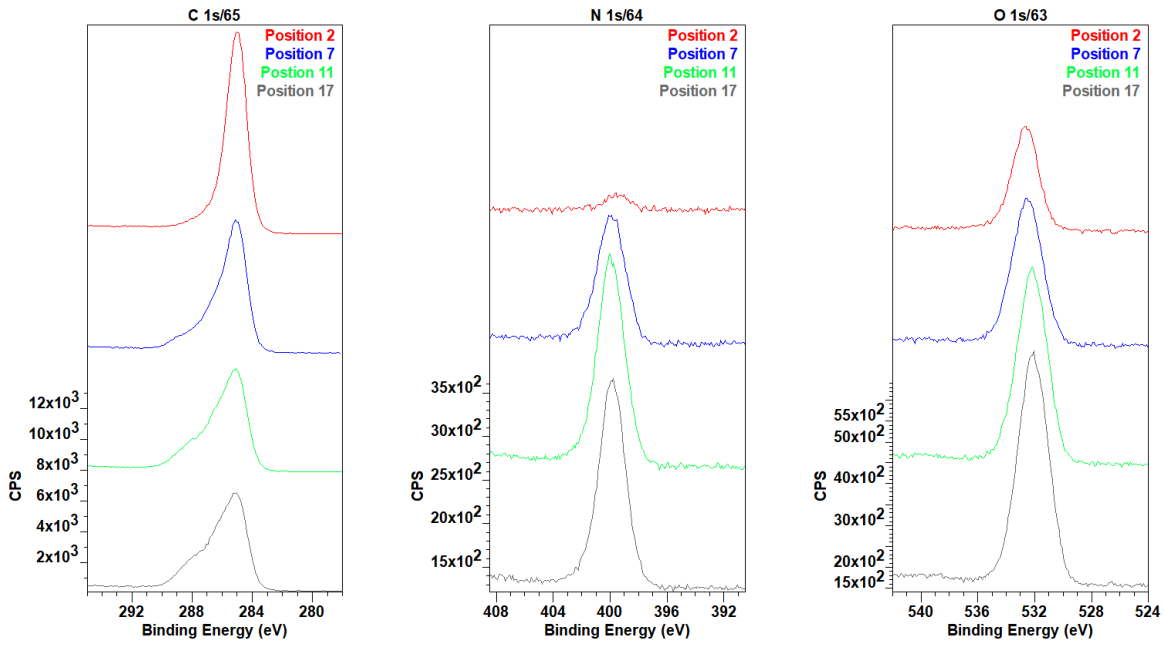

Figure 58. High-resolution XPS peaks obtained for C1s, N1s and O1s, at four points along the plasma polymer gradient, each corresponding to one of the 4 deposition conditions: position 2: NH_3/C_2H_4=0/7, position 7: NH_3/C_2H_4=4/7, position 11: NH_3/C_2H_4=7/7, position 17: NH_3/C_2H_4=7/7, 2P.

A noticeable point in the C1s plot was the gradual evolution of the left shoulder along the gradient (from position 2 to position 17), which is accompanied by further peak widening due to the incorporation of more nitrogen and oxygen in the coatings. Therefore, it was decided to investigate the carbon chemical environment further at each scanned position. The curve fitting applied to C1s proves the emergence of several overlapping curves originating from various carbon bonds with N, O and both, as listed in the respective tables. There are two possible scenarios for C1s deconvolution based on whether or not the C-N functional group is separated from the C-O bond, given that the two bands may overlap in some regions when moving from the hydrocarbon peak, C-(C,H), at 285 eV. The first and second scenarios with corresponding peak attributions are demonstrated in Figure 59 and Figure 60, respectively. This consideration arises from the fact that the two bonds appear in a close region can cause overlap: the C-O shift from C (C-H) is usually 1.5 eV (1.13 eV-1.75 eV), whereas the chemical shift for C-N from C (C-H) is found to vary between 0.56 - 1.41 eV. So, to group the two bonds (1st scenario), 1.4 eV was considered for the curve containing C-O and C-N. However, for the separation of the two bonds (2nd scenario), a shift of 0.7eV for C-N and 1.5 eV shift for C-O was considered.

A) A total of four curves identified with the first attributed to the hydrocarbon peak at 285 eV, the highest in all four regions. However, this follows the gradual decrease in peak

intensity along with the gradual peak widening as the chemical environment of the C1s changes. The first shift from the hydrocarbon bond was set to +1.4 eV so, the second curve was attributed to the grouped C-(O,N) bond appearing at 286.4 eV. As presented in the respective table in Figure 17, an initial sharp increase is evident in the second coating because of it being the first coating deposited in the presence of ammonia in the discharge. However, a further increase in ammonia did not affect this peak as a constant intensity in the last three coatings was observed. While the third curve attributed to the O-C-O/(N)-C=O at 288 eV showed a smoothly increasing trend along the four coatings, the last shift corresponding to the O-C=O bond at 289 eV was negligible in intensity for the first coating and then remained constant in the next three coatings. This peak was assumed to come from the upper layer contaminations of the surface rather than the polymer coating.

The C1s curve fitting results suggested that the initial coating with the high C-(C,H) peak, where the only precursor introduced was ethylene and the main deposited components were a series of stable hydrocarbons, shifted toward the coating with a slight increase of C-O,N functionalities after the introduction of ammonia. This was accompanied by a subsequent decrease in the C-(C,H) peak due to the fragmentation and degradation of the hydrocarbon structures. By further increasing the N and O content in plasma, the continuous decrease in the hydrocarbon peak and formation of more complex functionalities containing N and O was demonstrated. As the O-C-O/(N)-C=O peak followed a gradual increasing trend and since the bond is indicative of the carbamic acid structure and its derivatives, it can be hypothesised that the continuous formation of CO_2, as a result of an increase in oxygen values present in the chamber, favoured the reaction of CO_2 with primary and secondary amino functionalities, leading to the formation of carbamic acid and carbamate groups (253).

B) The C1s deconvolution produced a total of five underlying curves, beginning with the hydrocarbon peak at 285 eV, which was the highest in all four regions, identical to the previous fitting, with a decreasing trend in peak intensity along the four coatings. A second peak at 285.7 eV may be due to a C-N bond signifying a main amine functional group. The curve was broad with a small intensity that was absent in the first coating but developed in the second coating after a slight increasing tendency (nearly constant) in the last coatings. The third moderately intense peak at 286.5 eV was attributable to C=O, imine, and nitrile groups, which were lower in the first coating and rapidly increased in the second coating due to an increase in the NH_3/C_2H_4 ratio which later

remained constant for the last two coatings. The fourth peak at 287.8 eV was assigned to O-C-O and N-C=O groups, and because the peak was observed in higher binding energies, it implied that the degree of oxidation in the polymer was steadily increasing in parallel to the increase in O_2% in discharge. These fragments could have formed in the coating's upper molecular layers, where the coating was exposed and could easily react with air. The final peak, corresponding to O=C=O, occurred at 288.9 eV in the second coating and remained nearly constant over the successive coatings.

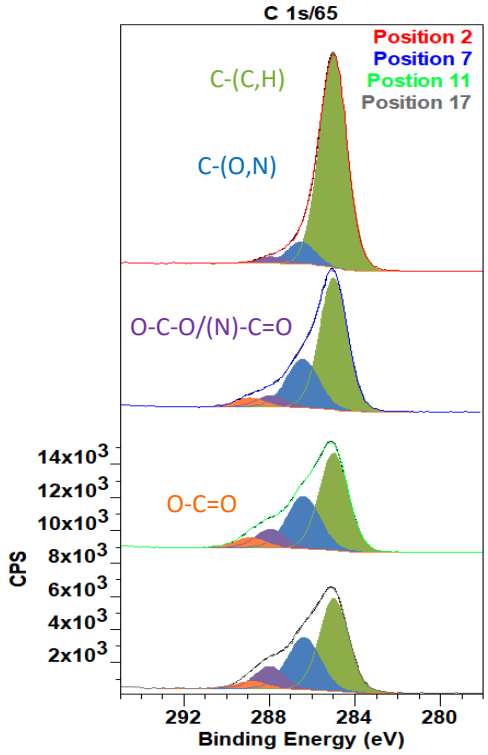

Sample Identifier	C-(C,H) %	C-(O,N) %	O-C-O/(N)-C=O %	O-C=O %
Position 2	88	9	3	<1
Position 7	64	27	5	4
Postion 11	53	32	10	5
Position 17	51	32	12	4

Figure 59. Curve fitting of the high resolution C1s peak at the four positions selected along the gradient corresponding to each deposition condition. The table on the right shows the quantification results in the area under the peaks for the four underlying curves.

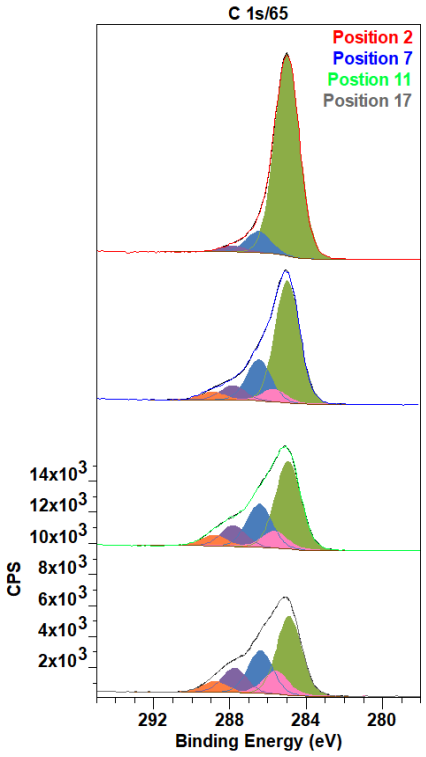

Sample Identifier	C-(C,H) %	C-N %	C-O/C=N, nitrile %	O-C-(O,N)/(N)-C=O %	O-C=O %
Position 2	88		9	3	
Position 7	64	2	22	8	4
Postion 11	52	3	26	12	6
Position 17	48	4	26	15	6

Figure 60. The second curve fitting of the high resolution C1s peak of the four positions selected along the gradient corresponding to each deposition condition. The five underlying curves and the quantifications, in the area under the curves, are presented in the table.

Table 8 is intended to summarise the peak assignments for the C1s fitting for the similar coatings based on literature reports.

Table 8. The four content C1s curve fitting and respective peak assignments obtained from the literature (24, 25).

	Treatment conditions					
Reference	**Power, Pressure**	**Flow ratio**	**C1**	**C2**	**C3**	**C4**
3	20 W, 600 mTorr	0.25-0.75	284.3	C1+0.56	C1+1.54	C1+2.61
4	10 W, 600 mTorr	3	285	C1+0.7	C1+1.7	C1+2.7
			C-C, C=C, C-H	C-N, C-NO2,	C=N, C≡N, C-O-C	C=O, N-C=O, N-C-O

Figure 61 presents the average nitrogen percentage of the points scanned on each distinct coating obtained from the N1s peak quantification. The quantification results for the first coating showed minimal nitrogen content of 0.8-1.4%, which can be explained by the contaminations of the coating with atmospheric nitrogen. The same applies for the presence of oxygen, in even higher percentages (6.7-17.2%) compared to the nitrogen, all along the

gradient coating. As can be seen in Figure 61 (blue columns), the transition between the first and the second coating was extremely sharp, implying that immediately after ammonia introduction, nitrogen was incorporated into the polymerisation process. The next transition, from the second to the third coating, was also sharp as expected due to a 1.75-fold increase in the ammonia flow rate in the plasma. Despite applying two-fold plasma pressure, an unanticipated slight drop in N% content in the final coating was observed. The purpose of raising pressure with a constant ratio and power input was to reduce the average energy input per molecule while maintaining top layer functionality by minimising fragmentation. However, the outcome suggested that manipulating pressure might have caused changes in the mechanism of polymerisation rather than increasing the incorporation of nitrogen in the coating. Therefore, the reverse trend in nitrogen content was observed. This indicates that the chemistry of the coating was altered in coating 4 when compared to the prior two coatings containing N. Because the gradient generation was not performed dynamically and continuously, and because each coating was deposited after the chamber was opened and the mask was replaced, oxygen incorporation appeared to be unavoidable.

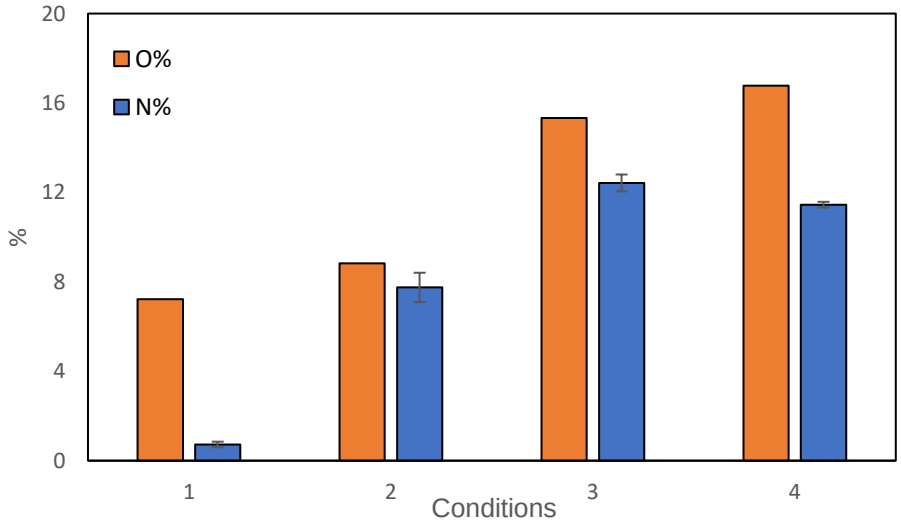

Figure 61. The average nitrogen and oxygen content evolution on gradient coatings obtained from XPS high-resolution spectra.

In conclusion, the quantification of primary amines in this work was based on C1s because N1s did not provide enough resolution to perform curve-fitting, which would normally otherwise provide much more direct quantification data. On the other hand, some investigations in the

literature have reported the chemical derivatisation of the surface with a molecule binding specifically to a primary amine (e.g., 4-trifluoromethylbenzaldehyde (TFBA)) (245, 254). However, due to less control over the reaction, this approach was not preferred for primary amine quantification after a trial experiment. Based on C1s deconvolution, the second scenario for peak assignments and the carbon environment interpretation was considered due to good consistency with previous studies in the literature. Because of its instability and conversion to various forms of nitrogen functional groups, the curve fitting revealed a reduced presence of primary amine in all coatings (maximum 4%). Instead, imine, nitrile, and carbonyl groups were shown to be the most abundant, particularly in the last two coatings deposited with the highest ammonia ratio, indicating that the majority of the nitrogen content is present in the form of these unsaturated groups. The following groups had a higher proportion of oxygen heteroatoms, i.e., O-C-O, N-C=O, which resulted directly from polymer oxidation with a progressively varying trend parallel to the increase of the ammonia during the deposition process (and nitrogen content in the coating). This verifies the prior observation of the higher oxidation susceptibility of coatings containing nitrogen. Finally, traces of the carboxylic acid functional group were detected, most likely resulting from postdeposition processes such as humidity uptake during storage.

3.4.2.2 Surface imaging with TOF-SIMS

- ***Gradient sample deposited with a mask***

TOF-SIMS was used to characterise the surface chemistry of the chemical gradient created in order to obtain molecular information regarding the deposited polymer. To avoid contaminations, samples were kept inside argon bags prior to analysis and were handled with the appropriate gloves (i.e., polyethylene and not nitrile to avoid silicone traces from nitrile gloves). When evaluating the TOF-SIMS data for the gradient coating, the general variation in the intensity of the fragments, as well as the direction of the variation, was considered. Several aliphatic hydrocarbon fragments (e.g., $C_xH_y^+$) and fragments containing nitrogen (e.g., $C_xH_yN_z^+$) were observed in the positive scan mode, as summarised in Table 9 with the accompanying micrographs presenting their intensity over the four deposited coatings. Similarly, Table 10 summarises a number of significant peaks obtained from the negative scan mode.

While it would have been desirable to compare the elemental quantification, the results obtained by XPS, and the molecular qualitative results obtained by TOF-SIMS micrographs to interpret the surface chemistry variation, due to the fundamental differences between the two

techniques the quantitative intensity variation trend of those nitrogen-containing characteristic fragments was not expected to follow the total N% variation from XPS. A visual comparison of the fragment intensities, on the other hand, was supposed to give a direction for understanding TOF-SIMS results. Because all of the identified fragments in TOF-SIMS resulted from fragmentation and potential recombination (or multi-recombination) during the analysis process, rather than being directly generated from surface sample, the interpretations were handled with care.

Among the identified fragments, the most straightforward fragments (with fewer fragmentations and dissociations), which were expected to be formed from direct interaction of ethylene and ammonia were $C_nH_{2n+2}N$ such as $C_2H_6N^+$ followed by CH_4N^+ after the cleavage of the β bond. TOF-SIMS analytical results confirmed that the variation trend for these fragments was closer to the trend observed from XPS quantifications among the rest of the identified fragments. As shown in Table (4), the intensity variation shown in the CH_4N^+ image indicates the gradual surface primary amine density/number evolution. The other fragment that presented a similar trend with CH_4N^+ was the next positive fragments of $CH_3N_2^+$ containing nitrogen, which clearly resulted from multiple fragmentations and recombination. For more fragmented and recombined ions, it is generally possible to see the similar trends (or not) due to the kinetics clues, which makes the trend unpredictable. Similarly, considering the negative ions, the contrast between the four gradient coatings observed for CHN_2^- (m/z 41) reminded us of the variation of the N% from XPS quantification.

While $C_{17}H_{38}NO_2^+$ showed the same trend with the abovementioned fragments, the origin of the fragment did not seem to be plasma-deposited coating (or secondary ions), as plasma polymerisation often yields crosslinked coatings with a shorter hydrocarbon length. Therefore, it seemed more likely that contaminations occurring during a deposition or transportation step might have led to the formation of this fragment. Among fragments containing nitrogen, ammonium ions (NH_4^+) showed an intensity gradient over four coatings as can be seen in Table 9. This fragment might have resulted from the dissociation of a primary amine or the protonation of ammonia. The other prominent fragment containing nitrogen identified was cyanide (CN^-), which showed an intense peak, suggesting that this fragment was likely saturated over all three final coatings, with a relatively lower intensity in the first coating. This fragment will not be discussed further as a potential characteristic fragment because it is typically abundant in saturation amounts in all plasma-polymerised coatings containing. Also, CNO^- showed an intensity similar to CN^-, albeit with a lower intensity; thus, the source of this

fragment was expected to be the same as CN^-. The next identified $C_xN_y^-$ fragment was C_3N^-, with a different variation trend compared to N% from XPS, as the intensity observed in coatings 3 and 4 was lower than in coating 2.

After considering the potential nitrogen-functional characteristic fragments aiming to confirm the gradient, the carbon evolution along the gradient also had to be tracked. The interpretations of hydrocarbon fragments require even more attention as the origin of the hydrocarbon fragments could be more ambiguous due to carbon residues from the TOF-SIMS instrument, which can easily appear on the spectrum. Considering negative-mode fragments, the C_4H^- micrograph (see Table 10. Negative mode TOF-SIMS images obtained on a 10×9 mm area along the gradient coating.) indicated a gradient that was well-defined in intensity, in opposition to the direction of the formation of compounds containing nitrogen, thus making this fragment a possible indicator of gradual ethylene precursor consumption by increasing in ammonia in discharge. On the other hand, the intensity images of two hydrocarbons, $C_4H_7^+$ and $C_2H_5^+$ with odd m/z values of 55 and 29, respectively, indicated a similar variation trend but the opposite of the intensity variation observed for $C4H^-$ fragment. Despite their high intensity, these fragments could not be conveniently used to draw a conclusion due to their unknown origin. Finally, the presence of OH^- fragments throughout the examined area may be attributable to the effect of humidity and water absorption during storage. The presence of more of this fragment in nitrogen-rich regions reflects the stronger interaction of water with groups containing nitrogen.

Table 9. Positive mode TOF-SIMS images of secondary ion species obtained on a 10×10 mm area along the gradient coating.

Ion	Structure	Micrograph
Na^+		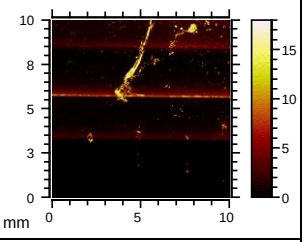
CH_4N^+	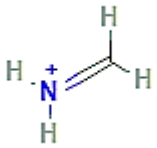	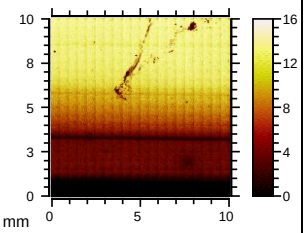
$CH_5N_2^+$	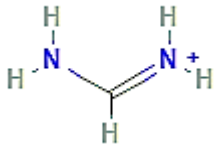	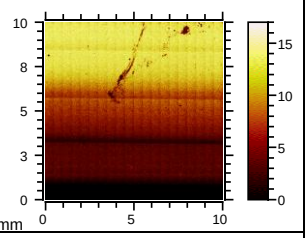
$C_4H_7^+$	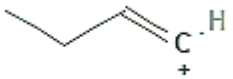	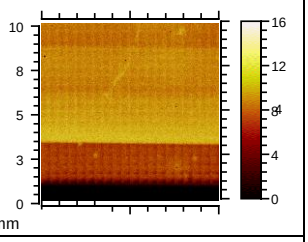
NH_4^+		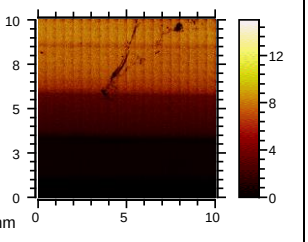
$C_2H_5^+$	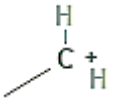	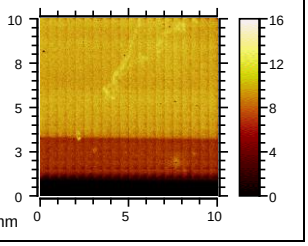

$C_3H_8NO^+$	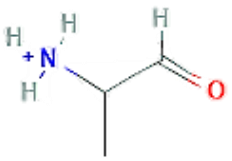	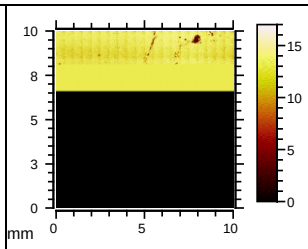
$C_{17}H_{38}NO_2^+$	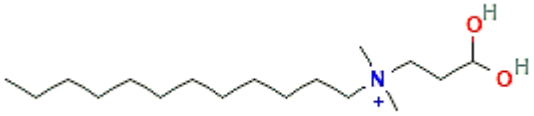	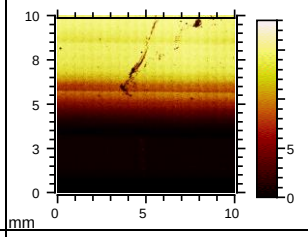
$CH_3N_2^+$	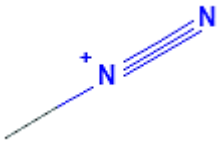	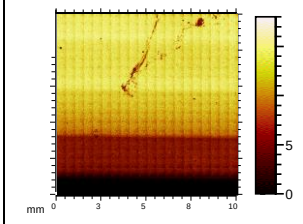
$C_2H_3^+$		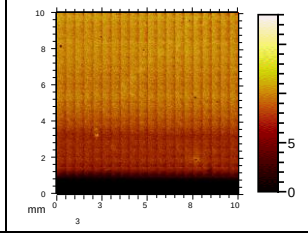

Table 10. Negative mode TOF-SIMS images obtained on a 10×9 mm area along the gradient coating.

Ion	Structure	Micrograph
NH_2^-		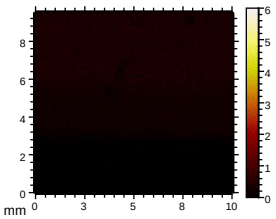
OH^-		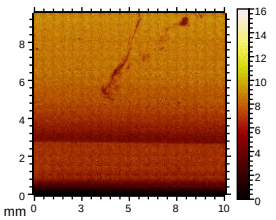

C_3N^-	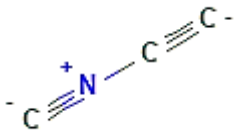	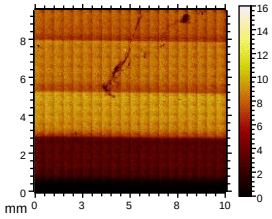
CN^-		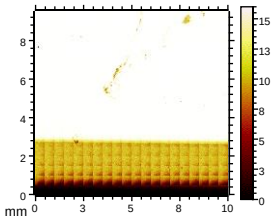
CNO^-	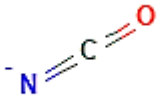	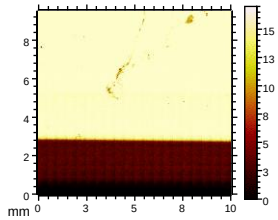
C_4H^-	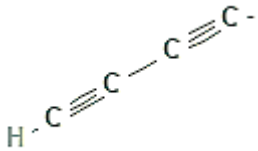	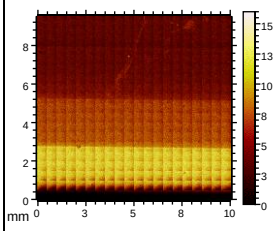
CHN_2^-	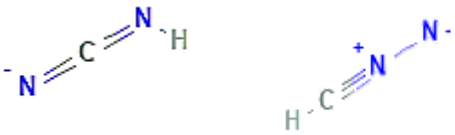	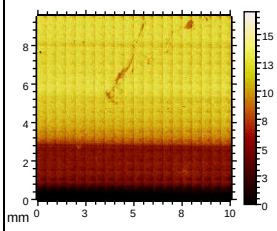

The surface topography of all nitrogen-rich coatings obtained, that is both reference samples and the gradient, remained almost unchanged, revealing a smooth surface with an average roughness value (R_q) of 0.2nm. As a result, roughness discussions and associated AFM pictures are not presented in a separate section.

3.4.3 Properties of chemistry gradients

3.4.3.1 Wettability properties of 1-D chemistry gradient containing oxygen

- ***Statically deposited samples***

Surface wettability studies reflect the topography and chemistry of the uppermost layer of the surface. Because of its vast range of applications in material science and biomedicine, surface wetting is a significant surface property that serves as the focal point for many surface engineering initiatives. Surface wettability can be altered by changing the surface chemical and/or texture. According to reports (255), the wettability of organosilicons is determined by the surface hydrocarbon content and surface roughness factors. The direct impact of O_2 gas introduction on the enhancement of surface hydrophilicity during the plasma polymerisation of HMDSO has been reported. This effect is due to reactive oxygen molecules, which, when present in the gas-phase, enhance the in-flight reaction rate, leading to rapid precursor fragmentation, the removal of the methyl groups and a decrease in the organic character of the deposited coatings (256, 257).

The wettability of the statically deposited coatings was characterised with sessile drops in the middle of the coating. Figure 62 presents the measured surface wettability variation of the coatings versus oxygen flow rate in the plasma. The results demonstrated an overall decrease in WCA (or increase in the water wettability) of the coatings by increasing oxygen in the argon discharge. This decrease is in compliance with the reduction of the organic features of the coating as a result of the fragmentation and substitution of methyl groups with the polar groups containing oxygen. The observed wettability variation was mostly due to the change in chemistry from the first highly organic PDMS-like coating to the inorganic silica-like coating in the last sample. Additionally, the surface roughness and morphology might have contributed to a further increase in the wettability of the coating down to complete wetting (WCA=0°) by increasing the oxygen content. The maximum WCA value for the hydrophobic initial layer coated with 0% O_2 was roughly 97°, which was consistent with the 100° value recorded for ordinary bulk PDMS with a flat surface (258). However, the full wetting surface (WCA=0°) obtained for the maximum oxygen rate (7.4%) in silica-like chemistry was much lower than the reported value for the amorphous smooth silica surfaces (40-50°) (259). This superhydrophilicity behaviour appeared to be independent of the surface roughness increase because the roughness factor variation never exceeded 1.3, which suggests that it could not have drastically affected the wettability, as explained in (260). As a result, the existence of more silanol hydrophilic groups in this silica-like coating, with the associated peak emerging

at 950 cm^{-1} (see Figure 47) is the likely cause of this unexpected superhydrophilic character. The lengthy plasma exposure under the most oxidant conditions probably have led to the presence of silanols and this exceptionally high wettability of the SiO_2 films. Also, the evidence of microstructural defects possibly formed after etching in the gas phase and surface phase suggests that the precursor exposure to the most oxidant conditions might have led to the post-deposition reactions of the coating after being exposed to atmosphere humidity. Similarly, lower WCA are observed on the edge of the plasma coatings, as evident in the corresponding curves (Figure 62, yellow plot), because more reactive species are typically formed in the interface region due to heterogeneities in the discharge or gas stream, resulting in defect sites (e.g., strained SiO_2 bonds) susceptible to silanol production once exposed to air.

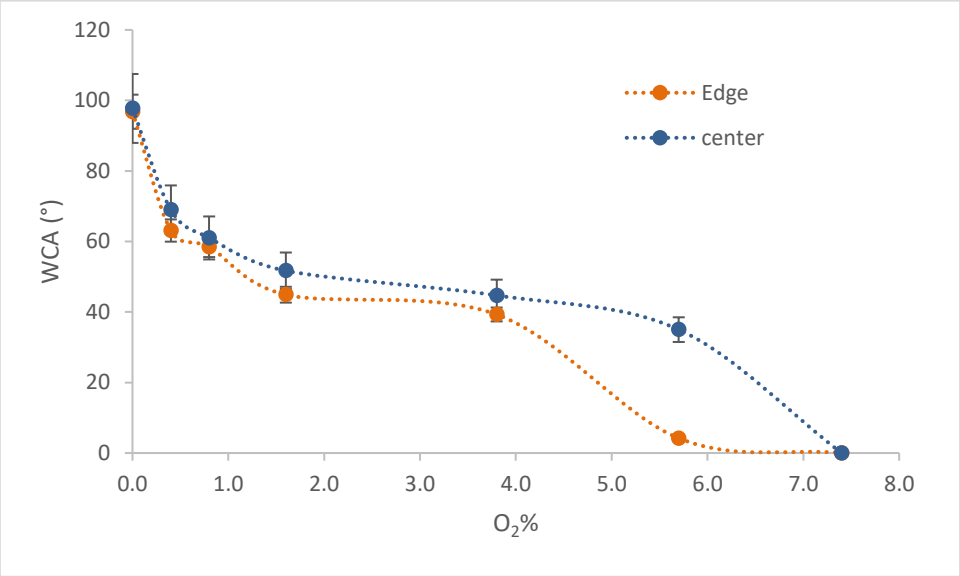

Figure 62. Water contact angle analysis results for the coatings deposited statically. The measuremets were performed at the centre and on the border of the coatings and plotted as a function of O_2 content in the discharge.

- ***Dynamically deposited coating (chemistry gradient)***

The gradient coating was characterised after deposition with sessile drops at several points in the centre of the coating. The wettability variation plotted versus oxygen flow rate can be seen in Figure 63. When compared to static depositions, the wettability evolution showed a comparable pattern, confirming the successful formation of the wettability gradient along the coating. Starting with the highly hydrophobic organic coating (109°) formed in the absence of oxygen, the evolution may be separated into three distinct phases. A sharp decline was observed in the beginning as soon as oxygen was introduced, which continued to decline up to

0.8% of the O_2 admixture due to a rapid change in the CH_x content of the coating (phase 1), followed by a steady state for the intermediate O_2 flow rate introduction ranging from 0.8% to 3.8%, similar to the trend observed in static depositions (phase 2).This state suggests the complete fragmentation of the precursor, the maximum elimination of CH_x groups and the highest presence of Si-O-Si bonds. Upon further increase in the oxygen rate, a second sharp decreasing trend was observed (phase 3). This significant decrease in WCA is related to the surface chemistry and increase in the quantity of hydrophilic functional groups, rather than a change in the surface roughness, as explained in the preceding section. This is most likely due to a change in chemical composition, as evidenced by the FTIR spectra (i.e., the existence of hydrophilic groups such as silanol and OH, as well as the development of the TO4 bond) and the occurrence of local microstructural defects in the coatings. However, the situation is less remarkable for the gradient than for static depositions, since dynamic deposition is accompanied by the mixing of the ambient air with plasma jet and a delay in the response time of the flow meter, resulting in a lower concentration of the reactive Oxygen content due to mixture with air and comparatively less hydrophilic coating.

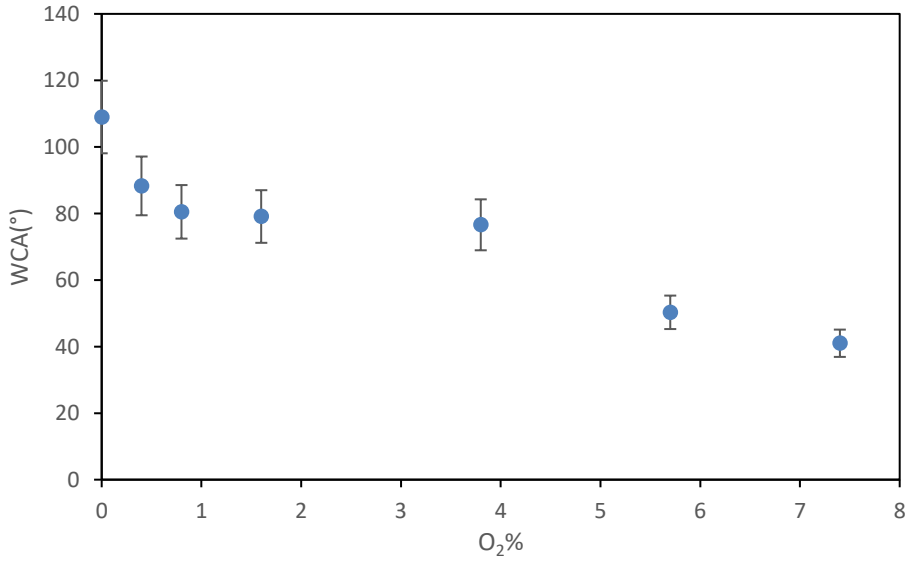

Figure 63. Water contact angle analysis results for the gradient coating measured at the centre of the coating as a function of O_2 content in the discharge.

In conclusion, the chemistry of the coating, rather than surface topography, dictated the WCA values of the surface. Overall, the wettability variation trend for both sets of coatings was very similar, and the only meaningful difference between WCAs of static and dynamic deposition

was observed in the most oxidative deposition conditions, where the highest concentration of oxygen led to polymer etching and post reaction with humidity during static composition.

3.4.3.2 Wettability properties of 1-D chemistry gradient containing nitrogen

3.4.3.2.1 Static and dynamic contact angle analysis on the homogenous reference samples

The four homogenous plasma polymer coatings containing nitrogen, each representing a condition in a chemistry gradient, were prepared and characterised by static and dynamic contact angle measurements. Since considerable differences were noted for the wettability behaviours of the chemistry gradient and its homogenous representative coatings, the fabrication methodology of the homogenous coatings was modified to ensure the same chemistry. As a result, the homogeneous coatings were treated as gradient coatings employing the masking apparatus but without the need for a top cover (including slits). The purpose behind this was to maintain the same distance between the silicon substrate and the bottom electrode, which was thought to alter the coating qualities. The objective for conducting dynamic wettability tests on homogeneous samples was to use the larger surface area to quantify dynamic contact angles using the droplet volume variation approach, which would otherwise be impossible to apply on gradient coatings with a width of 2.5 mm. The results for static and dynamic water contact angle measurements on each of the four nitrogen-rich plasma depositions are shown in Figure 64 and Figure 65 respectively.

The static measurements were performed with a droplet volume of 0.3 µl to make them comparable with the chemistry gradients, which were also characterised with the same droplet volume. The dynamic angle measurements with an increasing/decreasing droplet volume, on the other hand, were accomplished with an initial volume of 2 µl.

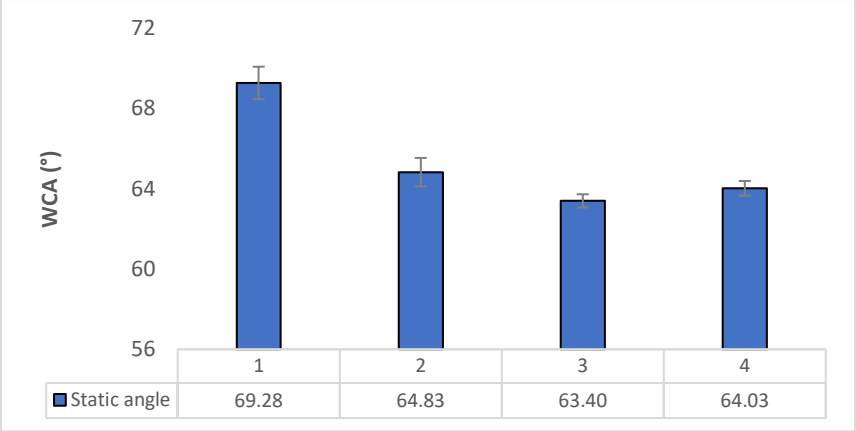

Figure 64. The results for static contact angle measurements on homogenous samples with 0.3 µl droplet. The reported contact angles were obtained on average 3-4 scanned points on each sample.

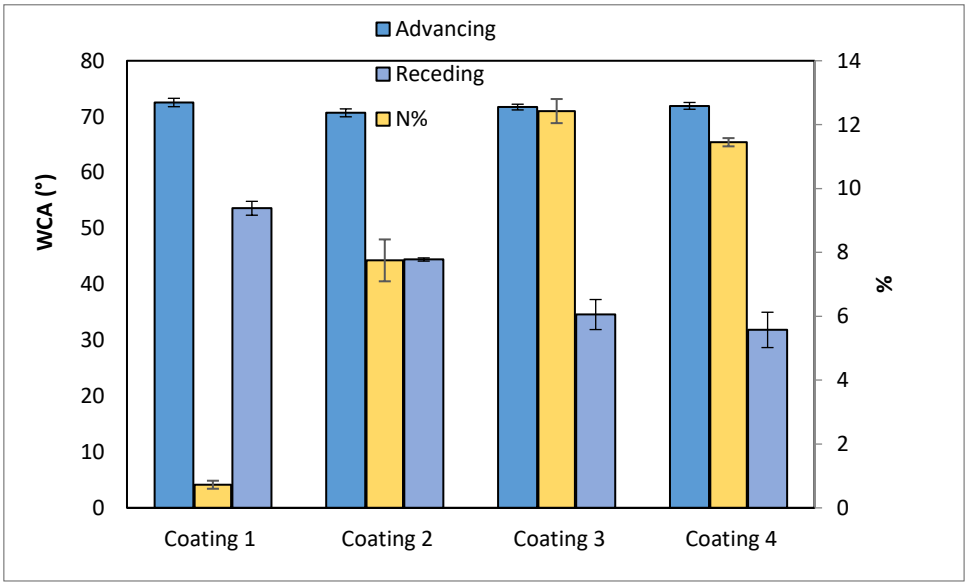

Figure 65. Dynamic contact angle measurements were carried out on each homogenous sample with an initial 2 µl droplet with slow volume variation (0.03 µl/second) for 100 s and 120 s duration for advancing and receding angles, respectively.

The static contact angles measured were overall indicators of a slightly hydrophilic surface (< 75°) with a variation of a few degrees. Here, the surface energy was also mainly guided by the C_xH_y bonds, which always consisted of more than 85% of the bonds present at the surface. An amplitude of WCA variation of 7-8° was induced by increasing the N content from 1 to 11 at. %, as well as an unintended oxygen increase from 7.23-16.8 at.%. The three ammonia-

deposited coatings (coatings 2-4) demonstrated identical WCA values, however, the WCA values observed on coatings 2 and 3 were marginally larger than those reported by Hegemann et al. (106) for the relevant coatings deposited under identical conditions, which were recorded after deposition (the same day). The values were ~54° vs 64° for coating 3 and~57° vs 64° for coating 2, and were measured using static sessile drop method via 2 μl water droplets. The discrepancies in the reported results could be ascribed to droplet size and duration of storage prior to wettability measurements, as they showed in their study that WCAs rose progressively up to roughly 60° when stored in the air for several days.

The dynamic contact angle measurements reflect surface imperfections, such as hysteresis or the difference between advancing and retreating contact angles. Because of the low surface roughness (0.2 nm R_q) in the present samples examined and since the main predicted source of hysteresis is a surface that is not smooth, stiff or uniform enough (261), it was required to look for the reasons other than surface topography.

A substantial discrepancy between the advancing and receding angles (Figure 65) implies strong hysteresis, which, considering the low surface roughness, can only be explained by the surface's chemical heterogeneity. It has been established that chemical heterogeneity deriving from molecule-size domains may influence hysteresis even at the nanoscale (262). Practically constant values of advancing angles along the gradient and the steadily decreasing receding angles were observed, which can disclose information about the film properties. During preliminary observations using the tilted dynamic angle method, it was noted that the water droplet tended to attach itself strongly to the surface on all coatings containing nitrogen even when big droplet volumes of 20 μl were employed, making it challenging to record the sliding angle for this the method. Therefore, the observed hysteresis might be attributed to the surface's sticky nature and chemical heterogeneity. This adhesive aspect of the coating could be due to the incorporation of significant amounts of O_2 in addition to nitrogen in the coating, which increased the probability of hydrogen bond formation between the coating and the droplet.

Comparing the dynamic WCA values from the current study and the similar work reported by Vandenbossche et al. (247), a good compatibility between the receding WCAs for coatings 2 and 3 with the receding angles reported in the literature for the same coatings deposited under identical conditions is realised. The receding WCAs for the coating equal to coating 2 was 44° (vs 44° for coating 2), and 36° for the coating equal to coating 3 (vs 35° for coating 3). However, the advancing angles were lower than those reported in the current study for the same

coatings deposited under identical power and flow rate ratio conditions, i.e., 72° vs 60° for coating 3 and 71° vs 66° for coating 2.

The measured static contact angles and advancing angle reflected the same pattern, but with somewhat different magnitudes. The minor dissimilarity between the advancing and static angles was expected, as static angles were measured a few seconds after the droplet made contact with the surface, and thus, unlike the advancing angle, it did not reflect the contact angle recorded upon the droplet's initial contact with the fresh dry surface (263). On the other hand, for dynamic angle measurement, the measured receding contact angles were overall lower than the advancing ones, which is typical since receding angles are recorded after advancing measurements and they present values obtained from the already wetted surface (droplet was slowly collected from the surface). During the advancing angle measurements, a small water droplet was initially placed on a neutral unwetted amine-functional coating, which is less hydrophilic than the protonated form, then the droplet volume was gradually increased through dispensing, and after 100 seconds of interaction with the droplet, the exposed surface rendered a protonated and positively charged surface in the exposed region. Therefore, receding angle results reflected a hydrophilic surface with contact angles as low as 32° (in the region with higher nitrogen and oxygen content). The decreasing trend in receding WCAs may then be correlated to the increase of N% values and O% over the four coatings. The total variation in receding angles was 22°, which is considerable and meaningful, since this variation is aligned with the formation of the chemistry gradient.

3.4.3.2.2 Static contact angle analysis on the gradient coating

The gradient coating was characterised using two different droplet volumes of 1 µl and 0.3 µl, which we believed fit better within each coating and avoided the interfaces where thickness and chemistry possibly varied. because the reason for this was that when the droplet spreads, it may come into contact with the narrow interfacial region of the two neighbouring coatings, where there is a shallow groove, potentially tilting the droplet. The results of two WCA measurements performed on the chemistry gradient are presented in Figure 66. Based on the observations, it is possible to infer that, while an acceptable wettability variation was attained, the surface WCA values for all deposition conditions remained below 90°. The wettability variation of 33° to 78° was observed when a smaller droplet was used, and there was an overall decreasing trend for both sets of observations upon the incorporation of more polar groups, i.e., O and N, in the coating along the gradient direction.

The wettability values generally followed the XPS quantification results obtained for polar group content except for coating 2, which showed a slightly higher WCA than coating 1. Since topography was expected to remain largely smooth, the chemistry was assumed to rule the surface wettability gradient.

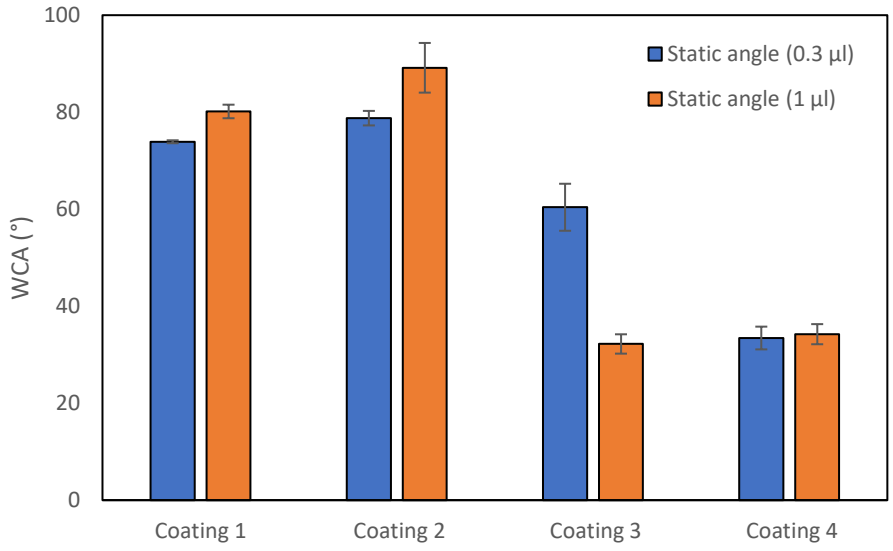

Figure 66. Wettability values obtained for each coating along the gradient using droplets of 0.3 µl and 1 µl volume. Each presented bar graph is the average of four measurements performed on each region. The WCAs were taken with 0.5 mm intervals along the 20 mm sample length.

To summarise, static angle measurements on the gradient reference samples using smaller droplets (0.3 µl) revealed an overall variance of 46°, indicating a variation in wettability. The second coating demonstrated a higher hydrophobicity of static WCA than coating 1, which cannot be explained by chemistry because there are more polar groups in coating 2 compared to coating 1, suggesting that some local surface heterogeneity may be the source of this unexpected increase in WCA value. Later, there was a sharper increase rate in the wettability of the surface from coating 3 to coating 4 (16 °). The WCA of ~80° measured with a 1 µl droplet for coating 1 is in accordance with the value reported in the literature (264) for a plasma polymer deposited with ethylene precursor at varying treatment times and characterised with a water droplet of 1-3 µl.

In contrast to the relatively high wettability variation (41°) recorded for the gradient sample coated with a mask, the static WCA variation for the homogeneous coatings (deposited without

a mask) was only 6°. This considerable difference may be attributable to deposition circumstances, which may have influenced the thickness and/or chemistry of the coatings formed using two different pathways, despite efforts to keep deposition conditions equal. As previously stated, all samples were handled inside the masking device (the sample holder) to maintain the same distance between the electrode and the chip for both the homogeneous and gradient depositions. One possibility is that during the homogeneous sample processing, when treatment within the plasma chamber was completed, the chamber was opened, and samples were moved to sample holders and an argon bag until analysis. However, during the treatment of the gradient samples, the chamber had to be completely opened three times in order to displace the mask for the next coating, and despite argon purging, air and humidity were engaged in the process, resulting in more hydrophilic coatings than for the homogeneous samples. This is especially true since the order of plasma treatment went from the most nitrogen-rich coating to the least nitrogen-rich coating. This implies that the nitrogen-rich coating, which has the highest potential to oxidise, was exposed to air three times, but the coating with the lowest nitrogen-functional group was exposed to oxygen/moisture less frequently.

3.5 Conclusion

The 1-D surface chemistry gradients discussed here are based on two separate plasma processes and are meant to demonstrate the benefits and drawbacks of each methodology for generating gradually changing surface functional groups. Regardless of the substrate, each approach may be used to deposit any chosen mix of monomer/precursor and non-polymerisable gas. While both plasma-polymerised techniques put forward are similar, the second plasma approach with low-pressure plasma is preferred when the end application criteria of homogeneity, reduced thickness, and repeatability are the main focus. This is because the low-pressure deposition with homogenous discharge offers good control over plasma deposition conditions, a better film homogeneity, and lower attainable thickness. However, if the key desired criteria of the study are high throughput, quick deposition, maskless surface patterning, and low cost, the first plasma jet technique based on atmospheric pressure corona jet may be preferential. Furthermore, the selectivity of the targeted functional group (e.g., NH_2 vs the rest of N-functional groups) is a criterion considered when choosing between the two techniques.

The first method for polymerising HMDSO with a varying oxygen gas flow rate developed a continuous gradient with a wide variation in surface chemistry, beginning with a polymer coating with the greatest similarity to the starting precursor (HMDSO) with the highest carbon

content, and ending with a coating with a silica-like character and the lowest carbon content with a WCA variation of 109°- 41°. The gradient was deposited along approx. 10 cm of polyethylene foil using a moving jet that could travel along the appropriate axis prior to deposition. While the width of the deposited coating is restricted by the discharge dimension (a few cm), it is also appropriate for deposition on very large surfaces, such as a whole silicon wafer, by performing numerous parallel runs. The smallest achievable increment of the coating (about 1 mm) during dynamic deposition is restricted by the response speed of the apparatus while changing from one deposition condition to the other. As the oxygen flow rate increases, the surface roughness increases, and the surface properties become more reliant on the plasma parameters. Because the discharge is created in the open air, this method is more prone to contamination during the deposition stage; however, the contamination is somewhat controlled by employing a shielding gas, such as N_2.

The second gradient, on the other hand, was deposited on diced silicon chips under vacuum conditions using a capacitively coupled plasma with a variable ammonia to ethylene flow rate. A masking device was used to delineate narrow regions for static deposition. Each treated region was 2.5 mmx20 mm in size, and the mask was expected to be as near to the surface as possible to avoid diffusion from under the mask to neighbouring surfaces. Over the four coatings, an N% range of 0.7%-11.45% and a WCA variation of roughly 79° down to 33° were achieved. The advantages of homogeneous discharge include better homogeneity and smoother surface, lower thickness, isolated process and more repeatable conditions. However, the shortcoming of the second approach, the nitrogen-functional gradient, was the limit for the incorporation of the nitrogen inside the coating due to the nature of the employed precursors, such as ammonia. It has already been reported that the higher rates of ammonia lead to the chemical and physical etching effect inside the discharge and on the surface, causing a decrease in the deposition rate (coating thickness) rather than further incorporation of nitrogen inside the coating (175). The wettability variation scale of the surface, along the gradient, was lower than the HMDSO/O_2 gradient due to the higher presence of carbon in the coating even within the one with the highest N% (corresponding to an average of 72% carbon). This was in contrast with the first approach where the HMDSO/O_2 gradient could be extended up to the point where all the carbon groups were substituted with oxygen, yielding a silica-like coating (glass-like coating). The other shortcoming addressed by Vandenbossche et al. (247) and applied in the current study was the improvement of the stability of the coatings with higher nitrogen group

concentration in water by developing bilayers with a highly crosslinked supporting bottom layer.

3.6 Perspectives and potential applications of the chemistry gradients

The application of nitrogen and oxygen-functional coatings for biomedical applications is emphasised. The N-functional gradient with thin bilayer structure developed (total 25 nm) with the specific advantage of good durability in water could be utilised to investigate the crucial N% necessary for promoting cell adhesion. Nonetheless, N% window of the present approach might be examined further and expanded to be relevant to a greater number of cells and cell growth settings. This is particularly interesting as there have been several previous attempts in this field using plasma polymers developed with NH_3 or N_2/ethylene precursors searching for the critical N% which triggered the adhesion of a specific cell type. For instance, the coating deposited with low pressure plasma using NH_3/C_2H_4 (0.75-1.5) yielded coatings with 200 nm thickness and a nitrogen content of 16-31%, which showed a critical N% of 16% against U937 monocytes cells to initiate surface adhesion (105, 265). However, while this critical N% corresponding to NH_3 /ethylene =0.75 presented satisfactory stability in milli Q water after 24 hours of incubation (less than 10% in loss of the coating thickness), a larger N%, which could result in better adherence, suffered from lower stability in water (30-70% loss in thickness) (266). This highlights the necessity of the stability and function of the coatings along with all attempts to increase primary amine selectivity in the coating. Therefore, future attempts will investigate the methods of fabricating an amine-functional plasma coating to increase the nitrogen content up to 30-40% while maintaining stability for bio-interface applications.

Similarly, plasma-polymerised HMDSO/O_2 offers the possibility of tuning the surface wettability from a full hydrophobic (106° in the absence of O_2) to a superhydrophilic surface. It has been reported that surface wettability is responsible for cell adhesion through the interaction of cell adhesion promoting glycoproteins (e.g. albumin and fibronectin) with the material surface and the cellular response arising from this interaction (267). The interaction of albumin and fibronectin on multiple individually deposited plasma-polymerised HMDSO surfaces with varying chemistry is not efficient and complicates this study. The interactions of each individual protein in separate form, in competitive form, and later, in the interaction of mouse osteoblastic cells (MC3T3-E1) demonstrated an increase in cell adhesion by increasing surface wettability. These findings were consistent with those obtained for fibronectin but contradicted the preferential adherence of albumin to hydrophobic surfaces (268). Similar experiments have been performed for tissue engineering employing HMDSO/O_2 with varying

deposition times and electrical factors, i.e. voltage, which demonstrated the affinity of NIH-3T3 (mouse embryonic fibroblast) cells to silica-like surfaces with higher polar functions (269). These highlight potential applications for optimising the process using a plasma-polymerised HMDSO/O_2 functional gradient coating for protein or cell-surface interactions, whether adhesion is desired (as in tissue engineering studies) or for cell/protein repellence (as in antifouling coatings). The oxygen-functional gradient developed in the framework of this thesis, with a wide range of surface chemistry variation (organic/inorganic, functional polar groups, surface charge, etc.) and wettability variation spanning from hydrophobic to hydrophilic, is indeed a potent candidate for bio-interface optimisation. Aside from the abovementioned applications in the biomedical field, the HMDSO/O_2 plasma-polymerised gradient could be considered an efficient solution wherever optimisation of the desired surface properties is required, e.g. wettability of the microfluidic chips (270), icephobic properties of the coatings (271), and anti-O_2 permeability properties for food packaging (272). The surface variables could also be further extended and improved to cover larger variations.

Additionally, the fabricated plasma-polymerised gradients proposed in this work could be used as a template to generate a second type of functional gradient, for example, the electrostatic immobilisation of the charged nanoparticles and covalent binding of peptides or proteins (273).

Chapter 4: Unidirectional stochastic and periodical topography gradients

4.1 Introduction

Advancements in material interface nanoengineering enable the outcome of surface reactions to be modulated and monitored. Performing the large number of trials required to establish correlations between nanostructure and biological outcome has proven challenging. The cost of fabricating surface structures at the nanoscale, as well as of considering the numerous experimental aspects that influence the outcome, make these studies prohibitively expensive. The nanostructure gradients, providing control over the nanostructure size, shape, density, and periodicity, are a significant step forward in this approach. While a variety of strategies have been demonstrated to generate nanostructures and their gradients (see chapter 1, 1.5.2), the utilisation of nanoparticle self-assembly is particularly interesting. Various nano- and micro-roughness gradients fabricated on the basis of self-assembled colloidal particles are discussed in chapter 1 (see Table 3). The simplicity of altering nanoparticle size, shape, material type, and chemical composition to benefit from nanoparticle assemblies has positioned this technique as a suitable interface nanoengineering technique. We offer a novel method for creating nanostructure gradients based on the self-assembly of gold nanoparticles along the functionalised surface. The gradient formation takes advantage of the time dependency of nanoparticle adsorption to the surface functional groups/domains to create spatial spread in the density of nanoparticles along the surface. In conjunction with the selection of surface coatings, we demonstrate the development of both stochastic and periodic nanoparticle arrangements. The well-established nanoparticle synthesis approach offers the possibility of obtaining colloidal nanoparticles with narrow standard deviation in geometric variables (diameter, sphericity, etc.) which ensures repeatability and is the primary step in controlling surface nanofeatures. Surface nanoparticle gradients are formed based on the adsorption of the synthesised nanoparticles from the colloidal suspension to the solid templated platform (274, 275). Several surface nanoparticle gradient fabrication approaches have been reported to date, such as diffusion-controlled transport with polymer melts (276), attraction of anionic nanoparticles to cationic molecular gradients (141, 152, 153) and kinetic-controlled nanoparticle deposition by dip-coating approach (139, 147). The geometric properties of the nanoparticle gradient (e.g., the size and slope) are reported to be readily tuned via the controlling of the kinetic processes using dip-coating approaches. The dimension of the gradients developed via dip-coaters is however restricted to the process conditions, as the size

of the dip-coater dictates the maximum dimension of the sample and the applicable immersion/withdrawal rate.

We report here for the first time the possibility of tuning the density and size of the nanostructure gradients using a single versatile setup that allows unidirectional gradients to be developed with either stochastic or periodic arrangements. The proposed setup offers a volumetric flow rate that can compete with linear speed achievable with conventional commercial dip coaters. The process is based on controlling the adsorption/growth kinetics of nanoparticles on various surface chemistries (homogenous and patterned templates) in order to fabricate three different classes of nanoparticle gradients: nanoparticle density gradient per area, nanoparticle density gradient per cluster and nanoparticle size gradient.

4.2 Fabrication of Nanostructure Gradients

4.2.1 Setup

Prior knowledge of the surface density of the adsorbate as a function of the exposure time allows the process parameters to be designed rationally. The duration of surface exposure to the adsorbate that leads to surface saturation can be obtained with real-time analysis techniques, e.g. surface plasmon resonance (SPR) or Quartz Crystal Microbalance (QCM). In this work, QCM was preferred for investigating adsorption kinetics since the optical characteristics of the adsorbate do not hinder the transduction. Even though the mass flow of the adsorbate onto the functional layer of the chip during dynamic gradient fabrication results in adsorption isotherms that are not identical to those obtained from the static QCM experiment due to the differences in configurations, the QCM study nevertheless provides a useful indication before conducting the main experiment. Hence, the resultant gradient would be the equivalent of an adsorption isotherm taken from QCM extending across the length of the chip, showing all the adsorbate densities versus exposure time until the saturation state. All experimental processes, from the rational design to the experimental setup used for gradient fabrication are illustrated in Figure 22. The intended gradient length and time of saturation, and the rate at which the height of the chip is exposed to nanoparticle suspension/precursor can be controlled by establishing a specific volumetric flow rate (f) for introducing the adsorbate into an experimental vessel with an appropriate cross-section (cylindrical glass tube with radius r was selected in this work). The design requirements for converting the temporal aspects of processes acquired from QCM measurements into spatial properties of the final gradient are detailed below:

- The time (t) that allows the surface saturation (N) of nanoparticles or adsorbate, which is obtained from QCM measurements

-The volumetric flow rate corresponding to the rate by which the solution rise inside the experimental vessel having the desired gradient length (L) and the saturation time (t) and placing them into equation 2.1. to achieve a gradient of density from minimum up to N.

$$f = \pi r^2 L t \tag{2.1}$$

$$t - t_l = t - \frac{l}{\frac{L}{t}} \tag{2.2}$$

$$\boldsymbol{l = L - \left(\frac{L}{t}\right) t_l} \tag{2.3}$$

The method was demonstrated to be applicable for fabricating two different classes of well-controlled topography gradients: (a) nanoparticle density/number gradient (b) nanoparticle size gradient by using three different types of functional layers, i.e., two homogenous molecular templates and a nanopatterned copolymer template.

Each functional surface was used as a platform to fabricate nanoparticle density gradient and represents a different class of surface chemistry with complementary advantages. The objective was to evaluate the applicability of the developed experimental setup, which translates exposure time-control to the spatial control of the surface immobilised nanoparticles. For this, the following surface functionalisation pathways were used: a) vapour-phase deposited self-assembled monolayer of well-known primary amino-functional silane with a thickness of 1.7 nm (277), b) a plasma polymerised CHN thin bilayer film of approx. 20 nm with optimised stability in aqueous media, and c) a template 2D arrangement of micellar block copolymers.

The density gradients reported here are expected to follow random sequential adsorption which applies to the strong electrostatic interaction of the adsorbate and the surface. The size gradient was also generated based on random sequential adsorption rules however through the in-situ growth of nanoparticles as a result of electrostatic attraction and insertion of the gold chloride anions inside the micellar structures with positively charged core followed by subsequent ion exchange processes.

The surface characteristics of all the fabricated gradients were compared in order to study the effect of different functional layers on gradient development.

4.2.2 Fabrication of nanoparticle gradients with a stochastic arrangement of nanoparticles

For both homogenously functionalised surfaces, a stochastic arrangement of nanoparticles was expected with no considerable aggregations due to repulsion between the charged particles. The expected arrangement was in contrast with the templated or patterned surfaces (block copolymer) on which, an ordered arrangement of particles on confined charged features was envisioned. An upper limit of the surface coverage to 54.7% is predicted in theory for colloidal assemblies on the surface resulting from random sequential adsorption (RSA) (278). In literature, 10-15% (citation) surface coverage is often reported for APTES and similar monolayers while, for non-electrostatic depositions of nanoparticles, (e.g., spin coating, dry casting, etc.) higher particle coverage could be envisaged.

The major defining factor for the surface coverage is the density of positively charged functional groups, for instance, primary amine-functionalised SAMs are expected to have higher density of amine groups, hence higher density of positively charged domains, compared to amino-functional plasma coatings. However, the porosity and swelling in an aqueous media in polymeric thin films (hydrophilic polymers) might produce a 3D structure and greatly improve the adsorption of nanoparticles on the surface compared to 2D SAMs, resulting in closer interparticle separation and therefore higher particle density. When the volume of nanoparticle dispersion is increased upwards in the vertical direction along the functionalised surface, the capillary action of polymeric surfaces during gradient experiments may attract higher density of adsorbed nanoparticles on the surface. Therefore, while it is expected that all classes of charged surfaces and any oppositely charged nanoparticles attain surface coverage with adsorbed particles, the rate of surface saturation, maximum possible density, and interparticle separation may differ for each surface depending on the chemistry of the surface as well as film properties.

4.2.2.1 Nanoparticle density gradients on amine self-assembled monolayers

To perform the gradient experiment, chips were prepared by applying a monolayer of APTES as a functional layer on silicon and glass substrates via the vapour phase deposition method described in chapter 2 (2.1.3.2). The synthesis of citrate-capped gold nanoparticle suspension was explained in detail in chapter 2 (2.1.3.1).

To draw the initial outline of the gradient experiment, the kinetics of gold nanoparticle adsorption to the APTES surface were monitored using QCM-D. For this, the silicon oxide

functionalised QCM sensor chips were subjected to APTES vapours to form the functional layer as previously implemented on silicon and glass chips. Then, to determine the kinetics of adsorption, QCM chips were incubated with ~ 11.80 nm citrate stabilised gold nanoparticles under static conditions. The adsorption isotherms recorded in the QCM experiment enabled an approximation of the saturation time (2.5 hours in this specific case), corresponding to the total time required to prepare gradient samples (see Figure 67). In the final step, the gradient experiment was carried out by placing the APTES-functionalised chips vertically inside a glass cylinder with a diameter of 7 mm. The chosen length of the gradient was 15 mm of the total 20 mm chip length. The constant flow rate of 15.4 L/min, obtained from Eq. 2.1, was set to the microfluidic pump to introduce nanoparticle suspension into the experimental vessel. Once the fluid (nanoparticle suspension) started filling the experimental vessel, the meniscus gradually travelled upwards, advancing across the chip. Since the bottom edge of the chip remained in contact with the fluid for the whole duration of the experiment (time of saturation), this region occupied the maximum number of nanoparticles and was defined as the zero point of the gradient. On the other hand, the opposite end of the gradient coating (set as 15mm), where the surface was exposed least to the fluid was expected to show the minimum density of particles.

The SEM image acquisition was started from the point zero where the chip was incubated with colloidal dispersion for the longest duration and was carried out along the whole coating at certain intervals (see Figure 68a). Image analysis was implemented on the SEM micrographs using ImageJ software and the number of the particles counted on each micrograph was plotted versus time of incubation and the corresponding position along the gradient, as shown in Figure 68b. Meanwhile, the Langmuir-Hill function (red line) was fitted to the experimental plot to compare the expected evolution of nanoparticle density and those obtained from the SEM images. The experimental curve indicated a systematic non-linear increase of nanoparticle densities versus exposure durations (or the corresponding position on gradient). Additionally, the observed trend corresponded well with behaviour expected from the theoretical adsorption isotherm. The nanoparticle density was found to be 1780 NPs/μm^2 for 150 minutes of the incubation time. Based on the random sequential adsorption (RSA) theory, the maximum adsorbate densities, or the jamming limit, that can be obtained on a surface is a surface coverage of 54.7% (279). By considering the current particle size, the maximum theoretical coverage after applying this percentage is 4938 NPs/μm^2. However, based on the experimental data, the density obtained at the time of saturation was 33% of the RSA value or 18% of the APTES-functionalised surface coverage. Hence, compared to the expected coverage, rather slower

kinetics of nanoparticle adsorption onto the APTES surface during the gradient experiment were observed.

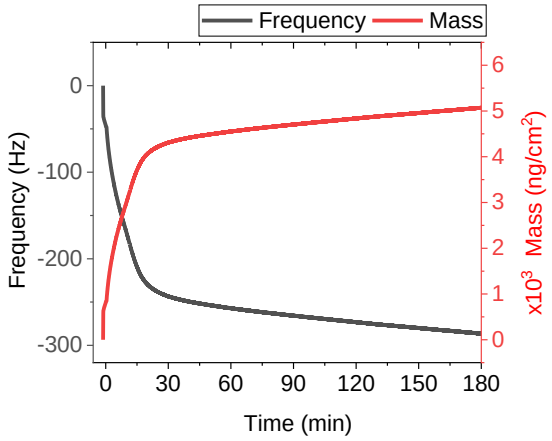

Figure 67. QCM-D kinetic curve recorded in-situ during a nanoparticle- APTES-functionalised surface interaction. The black curve indicates crystal frequency variation upon mass uptake and the red curve indicates mass variation as a function of time obtained from the first curve.

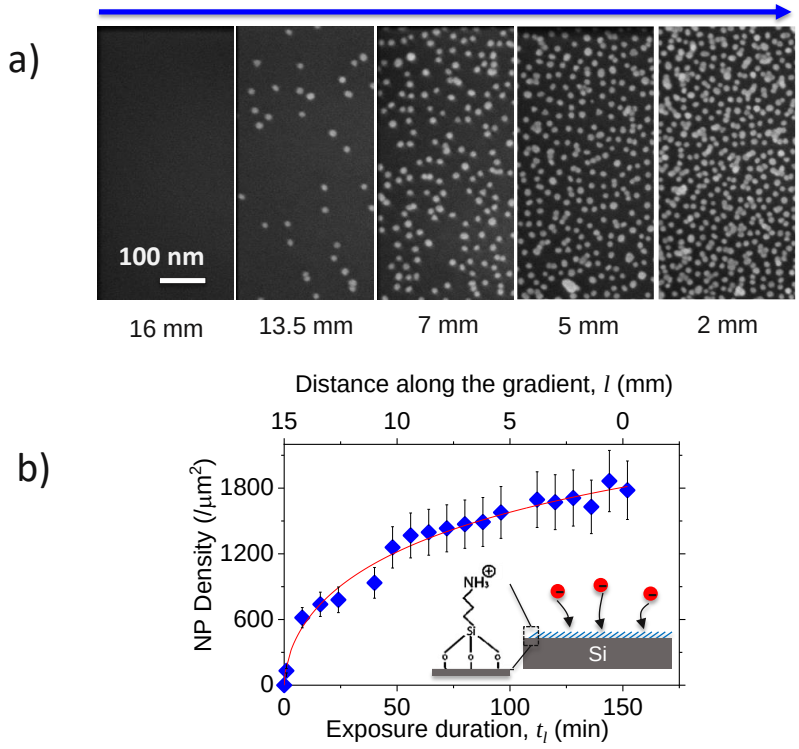

Figure 68. 1-D gradient in AuNPs densities on the APTES-functionalised surface (a) FESEM images showing a gradual increase in density of gold NP versus distance along the gradient for 2, 5, 7, 13.5, and 16 mm from the nanoparticle-dense edge of the coating, (b) The surface NP density variation as a function of distance (top-X axis) and corresponding time of incubation with nanoparticle dispersion (bottom-X axis). The red curve indicates theoretical fir based on Langmuir-Hill isotherm.

On the other hand, the higher density of particles, 2737 NPs/μm^2, was observed after the static interaction of particles with the APTES surface during the QCM experiment for the same incubation time. The difference in density between the gradient and QCM experiments arises from the difference in the experimental configuration between them. It is assumed that the diffusion-limited transport is responsible for the lower nanoparticle density recorded on the gradient surface after the dynamic experiment (280).

4.2.2.2 Nanoparticle density gradients on a plasma-deposited CHN layer

A similar procedure was repeated for the fabrication of nanoparticle density gradient on the CHN functional layer. The CHN plasma polymer layer was deposited with a total thickness of 20 nm using low-pressure CCP plasma as described in chapter 2 (2.1.3.2). Briefly, the deposition was performed by generating an initial crosslinked hydrocarbon-rich base layer and then deposing a thinner functional nitrogen-rich top layer. The bilayer structure of the thin film obtained by the plasma deposition was intended to increase the stability of the surface amine functional groups in aqueous media. The base layer, with approximately 18 nm, acted as a support to the upper layer with 2 nm thickness. Compared to the conventional single layer with the same structure as the top coating, considerably less film degradation and amine functional group loss was observed in the optimised bilayer surface as the bottom crosslinked layer prevented the thin top layer from restructuring, hydrophobic recovery and ageing (106).

To investigate the kinetics of adsorption and to estimate the time of saturation, the functional CHN layer was also deposited on QCM chips as described above and the QCM measurements were carried out during nanoparticle adsorption on the CHN-functionalised substrate (See Figure 69). The saturation time was defined as 1 hour and was used to fabricate nanoparticle gradient experiments. The SEM images presented in Figure 5a indicated a gradual increase in nanoparticle density as a function of the increase in the time of surface exposure to the nanoparticles. The corresponding plot (Figure 70b) revealed a nonlinear gradual increase in particle density as a function of time and position along the gradient, which corresponded well with the theoretical adsorption fit (red curve). The number of particles at the plateau was determined to be 1350/μm^2, which corresponds to 15% surface coverage. For the same duration, the density of AuNP adsorption on CHN layers as measured with QCM was 1597 NP/μm^2, which was 18% higher than the density of gradient sample. The discrepancy in densities achieved for the AuNP adsorption at the QCM sensor and after conducting the

gradient experiment for the equivalent exposure durations was smaller for the CHN layers than for the APTES layers. It implies that, in contrast to APTES layers, the polymeric CHN layers may have demonstrated better adsorption kinetics due to capillary effects.

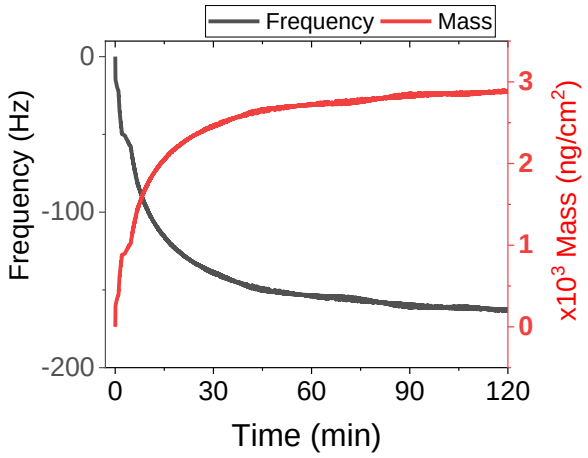

Figure 69. QCM-D kinetic curve recorded in-situ during the incubation of nanoparticle suspension with CHN thin film. The black curve indicates crystal frequency variation upon nanoparticle adsorption to the functionalised surface and the red curve indicates surface mass uptake evolution as a function of time, obtained from converting the frequency-time curve.

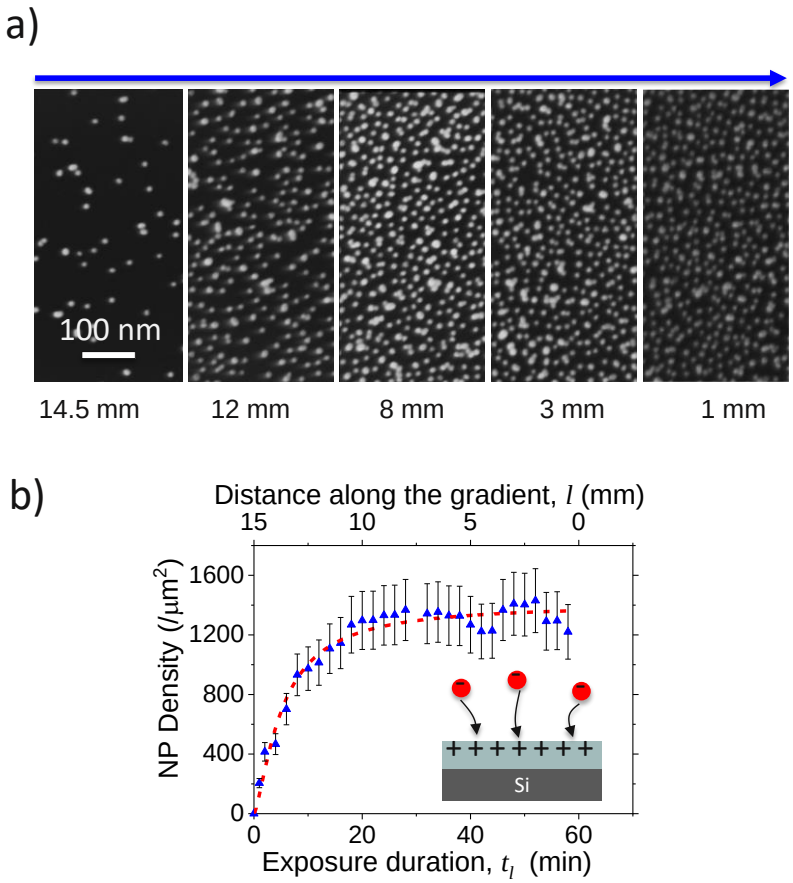

Figure 70. (a) FESEM images obtained on CHN-functionalised chip, demonstrating the increasing density of gold NP versus distance for 1, 3, 8, 12, and 14.5 mm away from the dense edge of the

coating (b) NP density plot as a function of distance (top-X axis) and as a function of corresponding incubation time (bottom-X axis). The red curve represents a theoretical fit based on the Langmuir-Hill equation.

Comparing the nanoparticle density gradient on CHN and APTES suggested that the porosity and polymer swelling might have accelerated the particle adsorption on the CHN surface, reflecting a higher initial reaction rate for this surface chemistry. However, since APTES has a larger number of primary amines, which is accounted for as the only form of nitrogen functional group (with around 3%) (281) adopted a higher number of nanoparticles in the long run compared to CHN thin film, which are known for having a complex structure with varieties of nitrogen-functional groups including primary amine. The presence of these functional groups on CHN was confirmed by the XPS characterisation of the CHN thin film (chapter 3, 3.4.2.1).

4.3 Fabrication of nanoparticle gradients with a periodic arrangement of nanoparticles

It was designed to show that the random sequential adsorption principles may be used to produce not only the stochastic organisation of nanoparticles on the surface, as in the case of APTES and CHN layers, but also a periodic arrangement of nanoparticles. Previously, we demonstrated that selective electrostatic attraction of anionic citrate-capped gold nanoparticles to a surface coated with periodic arrays of cationic block copolymer can be used to generate periodic arrays of gold nanoparticle clusters (178, 282). For this purpose, block copolymer arrangements were used to form both the nanoparticle density gradient (gold nano-cluster gradient arrays) and the nanoparticle size gradient (gold nano-domes gradient), benefiting the core-shell structure of the reversed micellar feature, which would not be accomplished in a single run using homogenous functional coatings.

4.3.1.1 Gradient in nanoparticle cluster dimensions

Prior to fabricating gradients, the functional surfaces were prepared as described in chapter 2 (2.1.3.2). Briefly, polystyrene-block-polyvinyl pyridine (PS-b-PVP) were spin-coated on substrates and heated to form a thin layer of templates of reverse micelles. Later, the developed micellar patterns were further etched by reactive ion etching (RIE) to remove remaining polymers between micelles and better define the patterns. As each reverse micelle was utilised as a template for fabricating nanoparticle clusters, the desired template size and cluster spacing

were optimised using an oxygen reactive plasma etching process. Then, the nanoparticle adsorption experiment was performed on QCM chips modified with copolymer templates to record the kinetic curves and obtain the time of saturation as presented in Figure 71. Based on the maximum period of exposure time attained by QCM, the gradient experiment was carried out for 1 hour with the same procedure as described in previous sections with no modifications to the gradient size, vial size, or gold nanoparticle suspension.

The clusters were generated by electrostatic attraction and stabilization of negatively charged gold nanoparticles with core-shell structures having cationic pyridine groups in the core that bear positive charge at a pH lower than its isoelectric point (pH=8.1). As a result, the size of the template features defined the maximum nanocluster size, and the created cluster arrays followed the periodicity of the original templates. PS-b-PVP with a molecular weight of 443 kDa was employed to create templates with 34 nm height, 83 nm diameter, and 170 nm pitch, respectively.

SEM micrographs of the scanned spots on reverse micelle as shown in Figure72 a revealed confined nanoclusters with a steady increase in cluster density as a function of distance/exposure duration. Bare micelles were clearly visible at the end of the gradient as black circles in the respective SEM images corresponding to 19.5 mm distance away from the dense side of the coating, where no particles were accumulated on the micelles. Except for a few cluster fusions where more particles were adsorbed, well-defined periodic patterns emerged at the denser part of the gradient. The size and periodicity of the produced cluster were dictated by the properties of the original micellar template at maximal NP coverage.

To evaluate the evolution of cluster density, the numbers of adsorbed gold nanoparticles in 10 randomly selected clusters were counted on each obtained SEM micrograph and the average value obtained was plotted versus exposure time and gradient distance, as presented in Figure 72b. When compared to APTES and CHN functional layers, the micellar template showed faster saturation of adsorbing nanoparticles, perhaps as a result of the high density of tertiary amine functional groups contained inside the micellar core.

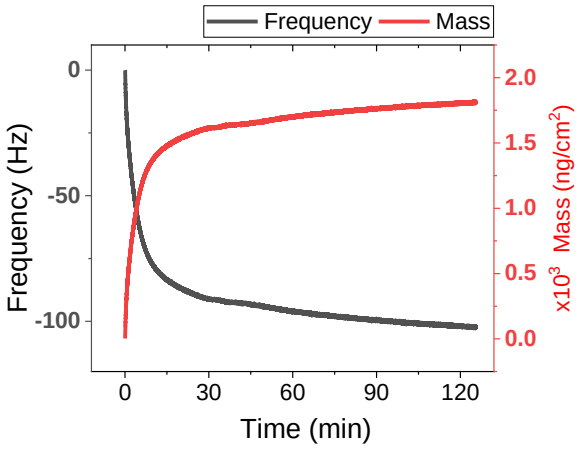

Figure 71. QCM-D kinetic curve recorded in-situ during the incubation of nanoparticle suspension with a micellar template. The black curve indicates crystal frequency variation during nanoparticle adsorption to micelles and the red curve indicates mass variation as function of time, obtained from the first curve.

The maximum AuNP density of 34 NP/cluster was observed from the QCM measurement, which is similar to the values resulting from the gradient experiment carried out for 60-minute exposure times. Assuming hemisphere geometry for micelles and considering the current micelle dimensions, the maximum particle surface coverage of 36% was observed.

To evaluate height variation, the 3D micrographs of the nanocluster gradient were achieved using AFM tapping mode on a 4µm^2 area along the gradient, as presented in Figure73 A. Comparison between the cross-section profiles of the 3D features proved that rather than variation in height, the volume and width of the generated clusters considerably varied along the gradient direction (see Figure73 B). Thus, at the zero-point on gradient surface, bigger clusters, and consequently smaller inter-cluster separations were observed, which gradually varied as a function of the time of surface exposure to nanoparticles. Also, analysing the evolution of surface coverage and cluster volumes based on bearing analysis provided useful information about the gradient evolution. The bearing analysis on the scanned area (2x2 µm^2) revealed a ~32.7% surface coverage with nanoclusters on the most densely occupied region, which corresponded well with SEM analyses. The comparison between the volumes of two opposite edges demonstrated an almost 6-fold difference in the total surface feature volumes (approximately 0.006 vs 0.001 µm^2).

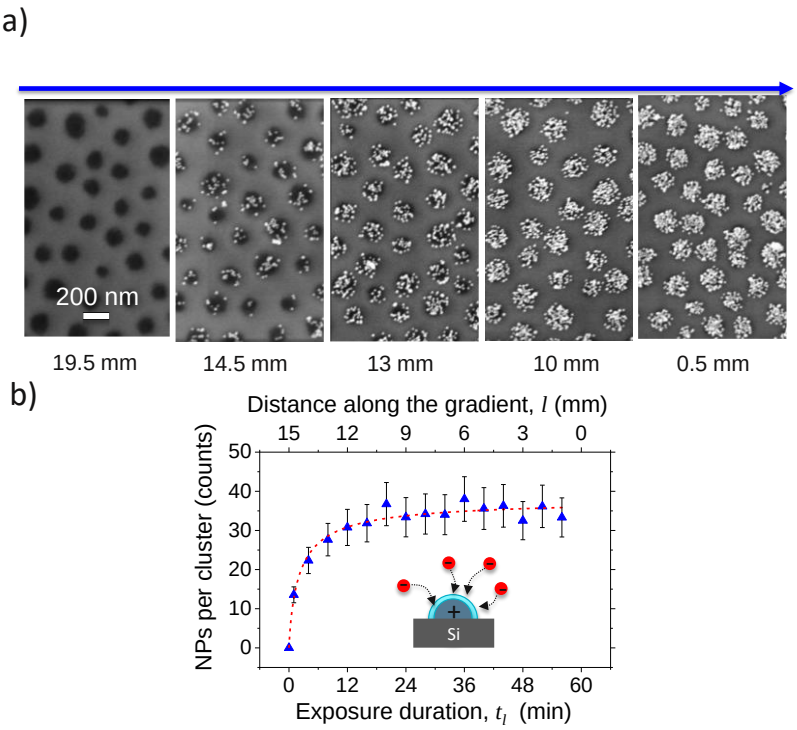

Figure 72. Unidirectional cluster size variation in periodic AuNP cluster arrays. (a) SEM Top-view micrographs obtained along the length of the nanoparticle cluster gradient; (b) The cluster size (nanoparticle per cluster) evolution as a function of exposure time to nanoparticle suspension (bottom-X) and distance across the gradient (top-X). The Langmuir-Hill equation (shown by dotted lines) was used to fit the experimental values.

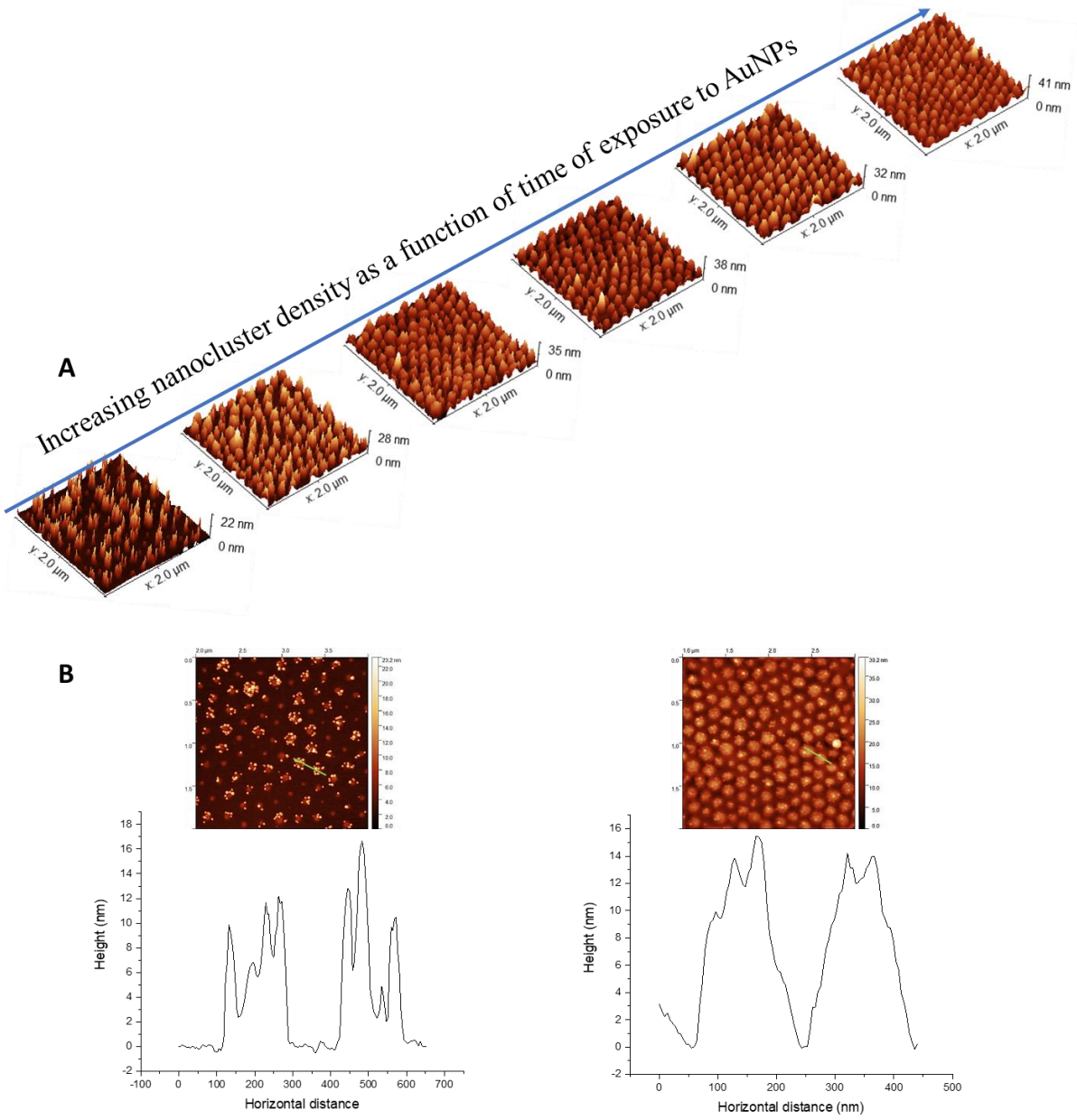

Figure 73 . Topography of nanoparticle cluster arrays along the gr2adient: A) 3D topography micrographs obtained from AFM in tapping mode along the nanocluster density gradient. The micrographs from left to right correspond to 16, 13, 10, 7, 4 and 1 mm from the start (high particle density edge). B) 2D top view images of the two extreme edges, low dens2ity and high particle density from left to right, respectively, along with the corresponding cross-section height profile curves, along an arbitrarily chosen line segment (shown in green colour) on each AFM micrograph.

4.3.1.2 Gradient in size of the gold domes

The concept of time-dependent adsorption of nanoparticles to prepare nanoparticle gradients can be also applied to produce gradients of nanoparticle size by exploiting the time-dependent adsorption of nanoparticle precursors. The same block copolymer template which was used to

form NP cluster arrays can be utilised to incubate with gold chloride anions from a gold chloride solution via an ion-exchange process. Previously, there have been investigations into the in-situ growth of inorganic nanoparticles via the exchange of anionic organometallic adsorbates inside block copolymer templates (283, 284).

The identical reverse micellar arrays as previously used for cluster formation were used to functionalise the surface and develop domes. The 0.1 M gold chloride solution was prepared with distilled water. After incubation of the micellar patterns with a gold chloride solution, the samples were subjected to a further reactive ion etching (RIE) process with O_2 for three minutes. Domes were developed after the removal of the outer shell of the micelle after the RIE process, which led to the generation of gold oxide, which was simultaneously reduced to gold (0), as it was unstable in atmosphere conditions. Similar to the process described previously for the three functionalised surfaces (CHN plasma bilayer, APTES and micellar template), QCM measurements were also conducted to monitor the adsorption kinetics of the modified chip with gold chloride solution (see Figure 74). The saturation duration of 1 hour, taken from the QCM isotherms was considered to perform the nanoparticle-size gradient experiment.

The SEM characterisation results of the in-situ produced gold dome gradient arrays shown in Figure 75A demonstrate homogeneous spherical domes with significantly larger diameters in the starting edge of the gradient, where it was treated for a longer incubation time (56 min) with the gold chloride precursor. The size of the domes gradually reduced toward the gradient's opposite edge, resulting in a successful size gradient. This could be explained by the incorporation of more gold anions into the positively charged p2vp domains over time, resulting in a higher concentration of gold precursors and larger domes near the gradient's starting edge. As the micelles are surface-confined, they served as a good template to control the morphology of the generated gold domes.

The top view SEM micrographs were analysed to plot the average diameter of the domes versus exposure time and distance along the gradient (Figure 75B). The diameter evolution demonstrated a slight variation along 12.5 mm distance from the sample's starting edge, remaining in the average 50nm value, then following a declining trend with a relatively steep slope beyond this point, finally reaching the minimum value of 33.60 nm at a 15 mm distance from the starting edge.

AFM analysis was performed to follow the height of the surface features. The respective 3D images obtained from image analysis are presented in Figure76 A.

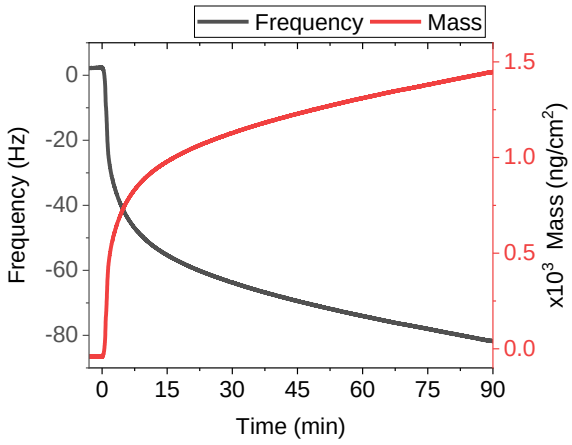

Figure 74. QCM-D kinetic curve recorded in-situ during the incubation of gold chloride solution with micellar template. The black curve indicates frequency variation during the adsorption process and mass uptake and the red curve indicates mass variation as a function of time, obtained from the previous curve.

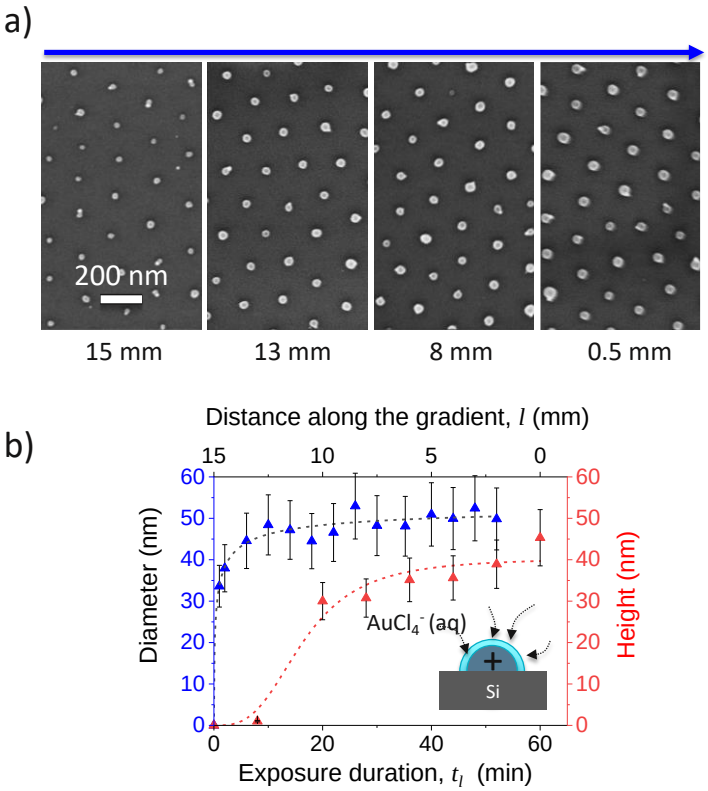

Figure 75. A) SEM micrographs representing scanned points along the gold dome gradient. B) Plot of average diameter and height of the gold dome features as a function of the time of incubation (bottom-X) and distance along the gradient (top-X). The number of particles was expected to remain invariable in each micrograph, while height and diameter is increased as a function of increasing exposure to the gold nanoparticle precursors.

AFM micrographs demonstrated the formation of uniform periodic gold domes with gradual size evolution versus the time of incubation with the gold salt solution. The gradual growth in the height and diameter of the features along the gradient was attributed to the increased loading of gold anions into the P2VP domains of the di-block copolymer, increasing the number of generated seed particles and finally leading to the emergence of bigger domes. Here again, the maximum size was determined by the size of the initial core size. The height profiles extracted from the cross-section profiles of the 2D micrographs (Figure76 B) demonstrated a total 2-fold variation in the height of the domes comparing the heights of the features in two extreme edges of the gradient.

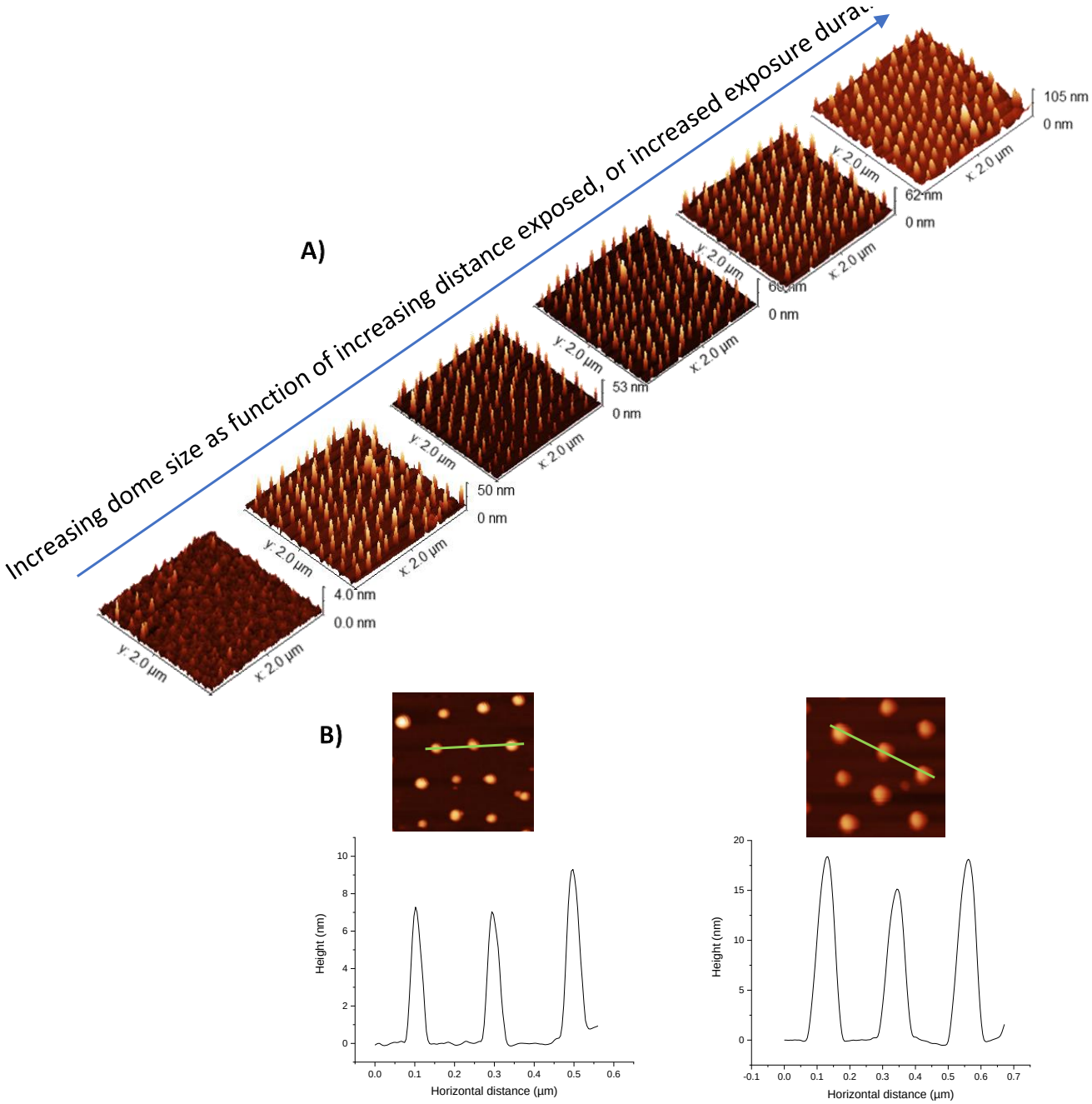

Figure 76. Topography of the gold nanodome gradient. A) 3D topography from AFM measurements of the gold domes scanned along the length of the gradient. B) 2D top view images of the two extreme edges, with low and high particle dimensions. Representative height profiles are shown along an arbitrarily chosen line (shown as a green line segment).

Comparing the diameter of the two extreme edges (peak base), for this parameter, the variation seems to be overall lower than for the height of the features, proving that the height of the domes is more affected during the particle growth, possibly due to the direction of the growth.

4.4 Properties of nanoparticle gradients

4.4.1 Surface-Enhanced Raman spectroscopic response on nanoparticle gradients

The proof of variations in the plasmonic properties of each substrate could be best provided by SERS measurements due to the sensitivity of the Raman signals of a probe molecule to the changes in nanostructure attributes on the surface. After applying the Raman-sensitive molecule, 1-naphthalenethiol (1-NT), to each substrate, 1-NT can specifically bind to gold particles through the formation of a chemical bond between sulphur and gold. The Raman signal intensity variations were recorded along the gradients and compared in the fingerprint region of the molecule (1368 to 1594 cm^{-1}). The intensity of the Raman signals was expected to vary along the gradient due to the variation in density of the particles and the ensuing variation in interparticle separation. While the density of nanoparticles defines the surface area available for the binding of SERS-sensitive molecules (i.e., 1-NT), the inter-particle separations contribute to electromagnetic (EM) enhancements at the junctions, which non-linearly increases as the size of junctions decreases. The highly enhanced EM fields at narrow junctions are technically referred to as EM hotspots. It is known that analytes that sit at the EM hotspots make disproportionately high contributions to the signal. 18 Thus, the impact of densities on the interparticle distances is expected to far outweigh the contributions due to the 1-NT concentrations on the surface. In addition, even small geometric changes on the surface should be easily picked up by monitoring the evolution of the Raman signals of the probe molecule. Here, the aim was to evaluate whether the geometric variation, as presented by the gradient, would also be reflected in the variation of the SERS signal intensities.

The Raman spectrum of the three fabricated gradients (APTES, micelle 1, and CHN respectively) as control samples and the SERS spectrum of the same three gradients functionalised with 1-NT are presented in Figure 77. The SERS spectrum for 1-NT-functionalised samples showed major peaks in approximately 1374, 1450, 1500, 1553 and 1580 cm^{-1} corresponding to ring stretching vibrations with slight shifts on different scanned positions (Figure 77b). The intensity of characteristic peaks was highest in the densest region, as seen in the spectrum corresponding to the APTES substrate (Figure 77B (a)). However, no significant peak increase in the fingerprint region was observed in the spectrum obtained in different regions starting from the low-density edge and up to this point. This finding indicated that the particles were not close enough together to produce hotspots and thus boost the SERS signal.

It also indicated that even though the surface nanoparticle packing was dense, the essential interparticle gap appeared to have a greater impact on SERS. Arrays of nanoclusters, on the other hand, demonstrated a successful gradual enhancement of the SERS signal (Figure 77B (b)) confirming the previous statement on the impact of the interparticle gap. Because of the homogenous distribution of the accumulated plasmonic particle arrays, this result was expected. Thus, the short inter-particle distances resulted in both an increase in hotspot densities and an increase in EM field enhancements at the hotspots. Cluster formation is particularly important, since it increased particle proximity even for smaller clusters, resulting in hotspots with adequate EM enhancements to detect 1-NT.

Comparing the SERS peak intensities in the fingerprint region acquired on the CHN gradient (Figure 77B (C)) with the most intense peak recorded for APTES and nanocluster gradients, a significant almost 7-fold increase in signal intensity was observed. The Raman intensity variation, on the other hand, was not constant throughout the CHN gradient region as two discrete gradients in intensity were observed in opposite directions. This could be explained by local non-uniformities in nanoparticle densities, which were not visible in SEM micrographs but were detected by Raman signals. Because Raman intensities reflect sub-nanometric changes in inter-particle distances at hotspots, the observed trend is not surprising. The origin of this SERS behaviour on the CHN thus necessitates additional investigation of the surface features, which cannot be completed within the scope of this thesis.

Due to the lack of a representative peak in the fingerprint region, the spectrum collected for the gold domes was not included here. The comparison of the SERS data of gold domes with the three other substrates could be misleading because, unlike the gold dome gradients, the size of the plasmonic nanoparticles on the three other substrates remained constant. The gold dome gradient, on the other hand, is a size-variation gradient, with particles (domes) of varying sizes produced. The nanodome gradient did not offer significant EM enhancement, resulting in the detection of 1-NT. The largest average gold dome size (assuming a circular form) was determined to be 175 nm, with average particle separations of 100-150 nm, presenting neither sharp corners nor short inter-particle distances to obtain substantial EM enhancements. In future studies, nanodome gradients should focus on high feature densities, as this might allow interparticle distances in the sub-50 nm range, where the EM fields will be greatly improved.

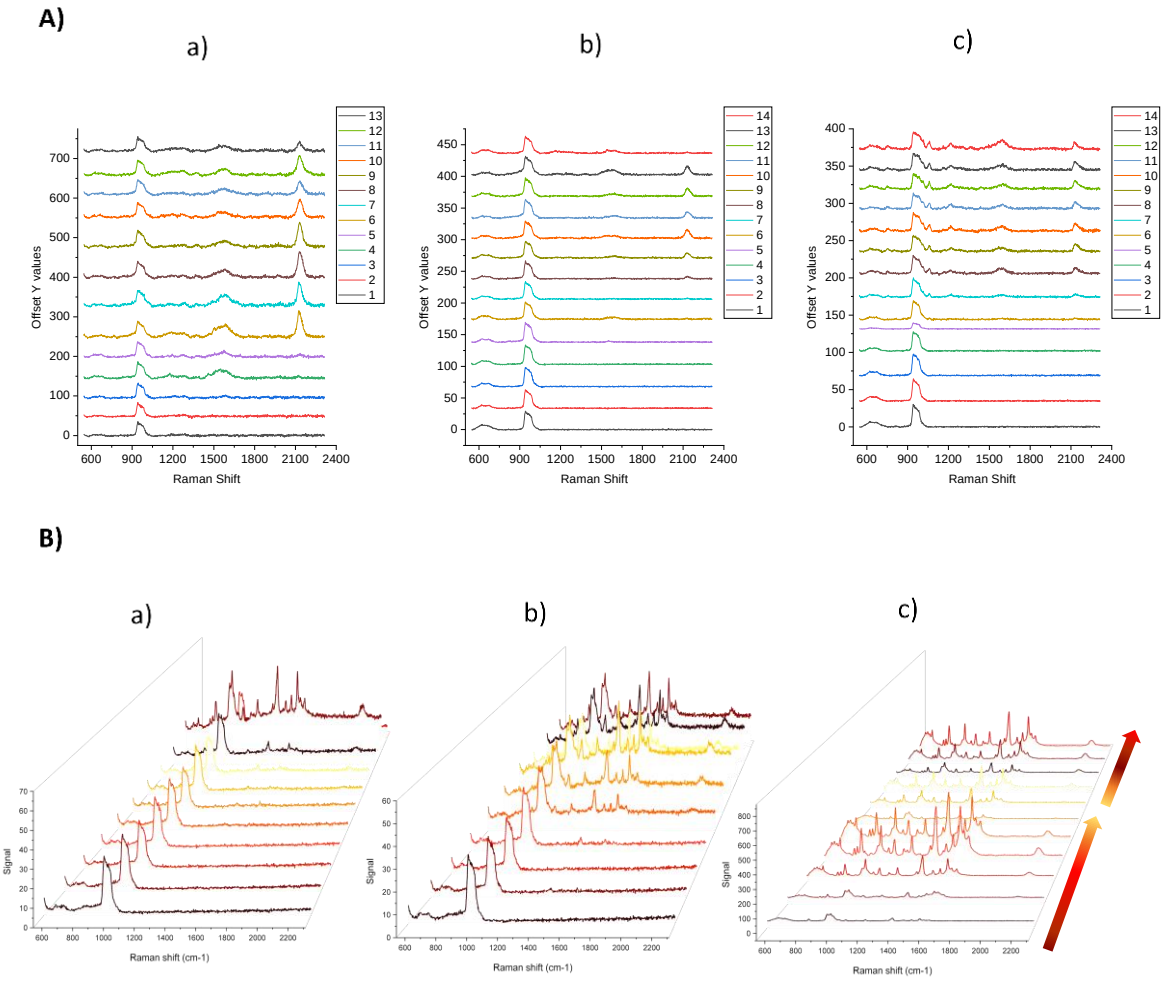

Figure 77. A) SERS spectra of control samples: a) APTES, b) 1-micelle and c) CHN plasma polymer each incubated with 1NAT are presented. The points are scanned at 1.5 mm intervals. B) SERS spectra of 1-NAT on nanotopography gradients recorded along the density gradients for: a) the APTES platform, b) nanoclusters and c) the CHN plasma polymer platform are presented. The spectra were recorded on 11 points with 2 mm intervals. The laser was excited at 633 nm.

- ***Application of nanogradients for SERS sensing***

It is widely known that fabricating a sensitive (bio)sensor requires the fast and high throughput optimisation of the bio-interface by tailoring those effective surface variables that are linked to the performance of the sensor. When light interacts with noble metal nanoparticles, conduction electrons oscillate at a precise resonance frequency determined by the nanoparticles' geometrical features. Due to localised plasmon resonance, these structures may absorb and emit light several million times more intensely than a normal fluorophore (285). Because even minor changes in nanostructure proximity cause noticeable changes in the refractive index and, eventually, in the plasmon bands of the nanostructure arrays, label-free detection of specific

analytes is possible by monitoring the plasmon spectra of surface-confined nanostructures during the binding event (e.g., antibody-antigen coupling).

Studies show that an interparticle gap of less than 10 nm is critical for obtaining maximal enhancements in hotspot development. (286) as most ordinary chemicals and short peptides are in the sub-1 nm size range, many molecules can be found inside the hotspot region depending on the molecule binding orientation (tilted, perpendicular, or parallel). However, larger molecules, particularly proteins, require a greater gap size to fit and avoid steric hindrance. This requires the optimisation of the interparticle gap for the target molecule. In this regard, unidirectional micro or nanoarrays of noble metal structures with a gradually varying parameter (i.e. shape, size or interparticle gap), can be translated into the formation of a plasmonic gradient that allows the optical responsiveness to be mapped to bioreactions in the form of plasmon peak intensity variation and/or shift (287). Table 11 includes the topography gradients prepared under the framework of the current study with the potential future biosensing applications. The attributes for three types of gradient samples for gold nanoparticle density gradient on a) CHN and b) APTES and finally c) gold nanocluster density gradient is listed in the table.

Table 11. The four 1-D nanostructure gradient samples studied in the current work attributes are presented with relevant gradient. The gradients were prepared on 20x10 mm si chips with a total gradient length of 15mm.

Gradient	Average size	Gap variation (edge-to-edge nm)	Extinction coefficient (unit)
Gold NPs on CHN	11 nm	4.6 - 27.3	$6.8X\ 10^{-2}$-$11X\ 10^{-2}$
Gold NPs on APTES	11 nm	1.63-73.45	$2\ X10^{-2}$-$16\ X10^{-2}$
Gold clusters	390.3 ± 25.8 nm diameter ~14 nm height	-	$3\ X10^{-2}$- $8.9\ X\ 10^{-2}$

As can be seen in the table, the monodispersed gold nanoparticle gradients on two different chemistries (APTES and CHN) led to different scales of interparticle gap variation as well as different gradient slopes. The optical results obtained from SERS confirm the gradient results and outcomes of previous discussions, showing an initially enhanced particle adsorption rate on CHN functional film and a higher density of adsorbed particles on the APTES coating at

the saturation point if the number of the particles is taken proportionate to the SERS signal (Extinction coefficients). The lower interparticle gap obtained for APTES (1.63 nm vs 4.6 nm) at the saturation point is a direct outcome of the higher density of the particles on the monolayer compared to CHN.

As mentioned earlier, the other alternative for generating interparticle gaps below 10 nm is to design 3D structures, e.g., nanoclusters with enormous accessible binding sites and several hotspots on every single structure compared to monodispersed gold nanoparticle arrays. The densest structures in the generated nanocluster gradient allow for a 3D structure with an increased gold surface and many available binding sites for the analyte, as well as many hotspots, owing to the tiny interparticle gap. Previously, the similar gold nanocluster arrays prepared with a PS-b-P2VP reverse micellar template were analysed for SERS enhancements as a function of the number of particles per cluster (3 to 18 particles/cluster) and per separation between the clusters (10 to 40 nm) for 18 particles/cluster. While the first analysis proved a three-fold SERS enhancement by increase in nanoparticle density, the second showed a 1.5-fold SERS enhancement as a function of the decrease in inter-cluster separation (16).

One significance of density gradient is that through the rational design of a SERS substrate, one can establish a balance between the cost and performance of a sensing platform. It means that even for small molecules and chemicals, after a certain critical cluster density, further increases in density or in the number of particles may not lead to noticeable field enhancement, hence, identifying the minimum density that allows for the greatest enhancement will yield savings in experimental costs and time. Also, while a dense structure with multiple hotspots is advantageous, particularly for the SERS-enabled detection of chemicals (even small proteins), the same may not be true for larger proteins/biomolecules.

The number of clusters attained in the current work was approximately 35, with a wide range of interparticle distance, ensuring strong field enhancement in the hotspot region formed, making this gradient interesting for future plasmonic applications. This potential was indeed confirmed by investigating SERS response along the gradient length. Based on SERS assessment, the intensity variations as a function of cluster density for nanocluster gradient sample indicated that the maximum intensity was attained on point 7 (light blue) rather than the point with the highest cluster density, as shown in Figure78 (Figure 77B (b)). This confirmed that the highest density does not always result in the highest SERS intensity, implying that factors other than density were most likely involved. The steric hindrance

imposed by citrate groups in narrower gaps could be one influencing parameter. Meanwhile, for contacting particles (zero gap), due to the absence of 1-NT, there is no EM increase at the interparticle gaps. Furthermore, SERS quenching can be expected when a SERS-insensitive molecule fills the inter-particle gap and prevents 1-NT molecules from entering this region.

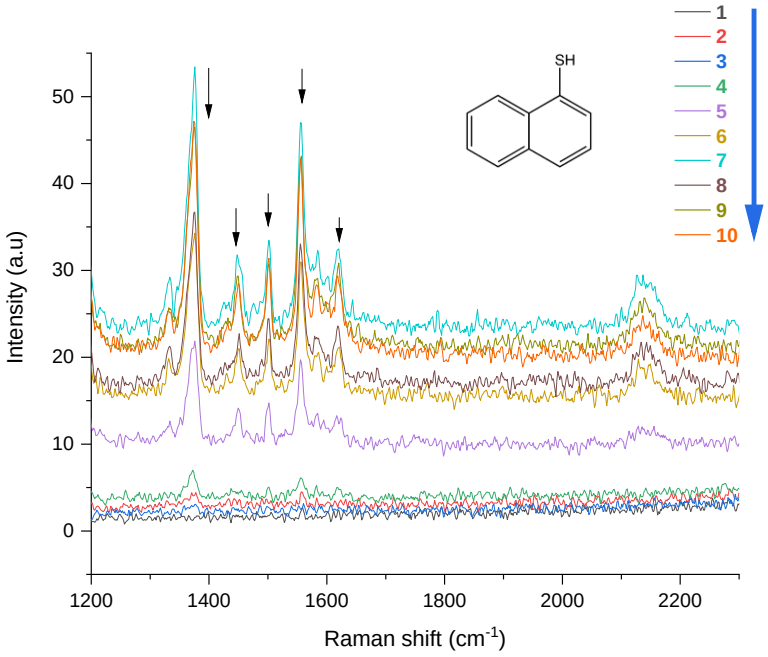

Figure 78 . SERS spectrum of 1-NT obtained on 10 points with 2mm intervals along the gold nanocluster gradient sample in the direction of cluster density increase. The excitation wavelength used was 633 nm. The main peaks corresponding to ring stretch are observed at 1375, 1449, 1501, 1556 and 1629 cm^{-1}.

Once the possibility of identifying SERS-active 1-NT has been proven, the applications can be extended for the detection of various classes of chemicals which can either chemisorb directly on the gold or interact electrostatically with the negatively charged capping agent on gold nanoparticles. Meanwhile, the wide scope of interparticle gap resulting from the cluster density gradient generated over 15 mm allows the identification of bigger molecules, such as proteins, which require bigger gaps in order to penetrate and avoid the hindrance. This underlines the great potential of this class of structural gradients to be employed for the optimisation of nanostructure characteristics aiming to maximise SERS performance.

4.4.2 Wettability characteristics of nanoparticle gradients

The 1-D topography gradient on CHN was characterised at several points as a function of distance along the gradient with static contact angle measurements, as presented in Figure 79. A gradual decrease in contact angles (hydrophobicity) of the surface was observed with an almost exponential decay trend as the particle density gradually decreased along the gradient. An overall 18° variation was recorded, shifting from a hydrophobic surface (≥90°) at the extreme high-density edge of the sample to 73° at the opposite edge. It should be remembered that this result was obtained on a substrate with the base coating, amine-functional plasma polymer, with hydrophilic nature (62.2° measured with 2 µl droplet and 55.52° with 0.3 µl water droplet) deposited with hydrophobic citrate-capped gold nanoparticles (95° for a dried film of citrate-capped nanoparticles and 84° for pristine flat Au (5)). Therefore, it seemed that initially, in the low-density region of the gradient, the surface wettability was ruled by the chemistry of the plasma polymer platform, while upon the gradual appearance of the particles, wettability was influenced by the blend of the chemistry and topography parameters.

To assess this hypothesis, it was necessary to compare the trend with classic wettability theories. Accordingly, a model consisting of two spherical particles with the same size and varying edge-to-edge distance was considered (see chapter 2, section 2.2.4.2.2). Based on this model, the following parameters were taken into account: area including the two particles, the area of particles (area of a sphere in the Wenzel regime or area of a spherical cap in the Cassie-Baxter regime) and the fraction of the particle and air in contact with water droplet (Cassie-Baxter regime). The aim was to depict the expected (theoretical) contact angle values as a function of the nearest neighbouring distance (NND) between particles.

Initially, the SEM micrographs for the topography gradient generated on CHN plasma and APTES samples were analysed with image analysis software and the number of particles obtained at each scanned point was plotted versus the NND (calculated from edge-to-edge) of that point. The results are presented in Figure 80 for the CHN plasma polymerised film and APTES gradient, as a conventional nitrogen-rich coating. To conform to the trend with the theoretical equation, NND was calculated by simply assuming a four-particle system for nanoparticle distribution. The model was developed by considering the whole surface as a big square divided into numerous square cell units of the same size in which each nanoparticle is located on the edges of unit squares and separated from the adjacent particle with NND. The following equation was used to fit the experimental plot:

$$N = \left(\sqrt{\left(\frac{A}{(2r+NND)^2}\right)} + 1\right)^2 \quad 4.1$$

While A presents the total area covered with particles, N and r present the number and radius of the particles, respectively.

As can be seen, the model (red curve) and the experimental values (scattered plot connected with dotted line) are compatible with some variances. The primary reason for the discrepancy is that the model assumes the well-organised distribution of particles on the surface, whereas in practice, as observed in SEM and AFM micrographs, the particle distribution is random. The second problem is the variability in particle size distribution, which is difficult to control during synthesis. Finally, the data from the first two plots, WCA vs distance and number of particles per area versus NND, were combined to obtain the third plot, WCA versus NND (see Figure 81). The experimental curve (grey scattered plot) indicated a declining trend as a function of interparticle distance, suggesting that upon decrease in the particle density, wettability of the surface rose (reduction in WCA). Even if the data was not covered by the fitting, the direction of variation is in accordance with the Wenzel curve (red curve) obtained from the model, implying that the water droplet follows the contour of the structure and fills the gaps in between particles. It suggests that the surface topography was not rough enough to allow air pockets to form beneath the droplet, causing the system to enter the Cassie-Baxter regime, which would otherwise have revealed a superhydrophobic behaviour (see the blue curve).

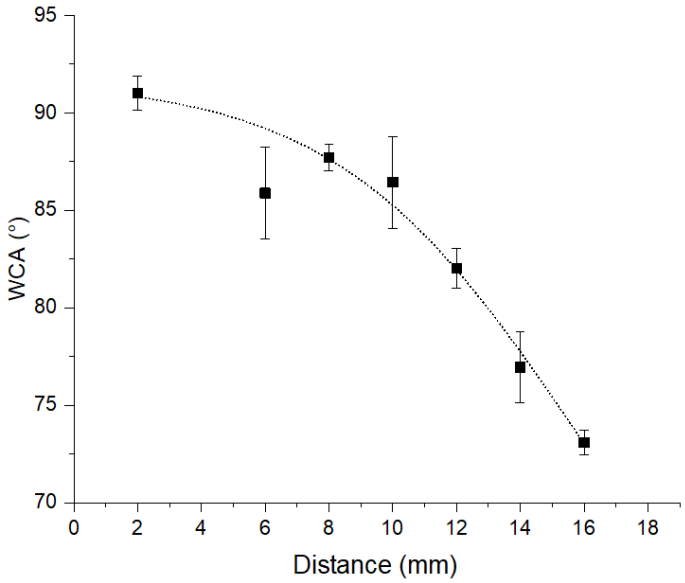

Figure 79. Wettability gradient generated along the nanoparticle density gradient on CHN. The values are measured at 2, 6, 8, 10, 12, 14 and 16 mm from the particle-dense edge of the coating.

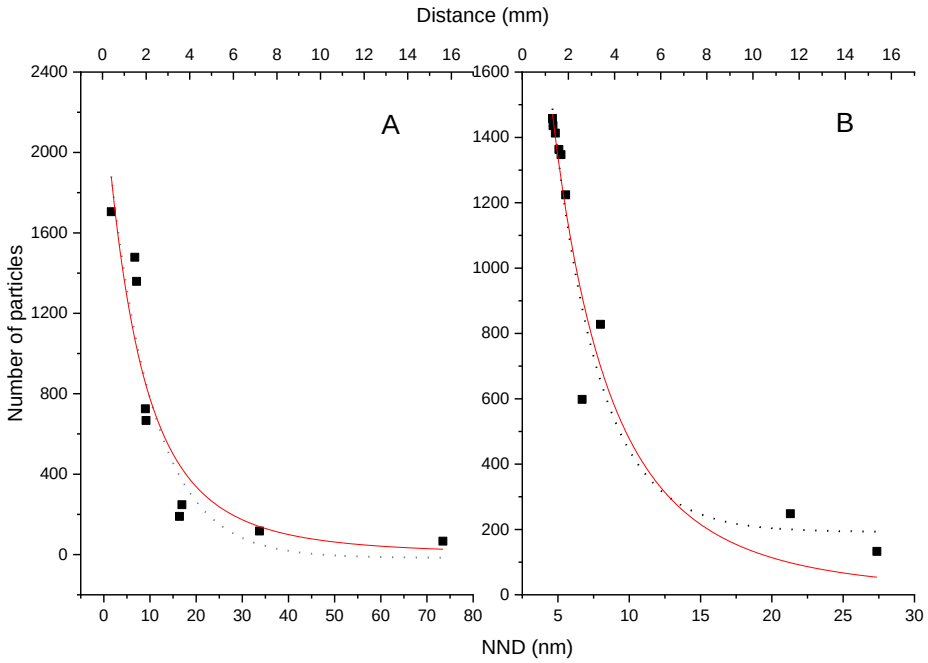

Figure 80. The particle count numbers obtained from SEM micrographs for A) APTES and B) CHN samples are plotted against the average nearest neighbouring distance (NND) corresponding to each scanned area (scattered plots). The red solid line is the fit developed based on the orthogonal particle distribution model. The variation from the model is expected, as the nanoparticle assemblies do not represent a regular arrangement as used for the model.

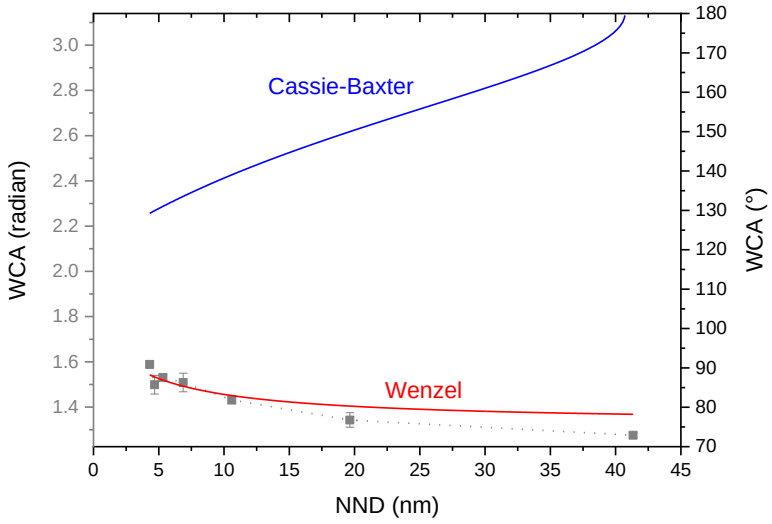

Figure 81. The wettability values obtained along the gradient plotted as a function of NND. The solid lines correspond to Wenzel and Cassie-Baxter curves (red and blue curves, respectively) developed based on the model. The adjusted experimental parameters were particle radius, area of particles, etc.

The model is clearly detailed in Chapter 2 section (2.2.4.2.2). The following equations were established based on the model adopted for totally covered surface features with water droplets (semi-Wenzel regime):

$$\theta^* = \cos^{-1}(4\cos\theta_1 + \left(1 - (\frac{\pi R}{FR} + NND)\right)\cos\theta_2) \quad 2.26$$

where θ*= Apparent contact angle, θ_1 is the WCA of intrinsic citrate-capped gold nanoparticle, θ_2 is the WCA of CHN plasma polymer, which is eventually converted to:

$$\theta^* = \cos^{-1}(0.24 - \frac{1.75\,R}{4R+NND}) \quad 4.2$$

after replacing the parameters with R=5.5 nm as the initial radius value and allowing the curve to iterate between 1<R<11. In this equation, NND is the independent variable while R is the parameter and θ* (WCA) is the dependent variable. For partial surface coverage with the water droplet or so-called the previously described Cassie-Baxter regime was used:

$$\theta^* = cos^{-1}(\frac{2\pi R^2\,(1 - cos\,\alpha)}{\pi R^2(sin\,\alpha)^2})\,cos\,\theta_1 - 1 + \frac{2\pi R^2(sin\,\alpha)^2}{(4R + NND)2R} \quad 2.30$$

which was converted to:

$$\theta^* = cos^{-1}(4\,cos\,1.65\,(1 - cos\,\alpha)\,(sin\,\alpha)^2 - 1) + (\frac{17.27(sin\,\alpha)^2}{(22+NND)2R} - 1)) \quad 4.3$$

by replacing initial α=1.5 and allowing it to iterate between 0.6 < α <1.9.

4.5 Conclusion and Perspectives

The fabrication of unidirectional surface gradients with a gradual evolution of densities, diameters and the dispersion of gold nanoparticles is presented using a rational and adaptable technique. The applicability of the approach was demonstrated utilising different surface chemistries from homogenous conventional self-assembled monolayer to plasma polymerised 3D coatings and patterned micellar periodic arrangements. The possibility of forming both stochastic and ordered arrangements in nanoparticle distribution was achieved by the choice of functionalised surface as a separate controlling factor. Two stochastic nanoparticle density gradients with a comparable nanoparticle density scale (interparticle gap scale) were achieved by selecting one of the two different surface chemistries of monolayers and plasma polymers. The same micellar template was utilised to generate two different periodic arrays: one with a variation in nanoparticle cluster density and the other with a variation in nanoparticle size by

selecting between two different precursors, gold nanoparticles and gold chloride solution, respectively.

The experimental design allowed the conversion of the volumetric rate of the rise of nanoparticle/precursor dispersion into the linear variation of contact times with the stabilised surface-functionalised chip. Independent of the chip size, the proposed approach can be adapted to form gradients with a intended lengths and variation magnitudes thus, surpasses the flexibility that is currently possible with motorised or piezo-based dip-coating systems. Meanwhile, the gradient experiment benefits from the contained environment of the closed chamber that reduces possible evaporative losses and contaminants during the experiment. The set-up also benefits from a compact, portable design and user-friendly operation. The approach is believed to motivate future advanced rationally designed nanostructure gradients based on time-dependent surface reactions.

The versatile approach presented here benefits from simple electrostatically driven adsorption processes, which are easily adaptable in order to construct gradients of any kind of nanoparticles, independent of the material and substrate of choice.

When investigations into optimal nanostructure features are necessary (e.g., dimension, interparticle gap, density, etc.) for various applications related to the optical and electrical properties of gold nanoparticles e.g. fabricating plasmon-enhanced spectroscopic sensors (178, 288-291), photocatalytic devices (292, 293), charge storage devices (292, 293), and bio-interfaces (294, 295), these nanostructure gradients could serve as potent optimisation platforms. Apart from the unique intrinsic properties of noble metal nanoparticles, the physical properties could be tuned to alter surface topography e.g., by changing the geometrical shape, density and orientation of the nanoparticles. The versatility of the developed nanoparticle gradients allows further modifications to be made to develop different nanoparticle geometries (e.g., nanopillars, nanoholes, etc.) via nanolithography techniques and based on using nanoparticles as etch masks.

Chapter 5: Fabrication of orthogonal surface gradient

5.1 Introduction

Directionality is one important attribute of a surface gradient that defines the direction along which surface property(s) vary. While unidirectional gradients have received the most attention over the last 50 years, there have also been reports of gradients of multiple variables evolving in radial, orthogonal, or triangular directions (296). An orthogonal gradient is a surface gradient fabricated using two variables that evolve steadily and independently in a perpendicular direction. The 2D or, orthogonal gradient surface is a potent screening tool that enables fast and high throughput surface studies with diverse applications from material science to biology (297). These two distinct variables can be seen at any point on the modified orthogonal surface. This enables the rapid monitoring of two surface parameters concurrently, meaning that while single surface gradient offers faster and more efficient optimisation compared to the classic time and resource-intensive optimisation approaches, the double optimisation offered by orthogonal gradients doubles the advantages compared to the classic approaches. Furthermore, it allows the systematic investigation of a third surface parameter that varies in relation to both surface gradients. For example, with correct surface engineering, it is possible to obtain a variation in surface wettability on an orthogonal gradient that is broader in scope and magnitude than the wettability obtained using each component (e.g., the 1-D chemistry gradient or the 1-D topography gradient) alone. This suggests that greater flexibility can be achieved in modulating the surface wettability properties through an orthogonal gradient. Alternatively, the orthogonal gradient generated can be further enhanced as a platform to form a brand-new extrinsic gradient. There have been reports on the forming of 2D distributions of nanoparticles (157) and proteins (298, 299) on orthogonal gradients, with implications for material and biomedical investigations.

The first case studies on orthogonal gradients were published two decades ago (157, 300, 301), and progress is still being made in this field, in parallel to advances in surface engineering techniques. However, despite all of their advantages, the number of published multigradients with potential applications in the monitoring of physico-chemico-biological events remains relatively low compared to the massive number of published unidirectional gradients. This is most likely due to the multiple fabrication steps involved and the cost of fabrication. As previously discussed for unidirectional gradients, fabricating orthogonal gradients with complicated techniques improves control over the generated surface features, thus increasing reproducibility; however, this often comes at the expense of time and resources, thus limiting

the upscaling that is required for applied research purposes. Therefore, innovative manufacturing technologies that allow simpler sample handling, while at the same time reducing time and resource requirements, are beneficial in addressing these constraints. An example of outstanding strategy previously reported for developing orthogonal gradients was the orthogonal gradient of groove pitch and depth developed via photolithography, with the possibility of mass replication using injection moulding, which allows upscaling in production and enables the patterns to be transferred to a substrate of choice (302). The other interesting work employed a single experimental setup, based wholly on electrochemistry to form both the topography and chemistry gradients orthogonally, with the aim of assessing mesenchymal stem cell responsiveness to both surface variables (158). Anodisation was utilised to first create a pore size gradient (porous silicon (pSi) gradient), then a functional group gradient was electrografted orthogonally on the same surface and was then used to create and further functionalise a peptide ligand gradient. Similarly, a single technique was introduced in a recent report (303) in order to fabricating the orthogonal density gradient of two distinct metallic nanoparticles utilising mask-assisted deposition with a gas-aggregated nanoparticle source (GAS). The resulting 2D-linearly graded Ag-Cu nanocomposite with tuneable dual-plasmon resonance could be particularly applicable for developing plasmonic sensors, SERS substrates, etc.

In the scope of the current study, a simple and flexible multistep fabrication design, a combination of surface chemistry and surface physics, was explored for developing the orthogonal gradient. For this, the previously proposed versatile approach for generating stochastic nanotopography gradients (as described in Chapter 4 (4.2.2) was utilised to generate the first gradient and was subsequently combined with the second gradient developed via the fast, waste-free, readily tuneable, and substrate-independent chemical modification offered by plasma polymerisation (as described in Chapter 3 (2.1.2.1).

5.2 Fabrication of orthogonal gradient

Figure 82 displays the sequence of steps involved during the fabrication of the orthogonal gradient (1). The production of the Uni-directional nanoparticle density gradient on CHN plasma polymer (described in Chapter 4, (4.2.2)), was the first step in the fabrication of the orthogonal (2D) gradient. Shortly after, a homogenous functional nitrogen-rich layer was deposited on the Si substrate using low pressure CCD plasma and was then used as a molecular template to generate the nanoparticle density gradient. The electrostatic interaction of oppositely charged particles with the surface allowed for strong interactions and, eventually,

surface modification with particles via the dropwise and time-controlled introduction of the nanoparticle dispersion and position-dependent exposure of the vertically placed functionalised substrate. Once the fabrication of the first gradient was completed, the mask-assisted plasma polymerised chemistry gradient (as described in Chapter 3 (3.3), and chapter 2 (2.1.2.1) was deposited on top, perpendicularly to the first gradient to finally form the orthogonal gradient. For this, the chips were placed inside the grooves of the masking device as shown in Chapter 3 (3.3) then covered with the cap. The 4 distinct coatings with gradually varying nitrogen content were deposited in a perpendicular direction to the topography gradient and along 1cm width of the chips. For the final form of the 2D gradient based on the design, it was projected to obtain larger spheres (in comparison to the initial uncoated nanoparticles) with sufficient inter-sphere separation in low nanoparticle density regions and overlapping spheres in high particle density parts. Therefore, the thickness of the top coating (second gradient) was tuned after a few trials. Initially, plasma parameters were adjusted to deposit the 4 coatings, each with total thickness of approx. 25 nm. However, images obtained using helium ion microscopy (HIM) on a high-density region before and after coating indicated that some particles seemed to be buried beneath the coating (see Figure 83).

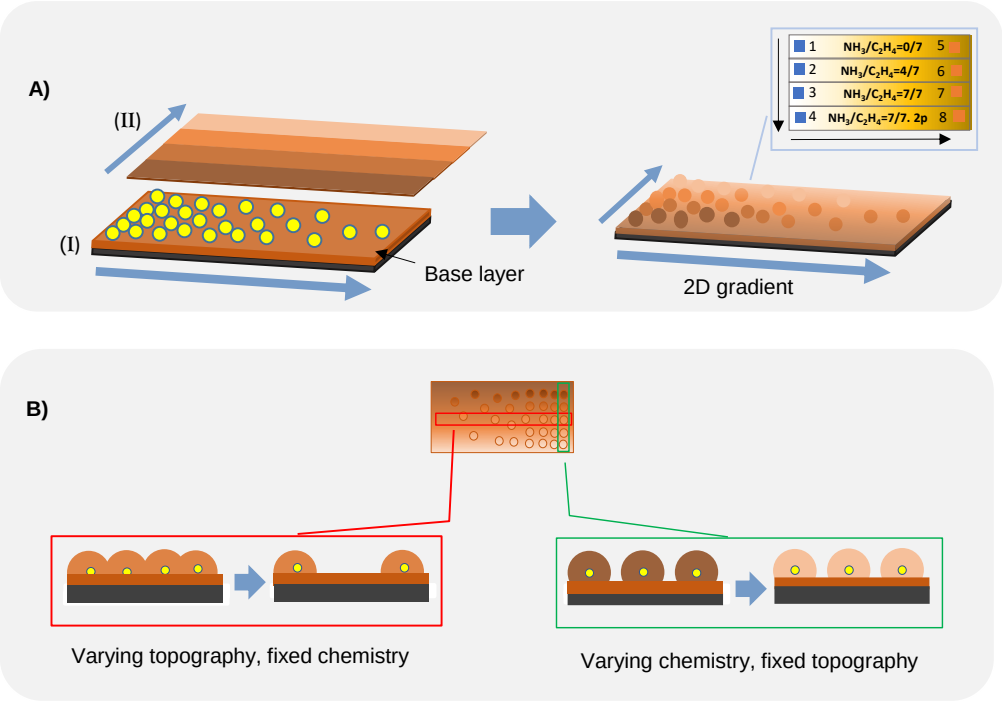

Figure 82. A simple illustration depicting the development of orthogonal gradients. A) The steps involved in fabricating a 2D gradient begin with (I) forming the base amino-functional layer using the deposition parameters described in Table 5, followed by generating topography or nanoparticle density gradient along the base layer in a horizontal direction using the approach described in Chapter 4, 4.2.2; and (II) depositing the amino-functional chemistry gradient on top of the topography gradient in a perpendicular direction using the deposition parameters described in Table 5. B) A top view of the orthogonal gradient and what outcome to expect in each direction. The density of the particles, and hence interparticle separation, varies in the horizontal direction, whereas the chemistry of the surface changes gradually in the vertical direction.

As a consequence, the surface texture could be termed smooth in areas where particle packing was close enough throughout the gradient length. This resulted in a limited span of surface roughness variation along the gradient after being coated, which was undesirable. Therefore, the overall thickness of the coating was decreased to 10 nm, which was expected to preserve the morphology of the 11 nm particles.

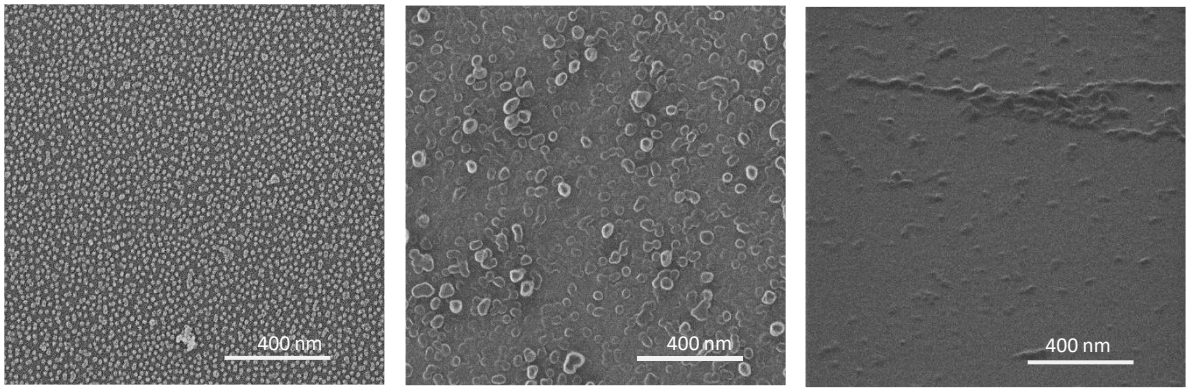

Figure 83. HIM micrographs corresponding to a) Top view of nanoparticles before coating b) top view of the particles after coating with 25 nm thick plasma deposition and c) tilted view (50 °) of the coated particles.

5.2.1 Elemental composition of the top layer (the chemistry gradient)

XPS was earlier used to perform an elemental analysis on the reference chemical gradient, as discussed in Chapter (3). 3.4.2.1. In summary, the XPS quantification was performed on 18 spots along the chemical gradient, and it was concluded that: 1) the O and N content increased moderately from coating 1 to coating 4, and 2) the carbon content decreased slightly in the gradient direction. 3) Carbon 1s peak deconvolution revealed that when ammonia was injected into the discharge, the initial C-(C,H) peak gradually decreased, and subsequent ammonia increases resulted in the formation of complex N and O-containing functional groups. On each coating, the functional groups predicted as being linked to C1s were identified using two different scenarios.

It is well recognised that the material characteristics of the substrate might have an impact on the analysis results, either due to changes in deposition/fabrication and/or analysis. Since the orthogonal gradient was generated using the plasma polymerisation of a gradient thin film on a gold nanoparticle-coated layer, the probable differences in coating chemistry or analytical response owing to the presence of conductive metal sub layer had to be studied. Therefore, it was decided to perform the elemental analysis on the orthogonal gradient on a total of 8 chosen spots (1 point for 1 coating) on the sample's two extreme edges. The XPS data was collected first in the low particle density zone at four spots along the chemical gradient length, and later at four points in the high nanoparticle density zone along the same direction. The objective was to investigate the variation of N and O along the gradient direction and compare the amount of each element individually in two low particle density and high particle density regions along the gradient direction. The XPS spectra were collected following survey scans over the width

of the orthogonal gradient (chemistry gradient direction), as shown in Figure 84 for both the low and high particle density zones. Accordingly, the quantification elemental analysis results for major elements are provided in Table 12.

Figure 84 shows the major detected peaks at 285, 530, and 400 eV, which were attributed to C1s (the largest peak), O1s, and N1s, respectively. As predicted, the Au (4S, 4p, 4f, and 4d) peaks originating from the sub-gold nanoparticle layer were only found in the high particle density zone. The existence of gold was confirmed by the powerful and sharp Au 4f peaks in the high particle area (Figure 84 (b)). The remaining peaks were attributed to the auger electrons N KLL and O KLL in both spectrums, as well as a minor amount of fluorine (F1s) contamination (approx. 0.1%) in the low gold density area. In addition to the survey scans, the high-resolution scans were performed on both zones for quantification purposes. The peak integration findings are displayed in Figure 85 and Figure 86 for elemental nitrogen and oxygen, respectively. Figure 85 illustrates the generation of a gradient through the four coatings, with a deviation noted for the final coating, which was deposited with NH_3/C_2H_4= 7/7 and double plasma pressure, aiming for a greater NH_2/C and N/C ratio. The variance in total N% content ranged from 1% to 11.5% at maximum value for the low gold particle zone and 0.8% to 10.4% for the high particle density zone. Applying two-fold pressure during the fourth deposition condition, was ineffective in raising N/C further as indicated via XPS analyses in Chapter 3 (3.4.2.1), so as is evident, positions 4 and 8 showed slightly lower N% compared to positions 3 and 7. One possible explanation for this observation is that the increase in pressure resulted in reduced energy (and ion bombardment) during film growth because of a higher number of collisions at high pressure, thus resulting in lower fragmentations leading to a less crosslinked plasma polymerised coating, which in this case may imply an increase in primary amine content but not necessarily an increase in total N%. The next noticeable point was the slight difference in total N% between low NPs density region and high NPs density region. This difference, however, was negligible since the previous XPS tests performed on the homogeneous reference chemical coating revealed about 1% variability in quantifications for the points scanned on an identical coating with the same chemistry.

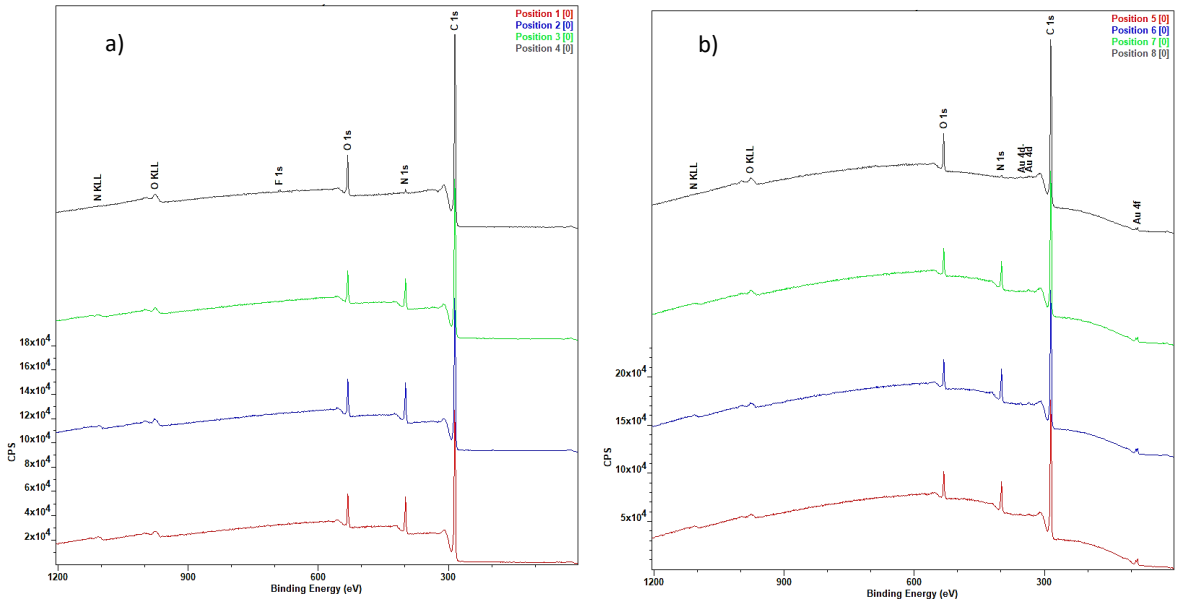

Figure 84. The XPS spectra obtained by a survey scan on a) a low gold nanoparticle density region starting from low N% coating (position 4) to highest N% region position 1. In this set of spectra, a negligible amount of fluorine is observed in position 4 and, b) a high particle region starting from low N% coating to high N% region. In this spectra, unlike the previous spectra, peaks corresponding to gold particles, with 4f Au being the most intense, are easily observable.

Table 12. Elemental analyses results for points scanned vertically along the amine gradient in a) low particle density and b) high particle density regions.

a)

Sample identifier	C1s%	N1s%	O 1s%	Au 4f%	Si 2p%	N/C (%)
Coating 8	83.7	10.4	5.6	0.2		12.5
Coating 7	83.5	10.7	5.6	0.2		12.8
Coating 6	85.5	8.9	5.4	0.2		10.4
Coating 5	91.4	0.8	7.7	0.1		0.9

b)

Sample identifier	C1s%	N1s%	O 1s%	Au 4f%	Si 2p%	N/C (%)
Coating 4	82.5	11.2	6.3			13.6
Coating 3	81.7	11.5	6.9			14
Coating 2	85.2	9	5.8			10.5
Coating 1	92.3	1	6.7			1.1

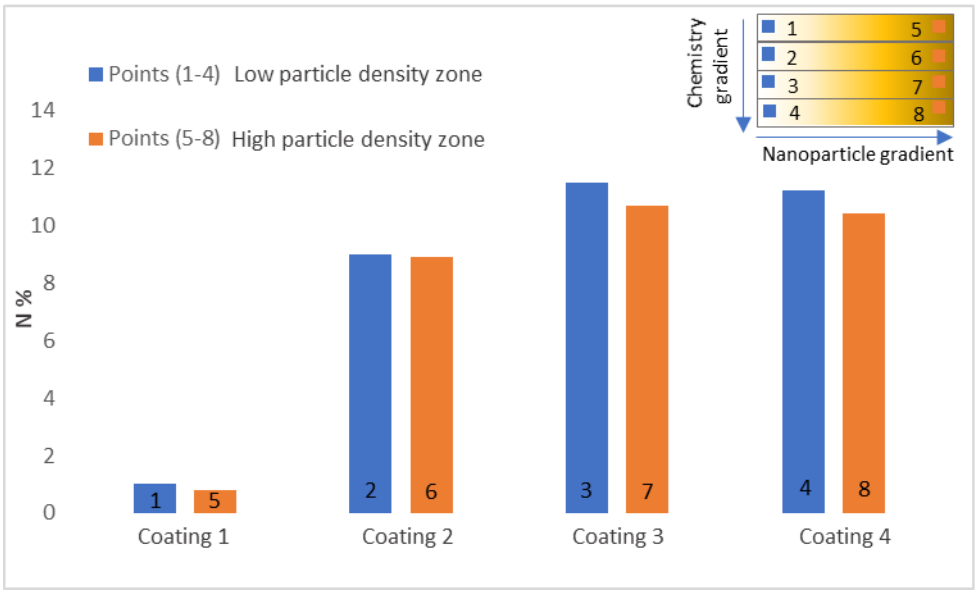

Figure 85. The high resolution N1s peak integration results at 8 points obtained at two extremes: low and high particle density regions. The orange and dark blue columns show the N% for the points scanned before the etching of the coating along the width of the sample on two extreme edges of low density and high density, respectively. The light blue and yellow bars show the results for etched coating for points (1-4) and (5-8), respectively. The points on each region are scanned at 1.2 mm intervals.

As previously noted in Chapter 3 and presented in Figure 61, there is a significant amount of oxygen contamination in the coating, which is thought to have occurred post-deposition and is likely due to trapped free radicals and chemical restructuring. To explore the source of the oxygen, the top layer of the coating was etched for 60 seconds with Ar^+, 2kV,100A. Given the depth of the coating, the elemental analysis obtained from high resolution scans for 8 selected spots before and after etching are expected to give insight into the source of this contamination. The quantification results for elemental oxygen for the coating analysed after etching the top layer in both zones are presented in Figure 86. A brief look at the bars shows a considerable overall drop in oxygen level after etching the sample surface in both zones. Before etching, the sample demonstrated roughly 7% elemental oxygen, which decreased to a high of 2.3% after etching the top layer. This indicates that the source of the oxygen was mostly the post-exposure to air, as only a small fraction was integrated into the polymer structure. This minor percentage of oxygen incorporated into the polymer structure was to be expected because, despite purging the plasma chamber with inert gas (argon) between each coating process, the opening of the chamber and displacement of the mask before each deposition may still have allowed minor O% into the polymer structure.

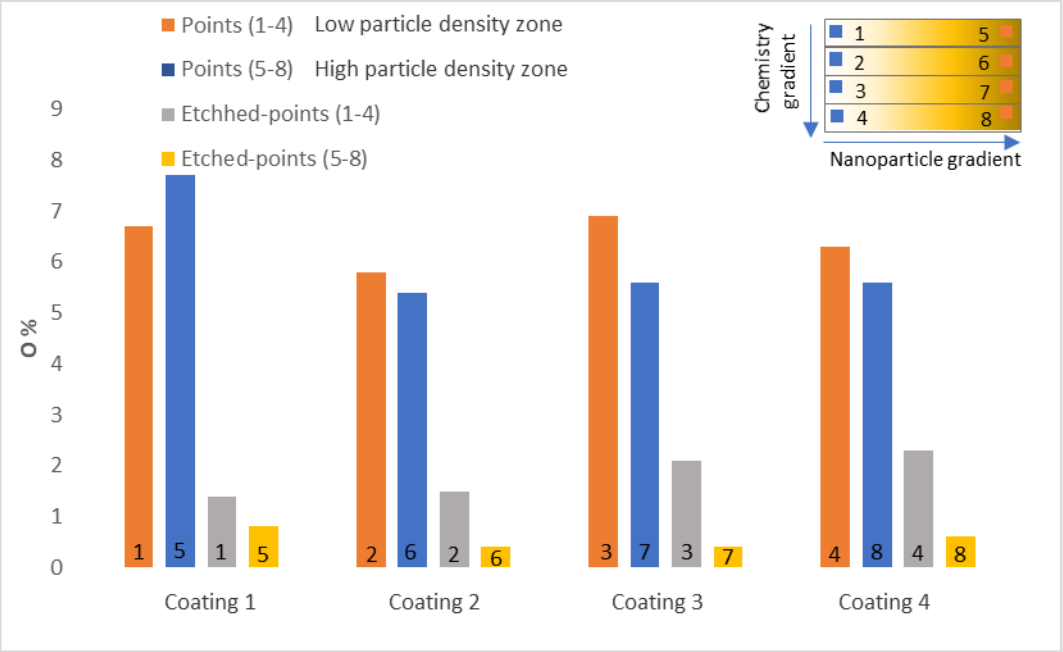

Figure 86. The high resolution O1s peak integration results at 8 points obtained at two extreme edges: low and high particle density edges. The orange and dark blue columns show the points scanned before the etching of the coating along the width of the sample on two extreme edges of low density and high density, respectively. The grey and yellow bars display results for etched coating for points (1-4) and (5-8), respectively.

Another point to note is that there was no discernible trend in oxygen variation for each zone before and after etching the sample, and a comparison of Figure 85 and Figure 86 confirmed the irrelevance of the oxygen content with the nitrogen content along the four coatings, emphasising the minor oxidation of nitrogen-containing groups. The maximum O% and variation were not in accordance with the reference chemistry coatings reported in Chapter 3 because for the reference gradient coating, O% varied parallel to N% with oxygen content reaching a maximum of 17%, nearly twice the current coating's maximum of 8 percent. Additionally, the C1s peak deconvolution was carried out to gain a better understanding of the coating compositions by comparing low- and high-density areas. The purpose was to see whether the presence of particles influences the nature of polymers by comparing functional groups in a C1s environment. As shown in Figure 87, the carbon peak analysis produced comparable results for peak components to the prior reference chemical gradient. It was observed that the shift of the C1s peak to higher binding energies from coating 4 to coating 1 along the gradient, parallel to the increase in the ammonia flow rate in the discharge, is an indicator of the transition from a hydrocarbon-rich coating to a functional coating with various polar electro-negative groups and unsaturated bonds. To understand the presence of diverse

functional groups, the following model, composed of three distinct vertical layers, is considered based on the post-exposure to air/moisture:

I) The uppermost part of the coating, including trapped free radicals and amine groups that could react more strongly with molecular oxygen or moisture from the air, leading to the incorporation of oxygen in the polymer structure and forming various carbon and oxygen containing groups like amide groups (304). Due to the higher interaction of the uppermost layer with the atmosphere, the most common group for this layer was the carboxylic group $O=C-O^-$.

II) The second layer beneath the uppermost layer, which was not directly exposed to air and which was expected to contain some oxygen and water incorporation through diffusion/permeation from the uppermost layer. In this layer, the hydrocarbon structure is likely to face slight oxidation leading to O- and N-containing groups like C=O, N-C=O, N-C-O.

III) The third layer sufficiently away from the air exposure mainly contains hydrocarbon and nitrogen-containing groups, i.e., amines, imines, nitriles and secondary or a tertiary form of the aforementioned groups resulting from the plasma polymerisation of ethylene with ammonia.

C1s curve fitting was conducted to investigate the carbon environment and explore different functional groups. For C1s curve fitting, the two scenarios previously described in Chapter 3 (3.4.2.1) were used:

A) With the first scenario depicted in Figure 87, based on the data (305) obtained from the analysis of conventional polymers with similar functional groups, the C1s peak consisted of 4 peak components at 285, 286.4, 287.9 and 288.9 eV, respectively. The large increase of intensity occurred from 9 to 23% for the second peak component corresponding to C-(O, N) at 286.4 eV, which was accompanied by a large decrease in the intensity of the main hydrocarbon peak i.e., C-(C-H) at 285 eV from 88% to 71%, between the first two coatings (position 3 and 4). The increase occurred after the introduction of ammonia in the discharge at a flow rate ratio of 4/7 NH_3/C_2H_4 (coating 2: position 3 for low particle density and position 7 for high particle density zone).It then remained constant for the next two coatings (positions 1, 2 and positions 5, 6). The next peak component at 288 eV, which contributed to around 5% of total C1s area under the peak, was supposed to result from O-C-O and O-C=N. The intensity for this peak remained constant for all three coatings deposited in the presence of ammonia. Here again, a more pronounced evolution of the intensity was expected from coating 1 to

coating 4, than was actually the case. The last peak component at 288.9 eV contributed to 1% or less of the total composition. As can be seen, this did not vary between the four coatings by a change in the composition since it concerned mainly the uppermost part of the coatings. This peak was expected to be caused by the carboxylic group O-C=O.

Due to the particular chemistry of plasma coatings, these results imply that the first scenario, which is suitable for XPS analysis of standard polymers, is probably not well adapted to the deposited coatings in the context of the current study. As a result, we offered a second scenario based on the study of comparable plasma coatings in order to achieve a more relevant interpretation of the XPS data.

B) Based on the second scenario, the C1s deconvolution yields 5 peak components, as shown in Figure 88. The first component, corresponding to hydrocarbon bonds, appeared at 285 eV. Then, with a slight shift, the second peak component occurred at 285.7 eV, which was attributed to the primary amine, C-N. The intensity of this peak was less than 1% in the first coating, increased to 8% in the second coating and remained constant at 11% in the last two coatings, which were deposited at a higher ammonia rate. This second fit seemed more pertinent as it showed a more constant increase of C-N bonds when adding ammonia to the discharge. The next peak component at 286.5 eV was related to the C-O/C=N/nitrile bonds with a total higher intensity than the primary amine intensity recorded in the previous peak. One probable reason is that oxidation reactions involving instable primary amines and other groups are involved. This assumption is supported by a continuous increase in peak intensity along the four coatings, starting with an almost twofold increase along the first two coatings (9% to 17%), before it increased, remaining at 19% along the last two coatings with higher primary amine groups.

The third peak was predicted to be mainly derived from imine functional groups with some nitriles in lower quantities for NH_3/C_2H_4 precursor depositions compared to plasma deposition with monomers such as cyclopropylamine and allylamine with initially occurring C-N bonds. Then, due to higher oxidation levels of the hydrocarbon and N-containing chemical groups, the fourth peak component at 287.8 eV corresponding to O-C- (O,N) and/or amide, N-C=O emerged. A slight increase in the intensity of this peak was observed from 3 to 6 at.% between coating 1 and coating 2, and it then remained constant for the next two coatings. The last peak component at 288.9 eV with marginal intensity, with 1% or less contribution, corresponded to

the carboxylic group originating from a higher oxidation of the coatings at the uppermost layer due to a higher interaction with surrounding environment.

In conclusion, the curve fitting results for both low and high Au nanoparticle density regions followed very similar trends, which proves the similar chemical composition of the C1s neighbouring groups for the two regions, regardless of the gold nanoparticle sublayers. It also indicates that the density of Au NPs does not generate an enhanced signal for some chemical groups. According to the second curve-fitting scenario, the unsaturated nitrogen groups (i.e., imine and nitrile), as well as the C-O group, had the largest abundance among functional groups. The creation of the primary amine gradient was confirmed by a clear gradual evolution of the C-N bond along the gradient surface immediately after ammonia introduction in the surface for the third and fourth coatings. The oxidated functional groups were identified in reduced abundance compared to the previous groups, with the carboxylic acid group having the least amount.

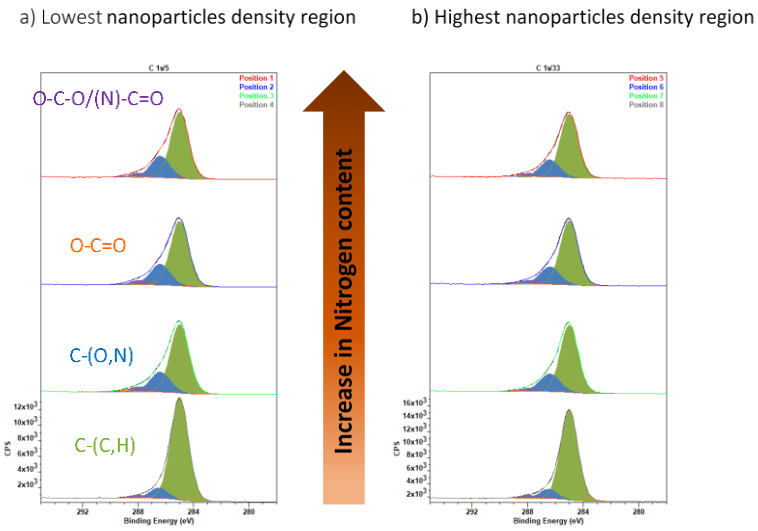

a)

Sample identifier	C- (C, H) %	C-(O,N) %	O-C-O/(N)-C=O %	O-C=O %
Position 1	70	24	5	1
Position 2	70	24	5	1
Position 3	71	23	5	1
Position 4	88	9	3	<1

b)

Sample identifier	C- (C, H) %	C-(O,N) %	O-C-O/(N)-C=O %	O-C=O %
Position 5	74	21	4	1
Position 6	73	22	4	<1
Position 7	74	22	3	<1
Position 8	88	9	3	<1

Figure 87. C1s high resolution peak deconvolution on 8 different spots analysed with XPS along the generated 2D gradient surface based on the first scenario. The curve fitting yielded a total of 4 underlying curves, each attributed to different functional groups. The peak assignments and respective quantifications are summarised in tables for a) 4 points in the low particle density zone and b) 4 points on the high particle density zone.

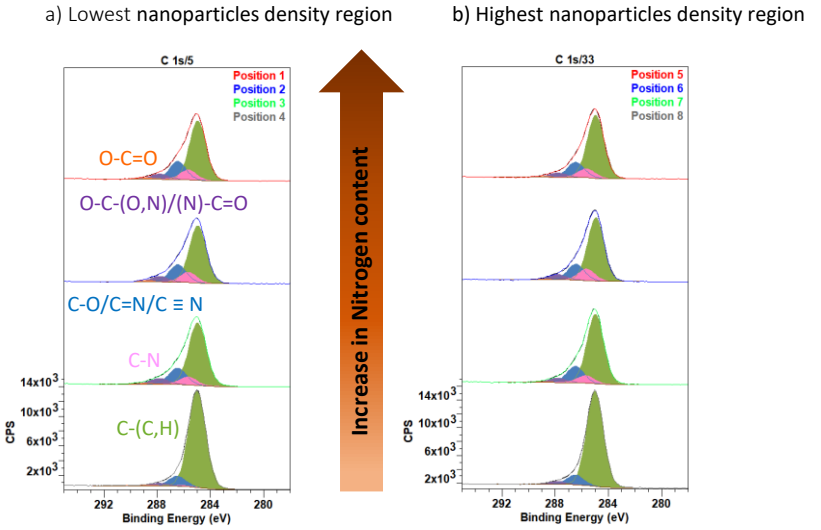

a)

Sample identifier	C- (C, H) %	C-N %	C-O/C=N/C ≡ N %	O-C- (O, N)/(N)-C=O %	O-C=O %
Position 1	63	11	19	6	1
Position 2	62	11	19	6	1
Position 3	67	8	17	6	1
Position 4	88	<1	9	3	<1

b)

Sample identifier	C- (C, H) %	C-N %	C-O/C=N/C ≡ N %	O-C- (O, N)/(N)-C=O %	O-C=O %
Position 5	68	10	17	5	1
Position 6	65	12	17	5	<1
Position 7	70	8	17	5	<1
Position 8	88	<1	9	3	<1

Figure 88. C1s high resolution peak deconvolution at 8 different spots analysed with XPS along the generated 2D gradient surface based on the 2nd scenario. A total of 5 underlying curves were found, each attributed to different functional groups. The peak assignments and respective quantifications are summarised in tables for a) 4 points in the low particle density zone and b) 4 points in the high particle density zone.

5.2.2 Molecular composition of the top layer

Besides elemental analysis, the molecular analysis was conducted on a 2D gradient to compare it with the reference chemistry gradient results, aiming to unravel the role of sub-layer conductive particles in the possible alteration of the coating or the intensity of characteristic fragments. Therefore, as with the XPS procedure, a total of 8 points were selected on the two extreme edges of the topography gradient (high particle density and low particle density), as well as along the width of the chip and in each chemistry gradient coating condition.

TOF-SIMS analysis was applied on 1x1 mm^2 spots on both edges of the sample and the spectrum obtained from the secondary ions were identified for positive and negative ion modes for a mass range varying between 0-300 Da, as demonstrated in Figure 89 and Figure90 for high particle and low-particle density zones, respectively. Some of the key fragments with high

intensity, which were easily visible in the current spectrum magnification are C_2H^-, CN^-, C_4H^-, $C_2N_2Au^-$ for the negative scanning and $C_2H_5^+$, CH_4N^+, $C_4H_9^+$, $C_2H_6N^+$ for the positive scanning mode. The most intense peaks were located in the 0-60 m/z region for positive and negative ions, with the exception of $C_2N_2Au^-$, which appeared at 249 m/z.

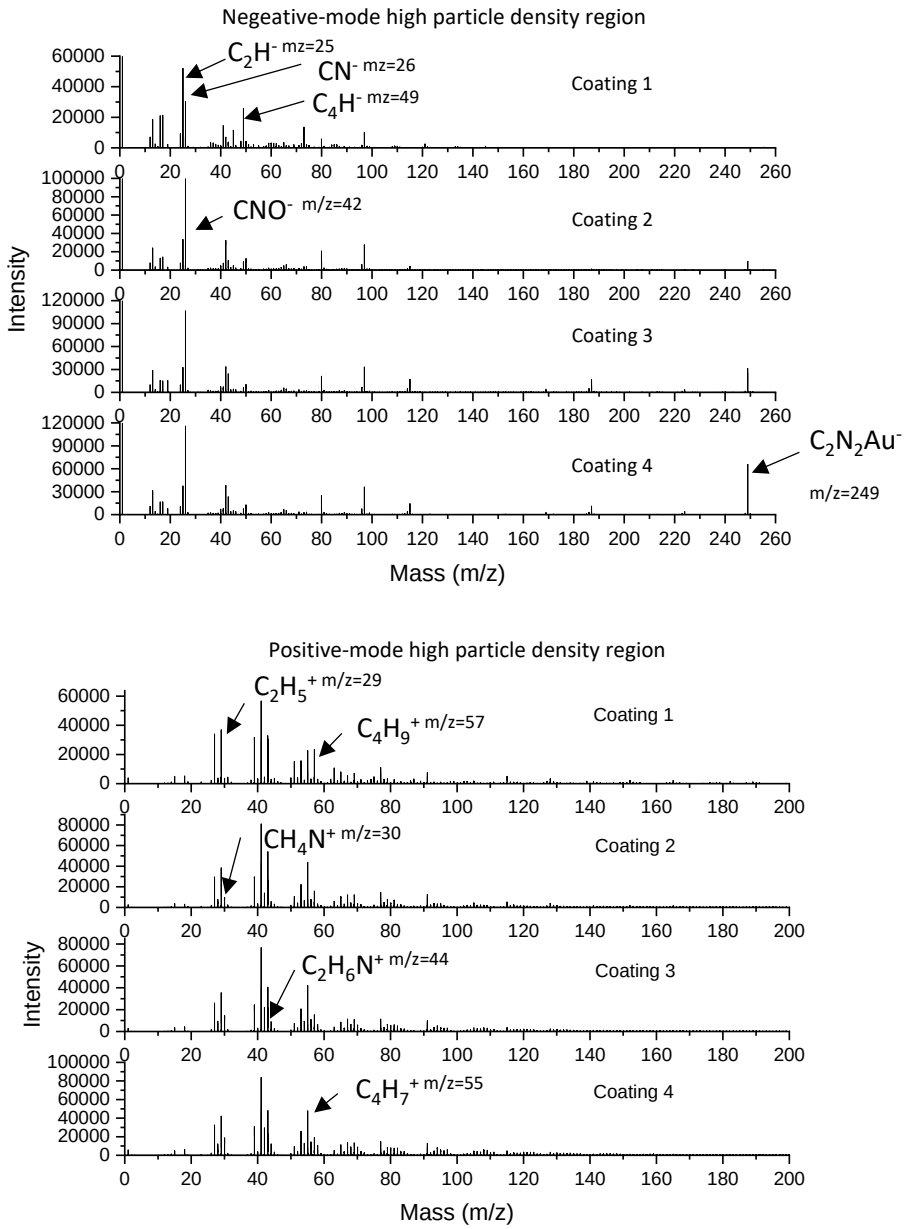

Figure 89. The ToF-SIMS spectra for negative and positive scan modes performed on 4 regions of interest (ROI) along the chemistry gradient in the high-particle density zone. Each investigated area was 1*1 mm^2 and was selected in the centre of the coatings. Some prominent fragments and the related mass numbers are assigned to the respective peaks.

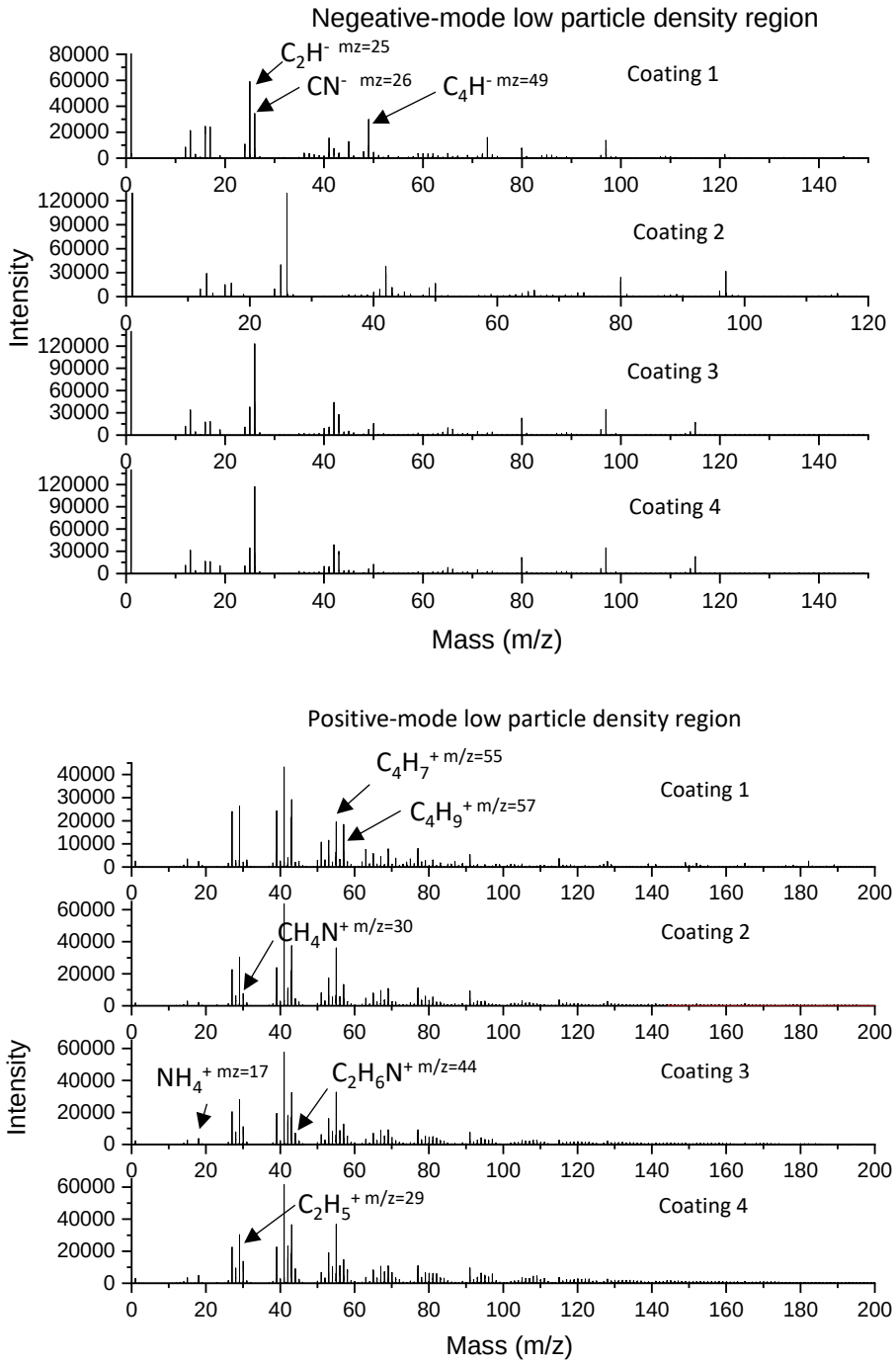

Figure 90. The ToF-SIMS spectra for negative and positive scan modes performed on 4 regions of interest (ROI) along the chemistry gradient in the low-particle density zone. Each prominent peak is identified by the molecular fragment and the related mass number.

- ***Chemistry variation along the length (topography gradient direction)***

To investigate the TOF-SIMS results on the topography gradient direction, the intensity of a fragment on each of the four coatings in the low-density region was compared to the intensity of the fragment in the high particle density area on the same coating (e.g., point 1 compared to point 5). Comparing the intensity of identical peaks in Figure 89 and Figure90 did not reveal any recognisable difference which could directly account for the influence of the nanoparticle density gradient sublayer. Considering the peak intensities along the topography gradient, the only noticeable difference between the intensity of fragments between two extreme regions among all the detected fragments was for the gold-containing fragment $C_2N_2Au^-$. This fragment was very abundant in the high-particle density zone as expected and the intensity of this nitrogen-containing fragment was amplified in parallel to the increase in the nitrogen content of the coating from coating 1 to coating 4.

- ***Chemistry variation along the width (chemistry gradient direction)***

The fragments which followed the evolution parallel to the increase in the ammonia/ethylene flow rate ratio in discharge were tentatively selected as markers to study the nitrogen-functional gradient composition. After investigating the most intense peaks showing gradual contrast based on the acquired images, $C_2H_6N^+$, CH_2N^+, and CH_4N^+ were selected. TOF-SIMS images for the pertinent fragments, $C_2H_6N^+$, $CH_2N^+$and CH_4N^+, presented a good gradual contrast in the direction of increase in N% from XPS. As the CH_4N^+ molecular fragment followed best the N% and C-N% (from XPS C1s fitting) variations along the chemistry gradient (see Figure91), it could be regarded as a pertinent representative of nitrogen-containing groups in the coatings. The next prominent fragments which did not display a gradient intensity were identified at 26 m/z attributed to CN^- and 42 m/z corresponding to CNO^- with high intensities. CN^- and CNO^- fragments were found to be the most abundant ions in the whole spectra showing a saturation in intensity with the applied analysis parameters for N-richer coatings.

As stressed in Chapter 3 (3.4.2.2), the hydrocarbon fragments tend to be less reliable for drawing a conclusion about the evolution of ethylene during polymerisation therefore, while the gradual variation of the intensity is desirable, there is still little certainty about the origin of these ions. Considering the hydrocarbon fragments, the intense peaks showing gradual contrast were identified as $C_2H_5^+$ m/z=29 and $C_4H_9^+$ m/z=57 in positive scan mode and C_2H^- m/z 25 and C_4H^- pair at m/z=49 in negative mode. In both topography zones (the high particle density and low particle density) along the chemistry gradient, these fragments decreased gradually in the

opposite direction to the increase in ammonia/ethylene ratio in the discharge, as expected. The next intense spotted peak was detected in coating 4 at 249 m/z corresponding to the $C_2N_2Au^-$ fragment arising from the gold nanoparticle sublayer, which possibly formed after a gas phase reaction of the gold with the CN^- fragment. The variation in intensity of this peak was gradual in the direction of the increase in ammonia in the discharge from coating 1 to coating 4. This fragment was not visible in low particle density spectra, as expected, due to the much lower abundance of gold. The increase in intensity of this fragment was not high enough to observe a metal enhancement effect and the significant thickness of the top polymer coating (10 nm) might have prevented an efficient signal enhancement. The contrast images for some fragments obtained from TOF-SIMS scanning on the points along chemistry gradient are presented in Figure 92 and Figure 93.

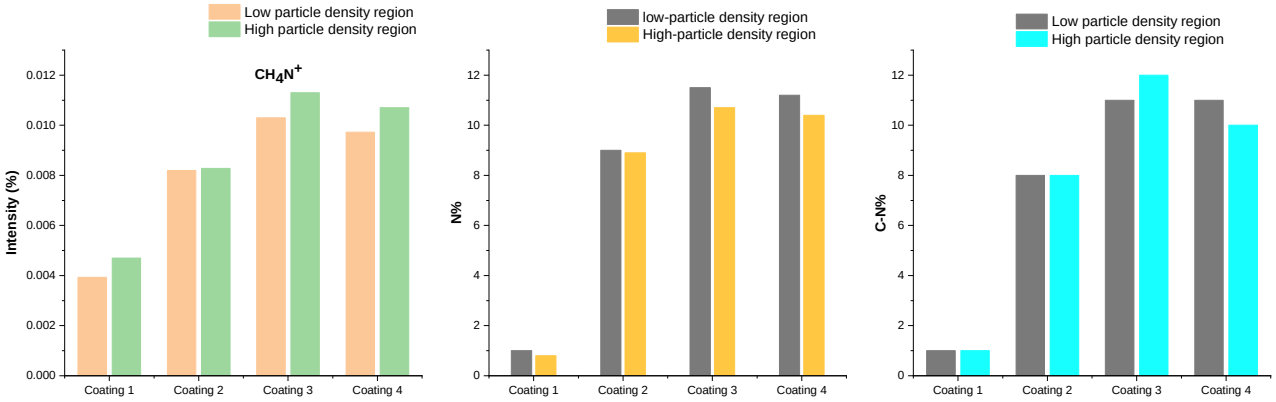

Figure 91. The TOF-SIMS signal intensities of the scanned points at low and high nanoparticle densities for some characteristic fragments: a) CH_4N^+ and, XPS quantifications results for b) N%, and c) C-N% obtained from C1s deconvolution peak are plotted versus the varied ratio of ammonia to ethylene in the discharge, on 4 distinct corresponding coatings.

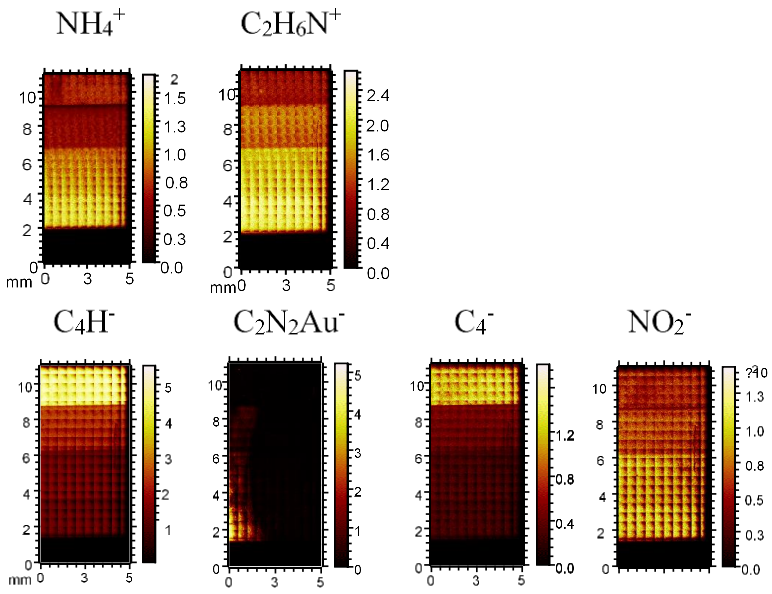

Figure 92. Positive mode TOF-SIMS images of secondary ion species obtained on 10×10 mm^2 area along the chemistry gradient direction.

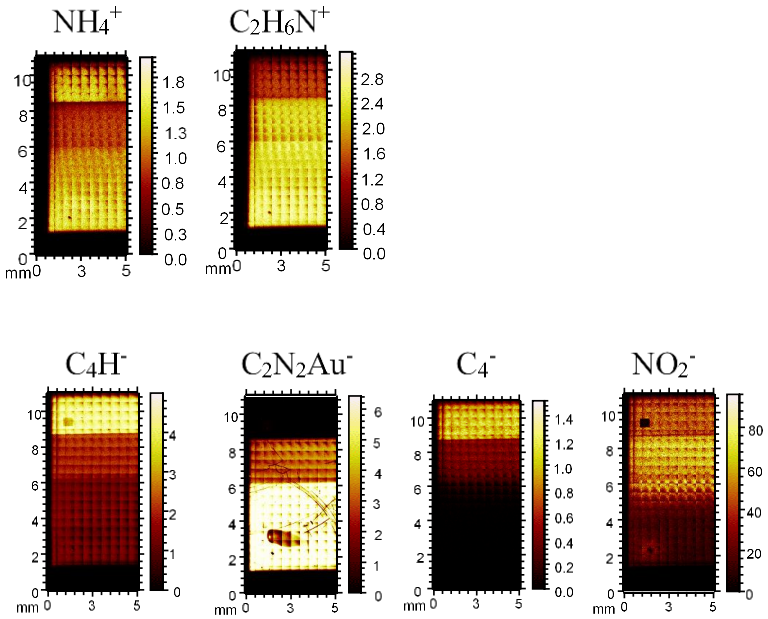

Figure 93. Negative mode TOF-SIMS images obtained on a 10×9 mm2area along the chemistry gradient (width of the chip).

The fragments listed in the contrast images show similarity for the low density and high-particle density zones, except for the two nitrogen-containing fragments, $C_2N_2Au^-$ (for the already explained reason) and NO_2^-. A detailed comparison of these two fragments reveals that they vary in opposing directions, so that in low density regions where $C_2N_2Au^-$ is rare, NO_2^- is abundant, and vice versa in high density regions. This might imply that these fragments are created from a single source fragment via two competing processes, which means that while one reaction prevails, the other is hindered, resulting in a high abundance of one and a low abundance of the other. Finally, while comparing two extreme zones of low particle density and high particle density, an intensity gradient of the $C_2N_2Au^-$ fragment was identified. Furthermore, because gold was attached to C-N, there was a parallel increase in the intensity of this fragment along the width of the chip (chemistry gradient direction). Also, CH_4N^+, the primary amine fragment, could be considered the most relevant fragment. As illustrated in the respective micrographs, a steady variation, parallel to an increase in ammonia in discharge was observed for this fragment, supporting the establishment of an amino-functional concentration gradient. This conclusion was likewise consistent with the results of the XPS N% and curve fitting results (C-N%). A few more significant fragments with XPS-supporting differences were discovered, which, as previously mentioned, might be directly linked to the surface coating or may have resulted from the analysis process following fragmentation and recombination.

5.2.3 Morphology of the surface before applying the top coating

The surface topography analysis was performed using the AFM tapping mode on selected points along the Uni-directional topography gradient before deposition of the top polymer gradient coating. The objective was to compare the surface topography of coated and untreated particles. Despite the fact that particles appear closer together in AFM micrographs than in actual electron microscopy images, AFM is a viable method for characterising electrical insulator coatings, such as polymers. The data that we intended to extract from AFM topography micrographs were root mean square roughness and the roughness factor to be used for surface wettability interpretations. Figure 94 presents the obtained AFM micrographs on a 1.04x1.04 μm^2 area at several points along the topography gradient prior to coating with a 10 nm nitrogen-functional chemistry gradient layer. As is evident from the particle distributions, a successful number density gradient was generated along the CHN template as a function of exposure time. Overall, there was only a modest variation in the total roughness of the scanned regions along the gradient coating, which never exceeded 4 nm.

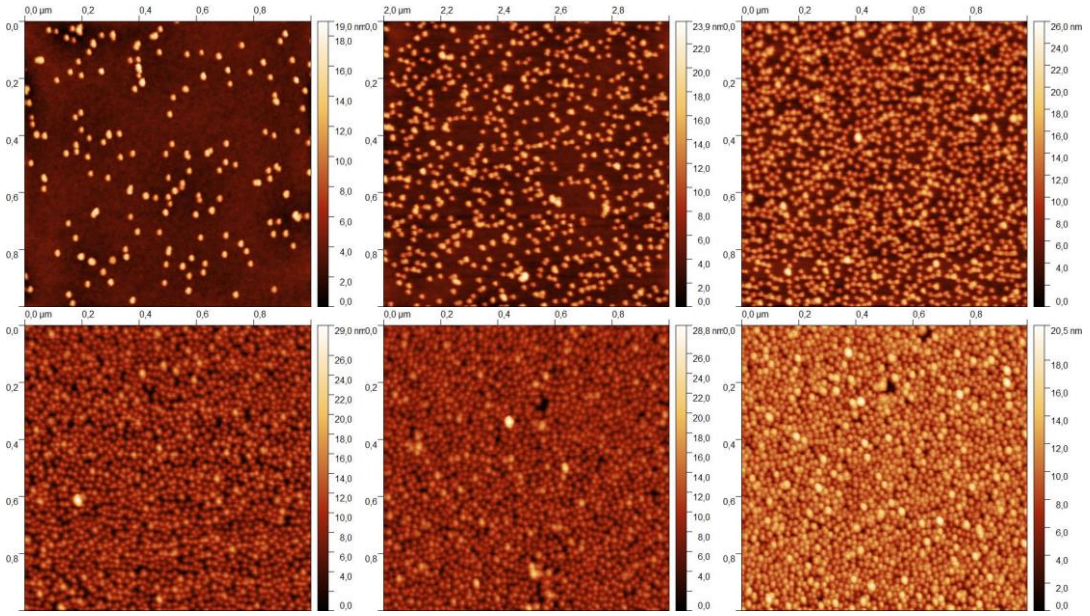

Figure 94. AFM tapping mode topography images obtained along a 1-D topography gradient (without the top coating layer). The scanned region was 1.04x1.04 μm^2 and the scanned points correspond to a) 2mm, b) 4mm, c) 6 mm, d) 8 mm, e) 10 mm, f) 12 mm and g) 14 mm from the edge.

As R_q values obtained from AFM micrographs support (see Figure 95), a lower surface roughness was observed where the surface was covered with few particles, followed by a gradual increasing trend in roughness values due to the increase in the number of the particles, implying that more heights and valleys contributed to the surface roughness. However, after reaching a plateau in R_q corresponding to a point scanned at 6 mm distance from the low particle density zone, where there still was a high surface coverage with particles appearing with a moderate interparticle separation, the roughness values started following a decreasing trend. This was due to the fact that a further increase in the density of approx. 11 nm particles decreased interparticle separations, and a gradual decrease in the height of the peaks and depth of the valleys was recorded in AFM surface profiles. Therefore, in the extreme high-particle density zone, the surface appeared smoother with fewer surface waviness. As noted in the topography variation trend of the uncoated particles (Figure 95, the black curve), the R_q values followed a gaussian-like trend with a maximum value obtained at a 6 mm horizontal distance from the particle-free edge. After this point, the curve followed a gradual and continuous decreasing trend until the last scanned point.

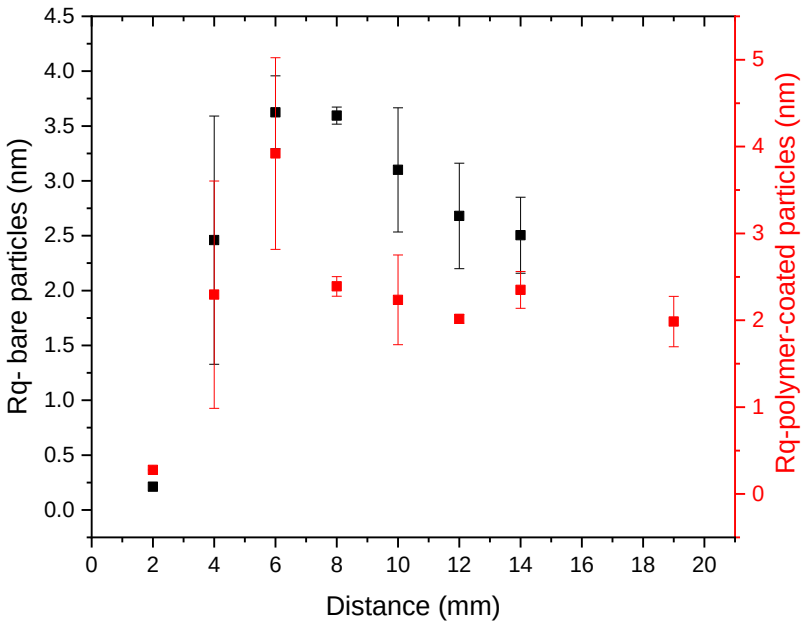

Figure 95. The root mean square surface roughness variation obtained from the AFM tapping mode at several points along the 1-D topography gradient (black squares) and orthogonal gradient (red squares) is presented as a function of distance from the low particle density edge of the gradient.

It should be mentioned that, due to tip convolution, the expected roughness values for the points scanned after the peak point (highest roughness value), when particles were becoming tightly packed, were quite different from the reality. This is due to nanoparticles with diameters considerably smaller than the AFM tip appearing larger, and the spacing between the structures being ignored by the tip, resulting in lower roughness values. Figure 96 depicts the described tip convolution effect (5).

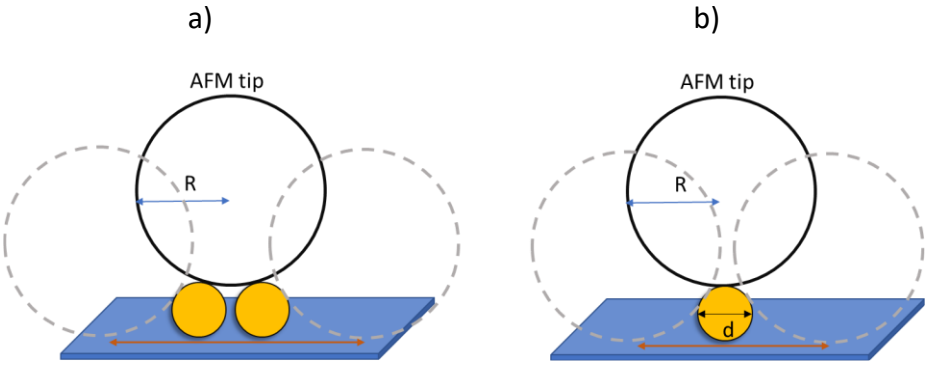

Figure 96. Comparison between tip diameter and structure size. a) high particle density zone is affected more by tip convolution and the separation between particles can even be neglected. The lateral distance sensed by the tip is longer in this case. b) The low particle density zone is less affected by tip convolution.

The following equation can be used to express the lateral length of a structure expected to be obtained from an AFM micrograph. (306):

$$d_{AFM} = 2\sqrt{2R_{tip} \cdot d_{particle}} \qquad 5.1$$

As an example, for the conventional AFM tip of 10 nm curvature radius and 11 nm particle diameter, the AFM lateral length is equal to d_{AFM}=14.83 nm, hence the topography analysis of the particles with an interparticle separation smaller than this number will suffer from the tip deconvolution.

5.2.4 Morphology of the 2D gradient surface (after applying the top coating)

The acquisition of AFM topography images was carried out along the topography gradient after coating the particles with a 10 nm plasma polymer top layer. The 3D micrographs obtained on a 1.04x1.04 μm^2 area are presented in Figure 97. The micrographs recorded at several points along the gradient showed a considerable variation in surface topography at the first three points, Figure 97 (a, b and c) corresponding to **i)** an initially flat plain recorded at 18 mm distance from the nanoparticle dense edge, where the surface was particle-free; **ii)** the gradual appearance of particles and, **iii)** the appearance of visibly thick particles as a result of the increase in density and the deposition of a top coating. After Figure 97 (c), where roughness was at its maximum, it was hard to differentiate the thickness of the surface features when comparing the micrographs. Figure 98 depicts the predicted surface topography, i.e., the geometry of surface features and interparticle spacing, after covering the nanoparticles density gradient with the top plasma polymerised gradient layer.

To compare the topographical properties of some scanned points for the uncoated and coated nanoparticles along the gradient length, and explain the roughness trend, the height profiles of the particles in both nanoparticle density zones were extracted as presented in Figure 99. The height profiles were obtained from AFM micrographs after drawing an arbitrary line along the surface for the two pairs of micrographs, corresponding to the 2nd and 6th scanned points for both the (unidirectional (uncoated) and orthogonal (coated)) gradients. Considering the total 15 mm length for topography gradients (on a 20 mm long diced Si chips), the selected 2nd point was 4 mm away from the particle-free edge showing a moderate nanoparticle density and the 6th point was located at 12 mm from this edge showing high nanoparticle density. When comparing micrographs, the first observable differential point between each set of images (a with b and c with d) was obviously the difference in dimension of the particles from the two gradients. As expected, when coated with a 10 nm thick conformal plasma coating (2D gradient), the gold nanoparticles of 11 nm diameter clearly appeared larger than the uncoated particles. However, considering the cross-section view in the height profiles, the diameter of the coated particles was underestimated in the height profiles since in theory, the uncoated gold nanoparticle with an average 11 nm diameter yielded a spherical cap structure with 28.98 nm diameter when coated with 10 nm thick polymer (at lower density zones), which was not recognisable in the profiles. Also, when comparing the height of the features in the low-density region (Figure 99a and Figure 99b), no considerable difference between the height of the features was noted. This was expected since 1) The height of the features both in coated and uncoated particles is approximately 10 nm based on theory (compare green and red arrows in Figure 98). It should be reminded that, besides particles, the base plane was also coated with the polymer coating up to 10 nm in height and the features were measured from the base line in AFM studies (illustrated with red arrows in Figure 98); 2) In the high-density region (Figure 99 c and d) as a result of fusions of the adjacent spherical caps and possibly due to the tip convolution effect, the height of the features decreased after being coated. Since the height of asperities and valleys in the height profile is directly proportionate to the surface roughness, it can be inferred that the surface roughness in point 6 corresponding to uncoated particles is higher compared to the coated particles (comparing height profiles in Figure 99 ii and Figure 99 iii). Also, the sticking of the coating on Au nanoparticles is expected to be slightly lower than the sticking on the plasma polymer film (plane surface), hence, the surface mobility of the film-forming species may have also contributed to the observed smoothening in the high particle density zone.

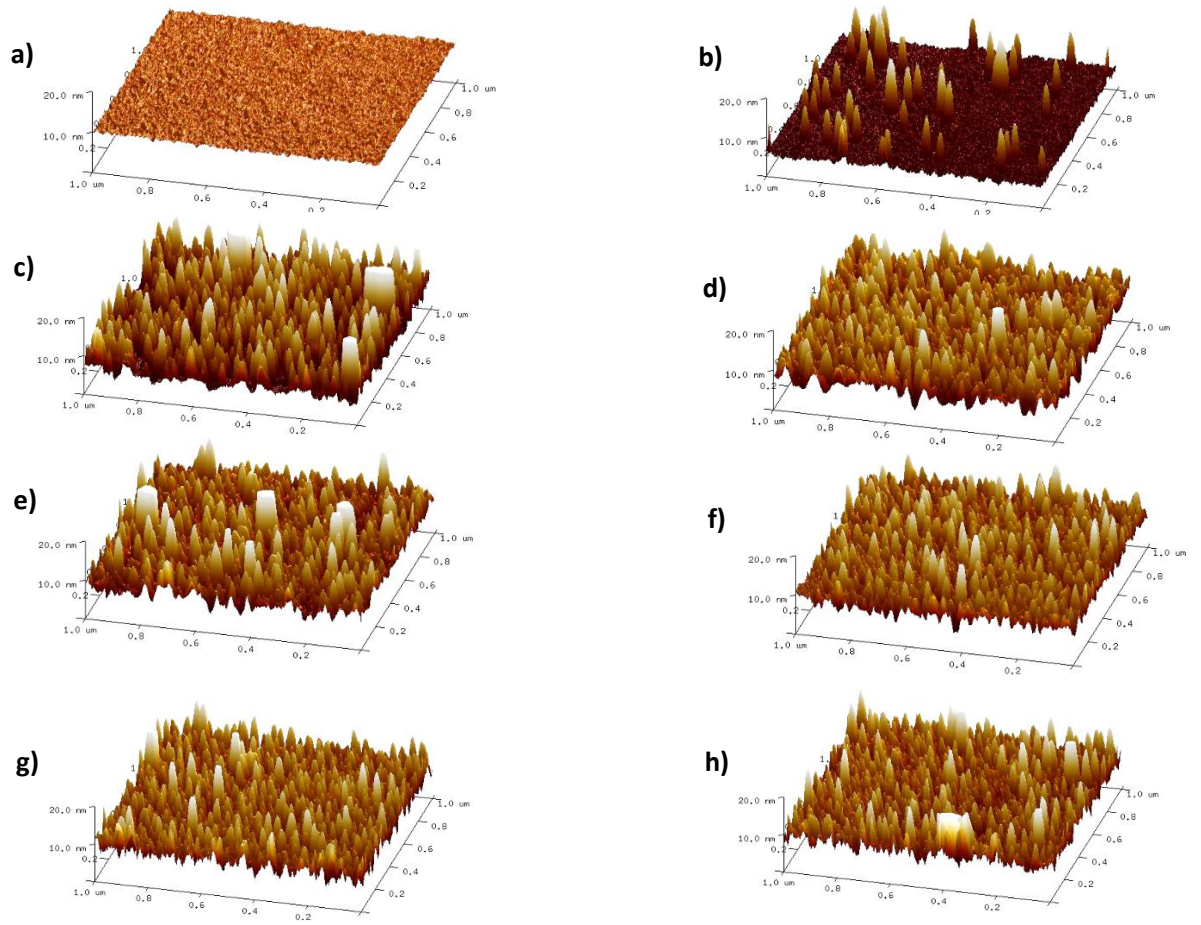

Figure 97. 3D AFM tapping mode topography images obtained at several points along the nanoparticle density gradient after being coated with a top layer. The scanned region was 1.04*1.04 µm2 and points were scanned every 2 mm (except for t the last point) starting from the low particle density edge of the sample. a) 2mm from the edge, b) 4mm, c) 6 mm, d) 8 mm, e) 10 mm, f) 12 mm, g) 14 mm and h) 18 mm.

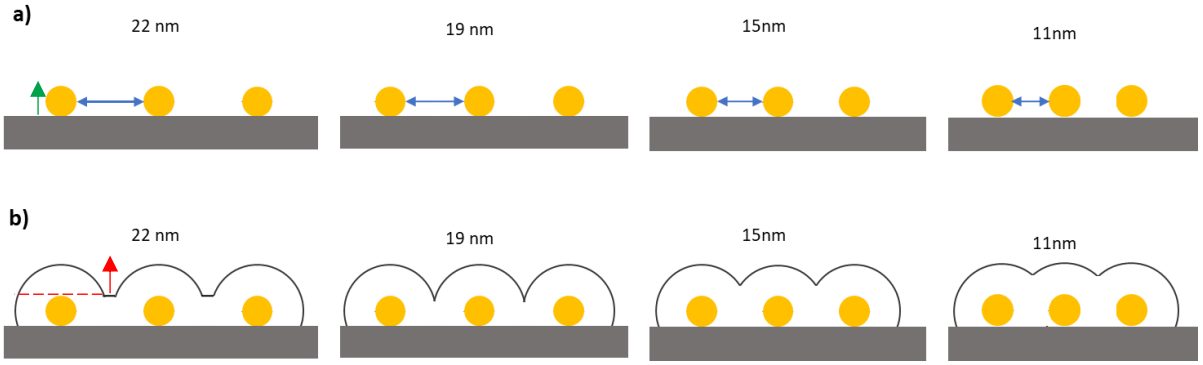

Figure 98. Simulation of separation/density gradient of 10 nm particles a) without top coating, which can suffer from tip convolution at higher densities and b) coated with 10 nm polymer. Fusion is inevitable when the interparticle distance is lowered. The difference recorded between roughnesses is expected to be negligible, giving rise to an almost linear trend.

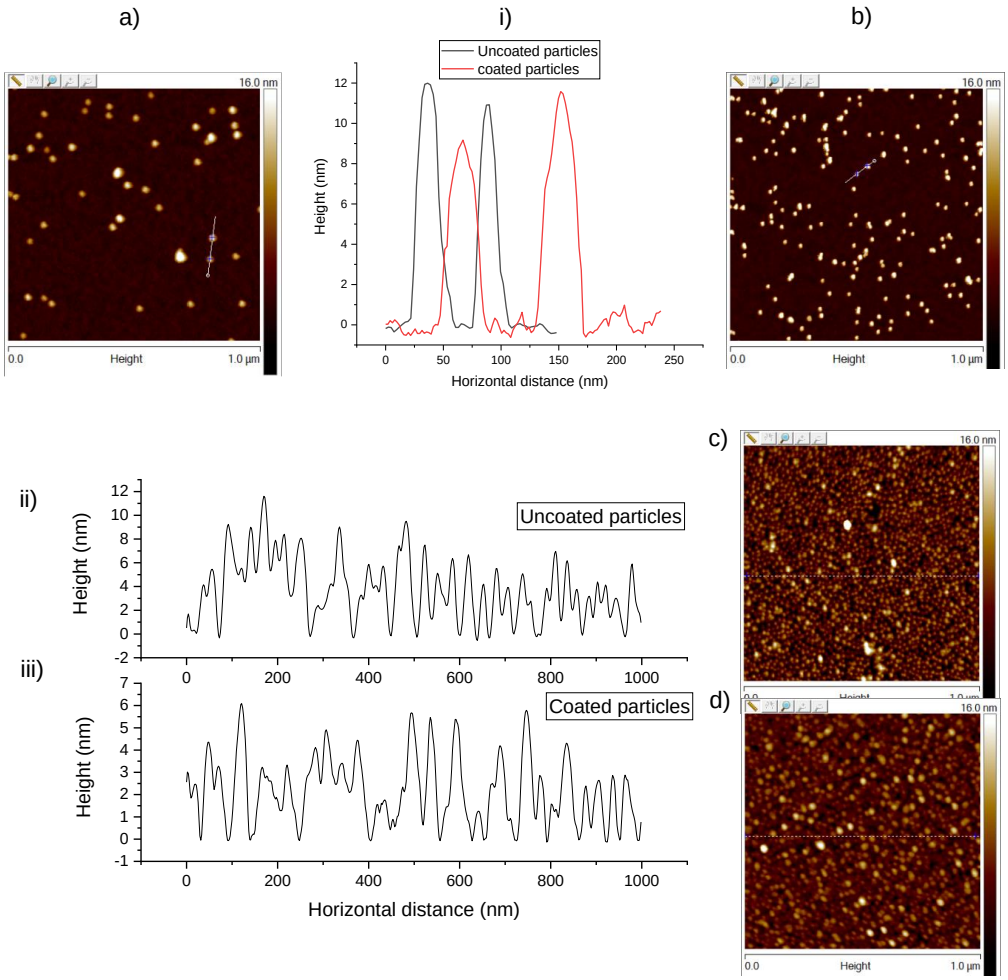

Figure 99. The 2D AFM micrographs of the a) uncoated and b) coated particles on the same scanned points corresponding to a low density region is presented. The height profiles extracted after drawing an arbitrary line on each of the surfaces are shown (i). Similarly, (c, ii) and (d, iii) correspond to the AFM micrographs and height profiles of the uncoated and coated particles obtained at a dense scanned zones, respectively.

The other important parameter extracted from the AFM tapping mode topography micrographs was roughness factor, which is described in detail in Chapter 2, (2.2.3). This parameter is mainly derived to interpret surface wettability behaviours in the subsequent sections. The roughness factor variation as a function of distance along the gradient is presented in Figure 100 for the 1-D gradient (uncoated) and 2D gradient (coated). Roughness factors follow a similar trend with R_q variation (shown in Figure 95) with the difference that for uncoated particles, the maximum roughness factor value was achieved at 8 mm while for coated particles, the peak value appeared at 6 mm from the particle-free edge (low density zone). This

difference is attributed to the intrinsic difference between the roughness root mean square value and roughness factor as two distinct parameters that consider different surface attributes.

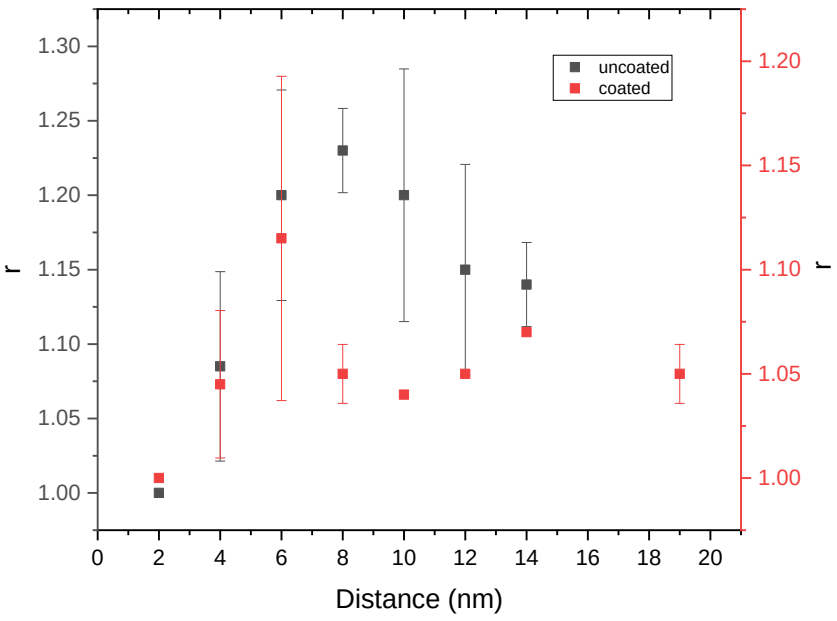

Figure 100. The roughness factor variation obtained from the AFM tapping mode on 1-D (black squares) and the orthogonal gradient (red squares), along the topography variation direction, is presented as a function of distance from the low particle density edge of the gradient.

5.3 Properties of the 2D gradient: Wettability of the surface

The static water contact angles were measured on the 2D gradient at several points along both gradient directions (chemistry gradient and topography gradient), as presented in Figure 19. Here, unlike the unidirectional topography gradient (uncoated particles), a water droplet placed on the surface touched a homogenous chemistry surface, which was roughened by the sublayer nanoparticles. Relying on this fact and the overall lower roughness values obtained on the 2D gradient compared to the uncoated sample (as demonstrated in Figure 101), the wettability is expected to be mainly impacted by the surface chemistry of the top-coating. Here, the observations from the wettability of the 2D gradient are summarised as:

i) The first three plasma coatings displayed a very similar wettability behaviour with no recognisable variation between the three coatings. However, the last coating deposited with high plasma pressure showed remarkably higher hydrophilicity.

ii) The highest particle density region scanned on each of the 4 coatings, consisting of the chemistry gradient, showed higher WCA values (lower hydrophilicity), especially for the first plasma coating, which was deposited without ammonia; a total variation of 11.9° was observed along the topography gradient.

Briefly, along the chemistry gradient direction, the highest wettability was recognised only for the last coating (coating 4), which had the highest hydrophilicity, and in the topography gradient direction, the last point scanned on the densest zone displayed the highest hydrophobicity. As previously practised with the unidirectional topography gradient (uncoated particles), it was attempted to model the wettability behaviour of the 2D gradient against variation of the nearest neighbouring distance (NND) between particles. As clearly proven in AFM micrographs, the conformal plasma coating with approx. 10 nm thickness retains the morphology of the particles after being deposited. Therefore, spherical particles (or more precisely, the spherical cap) with bigger dimensions and a closer interparticle gap are expected. And, since the surface roughness (R_q and r) declined overall in the 2D gradient, the Cassie-Baxter regime was unable to describe the wetting properties, therefore, a theoretical model was developed considering the full exposure of the surface structures to liquid, and the Wenzel regime was used for the modelling. Calculations and further details of the developed model are provided in Chapter 2 (2.2.4.2.2). Briefly, the following equation was developed for the NND≥20 nm:

$$r = \frac{\pi R'^2 (1 - \cos\beta)^2}{(S + 2R\sin\beta)^2} + 1 \qquad 2.32$$

After replacing β= 73.12° and R‘=15.5 nm, the equation was simplified as:

$$r = \frac{370}{(29.5+s)^2} + 1 \qquad 5.1$$

With this equation and assuming r=1 for 10<NND<20, the theoretical roughness factor curve as a function of NND and NND’ (for the coated particles) was obtained and the respective curve is presented in Figure 102. Here, the model indicates that the highest surface roughness belongs to the region on the surface where gold nanoparticles were immobilised with 20 nm interparticle distance, which led to the formation of tangential (not overlapping) spherical caps. The points before and after this peak point presented lower variation slope. To make processing the complicated geometrical structures simpler, the roughness factor was fixed at 1 for the

points before the peak value, assuming a smooth surface due to a higher degree of overlapping between the formed spherical caps (see Figure 98b). The minimum gap possible between the particles that enabled the structures to overlap was 10 nm. The points after the peak roughness factor point followed an equation in which the height of the generated spherical cap was a fixed value, and the only variable parameter was the distance between particles (NND) and accordingly, the gap between the spherical cap structures (s).

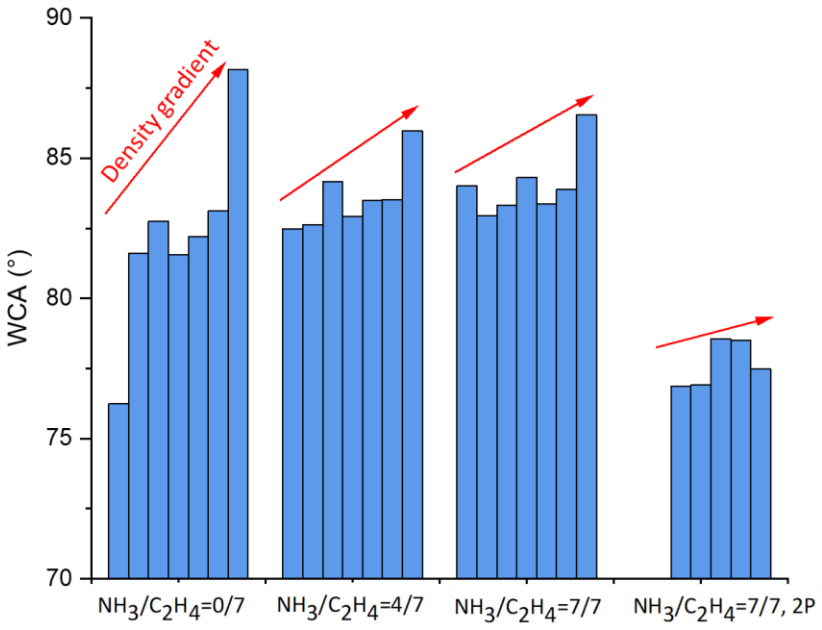

Figure 101. The static WCA values obtained at points along both the chemistry and topography gradients. There are four sets of data, each corresponding to one coating condition on the chemistry gradient. The red arrow shows the direction of the increase in particle density or decrease in interparticle gap. The WCAs are recorded every 2mm with automatic stage movement. The volume of the droplet was adjusted to 0.3 µl.

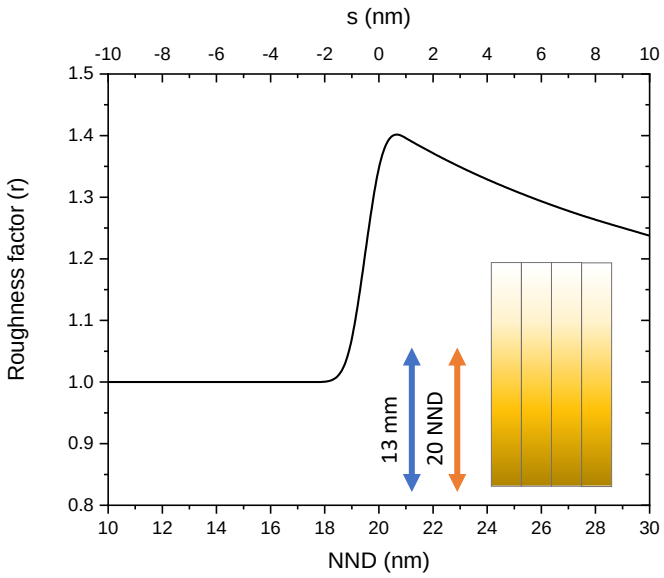

Figure 102. Theoretical roughness factor obtained by modelling the geometrical features of the orthogonal gradient surface as a function of both the NND between uncoated nanoparticles and the separation between coated structures (s). The peak in roughness factor value corresponds to 20nm NND and approximately 13 mm from the dense edge of the topography gradient.

Based on the Wenzel equation, the highest roughness on hydrophilic material generates the lowest water contact angle and highest hydrophilicity. Therefore, it was expected that the highest hydrophilicity value would be attained in the region where the average NND was close to 20 nm (i.e.,13 mm distance away from the denser edge and close to the end of the topography gradient) on the coating 4. On the other hand, based on the experimental roughness values, the peak value for surface roughness was found at 14 mm from the high-density edge, which was not far from the predicted value from the roughness factor model. To obtain the theoretical wettability trend as a function of s, the theoretical r from eq 5.1 and θ from intrinsic wettability values were placed in the Wenzel equation:

$$\theta^* = \cos^{-1}\left(\left(\frac{370}{(29.5+s)^2}+1\right)\cos\theta\right) \qquad 5.2$$

The expected WCA curves for each coating on the 2D gradient and the experimental values are presented in Figure 103 for comparison. It should be considered that to calculate the theoretical curves, WCAs obtained on the low-particle density zone of each coating, where the

surface was supposed to be almost smooth, were replaced in equation 5.2. The reason for taking these WCAs as intrinsic values in the Wenzel equation is that 1) there is no commercially available bulk representative material for this coating to be investigated for intrinsic WCAs; 2) reference chemistry gradient as presented in Chapter 3 demonstrated high values of oxygen, i.e. more than twofold, and since oxygen groups are more effective at increasing wettability than nitrogen groups, the observed WCAs or the reference coatings make them unsuitable for use as intrinsic WCA values.

The x axis of the two set of plots (NND and the distance along the sample) in Figure 103a is coherent and increases in the same direction. This means that moving along the x position shows an increase in particle density and decrease in the interparticle distance. The experimental results showed a minor variation in wettability values, which was in accordance with the theoretical curves. Overall, a declining trend with a shallow slope was observed as it moved to the low particle density zone, however, contact angles never exceeded 70° for either set of curves. Given the measurement errors, the experimental values did not follow the theoretical trend; hence, with the exception of the first point, values did not vary and the critical point with the lowest WCA values was not obvious. This makes sense for such a small magnitude of variation predicted by the theoretical model. The critical WCA values on the theoretical curves correspond to the highest r value, when the interparticle distance reaches 20nm NND; after this point, the WCAs rise with a slower transition. The minimum wettability achieved in the 20nm interparticle gap corresponded to approx. 13 mm distance from the densest end of the gradient, as had been obtained previously based on the experimental calculations on the unidirectional topography gradient.

It can be concluded that while the 2D gradient leads to the gradual alteration of wettability as the third surface property, the trend does not follow a gradual evolution as seen for each individual unidirectional gradient. To improve this trend, the thickness of the top coating must be optimised, meaning that once the overlapping between the coated structures was minimised and the topography was kept similar to 1-D topography gradient, the effect of the chemistry gradient on surface wettability, as the second dimension, can manifest better. However, the disadvantage of the thinner amino-functional plasma polymerised top-coating is the instability in aqueous media (e.g., for biomolecule immobilisation, etc). The counterbalance between stability and surface topography factors would ensure the generation of a successful wettability gradient by the orthogonal combination of the chemistry and topography gradient while maintaining the surface functional groups for intended applications. The second cause of

deviations from the theory as pointed out before is an inherent random distribution of the particles, which can be circumvented by developing ordered surface structures. In this regard, lithography etching techniques for fabricating highly ordered surface structures can be helpful however, the time and costs of the experiment, as well as the requirements for high throughput for developing few nanometre scale surface structures, would counterbalance the advantages.

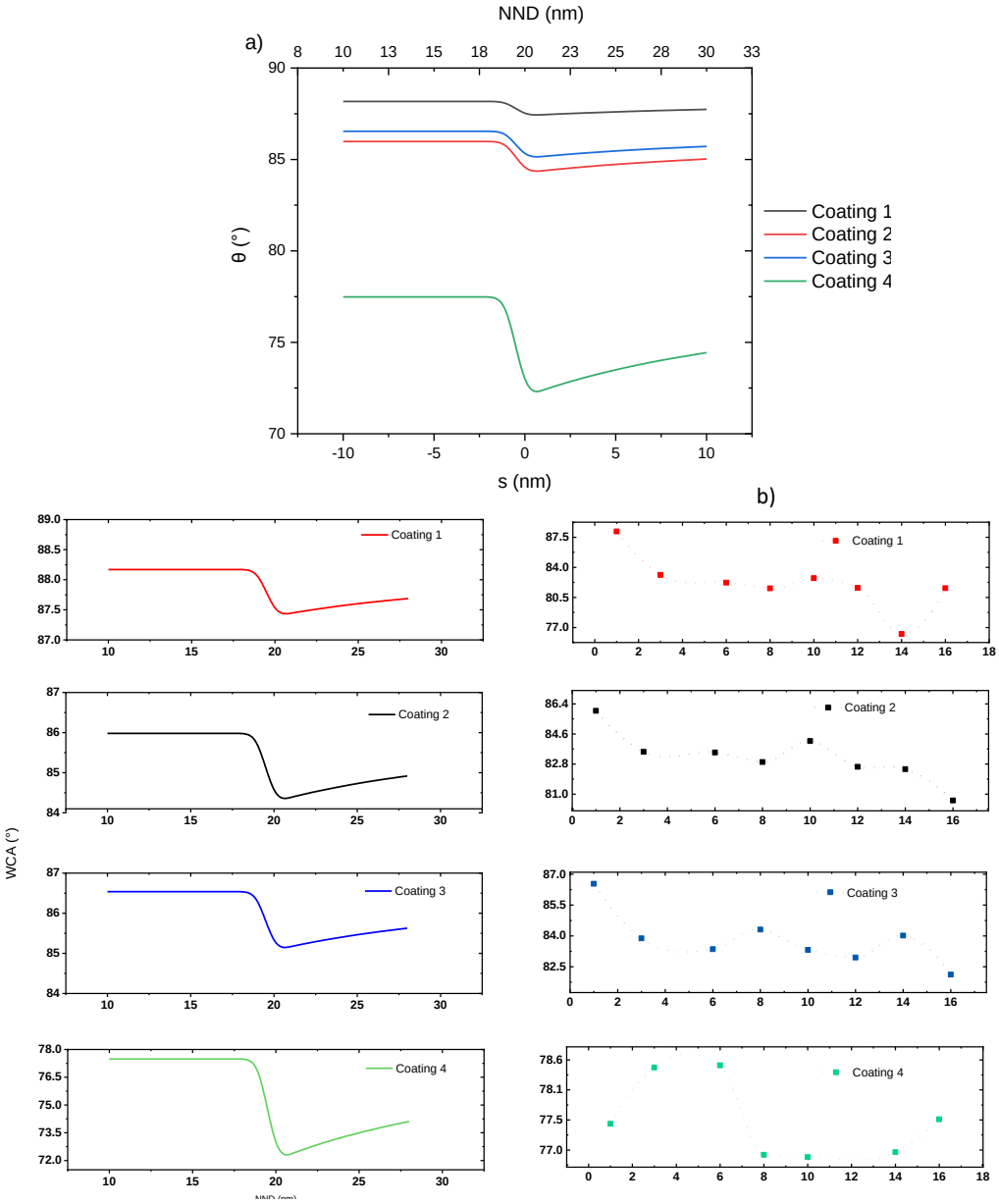

Figure 103. a) Theoretical WCAs obtained using the model developed for the surface roughness factor. The values are for the 2D gradient along the topography direction and as a function of border-border distance (for uncoated and coated) are presented; b) The experimental static WCAs recorded at several points along the 20 mm sample length (right panel) are compared to the corresponding theoretical WCAs versus the border-border gap between the particles (left panel).

5.4 Conclusion and perspectives

In this chapter, a simple and versatile surface modification approach was demonstrated, which combines two gradually varying distinct surface properties to form an orthogonal surface gradient. The generated gradient utilises the synergistic effect of both variables to create a biointerface that allows for high throughput screening and optimisation. As previously stated, surface chemistry and topography both trigger and initiate biological processes, allowing for either screening or driving a biological phenomenon, or even sorting a biomolecule of choice that responds selectively to specific surface variables out of a pool of many biomolecules. The chemistry and topography characterisations demonstrated the successful integration of both unidirectional gradients and the wettability feature of the resulting 2D gradient were studied for prospective applications. According to the surface chemistry characterisations, the presence of the underlying gold nanoparticle seemed to have no considerable effect on the surface chemical composition when compared to the coating deposited on the Si substrate, confirming that the same surface chemistry as for the unidirectional chemistry gradient was retained. The topography of the surface altered as expected after coating it with the top layer, with overall lower roughness compared to the unidirectional nanoparticle density gradient. Additionally, the wettability variation scale of the coating considerably declined when compared to the wettability variations of the incorporated unidirectional gradients.

The distinctive feature of the amino-functional coating was the enhanced stability in aqueous conditions, and since the stability is affected by the thickness of the bilayer coating (i.e., thickness of the crosslinked bottom layer), a future challenge could be optimising the thickness of the chemistry gradient to benefit from the plasmonic feature of the underlying gold nanoparticles, e.g., SERS signal enhancement, while maintaining the stability. Meanwhile, the wettability variation span of the top coating could be expanded through the optimisation of the coating thickness because, as the total coating thickness decreases, the topography effect becomes dominant on the wettability of the surface.

Finally, multigradients are thought to represent the next generation of gradients, with increased applications in the biomedical area. So far, the focal point of most reported 2D surface gradient investigations has been cell-surface interactions in the interplay of topography and chemistry (158, 159, 307). The influence of surface wettability on cell behaviours, an intrinsic outcome

of surface roughness and chemistry variations, is also considered in these studies. Aside from cell studies, the 2D gradient of the chemistry gradient combined with plasmonic nanoparticle gradients has the potential to be utilised in the development of plasmonic biosensing and bioimaging platforms (150).

Chapter 6: Conclusion and Future Outlook

In this work, initially the fabrication and characterization of unidirectional chemistry and topography gradients were presented. After validating the approaches, possibility of developing an orthogonal combinational of two independently varying chemistry and topography gradients based on the validated approaches was explored.

In chapter 3 based on the first approach to develop unidirectional chemistry gradients, a fast and economic way of optimizing surfaces was introduced. The surface modification was started from single static depositions, searching for optimum plasma parameters, and once confirmed, the atmospheric pressure corona jet was programmed to deposit a plasma polymerised continuous coating with gradually varying surface chemistry. For this, HMDSO precursor was polymerised by keeping HMDSO monomer flow rate constant while gradually increasing the oxygen admixture during jet movement along the PE substrate. A large surface chemistry variation was demonstrated based on FTIR spectra and WCA results showing a gradual transition from PDMS-like polymer to glass-like polymer.

The comparison between characterisations of the statically deposited and dynamically deposited coatings revealed good similarities in chemistry, wettability and surface topography (roughness) between both set of coatings however, demonstrating a more gradual transition between the surface variables in dynamically deposited coating compared to the statically treated coatings. Wettability variation of the surface was affected by the deposition conditions (static and dynamic) under identical plasma parameters, especially at higher oxygen admixtures which was attributed to the mixing of ambient air and dilution of plasma gas during jet movement which rendered lower hydrophilicity (higher WCA) at the most oxygen-rich coating compared to almost full wetting recorded for the static deposition condition. Additionally, higher roughness and WCA values were recorded for the dynamically deposited coating compared to the static depositions ,70 vs. 35 nm of roughness and 110° vs. 80° of WCA.

In summary, the gradient coating was obtained on PE substrate along several cm (approx. 10 cm) and width of 2 cm, demonstrating roughness variation of 10-70 nm and wettability variation of 110°- 40° WCA. Finally, the applicability of treating heat-sensitive materials (e.g. PE) was demonstrated with atmospheric pressure corona jet. The future challenge could be addressing the lateral resolution of the discharge by advancements in the instrumentations of plasma technology.

Later, using a different plasma technology, a mask-assisted four-step (non-continuous) approach was introduced aiming to obtain high control over deposition conditions, a lower film thickness, and smoother coatings with distinctive feature of high stability in aqueous media. The deposition parameters were inspired from previous extensive attempts (106, 247, 248) to

develop nitrogen-rich and amino-functional coatings. For this, a, manual masking agent was designed which allowed generating gradient with four distinct coating, which could generate 20 gradient samples after each successive deposition processes. As a monomer, ethylene was introduced with constant flow rate inside the deposition chamber of the low-pressure CCP plasma, while ammonia admixture was gradually increased in the discharge during the four-step deposition process. The functionality of the surface and degree of crosslinking was mainly adjusted by tuning plasma electrical parameters (power input) and the precursor flow rate ratio (ammonia/ethylene). The treated region was 1x2 cm rectangular Si chip, and the gradient was developed along 1 cm width of the chip. Characterisations demonstrated 0.7%-13% variation of elemental nitrogen [N%], and a WCA variation of 79° to 33° with negligible surface roughness variation. The elemental oxygen was dramatically increased parallel to increase in nitrogen-content reaching up to approx. 17%. On the other hand, the limited degree of the nitrogen-incorporation seemed to be due to the nature of the employed non-polymerisable gas, i.e., ammonia, since applying higher ammonia admixture as well as doubling the chamber pressure did not lead to a higher incorporation of nitrogen inside the polymer. Besides the higher rates of ammonia has proved the chemical and physical etching effect, decreasing the deposition rate. The future challenge could be conducting a systematic study of the plasma polymerisation of ethylene with various nitrogen-containing gases aiming to minimise etching effect and increase the incorporation of nitrogen (and likely primary amine) based on the same bilayer water-stable design to also establish a counterbalance between the increased amine content and stability in water media. Due to high impact of oxygen content in surface wettability properties, the next challenge could be controlling the maximum incorporated oxygen inside the coating and ideally achieving a reproducible oxygen content.

In chapter 4 a versatile and flexible experimental strategy capable of delivering gradients of various length and slope was introduced. The gradient generation was conducted benefitting from a compact and user-friendly unsophisticated design and a setup with a contained environment that limited evaporations or interferences during the process. Using the design, unidirectional stochastic and periodical nanoparticle and nanocluster density gradients were introduced. Additionally, using the same experimental strategy, in situ growth of nanoparticles were conducted to achieve a size gradient of periodical domes. A total three surface chemistries of different classes, Self-assembled monolayer, plasma polymerised thin film, and block copolymer templates were generated as platforms for gradient formation. The primary strategy was to obtain an approximation of surface coverage versus time of incubation using QCM-D to monitor surface-precursor interactions, which was implemented before gradient experiments. Accordingly, the time that allowed maximum surface coverage was employed as a control factor to develop the desired surface variation. In the next step, a volumetric speed

was defined by having the time of saturation, the volume of the chamber (where chip was vertically placed) and the intended total gradient length. The volumetric speed was then adjusted to a precise microfluidic pump, which drop-wisely transferred the precursor (whether nanoparticles, or salt solution) in the sample chamber allowing the solution to gradually rise inside the chamber for the defined time of incubation. The control over the speed was translated into linear variation of the contact duration of the surface with the precursor.

The generated gradients were evaluated for surface topography, and the surface coverage as a function of distance along the gradient agreed well with the Langmuir-Freundlich isotherms. Finally, the potential of the developed gradients for SERS applications were investigated. For the gradient generated on aminosilanes, the densest region exhibited considerable SERS signal however, no substantial peak rise in the fingerprint region was noticed up to this point. However, nanocluster density gradient formed on copolymers demonstrated a satisfactory, gradually varying SERS response suggesting the potential application of this gradient for SERS optimisations. On the other hand, a 7-fold increase in SERS signal for densest region was observed for nanoparticle density gradient formed on plasma polymer layer as compared to the maximum signals found for the previous two gradients. However, SERS was diminished at some points not showing a continuous variation in intensity. This could be looked into further for any clues that SEM analysis did not reveal. Finally, the gold domes size gradient did not show any signal improvement, however, as the periodicity was constant, the periodical arrays of domes could be optimised for the proper periodicity for future SERS studies.

In chapter 5 an orthogonal gradient of chemistry and topography were introduced benefitting from the two previously investigated gradients. The surface exhibited the same chemistry as the unidirectional reference gradient with no compositional variation caused by the gold nanoparticle sublayer. The resulted wettability variation was different with considerable decrease in the variation scale, which was accounted for the roughness and morphology of the coated nanoparticles. Optimizing the thickness of the top coating is expected to increase both the surface wettability variation scale, which is mostly affected by topography, and the plasmonic effect of the underlying plasmonic gold nanoparticles. However, since the thickness was adapted to ensure the stability of the amino-functional coating in aqueous environment, finding a good counterbalance between the stability and the gradient properties is expected to be a challenging task. Once the thickness is optimised, the presented orthogonal gradient can be utilised not only for optimising cell-surface interaction but also for optimisation of plasmonic biosensing platforms.

References

1. Lin C-T, Wang S-M. Frontiers in Bioscience. 2005;10(1):99-106.
2. Huang L, Guo Y, Peng Z, Porter AL. Technology Analysis & Strategic Management. 2011;23(5):527-44.
3. Morales MA, Halpern JM. Bioconjugate Chemistry. 2018;29(10):3231-9.
4. Ruardy TG, Schakenraad JM, van der Mei HC, Busscher HJ. Surface Science Reports. 1997;29(1):3-30.
5. Wiseman ME, Frank CW. Langmuir. 2012;28(3):1765-74.
6. Roseti L, Parisi V, Petretta M, Cavallo C, Desando G, Bartolotti I, et al. Materials Science and Engineering: C. 2017;78:1246-62.
7. Tsougeni K, Ellinas K, Koukouvinos G, Petrou PS, Tserepi A, Kakabakos SE, et al. 3D Plasma Nanotextured® Polymeric Surfaces for Protein or Antibody Arrays, and Biomolecule and Cell Patterning. Cell-Based Microarrays: Springer; 2018. p. 27-40.
8. Di Rocco G, Iachininoto MG, Tritarelli A, Straino S, Zacheo A, Germani A, et al. Journal of cell science. 2006;119(14):2945-52.
9. Dobbenga S, Fratila-Apachitei LE, Zadpoor AA. Acta biomaterialia. 2016;46:3-14.
10. Fiedler J, Özdemir B, Bartholomä J, Plettl A, Brenner RE, Ziemann P. Biomaterials. 2013;34(35):8851-9.
11. Wang S, Wan Y, Liu Y. Nanoscale. 2014;6(21):12482-9.
12. Bucaro MA, Vasquez Y, Hatton BD, Aizenberg J. ACS nano. 2012;6(7):6222-30.
13. Kuo CW, Chueh D-Y, Chen P. Journal of nanobiotechnology. 2014;12(1):54.
14. Özdemir B, Huang W, Plettl A, Ziemann P. Nanotechnology. 2015;26(11):115301.
15. Yang F, Zuo X, Fan C, Zhang X-E. National Science Review. 2018;5(5):740-55.
16. Xu H, Aizpurua J, Käll M, Apell P. Physical Review E. 2000;62(3):4318-24.
17. Xu H, Bjerneld E, Aizpurua J, Apell P, Gunnarsson L, Petronis S, et al.: SPIE; 2001.
18. Seney CS, Gutzman BM, Goddard RH. The Journal of Physical Chemistry C. 2009;113(1):74-80.
19. Zhang J, Li X, Sun X, Li Y. The Journal of Physical Chemistry B. 2005;109(25):12544-8.
20. Chilkoti N, Anal A. Size Anal Chem. 2004;76(18):5370-8.
21. Soler M, Estevez MC, Cardenosa-Rubio M, Astua A, Lechuga LM. ACS Sensors. 2020;5(9):2663-78.
22. Ukoba K, Eloka-Eboka A, Inambao F. Renewable and Sustainable Energy Reviews. 2018;82:2900-15.
23. Li Z, Aik Khor K. Preparation and Properties of Coatings and Thin Films on Metal Implants. In: Narayan R, editor. Encyclopedia of Biomedical Engineering. Oxford: Elsevier; 2019. p. 203-12.
24. Yang R, Asatekin A, Gleason KK. Soft Matter. 2012;8(1):31-43.
25. Meng X. Journal of Materials Chemistry A. 2017;5(35):18326-78.
26. Bhardwaj SK, Yadav P, Ghosh S, Basu T, Mahapatro AK. ACS applied materials & interfaces. 2016;8(37):24350-60.
27. Wink T, Van Zuilen S, Bult A, Van Bennekom W. Analyst. 1997;122(4):43R-50R.
28. Liang Y, Huang J, Zang P, Kim J, Hu W. Applied surface science. 2014;322:202-8.
29. Minko S. Grafting on solid surfaces:“grafting to” and “grafting from” methods. Polymer surfaces and interfaces: Springer; 2008. p. 215-34.
30. Akkahat P, Hoven VP. Colloids and Surfaces B: Biointerfaces. 2011;86(1):198-205.

31. Wang L, Mao W, Ni D, Di J, Wu Y, Tu Y. Electrochemistry Communications. 2008;10(4):673-6.
32. Chen W, Lu Z, Li CM. Analytical chemistry. 2008;80(22):8485-92.
33. Malekzad H, Zangabad PS, Mirshekari H, Karimi M, Hamblin MR. Nanotechnology Reviews. 2017;6(3):301-29.
34. Lu X, Zhang J, Zhang C, Han Y. Macromolecular Rapid Communications. 2005;26(8):637-42.
35. Kunzler TP, Drobek T, Sprecher CM, Schuler M, Spencer ND. Applied Surface Science. 2006;253(4):2148-53.
36. Cai P, Leow WR, Wang X, Wu Y-L, Chen X. Advanced Materials. 2017;29(26):1605529.
37. Gates BD, Xu Q, Stewart M, Ryan D, Willson CG, Whitesides GM. Chemical Reviews. 2005;105(4):1171-96.
38. Saha B, Toh WQ, Liu E, Tor SB, Hardt DE, Lee J. Journal of Micromechanics and Microengineering. 2015;26(1):013002.
39. Gates BD. Materials Today. 2005;8(2):44-9.
40. Gates BD, Xu Q, Love JC, Wolfe DB, Whitesides GM. Annual Review of Materials Research. 2004;34(1):339-72.
41. Li Y, Zhang X, Wang D, He F, Ni C, Chi L. Journal of Colloid and Interface Science. 2015;458:300-4.
42. Wood MA. Journal of The Royal Society Interface. 2007;4(12):1-17.
43. Chen Y, Pepin A. Electrophoresis. 2001;22(2):187-207.
44. Ahuja T, Mir IA, Kumar D, Rajesh. Biomaterials. 2007;28(5):791-805.
45. Siqueira JR, Caseli L, Crespilho FN, Zucolotto V, Oliveira ON. Biosensors and Bioelectronics. 2010;25(6):1254-63.
46. Scouten WH, Luong JHT, Stephen Brown R. Trends in Biotechnology. 1995;13(5):178-85.
47. Rusmini F, Zhong Z, Feijen J. Biomacromolecules. 2007;8(6):1775-89.
48. Morgenthaler S. Surface-chemical and-morphological gradients. 2008:419-34.
49. Sethuraman A, Han M, Kane RS, Belfort G. Langmuir. 2004;20(18):7779-88.
50. Wang P-Y, Clements LR, Thissen H, Tsai W-B, Voelcker NH. Acta biomaterialia. 2015;11:58-67.
51. Elwing H, Gölander C-G. Advances in colloid and interface science. 1990;32(4):317-39.
52. Tauk L, Schröder AP, Decher G, Giuseppone N. Nature chemistry. 2009;1(8):649.
53. Ionov L, Zdyrko B, Sidorenko A, Minko S, Klep V, Luzinov I, et al. Macromolecular rapid communications. 2004;25(1):360-5.
54. Poelma JE, Fors BP, Meyers GF, Kramer JW, Hawker CJ. Angewandte Chemie International Edition. 2013;52(27):6844-8.
55. Ballav N, Shaporenko A, Terfort A, Zharnikov M. Advanced Materials. 2007;19(7):998-1000.
56. Fuierer RR, Carroll RL, Feldheim DL, Gorman CB. Advanced Materials. 2002;14(2):154-7.
57. Krabbenborg SO, Huskens J. Angewandte Chemie International Edition. 2014;53(35):9152-67.
58. Kim MS, Seo KS, Khang G, Lee HB. Bioconjugate chemistry. 2005;16(2):245-9.
59. Pitt WG. Journal of colloid and interface science. 1989;133(1):223-7.
60. Alexander M, Duc T. Journal of Materials Chemistry. 1998;8(4):937-43.
61. Jeong BJ, Lee JH, Lee HB. Journal of colloid and interface science. 1996;178(2):757-63.

62. Giri D, Hanks CN, Collinson MM, Higgins DA. The Journal of Physical Chemistry C. 2014;118(12):6423-32.
63. Tomlinson MR, Efimenko K, Genzer J. Macromolecules. 2006;39(26):9049-56.
64. Stromberg C, Thissen P, Klueppel I, Fink N, Grundmeier G. Electrochimica Acta. 2006;52(3):804-15.
65. Li L, Zhu Y, Li B, Gao C. Langmuir. 2008;24(23):13632-9.
66. Pei J, Hall H, Spencer ND. Biomaterials. 2011;32(34):8968-78.
67. Morgenthaler S, Lee S, Zürcher S, Spencer ND. Langmuir. 2003;19(25):10459-62.
68. Smith JT, Tomfohr JK, Wells MC, Beebe TP, Kepler TB, Reichert WM. Langmuir. 2004;20(19):8279-86.
69. Ruardy TG, Moorlag HE, Schakenraad JM, Van Der Mei HC, Busscher HJ. Journal of colloid and interface science. 1997;188(1):209-17.
70. Yang H-C, Wu Q-Y, Wan L-S, Xu Z-K. Chemical Communications. 2013;49(89):10522-4.
71. Albert JN, Baney MJ, Stafford CM, Kelly JY, Epps TH. ACS Nano. 2009;3(12):3977-86.
72. Wu T, Gong P, Szleifer I, Vlcˇek P, Šubr V, Genzer J. Macromolecules. 2007;40(24):8756-64.
73. Kraus T, Stutz R, Balmer TE, Schmid H, Malaquin L, Spencer ND, et al. Langmuir. 2005;21(17):7796-804.
74. Choi S-H, Zhang Newby B-m. Langmuir. 2003;19(18):7427-35.
75. Wang X, Tu H, Braun PV, Bohn PW. Langmuir. 2006;22(2):817-23.
76. Wang X, Bohn PW. Journal of the American Chemical Society. 2004;126(21):6825-32.
77. Inagi S, Ishiguro Y, Atobe M, Fuchigami T. Angewandte Chemie International Edition. 2010;49(52):10136-9.
78. Terrill RH, Balss KM, Zhang Y, Bohn PW. Journal of the American Chemical Society. 2000;122(5):988-9.
79. Balss KM, Coleman BD, Lansford CH, Haasch RT, Bohn PW. The Journal of Physical Chemistry B. 2001;105(37):8970-8.
80. Banuprasad TN, Vinay TV, Subash CK, Varghese S, George SD, Varanakkottu SN. ACS Applied Materials & Interfaces. 2017;9(33):28046-54.
81. Tai F-I, Sterner O, Andersson O, Ekblad T, Ederth T. Soft matter. 2014;10(32):5955-64.
82. Ionov L, Houbenov N, Sidorenko A, Stamm M, Minko S. Biointerphases. 2009;4(2):FA45-FA9.
83. Mosnáček J, Popelka A, Osicka J, Filip J, Ilcikova M, Kollar J, et al. Journal of colloid and interface science. 2018;512:511-21.
84. Harris BP, Kutty JK, Fritz EW, Webb CK, Burg KJ, Metters AT. Langmuir. 2006;22(10):4467-71.
85. Schuh C, Santer S, Prucker O, Rühe J. Advanced Materials. 2009;21(46):4706-10.
86. Steenackers M, Küller A, Stoycheva S, Grunze M, Jordan R. Langmuir. 2009;25(4):2225-31.
87. Gallant ND, Lavery KA, Amis EJ, Becker ML. Advanced materials. 2007;19(7):965-9.
88. Harris BP, Metters AT. Macromolecules. 2006;39(8):2764-72.
89. Larsson A, Liedberg B. Langmuir. 2007;23(22):11319-25.
90. Yasuda H, Gazicki M. Biomaterials. 1982;3(2):68-77.
91. Zelzer DM. Plasma Polymer Gradients: University of Nottingham; 2009.
92. Vandenbossche M, Petit L, Mathon-Lagresle J, Spano F, Rupper P, Bernard L, et al. Plasma Processes and Polymers. 2018;15(4):1700185.

93. Harding FJ, Clements LR, Short RD, Thissen H, Voelcker NH. Acta biomaterialia. 2012;8(5):1739-48.
94. Reynolds PM, Pedersen RH, Riehle MO, Gadegaard N. Small. 2012;8(16):2541-7.
95. Meshkova AS, Liu Y, Elam FM, Starostin SA, van de Sanden MC, de Vries HW. Plasma Processes and Polymers. 2018;15(1):1700093.
96. Menzies DJ, Cowie B, Fong C, Forsythe JS, Gengenbach TR, McLean KM, et al. Langmuir. 2010;26(17):13987-94.
97. Menzies DJ, Jasieniak M, Griesser HJ, Forsythe JS, Johnson G, McFarland GA, et al. Surface Science. 2012;606(23):1798-807.
98. Coad BR, Bilgic T, Klok H-A. Langmuir. 2014;30(28):8357-65.
99. Robinson DE, Buttle DJ, Whittle JD, Parry KL, Short RD, Steele DA. Plasma Processes and Polymers. 2010;7(2):102-6.
100. Vandenabeele C, Buddhadasa M, Girard-Lauriault P-L, Snyders R. Thin Solid Films. 2017;630:100-7.
101. Meyer-Plath A, Schröder K, Finke B, Ohl A. Vacuum. 2003;71(3):391-406.
102. Hopp I, MacGregor MN, Doherty K, Visalakshan RM, Vasilev K, Williams RL, et al. ACS Biomaterials Science & Engineering. 2019;5(6):2834-45.
103. Liu X, Shi S, Feng Q, Bachhuka A, He W, Huang Q, et al. ACS applied materials & interfaces. 2015;7(33):18473-82.
104. Buddhadasa M, Girard-Lauriault P-L. Thin Solid Films. 2015;591:76-85.
105. Girard-Lauriault PL, Mwale F, Iordanova M, Demers C, Desjardins P, Wertheimer MR. Plasma Processes and Polymers. 2005;2(3):263-70.
106. Vandenbossche M, Dorst J, Amberg M, Schütz U, Rupper P, Heuberger M, et al. Polymer Degradation and Stability. 2018;156:259-68.
107. Dorst J, Vandenbossche M, Amberg M, Bernard L, Rupper P, Weltmann K-D, et al. Langmuir. 2017;33(40):10736-44.
108. Whittle JD, Barton D, Alexander MR, Short RD. Chemical Communications. 2003(14):1766-7.
109. Morent R, De Geyter N, Van Vlierberghe S, Dubruel P, Leys C, Gengembre L, et al. Progress in Organic Coatings. 2009;64(2):304-10.
110. Morent R, De Geyter N, Van Vlierberghe S, Dubruel P, Leys C, Schacht E. Surface and Coatings Technology. 2009;203(10-11):1366-72.
111. Kudrle V, Doležal V, Tálský A, Janča J. Rate Constant of HMDSO + O Reaction in Plasma Afterglow. Plasma Processes and Polymers2005. p. 95-102.
112. Alexander MR, Short RD, Jones FR, Stollenwerk M, Zabold J, Michaeli W. Journal of Materials Science. 1996;31(7):1879-85.
113. Silmy K, Holländer A, Dillmann A, Thömel J. Surface and Coatings Technology. 2005;200(1):368-71.
114. Bousquet A, Cartry G, Granier A. Plasma Sources Science and Technology. 2007;16(3):597-605.
115. Fanelli F, Lovascio S, d'Agostino R, Arefi-Khonsari F, Fracassi F. Plasma Processes and Polymers. 2010;7(7):535-43.
116. Wavhal DS, Zhang J, Steen ML, Fisher ER. Plasma Processes and Polymers. 2006;3(3):276-87.
117. Saloum S, Naddaf M, Alkhaled B. Vacuum. 2008;82(8):742-7.
118. Blanchard NE, Naik VV, Geue T, Kahle O, Hegemann D, Heuberger M. Langmuir. 2015;31(47):12944-53.

119. Schricker SR, Palacio ML, Bhushan B. Philosophical Transactions of the Royal Society A: Mathematical, Physical and Engineering Sciences. 2012;370(1967):2348-80.
120. Faia-Torres AB, Guimond-Lischer S, Rottmar M, Charnley M, Goren T, Maniura-Weber K, et al. Biomaterials. 2014;35(33):9023-32.
121. Kunzler TP, Drobek T, Schuler M, Spencer ND. Biomaterials. 2007;28(13):2175-82.
122. Faia-Torres AB, Charnley M, Goren T, Guimond-Lischer S, Rottmar M, Maniura-Weber K, et al. Acta biomaterialia. 2015;28:64-75.
123. Zhou Q, Kühn PT, Huisman T, Nieboer E, Van Zwol C, Van Kooten TG, et al. Scientific reports. 2015;5:16240.
124. Zhou Q, Castañeda Ocampo O, Guimarães CF, Kühn PT, van Kooten TG, van Rijn P. ACS applied materials & interfaces. 2017;9(37):31433-45.
125. Kant K, Low SP, Marshal A, Shapter JG, Losic D. ACS applied materials & interfaces. 2010;2(12):3447-54.
126. Wang PY, Clements LR, Thissen H, Jane A, Tsai WB, Voelcker NH. Advanced Functional Materials. 2012;22(16):3414-23.
127. Wu J, Miao J. ACS Applied Materials & Interfaces. 2015;7(12):6991-7000.
128. Kim D-H, Han K, Gupta K, Kwon KW, Suh K-Y, Levchenko A. Biomaterials. 2009;30(29):5433-44.
129. Rajput D, Crowder SW, Hofmeister L, Costa L, Sung H-J, Hofmeister W. Colloids and Surfaces B: Biointerfaces. 2013;102:111-6.
130. Kumar R, Urtizberea A, Ghosh S, Bog U, Rainer Q, Lenhert S, et al. Langmuir. 2017;33(35):8739-48.
131. Wu J, Tao K, Miao J, editors. Gradient lithography using graded tip array. 2017 19th International Conference on Solid-State Sensors, Actuators and Microsystems (TRANSDUCERS); 2017 18-22 June 2017.
132. Xue P, Nan J, Wang T, Wang S, Ye S, Zhang J, et al. Small. 2017;13(4):1601807.
133. Roy S, Bhandaru N, Das R, Harikrishnan G, Mukherjee R. ACS Applied Materials & Interfaces. 2014;6(9):6579-88.
134. Ding Y, Qi HJ, Alvine KJ, Ro HW, Ahn DU, Lin-Gibson S, et al. Macromolecules. 2010;43(19):8191-201.
135. Resnick D. 9 - Nanoimprint lithography. In: Feldman M, editor. Nanolithography: Woodhead Publishing; 2014. p. 315-47.
136. Ross AM, Lahann J. Journal of Polymer Science Part B: Polymer Physics. 2013;51(10):775-94.
137. Zhang G, Wang D, Möhwald H. Nano letters. 2007;7(1):127-32.
138. Hanarp P, Käll M, Sutherland DS. The Journal of Physical Chemistry B. 2003;107(24):5768-72.
139. Kunzler TP, Huwiler C, Drobek T, Vörös J, Spencer ND. Biomaterials. 2007;28(33):5000-6.
140. Bhat RR, Genzer J. Surface science. 2005;596(1-3):187-96.
141. Goreham RV, Short RD, Vasilev K. The Journal of Physical Chemistry C. 2011;115(8):3429-33.
142. Song F, Cai Y, Newby B-mZ. Applied Surface Science. 2006;253(5):2393-8.
143. Krämer S, Xie H, Gaff J, Williamson JR, Tkachenko AG, Nouri N, et al. Journal of the American Chemical Society. 2004;126(17):5388-95.
144. Lawn MA, Herrmann J, Jämting AK, Goreham RV. Journal of Micro/Nanolithography, MEMS, and MOEMS. 2012;11(1):011007.

145. Arnold M, Hirschfeld-Warneken VC, Lohmüller T, Heil P, Blümmel J, Cavalcanti-Adam EA, et al. Nano letters. 2008;8(7):2063-9.
146. Goreham RV, Mierczynska A, Pierce M, Short RD, Taheri S, Bachhuka A, et al. Thin Solid Films. 2013;528:106-10.
147. Huwiler C, Kunzler TP, Textor M, Vörös J, Spencer ND. Langmuir. 2007;23(11):5929-35.
148. Ramakrishna SN, Clasohm LY, Rao A, Spencer ND. Langmuir. 2011;27(16):9972-8.
149. Liu X, Xie Y, Shi S, Feng Q, Bachhuka A, Guo X, et al. Applied Surface Science. 2019;473:838-47.
150. Lundgren A, Hulander M, Brorsson J, Hermansson M, Elwing H, Andersson O, et al. Particle & particle systems characterization. 2014;31(2):209-18.
151. Zhang J, Xue L, Han Y. Langmuir. 2005;21(1):5-8.
152. Bhat RR, Genzer J, Chaney BN, Sugg HW, Liebmann-Vinson A. Nanotechnology. 2003;14(10):1145.
153. Bhat RR, Fischer DA, Genzer J. Langmuir. 2002;18(15):5640-3.
154. Haryono A, Binder WH. Small. 2006;2(5):600-11.
155. Bhat R, Tomlinson M, Wu T, Genzer J. Surface-Initiated Polymerization II, ed. R. Jordan. Springer, Berlin; 2006.
156. Bhat RR, Genzer J. Applied Surface Science. 2006;252(7):2549-54.
157. Bhat RR, Tomlinson MR, Genzer J. Macromolecular Rapid Communications. 2004;25(1):270-4.
158. Clements LR, Wang P-Y, Tsai W-B, Thissen H, Voelcker NH. Lab on a Chip. 2012;12(8):1480-6.
159. Yang J, Rose FR, Gadegaard N, Alexander MR. Advanced Materials. 2009;21(3):300-4.
160. Ohtsu Y. Physics of high-density radio frequency capacitively coupled plasma with various electrodes and its applications. Plasma Science and Technology-Basic Fundamentals and Modern Applications: IntechOpen; 2018.
161. Bruggeman PJ, Iza F, Brandenburg R. Plasma Sources Science and Technology. 2017;26(12):123002.
162. Gibbon P. arXiv preprint arXiv:200704783. 2020.
163. Friedrich J. Plasma Processes and Polymers. 2011;8(9):783-802.
164. Chang J-S, Lawless PA, Yamamoto T. IEEE Transactions on plasma science. 1991;19(6):1152-66.
165. Kaiser KL. CRC Press; 2005.
166. Zhang D, Sun Q, Wadsworth LC. Polymer Engineering & Science. 1998;38(6):965-70.
167. O'Hare LA, Leadley S, Parbhoo B. Surface and Interface Analysis: An International Journal devoted to the development and application of techniques for the analysis of surfaces, interfaces and thin films. 2002;33(4):335-42.
168. Chen J, Davidson JH. Plasma Chemistry and Plasma Processing. 2004;24(4):511-35.
169. Li J, Yuan Q, Chang X, Wang Y, Yin G, Dong C. Plasma Science and Technology. 2017;19(4):045505.
170. Thyen R, Weber A, Klages CP. Surface and Coatings Technology. 1997;97(1):426-34.
171. Rugner K, Reuter R, Ellerweg D, de los Arcos T, von Keudell A. Plasma Processes Polym. 2013;10:1061-73.
172. Barletta F, Liguori A, Leys C, Colombo V, Gherardi M, Nikiforov A. Materials Letters. 2018;214:76-9.

173. Körner E, Hanselmann B, Cierniak P, Hegemann D. Plasma Chemistry and Plasma Processing. 2012;32(3):619-27.
174. Lew C, Chowdhury F, Hosur MV, Netravali AN. Journal of adhesion science and technology. 2007;21(14):1407-24.
175. Hossain MM, Herrmann AS, Hegemann D. Plasma Processes and Polymers. 2007;4(2):135-44.
176. Zeng R, Pang Z, Zhu H. Journal of Electroanalytical Chemistry. 2000;490(1-2):102-6.
177. Turkevich J, Stevenson PC, Hillier J. Discussions of the Faraday Society. 1951;11:55-75.
178. Yap FL, Thoniyot P, Krishnan S, Krishnamoorthy S. Acs Nano. 2012;6(3):2056-70.
179. Manzi BM, Werner M, Ivanova EP, Crawford RJ, Baulin VA. Scientific Reports. 2019;9(1):4694.
180. Allen SJ, McKay G, Khader K. Journal of Chemical Technology & Biotechnology. 1989;45(4):291-302.
181. Corma A, Llopis F, Monton JB, Weller SW. Chemical Engineering Science. 1988;43(4):785-92.
182. Jeppu G, Clement P. Journal of contaminant hydrology. 2012;129-130:46-53.
183. Müller M. Vibrational Spectroscopic and Optical Methods. In: Stamm M, editor. Polymer Surfaces and Interfaces: Characterization, Modification and Applications. Berlin, Heidelberg: Springer Berlin Heidelberg; 2008. p. 47-70.
184. Brundle CR, Wilson L, Evans CA, Wilson S, Wilson G. Gulf Professional Publishing; 1992.
185. Brune D, Hellborg R, Whitlow HJ, Hunderi O. John Wiley & Sons; 2008.
186. Smith BC. CRC press; 2011.
187. Benninghoven A. Angewandte Chemie International Edition in English. 1994;33(10):1023-43.
188. Van Vaeck L, Adriaens A, Gijbels R. Mass Spectrometry Reviews. 1999;18(1):1-47.
189. Hagenhoff B. Microchimica Acta. 2000;132(2):259-71.
190. Palmquist A, Emanuelsson L, Sjövall P. Applied Surface Science. 2012;258(17):6485-94.
191. McClelland GM, Erlandsson R, Chiang S. Atomic force microscopy: General principles and a new implementation. Review of progress in quantitative nondestructive evaluation: Springer; 1987. p. 1307-14.
192. Giessibl FJ. Reviews of modern physics. 2003;75(3):949.
193. García R, San Paulo A. Physical Review B. 1999;60(7):4961-7.
194. Nishimoto S, Bhushan B. RSC Advances. 2013;3(3):671-90.
195. Nir S, Reches M. Current Opinion in Biotechnology. 2016;39:48-55.
196. Bhushan B. CRC press; 2000.
197. Dussan E. Annual Review of Fluid Mechanics. 1979;11(1):371-400.
198. Wenzel RN. Industrial & Engineering Chemistry. 1936;28(8):988-94.
199. Cassie A. Discussions of the Faraday society. 1948;3:11-6.
200. De Gennes P-G, Brochard-Wyart F, Quéré D. Springer Science & Business Media; 2013.
201. Di Mundo R, Palumbo F. Plasma Processes and Polymers. 2011;8(1):14-8.
202. Hawker MJ, Pegalajar-Jurado A, Fisher ER. Plasma Processes and Polymers. 2015;12(9):846-63.
203. Ramon-Torregrosa P, Rodríguez-Valverde M, Amirfazli A, Cabrerizo-Vílchez M. Colloids and surfaces a: physicochemical and engineering aspects. 2008;323(1-3):83-93.
204. Watts JF, Wolstenholme J. 2003.

205. Carlson TA. Fundamental Concepts. Photoelectron and Auger Spectroscopy. Boston, MA: Springer US; 1975. p. 65-97.
206. Andrade JD. X-ray photoelectron spectroscopy (XPS). Surface and interfacial aspects of biomedical polymers: Springer; 1985. p. 105-95.
207. Nisol B, Reniers F. Journal of Electron Spectroscopy and Related Phenomena. 2015;200:311-31.
208. Egerton RF. Springer; 2005.
209. Zhou W, Wang ZL. Springer science & business media; 2007.
210. Pilot R, Signorini R, Fabris L. Surface-enhanced Raman spectroscopy: Principles, substrates, and applications. Metal Nanoparticles and Clusters: Springer; 2018. p. 89-164.
211. Bhattacharjee S. Journal of Controlled Release. 2016;235:337-51.
212. van Veluwen A, Lekkerkerker HN, de Kruif CG, Vrij A. Faraday Discussions of the Chemical Society. 1987;83:59-67.
213. Berne BJ, Pecora R. Courier Corporation; 2000.
214. Xu R. Springer Science & Business Media; 2001.
215. Adamczyk Z. Elsevier; 2017.
216. Park S-J, Seo M-K. Academic Press; 2011.
217. Tantra R, Schulze P, Quincey P. Particuology. 2010;8(3):279-85.
218. Creighton JA, Eadon DG. Journal of the Chemical Society, Faraday Transactions. 1991;87(24):3881-91.
219. Haiss W, Thanh NT, Aveyard J, Fernig DG. Analytical chemistry. 2007;79(11):4215-21.
220. Yuan Y, Oberholzer M, Lenhoff A. Colloids and Surfaces A: Physicochemical and Engineering Aspects. 2000;165(1-3):125-41.
221. Rodahl M, Höök F, Krozer A, Brzezinski P, Kasemo B. Review of Scientific Instruments. 1995;66(7):3924-30.
222. Rodahl M, Kasemo B. Review of Scientific Instruments. 1996;67(9):3238-41.
223. Förch R, Chifen AN, Bousquet A, Khor HL, Jungblut M, Chu LQ, et al. Chemical Vapor Deposition. 2007;13(6-7):280-94.
224. Bazaka O, Bazaka K. 6 - Surface modification of biomaterials for biofilm control. In: Barnes L, Cooper IR, editors. Biomaterials and Medical Device - Associated Infections. Oxford: Woodhead Publishing; 2015. p. 103-32.
225. Sourjik V, Wingreen NS. Current opinion in cell biology. 2012;24(2):262-8.
226. Vandenbossche M, Butron Garcia M-I, Schütz U, Rupper P, Amberg M, Hegemann D. Plasma Chemistry and Plasma Processing. 2016;36:667-77.
227. Hossain MM, Hegemann D, Fortunato G, Herrmann AS, Heuberger M. Plasma Processes and Polymers. 2007;4(4):471-81.
228. Lee HJ, Jamison AC, Lee TR. Langmuir. 2015;31(7):2136-46.
229. Malekzad H, Gallingani T, Barletta F, Gherardi M, Colombo V, Duday D. Plasma Processes and Polymers. 2021;18(2):2000044.
230. Lommatzsch U, Ihde J. Plasma Processes and Polymers. 2009;6(10):642-8.
231. Morent R, De Geyter N, Jacobs T, Van Vlierberghe S, Dubruel P, Leys C, et al. Plasma Processes and Polymers. 2009;6(S1):S537-S42.
232. Schneider J, Akbar MI, Dutroncy J, Kiesler D, Leins M, Schulz A, et al. Plasma Processes and Polymers. 2009;6(S1):S700-S4.
233. Hegemann D, Bülbül E, Hanselmann B, Schütz U, Amberg M, Gaiser S. Plasma Processes and Polymers. 2021;18(2):2000176.

234. Creatore M, Barrell Y, Benedikt J, Sanden MCMvd. Plasma Sources Science and Technology. 2006;15(3):421-31.
235. Creatore M, Barrell Y, Benedikt J, Van De Sanden M. Plasma Sources Science and Technology. 2006;15(3):421.
236. Raynaud P, Despax B, Segui Y, Caquineau H. Plasma Processes and Polymers. 2005;2(1):45-52.
237. Hegemann D, Hossain MM. Plasma Processes and Polymers. 2005;2(7):554-62.
238. Sawada Y, Ogawa S, Kogoma M. Journal of Physics D: Applied Physics. 1995;28(8):1661.
239. Rügner K, Reuter R, Ellerweg D, de los Arcos T, von Keudell A, Benedikt J. Plasma Processes and Polymers. 2013;10(12):1061-73.
240. Azioune A, Marcozzi M, Revello V, Pireaux JJ. Surface and Interface Analysis: An International Journal devoted to the development and application of techniques for the analysis of surfaces, interfaces and thin films. 2007;39(7):615-23.
241. Babaei S, Girard-Lauriault P-L. Plasma Chemistry and Plasma Processing. 2016;36(2):651-66.
242. Hossain MM. Plasma technology for deposition and surface modification: Logos Verlag Berlin GmbH; 2009.
243. Truica-Marasescu F, Ruiz J-C, Wertheimer MR. Plasma Processes and Polymers. 2012;9(5):473-84.
244. Hegemann D. Comprehensive Materials Processing. 2014;4:201-28.
245. Girard-Lauriault PL, Truica-Marasescu F, Petit A, Wang HT, Desjardins P, Antoniou J, et al. Macromolecular bioscience. 2009;9(9):911-21.
246. Truica-Marasescu F, Girard-Lauriault P-L, Lippitz A, Unger WE, Wertheimer MR. Thin solid films. 2008;516(21):7406-17.
247. Dorst J, Vandenbossche M, Amberg M, Bernard L, Rupper P, Weltmann KD, et al. Langmuir. 2017;33(40):10736-44.
248. Vandenbossche M, Bernard L, Rupper P, Maniura-Weber K, Heuberger M, Faccio G, et al. Materials & Design. 2017;114:123-8.
249. Reuter R, Rügner K, Ellerweg D, de los Arcos T, von Keudell A, Benedikt J. Plasma Processes and Polymers. 2012;9(11-12):1116-24.
250. Li K, Gabriel O, Meichsner J. Journal of Physics D: Applied Physics. 2004;37(4):588-94.
251. Starostine S, Aldea E, de Vries H, Creatore M, Van de Sanden M. Plasma Processes and Polymers. 2007;4(S1):S440-S4.
252. Kilicaslan A, Levasseur O, Roy-Garofano V, Profili J, Moisan M, Côté C, et al. Journal of Applied Physics. 2014;115(11):113301.
253. Perry RJ. 6 - Aminosilicone systems for post-combustion CO2 capture. In: Feron PHM, editor. Absorption-Based Post-combustion Capture of Carbon Dioxide: Woodhead Publishing; 2016. p. 121-44.
254. Lerouge S, Barrette J, Ruiz JC, Sbai M, Savoji H, Saoudi B, et al. Plasma Processes and Polymers. 2015;12(9):882-95.
255. Nouicer I, Sahli S, Kihel M, Ziari Z, Bellel A, Raynaud P. International Journal of Nanotechnology. 2015;12(8-9):597-607.
256. Pandiyaraj KN, Arun Kumar A, Ramkumar MC, Kumar SU, Gopinath P, Cools P, et al. Vacuum. 2017;143:412-22.
257. Purohit V, Mielczarski E, Mielczarski JA, Akesso L. Materials Chemistry and Physics. 2013;141(2):602-12.

258. Keskin D, Mokabbar T, Pei Y, Van Rijn P. Polymers (Basel). 2018;10(5):534.
259. Śliwińska-Bartkowiak M, Sterczyńska A, Long Y, Gubbins KE. Molecular Physics. 2014;112(17):2365-71.
260. Drelich J, Chibowski E, Meng DD, Terpilowski K. Soft Matter. 2011;7(21):9804-28.
261. Good RJ. Journal of Adhesion Science and Technology. 1992;6(12):1269-302.
262. Bittoun E, Marmur A, Ostblom M, Ederth T, Liedberg B. Langmuir. 2009;25(20):12374-9.
263. Erbil HY. Surface Science Reports. 2014;69(4):325-65.
264. Lyakhovich A, Lyalina N. Journal of Surface Investigation X-ray, Synchrotron and Neutron Techniques. 2008;2(3):399-402.
265. Mwale F, Rampersad S, Ruiz J-C, Girard-Lauriault P-L, Petit A, Antoniou J, et al. Plasma Medicine. 2011;1(2).
266. Ruiz JC, St-Georges-Robillard A, Thérésy C, Lerouge S, Wertheimer MR. Plasma Processes and Polymers. 2010;7(9-10):737-53.
267. Zelzer M, Albutt D, Alexander MR, Russell NA. Plasma Processes and Polymers. 2012;9(2):149-56.
268. Wei J, Igarashi T, Okumori N, Igarashi T, Maetani T, Liu B, et al. Biomedical Materials. 2009;4(4):045002.
269. Pandiyaraj KN, Kumar AA, Ramkumar M, Kumar SU, Gopinath P, Cools P, et al. Vacuum. 2017;143:412-22.
270. Wu S-T, Huang C-Y, Weng C-C, Chang C-C, Li B-R, Hsu C-S. ACS omega. 2019;4(15):16292-9.
271. Jafari R, Momen G, Eslami E. Surface Engineering. 2019;35(5):450-5.
272. Deilmann M, Grabowski M, Theiß S, Bibinov N, Awakowicz P. Journal of Physics D: Applied Physics. 2008;41(13):135207.
273. Coad BR, Jasieniak M, Griesser SS, Griesser HJ. Surface and Coatings Technology. 2013;233:169-77.
274. Grzelczak M, Vermant J, Furst EM, Liz-Marzán LM. ACS nano. 2010;4(7):3591-605.
275. Huang C, Chen X, Xue Z, Wang T. Science advances. 2020;6(20):eaba1321.
276. Spinnrock A, Martens M, Enders F, Boldt K, Cölfen H. Nanomaterials. 2019;9(7):988.
277. Rani D, Rollo S, Olthuis W, Krishnamoorthy S, Pascual García C. Chemosensors. 2021;9(2):20.
278. Böhmer MR, van der Zeeuw EA, Koper GJ. Journal of colloid and interface science. 1998;197(2):242-50.
279. Hinrichsen EL, Feder J, Jøssang T. Journal of statistical physics. 1986;44(5):793-827.
280. Chen C-F, Tzeng S-D, Lin M-H, Gwo S. Langmuir. 2006;22(18):7819-24.
281. Böhmler J, Ploux L, Ball V, Anselme K, Ponche A. The Journal of Physical Chemistry C. 2011;115(22):11102-11.
282. Suresh V, Madapusi S, Krishnamoorthy S. ACS nano. 2013;7(9):7513-23.
283. Li X, Iocozzia J, Chen Y, Zhao S, Cui X, Wang W, et al. Angewandte Chemie International Edition. 2018;57(8):2046-70.
284. Krishnamoorthy S, Pugin R, Hinderling C, Brugger J, Heinzelmann H. Nanotechnology. 2008;19(17):175301.
285. Anker JN, Hall WP, Lyandres O, Shah NC, Zhao J, Van Duyne RP. Nanoscience and Technology: A Collection of Reviews from Nature Journals. 2010:308-19.
286. Adams SM, Campione S, Caldwell JD, Bezares FJ, Culbertson JC, Capolino F, et al. Small. 2012;8(14):2239-49.

287. Müller MB, Kuttner C, König TA, Tsukruk VV, Förster S, Karg M, et al. ACS nano. 2014;8(9):9410-21.
288. Krishnamoorthy S, Krishnan S, Thoniyot P, Low HY. ACS Applied Materials & Interfaces. 2011;3(4):1033-40.
289. Dinda S, Yap FL, Suresh V, Gupta RK, Das D, Krishnamoorthy S. Australian Journal of Chemistry. 2013;66(9):1034-8.
290. Moronshing M, Subramaniam C. ACS Sustainable Chemistry & Engineering. 2018;6(7):9470-9.
291. Mondal S, Subramaniam C. ACS Sustainable Chemistry & Engineering. 2020;8(20):7639-48.
292. Kumar MK, Krishnamoorthy S, Tan LK, Chiam SY, Tripathy S, Gao H. Acs Catalysis. 2011;1(4):300-8.
293. Sarina S, Waclawik ER, Zhu H. Green Chemistry. 2013;15(7):1814-33.
294. Rastogi R, Beggiato M, Dogbe Foli EA, Vincent R, Dupont-Gillain C, Adam P-M, et al. The Journal of Physical Chemistry C. 2021;125(18):9866-74.
295. Rastogi R, Dogbe Foli EA, Vincent R, Poovathingal S, Adam P-M, Krishnamoorthy S. The Journal of Physical Chemistry C. 2021;125(16):8647-55.
296. Genzer J. Annual Review of Materials Research. 2012;42:435-68.
297. Cremmel CVM, Zink C, Maniura-Weber K, Isa L, Spencer ND. Langmuir. 2015;31(30):8446-52.
298. Beurer E, Venkataraman NV, Sommer M, Spencer ND. Langmuir. 2012;28(6):3159-66.
299. Hao H, Huang J, Liu P, Xue Y, Wang J, Jia F, et al. ACS Applied Materials & Interfaces. 2020;12(18):20243-52.
300. Bhat RR, Tomlinson MR, Genzer J. Journal of Polymer Science Part B: Polymer Physics. 2005;43(23):3384-94.
301. Nebhani L, Barner-Kowollik C. Advanced Materials. 2009;21(34):3442-68.
302. Reynolds PM, Pedersen RH, Riehle MO, Gadegaard N. Small. 2012;8(16):2541-7.
303. Kratochvil J, Stranak V, Kousal J, Kúš P, Kylian O. Applied Surface Science. 2020;511:145530.
304. Truica-Marasescu F, Wertheimer MR. Plasma processes and polymers. 2008;5(1):44-57.
305. Beamson G. The Scienta ESCA 300 Database. 1992.
306. Kromka A, Babchenko O, Potocky S, Rezek B, Sveshnikov A, Demo P, et al. 9 - Diamond nucleation and seeding techniques for tissue regeneration. In: Narayan R, editor. Diamond-Based Materials for Biomedical Applications: Woodhead Publishing; 2013. p. 206-55.
307. Zhang J, Han Y. Langmuir. 2008;24(3):796-801.